Fall 2021

From Persistent Radicals to Conductivity: A Structure Property Investigation in a Series of Urea-Tethered Halogenated Triphenylamines

Muhammad Saddam Hossain

FROM PERSISTENT RADICALS TO CONDUCTIVITY: A STRUCTURE PROPERTY INVESTIGATION IN A SERIES OF UREA-TETHERED HALOGENATED TRIPHENYLAMINES

by

Muhammad Saddam Hossain

Bachelor of Science
University of Dhaka, 2016

Submitted in Partial Fulfillment of the Requirements

For the Degree of Doctor of Philosophy in

Chemistry

College of Arts and Sciences

University of South Carolina

2022

Accepted by:

Linda S. Shimizu, Major Professor

Aaron K. Vannucci, Committee Member

Andrew B. Greytak, Committee Member

Guiren Wang, Committee Member

Tracey L. Weldon, Interim Vice Provost and Dean of the Graduate School

DEDICATION

Dedicated to my beloved wife, Taiyaba Sultana Sifat. Thank you for always helping me find the answers to my questions, for helping me think clearly, and for giving me the courage to try.

ACKNOWLEDGEMENTS

First and foremost, I would like to say ‘Praise be to Allah’ for everything. I am grateful to Allah for continuous mercies and blessings.

I would like to especially thank Dr. Linda Shimizu not only for being my supervisor but also a great human being. I am grateful and honored to have an advisor as kind as she is. She understands my shortcomings and guides me to become a better scientist every day.

Next, I would like to thank funding sources National Science Foundation (NSF) (CHE-1904386, CHE-1800140), (DE-SC0020272) and (OIA-1655740) for their financial support.

I must express my sincere gratitude to my collaborators Dr. Mark Smith, Dr. Sophya Garashchuk, Dr. Andrew Greytak, Dr. Stavros Karakalos, Dr. Anna Gudmundsdottir, Dylan Shields, Dr. Thanh Do, Aleksandra Antevska.

Lastly, I want to thank all of my fellow Shimizu group members, specially Dr. Bozumeh Som, Dr. Baillie Dehaven, Dr. Ammon Sindt, Dr. Dustin Goodlett, and Md. Faizul Islam.

ABSTRACT

Triphenylamines (TPAs) are known to form persistent organic radicals either by chemical, electrochemical or photoinduced oxidation. Typically, fully *para*-substituted TPAs form stable radical cations while the radical cations in partially substituted systems quickly degrade. Herein, we study the effects of solid-state organization on a series of urea tethered halogenated TPAs **1** (X = H, Cl, Br, I) and compare their radical cation formation and persistence after UV-irradiation. These halogenated urea tethered TPAs were examined by single-crystal X-ray diffraction where their assembly was guided by three-centered urea hydrogen bonding interaction. As expected, all compounds form photogenerated radical cations in solution, but the structures quickly degrade. In contrast, supramolecular assembly enhanced the stability and persistence of the radicals, which appear to undergo charge recombination without degradation. Greater quantities of these radical cations are observed for **1Br** and **1H**. Theoretical calculations on single molecules and hydrogen-bonded dimers with time-dependent density functional theory (TD-DFT) suggest that the charge transfer (CT) is feasible upon UV-irradiation, favoring an intramolecular process for **1Br** versus an intermolecular CT process in **1I**. In addition, electrical charge coupling leads to faster charge recombination in **1I** versus **1Br**. Further modification of the *para* positions with iodine leads to needle shape crystals that are organized by hydrogen and halogen bonding. We have investigated the relationship of CT and radical formation with mobility and conductivity measurements as conductive assembled TPA have particular importance as hole transporters in organic solar cells.

Chapter 1 provides an overview of urea tethered TPA linear and macrocyclic derivatives prepared in the Shimizu group and compared with literature examples. Chapters 2 and 3 examine how the supramolecular assembly of linear TPA frameworks controls the resulting charge/electron transfer of materials. Finally, Chapter 4 focuses on assembled fluorinated TPA *bis*-urea macrocycles. The goal is to use ^{19}F NMR to follow transient radical cation and anion species formed as the sample is UV irradiated. TD-DFT was employed to investigate the spin density distribution in this macrocycle and predict if the position of the fluorine is reasonable to report on the TPA radical cations.

TABLE OF CONTENTS

LIST OF TABLES

LIST OF FIGURES

LIST OF SCHEMES

LIST OF EQUATIONS

CHAPTER 1

UREA DIRECTED ASSEMBLY OF LINEAR AND MACROCYCLIC TRIPHENYLAMINE FRAMEWORKS: STRUCTURES, FUNCTION, AND APPLICATIONS

1.0 ABSTRACT

Self-assembly of photoactive and electroactive organic molecules can give rise to new functional properties. Triphenylamine (TPA) and its derivatives have the intrinsic capability to tune its functional features which can be further tailored by self-assembly and self-organization. Here we review strategies to organize TPA into tapes, fibers, and 1-dimensional channels with the goal of probing how self-assembly influences their properties and functional features. This chapter aims to introduce urea tethered TPA linear and macrocyclic derivatives prepared in the Shimizu group and to compare their structures with literature examples. Also, the structures, functions, and properties of these materials will be highlighted.

1.1 INTRODUCTION

The nitrogen-centered triphenylamine (TPA) core is an important redox-active organic building block, which is widely employed in photoactive and electroactive materials.[1] Organization of TPA by controlled supramolecular assembly affords well-defined architectures that can give rise to emergent properties. For instance, the Giuseppone group demonstrated that supramolecular polymerization of TPA can trigger new functionality and enhance ionic, photonic, and electronic properties.[2] When all its *para* positions are substituted, TPA can act as a stable electron donor material. Thus, it is widely used in organic solar cell,[3] donor-acceptor conjugates,[4] high-spin polymers,[5] magnetic materials,[6] perovskite solar cells,[7] and cathodes in batteries[8]. A number of reviews have focused on TPA as a hole transporter and examined synthetic/structural modifications with respect to performance in solar cells and optoelectronic applications.[1,3,9,10,11,12] The Shimizu group utilizes ureas to control the assembly of TPAs and study how organization

modifies its core functional features including photophysics, radical generation, and stability, conductivity.[13,14] This chapter examines urea tethered TPAs from the Shimizu group and compares their structures and organization to literature examples. Notably, complete *para*-substitution is a prerequisite for stabilizing the TPA radical cations. Otherwise, TPA derivatives rapidly degrade forming benzidine or degradation by-products.[15,16] Recently our group demonstrated that a self-assembly strategy is viable for stabilizing TPA radical cations with unsubstituted *para*-positions.[17] Ion mobility spectrometry mass spectrometry studies in the gas phase suggest assembled oligomers can resist degradation.[14] The urea assembled linear and macrocycle TPA analogs form photogenerated radical cation/anion pairs.[13] The formation of these charged species is a reversible process and the kinetics of charge recombination likely depends on the organization of TPA within assembly motif. Controlled organization of these materials into crystals will aid understanding the architecture and specific structures which facilitate charge transfer and other processes.

1.2 INTRODUCTION INTO SUPRAMOLECULAR ASSEMBLY

Self-assembly implies the *spontaneous* generation of multi-component molecular systems into functional, ordered structures with little or no external stimuli.[18] Both covalent and non-covalent interactions can be utilized to self-assemble a simple molecule into supramolecular architecture. Covalent interaction is mainly driven by enthalpy to form the kinetically stable product. While the non-covalent interactions are driven by the balance between the enthalpy and entropy to form thermodynamically equilibrating products.[19] The non-covalent interactions include hydrogen bonding, π-π interactions, dipolar interactions, van der Waals forces, electrostatic and hydrophobic interactions.[20] These directional

interactions order simple molecular entities into hierarchical structures often with new properties. Some examples of properties that can be altered include proton conductivity,[21] antiviral applications,[22] CO_2 capture,[23] and solid-state dichroism.[24]

The directional stacking of disc-like molecules or macrocycles is a simple method for generating hierarchical structures, which has been employed with great success.[25]

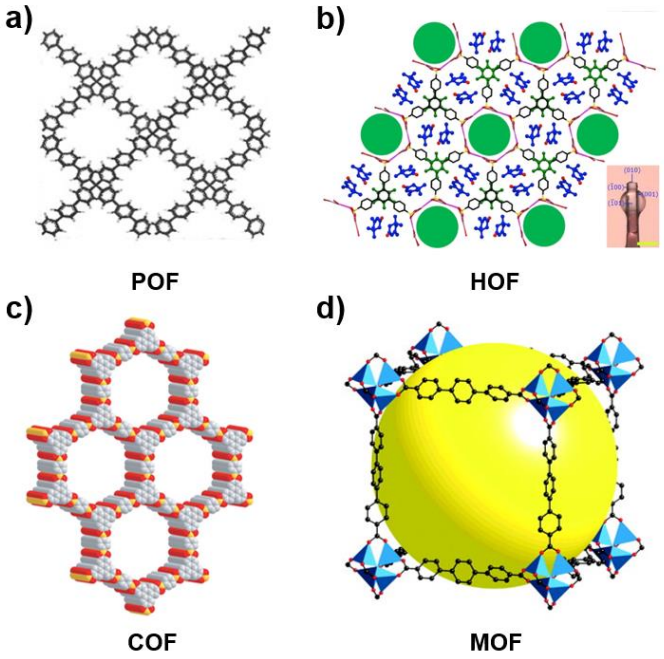

Figure 1.1. Different types of porous frameworks. a) Porous organic framework (POF) (ref 31). b) Hydrogen bonded organic framework (HOF) (ref 32). c) Covalent organic framework (COF) (ref 33). d) Metal organic framework (MOF) (ref 34).

Examples of these hierarchical structures ranging from cylindrical peptides,[26] carbohydrate nanotubes[27] to phenylacetylene macrocycle,[28] nanotubes of block copolymers.[29] Usually these materials are porous with 1-dimensional (1D) channels. Later another class of hierarchical structures emerged which self-organize into 1D or 3D architectures driven by both covalent and non-covalent interactions. These frameworks can be classified as porous organic frameworks (POF),[30] hydrogen-bonded organic frameworks (HOF),[31] covalent organic frameworks (COF),[32] metal-organic frameworks (MOF)[33]. These frameworks are

depicted in Figure 1.1. These frameworks contain pores that are usually filled with guest molecules. Such materials are useful for sensing,[34] catalysis,[35] storage,[36] separations.[37] Depending on the starting molecule and building block, the topology of the structure can vary from 3d network to 1D channel.

Simple, 1D channels are advantageous as they are readily modeled by multiple computational approaches.[38] The Shimizu group utilizes the self-assembly of *bis*-urea macrocycles to organize functional solid-state materials.[39,40] The initial design constitutes

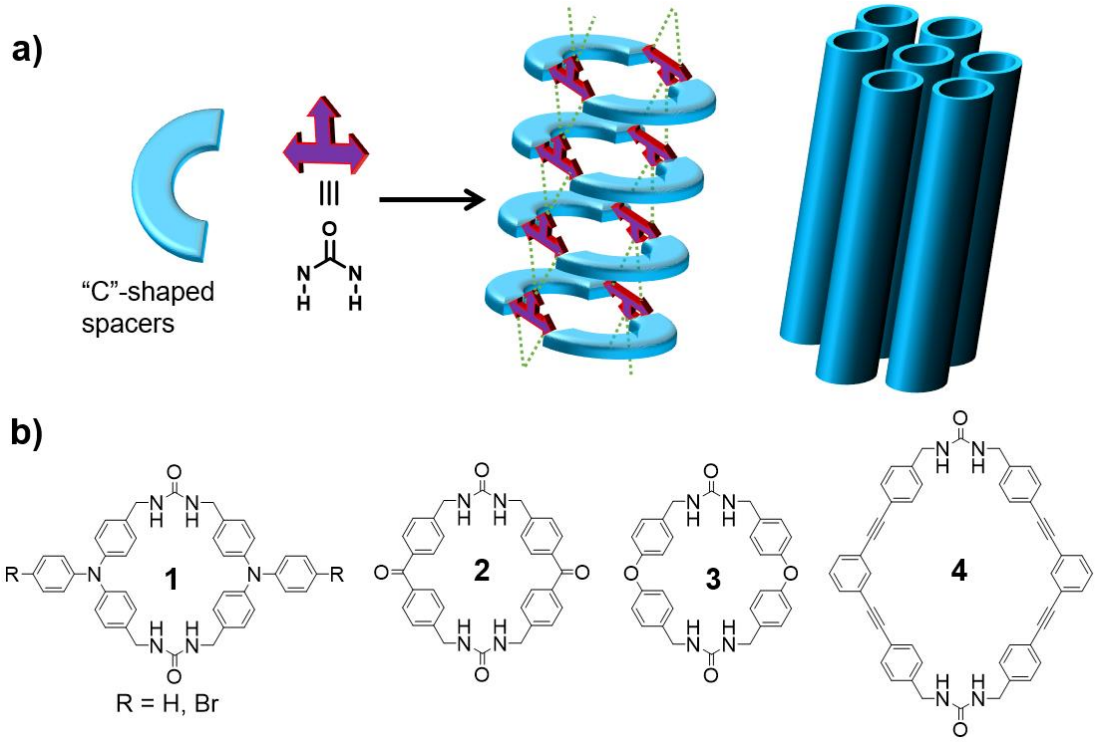

Figure 1.2. Overview of bis urea macrocycles (**1**-**4**). a) Each macrocycle contains two C-shaped spacers and two urea groups which self-assemble into 1-dimensional channel using urea hydrogen bonding interaction. b) Examples of bis-urea macrocycle prepared previously.

of attaching two rigid C-shaped spacers with two methylene urea groups to generate macrocyclic frameworks (Figure 1.2). Key to the design, is a relatively planar macrocycle structure in which the urea groups are approximately perpendicular to the macrocycle and

able to assume their preferred *trans-trans* conformation. Upon assembly, these frameworks are guided into hierarchical structures through three centered urea-urea hydrogen bonding and favorable aryl-aryl stacking interactions. This affords a porous structure with homogeneous channels which can be utilized to study processes of adsorption,[41] diffusion,[42] confinement of guest,[43] and reactions in low dimensional environments.[44] These functional nano-containers have found suitable applications for selective photocycloaddition,[45] photooxidations,[46] and polarizing agents[47]. Linear systems with two spacers and one methylene urea group provide controls, which are typically non-porous.[48]

Organizing TPA into ordered structures is important for its stability and tunable photophysical and electronic properties. Prior work focused on TPA with covalently appended electron acceptors, which then exhibit electron transfer from the TPA donor to acceptors.[49–52] Our work focused on how we can modulate these functional properties intrinsic to TPA, investigate structure-property relations, and include electron donors through host-guest chemistry. To date, TPA based host-guest system were formed either by doping guests on TPA matrices[53–55] or host-guest inclusion complex where TPA act as a guest[56,57].

In this chapter, we will first summaries structures and assemblies of methylene urea tethered TPA dimers and macrocycles. Then we will examine the formation and stability of its radical cations generated by electrochemical, and photoinduced processes where only neighboring TPAs are available as electron acceptors. The electron transfer mechanism will be probed by time-dependent density functional theory (TD-DFT). Finally, we will examine systems where favorable electron acceptors are included within the channels of the TPA macrocycles. Interestingly, a number of these systems include TPAs where the

phenyl groups have one or more unsubstituted *para* positions, which should be prone to degradation. Yet supramolecular assembly of these compounds afford greater stability of these radical cations. For example, in solution unassembled bromo substituted urea tethered TPAs generate persistent radicals upon UV irradiation but then degrades in minutes.[17] Once organized via urea hydrogen bonding, the photogenerated radicals are long-lived and show no signs of degradation, likely undergoing the reverse electron transfer to return to starting materials. We will further discuss the structural dynamics of the urea tethered TPAs related to the functions and applications.

1.3 OVERVIEW OF TPA BASED MACROCYCLE

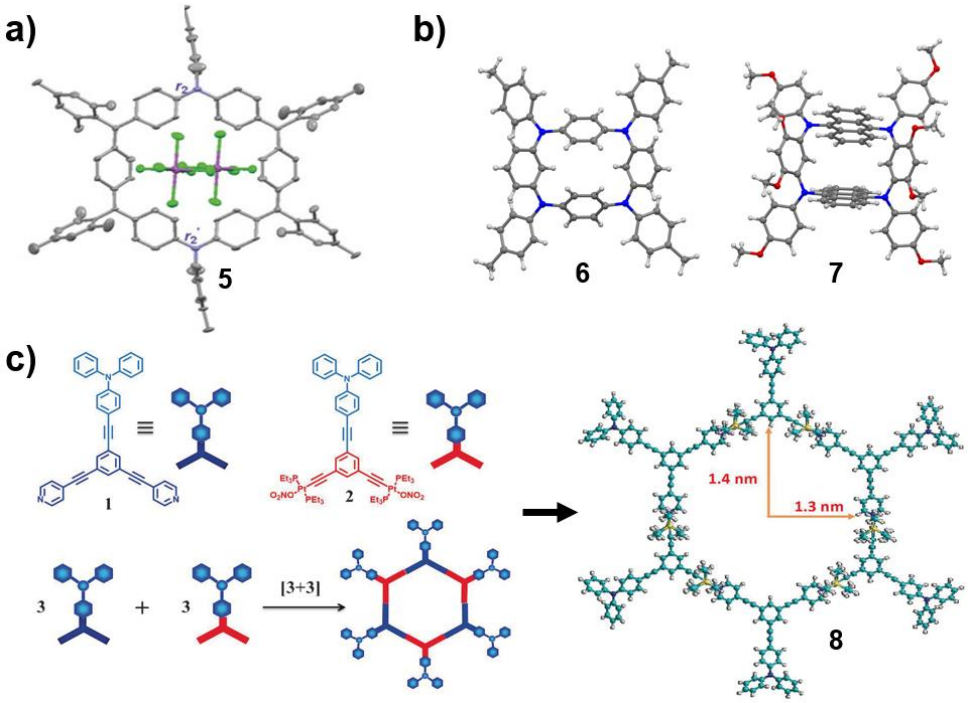

Figure 1.3. Examples of TPA based macrocycles **5** (ref 60), **6, 7**, (ref 61), **8** (ref 62). a) TPA and *para*-quinodimethane containing macrocycle **5**. b) Single crystal structure of *meta-para*-linked tetraazacyclophanes **6** and 9,10-anthracenylene moieties **7**. c) Graphical representation of assembly of TPA based metallacycle **8**.

TPA-based macrocycles have unique photophysical and electronic properties with potential applications in optoelectronic devices.[58] The *para* position of the exterior phenyl

group can be modified, providing flexibility to tune the functional nature of the macromolecule. For instance, the Chi group designed a π conjugated macrocycle

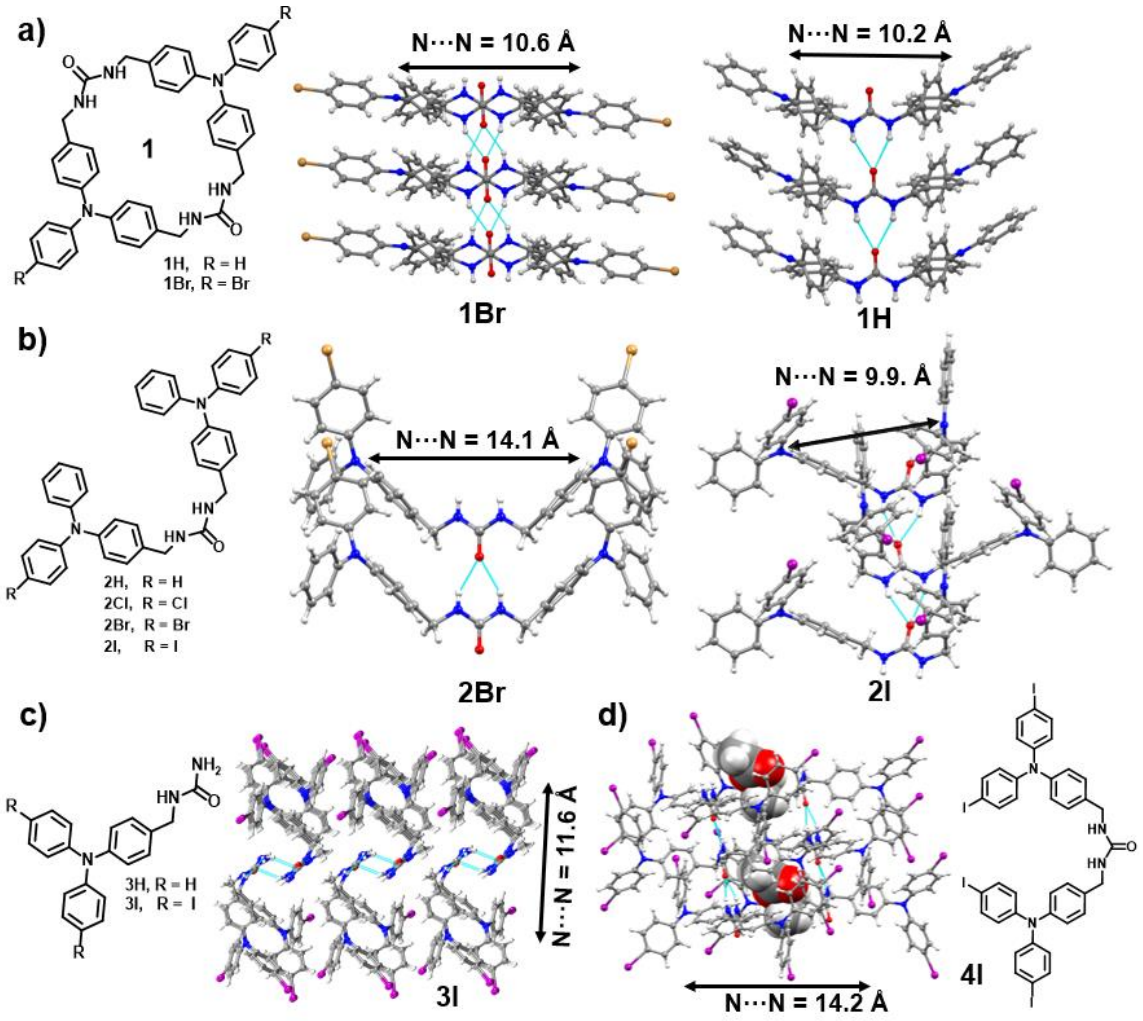

Figure 1.4. Urea tethered TPA Macrocyclic and linear structures, and control. N···N distance were measured between two N center tethered to same urea. a) TPA bis urea macrocycles chemdraw (left), hydrogen bonded urea tape showing anti conformation for **1Br** (middle), syn conformation of urea tape in **1H**. b) urea tethered linear structures chemdraw (left), hydrogen bonded crystal structure of **2Br** (middle), **2I** (right). c) TPA unit tethered to one side of urea chemdraw (left), crystal structure showing interchain hydrogen bond between two independent single TPA tethered to urea **3I** (middle), urea tethered TPA where both the exterior *para* position substituted by iodine (right).

containing alternating TPA and the *para*-quinodimethane group as can be seen in Figure 1.3a.[59] Depending on the ionic state (dication/tetracation), the macrocycle shows globally aromatic/antiaromatic character at low temperatures. The Ito group crystallized two kinds

of TPA-based macrocycle contain alternate-*meta-para*-linked tetraazacyclophanes and 9,10-anthracenylene moieties (Figure 1.3b).[60] Both the macrocycle are isolated as diradical dications. Surprisingly, the spin density distribution of the macrocycles can be tuned by coordinating with SbF_6^- salt shows either ferromagnetic or antiferromagnetic coupling between TPA and anthracenylene moieties. In these examples, the TPA unit is used as a building block of the macrocycle. TPA can also act as a handle to drive the self-assembly process. For example, Prof Yang and his group constructed porous metallacycles by coordination-driven self-assembly of TPA units which can be seen in Figure 1.3c.[61] This self-assembly is guided through electropolymerization of individual metallacycles unit.

1.4 OVERVIEW OF TPA BIS UREA STRUCTURES

Urea is a well-studied assembly motif, that has been used to assemble organic molecules into fibers, tapes, sheets, columns, capsules, and gels.[62,63] For the organization, hydrogen bonds play a key role which is reflected by the excellent α and β values of urea NH and urea oxygen (α = 3.0, β = 8.2).[64] TPA bis-urea macrocycles assembled through bifurcated urea hydrogen bonding interaction where the ureas in **1Br** alternate and are arranged in *trans* conformation compared to *cis* conformation for **1H.** (Figure 1.4). The size and shape of C shaped spacer control the pore aperture and functional property of the channel. Table 1.1 compares the dimensions of channel, void space, and intercolumnar stacking interactions for a small series of bis-urea macrocycles. On average, each macrocycle unit is spaced ~4.7 A away from each which is the urea repeat distance. Linear TPA dimers tethered through a methylene urea bridge as well as single TPA urea derivatives were prepared and crystallized to examine the effects of their organization on their photophysics and radical generation (Chapter 2).

Table 1.1. Structures and stacking comparison of different *bis*-urea macrocycles

Macrocycle Spacer	Approximate Pore Size (Å)[a]	Void Space (% per unit cell)[b]	Urea Repeat Distance (Å)	Inter-columnar π-stacking
Meta-xylene[65]	1.0 x 1.4	0	4.62	Offset π-stacking
Triphenylamine (in **1H**)	4.3 x 6.4	13.0	4.85	Edge-to-face
4-Bromotriphenylamine (**1Br**)	4.3 x 6.5	10.1	4.62	Offset π-stacking
Phenyl Ether[66] (in **3)**	4.5 x 6.7	14.5	4.65	Edge-to-face
Benzophenone (in **2**)	5.0 x 7.1	14.9	4.72	Edge-to-face
m-di(phenylethynyl)xylenene (in **4)**	8.4 x 13.0	22.2	4.69	Alkyne phenyl stacking

[a]Calculated in angstrom (Å) by subtracting the vdw radii, measured the distance between opposing carbonyls and diagonal hydrogens. [b]Initial guest were removed to make an empty channel and performed a contact surface void calculation in Mercury (probe radius 1.2 A, grid spacing 0.1 A)

The pore sizes vary from 1.0 X 1.4 Å represents the smallest spacer *m*-xylene to the largest spacer *m*-di(phenylethynyl)xylenene with pore size 8.4 X 13.0 Å which can be seen in the spacefill model in Figure 1.5a. These *bis*-urea macrocycles assemble into similar columnar structures but show different interior channel topology, depicted in Figure 1.5b. The small *m*-xylene spacer affords a macrocycle with no guest accessible pore. However, C-shaped spacers with larger diameters afford crystalline macrocycles with void spaces that can range from 10 – 22 % per unit cell. In the triphenylamine **1H** and bromo-triphenylamine **1Br**, the interior channel oscillates back and forth due to the propeller shape of the TPA phenyl rings, which stack by edge-to-face and offsets π stacking interactions. In comparison, macrocycle **4**, with its more planar C-shaped spacer di(phenylethynyl)xylenene, generates a smooth channel through alkyne phenyl stacking interactions. The channel of the benzophenone **2** is slightly distorted, gently oscillating back and forth due to the edge-to-face π stacking interactions, depicted by void space calculations.

1.5 OVERVIEW OF TPA SUPRAMOLECULAR ASSEMBLY

In general, packing of the TPA units within supramolecular structures is governed by a limited number of parameters that influence its functions and applications. The phenyl

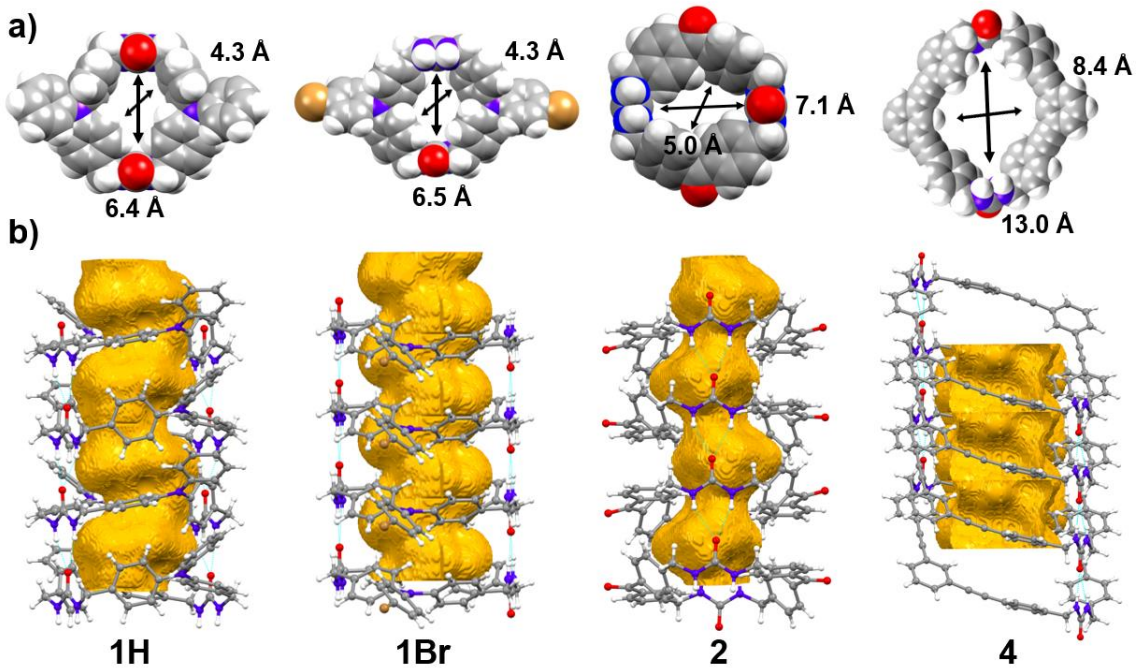

Figure 1.5. a) Comparison of pore sizes of different *bis*-urea macrocycles. Calculated by subtracting the vdW radii. From left, urea spacers are triphenylamine (**1H**), 4-bromotriphenylamine (**1Br**), benzophenone (**2**), phenylethynylene (**4**). b) Comparison of 1-dimensional column and corresponding void space.

groups of the TPA can interact with each other in a single supramolecular column or in between distinct columns. The *para* substituents effect the stacking behavior but also act to stabilize of the TPA core. Giuseppone and his co-workers performed an extensive study of the packing of TPA units and its effects in the photo- and electronic behavior of TPA supramolecular polymers. Figure 1.6 shows their formation of 1D supramolecular polymers, which is promoted by the packing of TPA units in favorable snowflake or Mercedes-Benz conformations (Figure 1.6a, b).[67] Giuseppone group observed these conformations by combining molecular simulations with small-angle X-ray scattering

(SAXS) data. These experiments suggest edge-to-face π stacking favored the snowflake conformation while face-to-face π stacking formed Mercedes-Benz conformation. In the

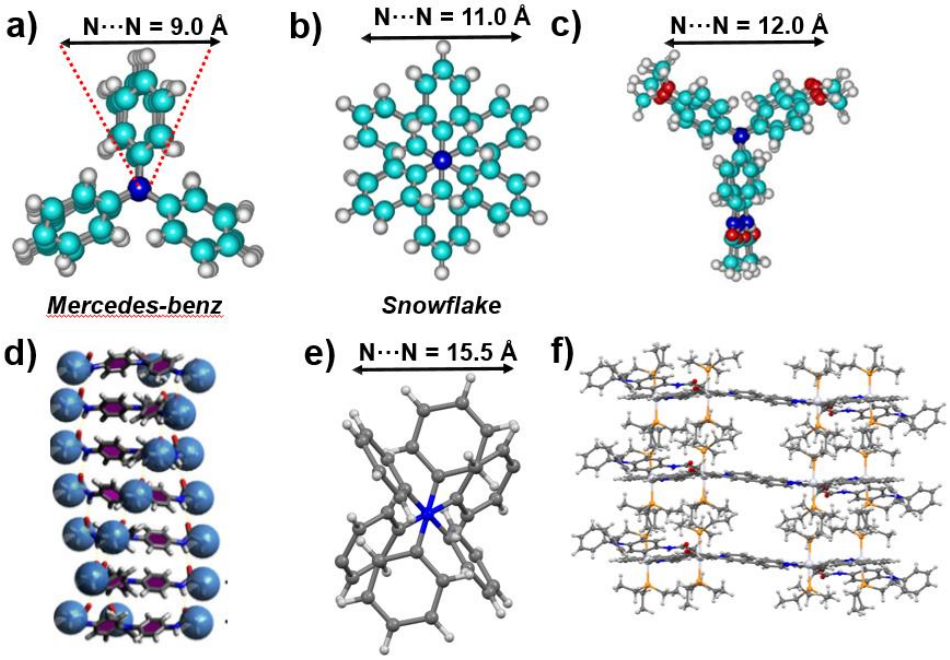

Figure 1.6. a) Modeling of molecular arrangement of TPA within 1D stacks by Giuseppone group (PM3, Amber96). a) Mercedes-benz conformation. b) Snowflake conformation. c) Pattern of triarylamine molecules. d) Assembly of TPA supramolecular polymers showing helical type structure (Atomic Force Microscopy (AFM) image). e) packing of TPA undergoes photoinduced self-assembly. f) Packing structure of TPA radical induced supramolecular coordination cages.

case of Mercedes-Benz conformation, slight rotation (1.5º) of the TPA core gives helical structures which are depicted in Figure 1.6d. The N···N distance can vary from 9 Å to 11 Å depending on Mercedes-Benz and Snowflake conformations respectively. These conformations are thought to help conduction of charged nanocarriers as well as the self-healing capability of the supramolecular synthons.[2] Yang and his co-workers show TPAs at the exterior of the metallacycles maintained a planar conformation which facilitates radical-induced hierarchical self-assembly.[68] Structural investigation suggests the formation of distorted snowflake conformation with longer N···N distance 15.5 Å as can be seen in figure 1.6e-f.

1.6 ASSEMBLY OF TPA UNITS IN BIS-UREA STRUCTURES

With Giuseppone's observed that these Snowflake and Mercedes-Benz conformations are likely stabilizing radicals and aid delocalization of charges within the stacks in their systems, we interested examining our methylene urea tethered systems,

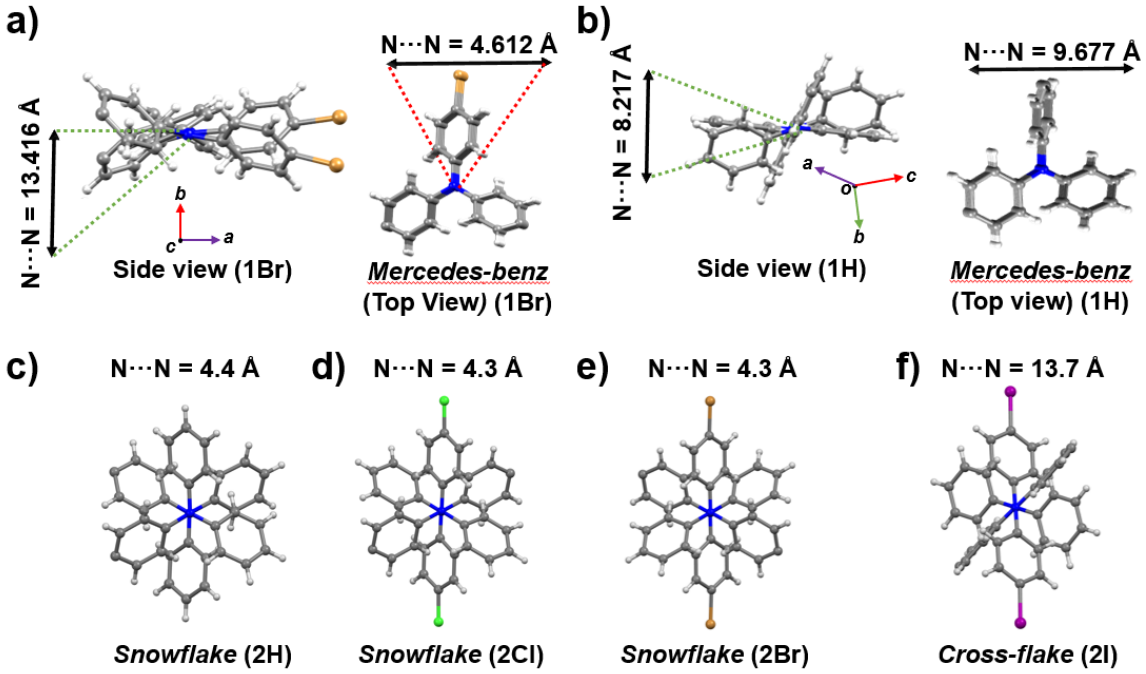

Figure 1.7. Orientation and packing of TPA units. Methylene urea and non-relevant parts were removed for clarity. Distance were measured fron N center to nearby N center. a-b)Packing and orientation of TPA units of macrocyclic **1Br**, **1H** (from left) in side and Top views. Top views show MercedesBenz stacking conformations. c-f) Packing and orientation of TPA units of linear **2H**, **2Cl**, **2Br**, **2I**. Top views shows Snowflake conformation for **2H**, **2Cl**, **2Br** and crossflake for **2I**.

whose structures are characterized by single-crystal X-ray diffraction. Do these systems show comparable snowflake or Mercedez-Benz conformations? Are these conformations important for stabilization of separated charges? Do they contribute to charge delocalization and modulate charge recombination?

Early depictions of TPA macrocycles (**1Br**, **1H)** and linear analogues highlight the assembled columns and tapes formed by the urea self-association (Figure 1.4b). However,

the packing of these 1-dimension columns/tapes is influence by interactions between the individual TPAs. Closer analysis of the SC-XRD shows that TPA in these systems indeed adopt both the Mercedes-Benz and snowflake conformations (Fig 1.7). The main molecular parameters that dictate the packing of the TPA units are (i) partial *para* substituents

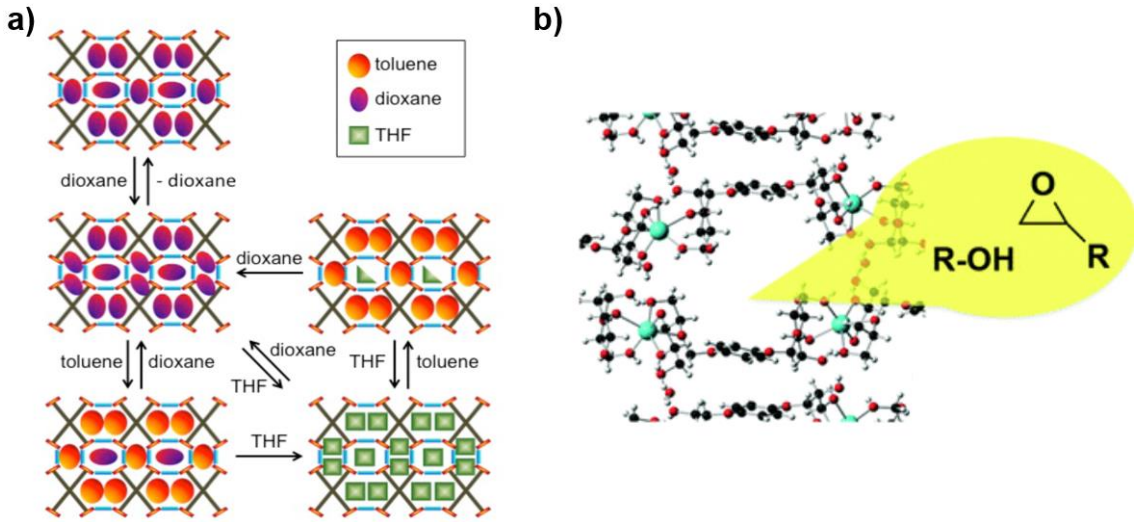

Figure 1.8. Examples of SC-SC transformation. a) Schematics of SC-SC transformation in hydrogen bonded framework. b) SC-SC transformation in a co-ordination network.

halogen/hydrogen (**1Cl**, **1Br**, **1I**/**1H**), (ii) the number of urea groups tethered to TPA, and (iii) the propeller/helical pitch of the TPA center. Viewed down the c-axis, **1Br** clearly adopts a Mercedes-Benz conformation as can be seen in Figure 1.7a (top view). **1H** also formed Mercedes-Benz conformation with slightly rotated external phenyl rings. Interestingly, the presence of heavy atom bromine decreases the packing distance of the intermolecular TPA N···N center from 9.6 Å for **1H** to 4.6 Å for **1Br**. The presence of bromine at the exterior phenyl ring promotes halogen-π and π-π stacking interactions which helps for close packing of TPA units. This was further suggested by Hirshfeld surface analysis and the observed the Br···C_{aryl} distance of 3.303(3) Å which is less than the sum of the vdW radii (3.5 Å). The exterior phenyl rings rotate out of the plane for **1H** while

increasing the distance of the packed TPA units through longer edge-to-face π-stacking interactions.[13]

Next we further investigate these conformation in urea tethered TPA linear derivatives. TPA derivatives **2H**, **2Cl**, **2Br** adopt Snowflake conformation as can be seen in Figure 1.7c-e. Contrary to macrocycle halogen bond formation increases the distance between packed TPA units while **2I** containing multiple halogen bond interactions with longer intermolecular N···N distance 13.7 Å compared to **2H**, **2Cl**, **2Br** with N···N distance 4.3 Å.[14]

1.7 SINGLE-CRYSTAL-TO-SINGLE-CRYSTAL (SC-SC) GUEST EXCHANGE

The robust architecture of a low dimensional channels are readily monitored and be loaded with guests, carefully selected to match the size, shape and polarity of the pore. In this process, sometimes the host framework retains its rigidity or crystallinity during this exchange process readily transforming from one crystal structure to a second crystal structure. This process is also known as single-crystal-to-single-crystal (SC-SC) guest exchange. A nice example of these reversible exchange processes was reported by the Ward group.[70] They showed the SC-SC transformations of a flexible hydrogen-bonded framework through release and adsorption of guest molecules, which can be seen in Figure 1.8a. A crystalline sponge from the Fujita group consisting of a mannose-based organic ligand and sodium ion through a coordination network is shown in Figure 1.8b.[71] This 'sugar sponge' network undergoes SC-SC transformations, exchanging diethyl ether with *n*-propyl alcohol. While experimental evidence suggests other bis-urea macrocycles load guests without disturbing the assembled framework, TPA macrocycle **1Br** was the first time our group had observed SC-SC guest exchange.[13] The additional intercolumnar

packing of the TPAs facilitated the assembly of **1Br** into larger needle shaped crystals, ~35 X 265 μm that were easier to handle and showed remarkable SC-SC guest exchange capability. Thermogravimetric analysis (TGA) can be used to monitor the guest removal

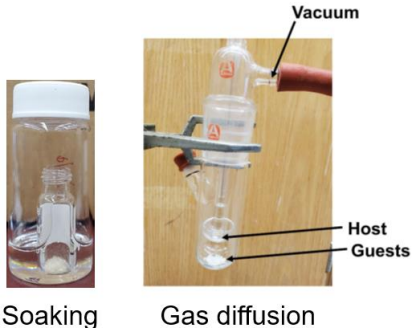

Figure 1.9. Experimental setup of guest loading methods in activated host **1Br**.

of host **1Br**. TGA of **1Br**·DME displays one-step desorption curves losses 5.3% between 0 and 90°. The rigidity of the empty host framework was monitored by SC-XRD compared with **1Br**·DME. Notably, the frameworks and packing of emptied host **1Br** were nearly identical with the **1Br**·DME with only the electron density of the DME missing. Further investigation of the pore aperture and intra-channel diffusion in **1Br** was done using ^{129}Xe NMR and ^{129}Xe PFG NMR experiments. The symmetric chemical shift anisotropy (CSA) powder pattern was observed with δ_{iso} = 217 ppm upon cooling from 295 k to 243 K. These studies suggest high Xe loading and inter-columnar pores are suitable for loading guest with similar dimension (vdW diameter 4.4 Å). The qualitative estimation of the exchange of Xe atoms between the channels and the surrounding of the host **1Br** crystal by ^{129}Xe PFG NMR suggests gas diffusivity of 6.7 X 10^{-7} m^2 s^{-1} at 298 k with no noticeable attenuation of the line corresponding to Xe atoms adsorbed in the channels. These results

suggest that there are no defects in the channel walls and that the architecture is retained upon removal of guests.

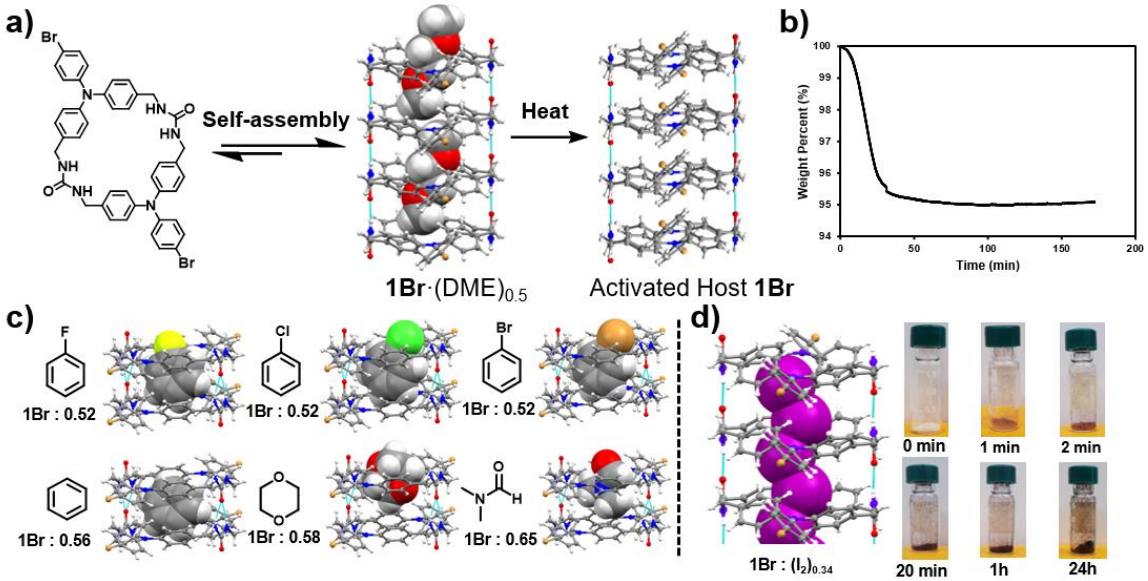

Figure 1.10. a) Bromo-substituted TPA bis urea macrocycle. Vapor diffusion of DME into DMSO solution generate 1D channels. Guest removed by heating. b) TGA graph showing one-step desorption curve of DME from **1Br**· $(DME)_{0.5}$ c) New guest loaded into the emptied host. SC-SC transformation afford host-guest complex. d) Single crystal structure of host **1Br**.$(I_2)_{0.34}$. Pictorial view of iodine loading over time.

Guest were loaded in the empty host **1Br** by two different loading methods: soaking and vapor diffusion (shown in Figure 1.9). In the soaking method, the activated crystals were immersed into the liquid guest (1 mL) for 1 day at room temperature. This method works best for materials that are liquid at ambient conditions, such as the halo-benzenes. In the vapor diffusion method, guests with low vapor pressures, such as I_2 exposed to the activated crystals. Alternatively, solid guests, such as dichlorobenzoquinone, could be heated to their sublimation temperature in a sealed vessel under vacuum and exposed to the activated crystals.

1.8 MODULATION OF RADICAL GENERATION BY HOST-GUEST INCLUSION COMPLEX

Organic radicals, contain unpaired electrons, are highly reactive to form dimers and polymers or may be quenched by environmental factors at ambient conditions.[72] It is

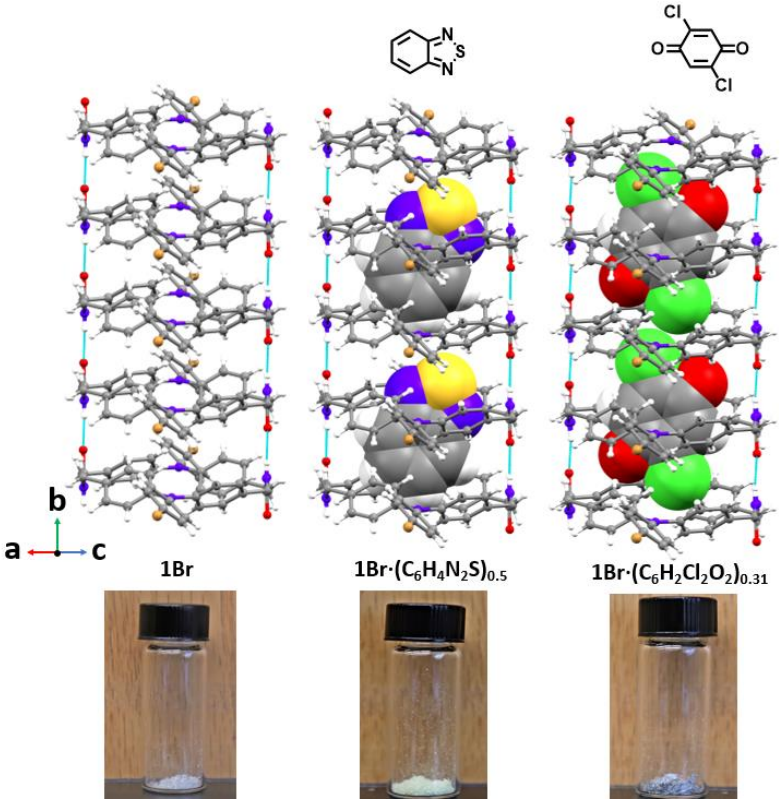

Figure 1.11. Columnar 1-dimensional channel of host 1Br. Two inclusion complexes obtained through SC-SC guest exchange. Pictorial view in bottom shows changes of color upon formation of inclusion complex.

possible to stabilize the organic radicals by careful control of the paramagnetic center, through either steric protections. TPA and its derivatives are also known to form persistent radical cations by chemical, electrochemical, and photoinduced irradiation. TPA *bis*-urea macrocycles exhibited enhanced stability of radical cations generated by photoirradiation using 365 nm UV LEDs.

In the assembled macrocycles, guests bound in the channel are in close proximity to the TPA moiety and thus likely to modulate the radical generation and lifetime. These guests were carefully chosen considering the polarity and heavy atoms, as both are known to influence photophysics and stability of radicals.[13] These photogenerated radicals can be monitored by EPR spectra as shown in Figure 1.12. Summarize the polarity of the guest on radical formation first. The size and shape of each EPR spectra were different suggest the local chemical environment of the radical center was modulated by the formation of the host-guest inclusion complex. It was observed that guest with higher polarity 1,4 dioxane and DMF generates less radical 0.38% and 0.15% as compared with 0.85% for C_6H_6.

Heavy atoms can facilitate spin-orbit coupling and populate triplets by faster ISC rate which is known as the heavy atom effect. Next, we set to explore the effect of guests containing heavy atoms on radical generation. To test this, mono-halogenated benzene

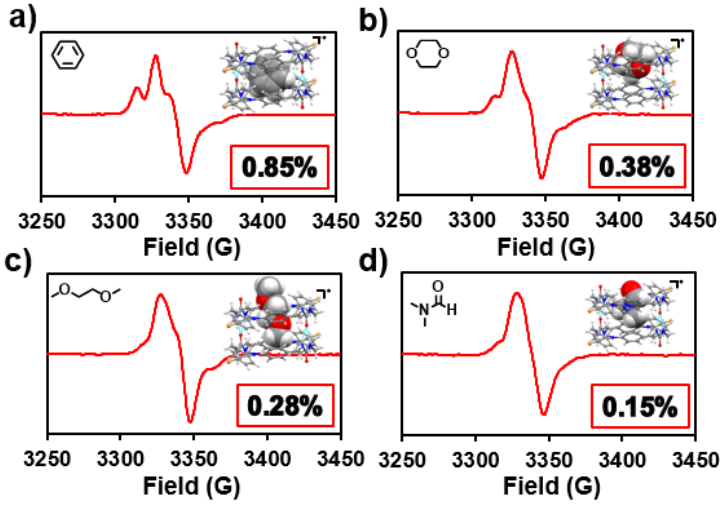

Figure 1.12. Host-guest complex of **1Br** generates radicals upon UV irradiation using 365 nm UV LEDs. EPR spectra of 4 these complexes were given. Inset shows the single crystal structure and maximum percent radicals generated compared with a calibration curve of standard concentration of magic blue in dry DCM.

derivatives were separately loaded into host **1Br**, generating a set single crystals with

benzene, fluorobenzene, chlorobenzene, bromobenzene and iodobenzene. Surprisingly, the guest containing heavy atoms such as **1Br**·C_6H_6Br generates less radical 0.23% compared with 0.85% radical for **1Br**·C_6H_6. Similar behavior was observed for a series of host-guest inclusion complexes.[13] After decay, likely through a reverse electron transfer process, the radicals in the host-guest inclusion complex could be regenerated simply by reexposure to the UV light. The derivatives that contain only one TPA unit **3H**, **3I** (Figure 1.4) do not generate significant amounts of radicals, suggesting the bridged TPA units tethered are important in this system.

1.9 EFFECT OF SELF-ASSEMBLY AND HEAVY ATOMS ON RADICAL GENERATION

Urea tethered TPA dimers (**2H**, **2Cl**, **2Br**, **2I**) were synthesized and crystallized where one of the *para* positions of the external phenyl rings was substituted by halogen

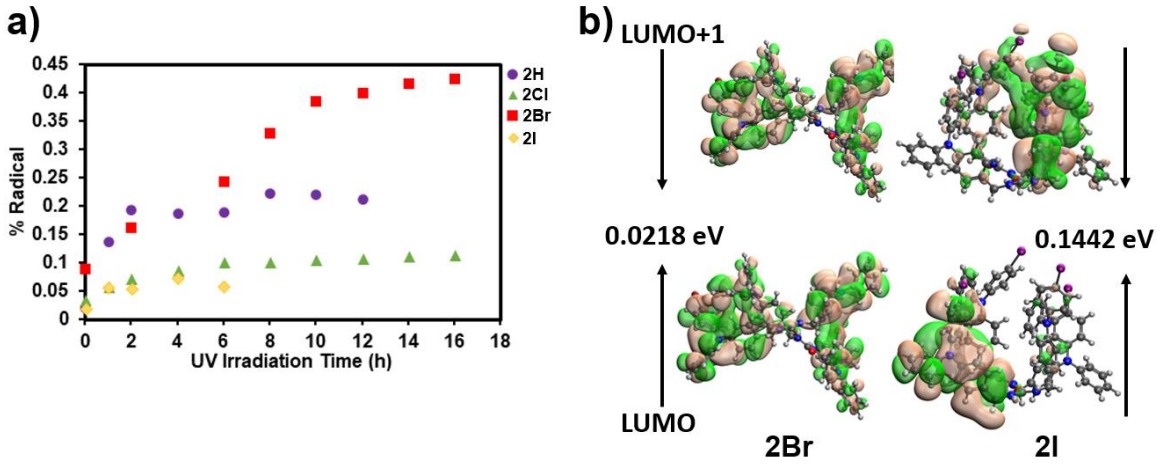

Figure 1.13. a) Percent radical formation as a function of UV irradiation time compared with a calibration curve of standard concentration of magic blue in dry DCM. b) Electrical coupling calculation of hydrogen bonded dimer **2Br** and **2I**.

(Cl, Br, I).[14] Derivatives **2H**, **2Cl**, **2Br** formed anti-parallel extended TPA conformation with average TPA N···N distance 14.1 Å. In comparison, **2I** formed a U shaped conformation with TPA N···N distance 9.9 Å. Radicals were found stable in the solid state

compared with unsubstituted TPA dimers. While **2Br** generates the highest percent radical 0.42% with half-life ~7 days, TPA dimer **2H** missing key *para* substituents making a significant amount of radical 0.22%. Surprisingly TPA dimer **2I** generates the least amount

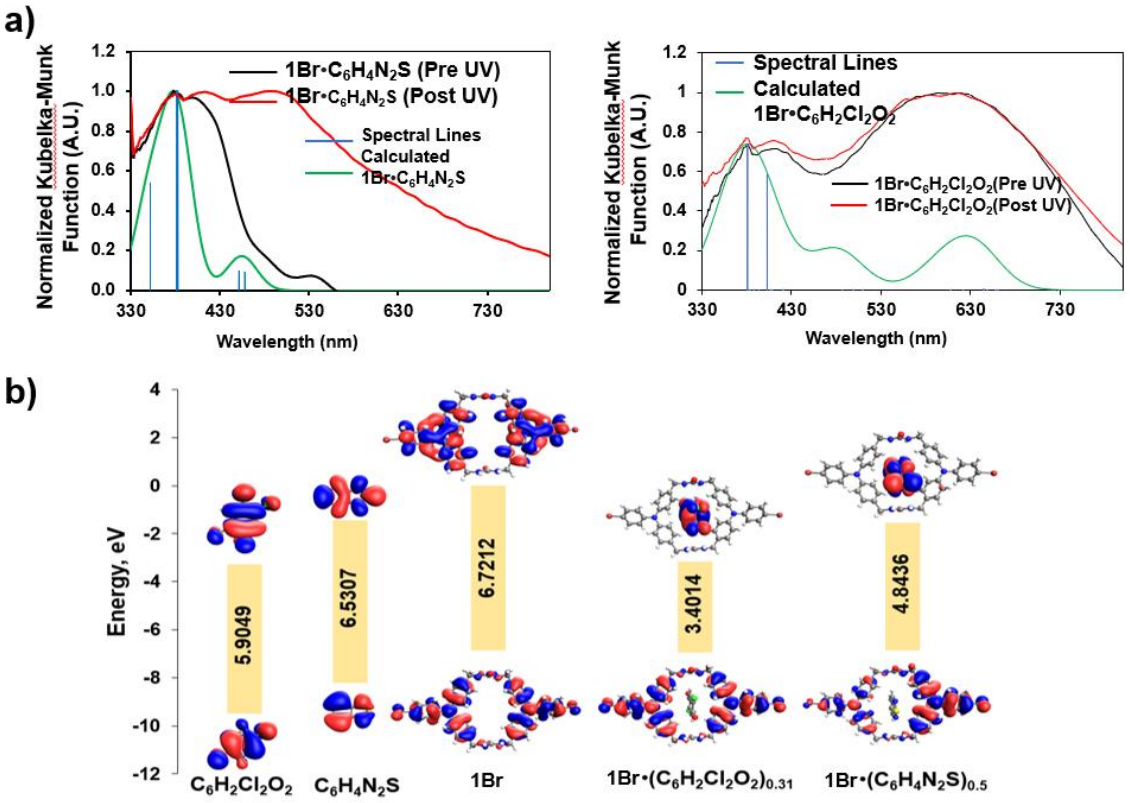

Figure 1.14. a) Comparison of pre and post-UV irradiated diffuse reflectance spectra of the host-guest inclusion complex. b) Frontier molecular orbitals and corresponding HOMO-LUMO gap of guest, host, and host-guest complex.

of radical 0.06%. TD-DFT calculation suggests charge transfer is feasible in these urea tethered TPA dimers. Electron density distribution in frontier orbitals suggests the formation of intramolecular charge separation for **2Br** compared to intermolecular charge separation for **2I**. Comparison of electrical coupling values for the hydrogen-bonded dimer calculation manifests charge recombination would be 7 times faster in **2I** compared to **2Br** further support the long lifetime of TPA radicals for **2Br**. Further details on these studies are presented in Chapter 2.

1.10 PHOTO-DRIVEN ELECTRON TRANSFER IN TPA BIS UREA MACROCYCLE

The oxidation potentials of activated host **1Br** were measured as 1.46 V and 1.86 V vs $Fc^{+/}Fc$, which should be accessible through photoirradiation. To test the potential of electron transfer, two-electron acceptor guest (2,1,3-benzothiadiazole and 2,5-dichloro-1,4-benzoquinone) were carefully chosen based on their size and favorable reduction potential (E_{red} = -1.12 V and 0.2 V vs Fc^{+}/Fc). In solid-state diffuse reflectance experiments, activated host **1Br** showed a single band at 366 nm, upon formation of the inclusion complex with 2,1,3-benzothiadiazole a new band arises at 399 nm, suggesting the possibility of formation of the donor-acceptor complex. Upon UV irradiation using 365 nm LEDs, a new broad third band arise at 486 nm, which was characterized as a photo-driven charge transfer band. In the case of 2,5-dichloro-1,4-benzoquinone with its more favorable reduction potential, the CT band at 594 nm is present upon formation of the inclusion complex. Furthermore, TD-DFT calculation suggests the Homo-Lumo gap can be tuned upon by the formation of donor-acceptor inclusion complex as can be seen in Figure 1.14.

1.11 CONCLUSION

In summary, the functional features of TPA can be tuned by self-organization by supramolecular polymerization, coordination, or urea guided crystallization. The Shimizu group has investigated the effects of solid-state assembly on a methylene urea tethered TPA linear analogs and *bis*-urea macrocycles. A series of partially *para*-substituted urea tethered halogenated TPA linear derivatives were synthesized and crystallized to investigate the effect of self-assembly and partial *para* substitution on radical generation, stability, and

lifetime, which will be the focus of chapter 2. Radical stabilization was not limited to the linear structures but was also observed in the assembled macrocyclic units.[13] In the macrocycles all the *para* positions are carefully blocked, which aids in stabilizing the radical cations formed. The 1-dimensional channel formed by the assembly of macrocycles offers a new handle to both study how the environment around the radical cation effects its persistence. The TPA *bis* urea macrocycles exchange guests in remarkable single-crystal single-crystal (SC-SC) transformations,[73] enabling detailed study of the effects of structure and proximal guests on radical generation and persistence. In addition, the bandgap of the TPAs can be tuned by adsorbing guests with favorable reduction potentials that can undergo charge transfer or triggered, photo-driven electron transfer. The utility of these materials was tested by probing the electrical conductivity on single crystals and in thin films, which will be discussed in chapter 3. The radical cation was characterized by EPR, cyclic-voltammetry, and transient absorption spectroscopy. However, the radical anions remained outside the window of the transient absorption studies. Further characterization of the radical anions remains an important parameter to study with the goal of understanding the kinetics of charge separation and recombination in these systems. Therefore, a new urea tethered TPA macrocycle was synthesized and crystallized with fluorine reporter group in the exterior *para* positions. Structural and computational investigation was performed to test the viability of using fluorine reporter to probe both radical cation and anion formation by ^{19}F NMR studies. This will be discussed in chapter 4.

1.12 REFERENCES

(1) Shirota, Y. Photo- and Electroactive Amorphous Molecular Materials—Molecular Design, Syntheses, Reactions, Properties, and Applications. *J. Mater. Chem.* **2005**, *15* (1), 75–93.

(2) Moulin, E.; Armao, J. J.; Giuseppone, N. Triarylamine-Based Supramolecular Polymers: Structures, Dynamics, and Functions. *Acc. Chem. Res.* **2019**, *52* (4), 975–983.

(3) Mahmood, A. Triphenylamine Based Dyes for Dye Sensitized Solar Cells: A Review. *Sol. Energy* **2016**, *123*, 127–144.

(4) Leli ege, A.; Blanchard, P.; eodulf Rousseau, T.; Roncali, J. Triphenylamine/Tetracyanobutadiene-Based D-A-D π-Conjugated Systems as Molecular Donors for Organic Solar Cells. *Org. Lett.* **2011**, *13* (12), 3098–3101.

(5) Murata, H.; Miyajima, D.; Nishide, H. A High-Spin and Helical Organic Polymer: Poly{[4-(Dianisylaminium)Phenyl] Acetylene}. *Macromolecules* **2006**, *39* (19), 6331–6335.

(6) Roquet, S.; Cravino, A.; Leriche, P.; Alévêque, O.; Frère, P.; Roncali, J. Triphenylamine-Thienylenevinylene Hybrid Systems with Internal Charge Transfer as Donor Materials for Heterojunction Solar Cells. *J. Am. Chem. Soc.* **2006**, *128* (10), 3459–3466.

(7) Zhang, J.; Xu, B.; Yang, L.; Ruan, C.; Wang, L.; Liu, P.; Zhang, W.; Vlachopoulos, N.; Kloo, L.; Boschloo, G.; et al. The Importance of Pendant Groups on Triphenylamine-Based Hole Transport Materials for Obtaining Perovskite Solar Cells with over 20% Efficiency. *Adv. Energy Mater.* **2018**, *8* (2).

(8) Su, C.; Yang, F.; Ji, L.; Xu, L.; Zhang, C. Polytriphenylamine Derivative with High Free Radical Density as the Novel Organic Cathode for Lithium Ion Batteries. *J. Mater. Chem. A* **2014**, *2* (47), 20083–20088.

(9) Agarwala, P.; Kabra, D. A Review on Triphenylamine (TPA) Based Organic Hole Transport Materials (HTMs) for Dye Sensitized Solar Cells (DSSCs) and Perovskite Solar Cells (PSCs): Evolution and Molecular Engineering. *J. Mater. Chem. A* **2017**, 1348–1373.

(10) Yen, H. J.; Liou, G. S. Design and Preparation of Triphenylamine-Based Polymeric Materials towards Emergent Optoelectronic Applications. *Prog. Polym. Sci*. **2019**, *89*, 250–287.

(11) Blanchard, P.; Malacrida, C.; Cabanetos, C.; Roncali, J.; Ludwigs, S. Triphenylamine and Some of Its Derivatives as Versatile Building Blocks for Organic Electronic Applications. *Polym. Int.* **2019**, *68* (4), 589–606.

(12) Yen, H.-J.; Liou, G.-S. Recent Advances in Triphenylamine-Based Electrochromic Derivatives and Polymers. *Polym. Chem.* **2018**, *9* (22), 3001–3018.

(13) Sindt, A. J.; DeHaven, B. A.; Goodlett, D. W.; Hartel, J. O.; Ayare, P. J.; Du, Y.; Smith, M. D.; Mehta, A. K.; Brugh, A. M.; Forbes, M. D. E.; et al. Guest Inclusion Modulates Concentration and Persistence of Photogenerated Radicals in Assembled Triphenylamine Macrocycles. *J. Am. Chem. Soc.* **2020**, *142* (1), 502–511.

(14) Saddam Hossain, M.; J. Sindt, A.; W. Goodlett, D.; J. Shields, D.; J. O'Connor, C.; Antevska, A.; G. Karakalos, S.; D. Smith, M.; Garashchuk, S.; D. Do, T.; et al. Effects of Self-Assembly on the Photogeneration of Radical Cations in

Halogenated Triphenylamines. *J. Phys. Chem. C* **2021**, *125*,19991-20002.

(15) Ito, A.; Ino, H.; Tanaka, K.; Kanemoto, K.; Kato, T. Facile Synthesis, Crystal Structures, and High-Spin Cationic States of All-Para-Brominated Oligo(N-Phenyl-m-Aniline)S. *J. Org. Chem.* **2002**, *67* (2), 491–498.

(16) Yano, M.; Sato, K.; Shiomi, D.; Ichimura, A.; Abe, K.; Takui, T.; Itoh, K. Synthesis of 1,3-Bis(Diarylamino)Benzenes as Model Precursors for One-Dimensional Organic Ferromagnetic Metals; Characterization of the Dications by Cyclic Voltammetry and Electron Spin Transient Nutation Spectroscopy. *Tetrahedron Lett.* **1996**, *37* (51), 9207–9210.

(17) Sindt, A. J.; Dehaven, B. A.; McEachern, D. F.; Dissanayake, D. M. M. M.; Smith, M. D.; Vannucci, A. K.; Shimizu, L. S. UV-Irradiation of Self-Assembled Triphenylamines Affords Persistent and Regenerable Radicals. *Chem. Sci.* **2019**, *10* (9), 2670–2677.

(18) Ercolani, G. Physical Basis of Self-Assembly Macrocyclizations. *J. Phys. Chem. B* **1998**, *102* (29), 5699–5703.

(19) Whitesides, G. M.; Simanek, E. E.; Mathias, J. P.; Seto, C. T.; Chin, D. N.; Mammen, M.; Gordon, D. M. Noncovalent Synthesis: Using Physical-Organic Chemistry to Make Aggregates. *Acc. Chem. Res.* **1995**, *28* (1), 37–44.

(20) Pagni, R. Modern Physical Organic Chemistry (Eric V. Anslyn and Dennis A. Dougherty). *J. Chem. Educ.* **2006**, *83* (3), 387.

(21) Meng, X.; Wang, H.-N.; Song, S.-Y.; Zhang, H.-J. Proton-Conducting Crystalline Porous Materials. *Chem. Soc. Rev.* **2017**, *46* (2), 464–480.

(22) Horne, W. S.; Wiethoff, C. M.; Cui, C.; Wilcoxen, K. M.; Amorin, M.; Ghadiri,

M. R.; Nemerow, G. R. Antiviral Cyclic d,l-α-Peptides: Targeting a General Biochemical Pathway in Virus Infections. *Bioorg. Med. Chem.* **2005**, *13* (17), 5145–5153.

(23) Samanta, A.; Zhao, A.; Shimizu, G. K. H.; Sarkar, P.; Gupta, R. Post-Combustion CO2 Capture Using Solid Sorbents: A Review. *Ind. Eng. Chem. Res.* **2011**, *51* (4), 1438–1463.

(24) Liu, M.; Zhang, L.; Wang, T. Supramolecular Chirality in Self-Assembled Systems. *Chem. Rev.* **2015**, *115* (15), 7304–7397.

(25) Bong, D. T.; Clark, D. T.; Granja, J. R.; Ghadiri, M. R. Self-assembling Organic Nanotubes. *Angew. Chem. Int. Ed.* **2001**, 988-1011

(26) Urry, D. W. The Gramicidin A Transmembrane Channel: A Proposed π(L,D) Helix. *Proc. Natl. Acad. Sci.* **1971**, *68* (3), 672–676.

(27) Harada, A.; Li, J.; Kamachi, M. Synthesis of a Tubular Polymer from Threaded Cyclodextrins. *Nat. 1993 3646437* **1993**, *364* (6437), 516–518.

(28) Venkataraman, D.; Lee, S.; Zhang, J.; Moore, J. S. An Organic Solid with Wide Channels Based on Hydrogen Bonding between Macrocycles. *Nature* **1994**, *371*, 591-593.

(29) Stewart, S.; Edition, G. L.-A. C. I.; 2000, undefined. Block Copolymer Nanotubes. *Wiley Online Libr.* **2000**, *39* (2), 3642.

(30) Ben, T.; Ren, H.; Ma, S.; Cao, D.; Lan, J.; Jing, X.; Wang, W.; Xu, J.; Deng, F.; Simmons, J. M.; et al. Targeted Synthesis of a Porous Aromatic Framework with High Stability and Exceptionally High Surface Area. *Angew. Chemie Int. Ed.* **2009**, *48* (50), 9457–9460.

(31) Li, Y.; Handke, M.; Chen, Y.-S.; Shtukenberg, A. G.; Hu, C. T.; Ward, M. D. Guest Exchange through Facilitated Transport in a Seemingly Impenetrable Hydrogen-Bonded Framework. *J. Am. Chem. Soc.* **2018**, *140* (40), 12915–12921.

(32) Côté, A. P.; Benin, A. I.; Ockwig, N. W.; O'Keeffe, M.; Matzger, A. J.; Yaghi, O. M. Porous, Crystalline, Covalent Organic Frameworks. *Science*, **2005**, *310* (5751), 1166–1170.

(33) Eddaoudi, M.; Kim, J.; Rosi, N.; Vodak, D.; Wachter, J.; O'Keeffe, M.; Yaghi, O. M. Systematic Design of Pore Size and Functionality in Isoreticular MOFs and Their Application in Methane Storage. *Science (80-.).* **2002**, *295* (5554), 469–472.

(34) Wales, D. J.; Grand, J.; Ting, V. P.; Burke, R. D.; Edler, K. J.; Bowen, C. R.; Mintova, S.; Burrows, A. D. Gas Sensing Using Porous Materials for Automotive Applications. *Chem. Soc. Rev.* **2015**, *44* (13), 4290–4321.

(35) Dhakshinamoorthy, A.; Alvaro, M.; Garcia, H. Commercial Metal–Organic Frameworks as Heterogeneous Catalysts. *Chem. Commun.* **2012**, *48* (92), 11275–11288.

(36) Kitagawa, S.; Kitaura, R.; Noro, S. I. Functional Porous Coordination Polymers. *Angew. Chemie - Int. Ed.* **2004**, *43* (18), 2334–2375.

(37) Sumida, K.; Rogow, D. L.; Mason, J. A.; McDonald, T. M.; Bloch, E. D.; Herm, Z. R.; Bae, T. H.; Long, J. R. Carbon Dioxide Capture in Metal-Organic Frameworks. *Chem. Rev.* **2012**, *112* (2), 724–781.

(38) Ishii, Y.; Matubayasi, N.; Watanabe, G.; Kato, T.; Washizu, H. Molecular Insights on Confined Water in the Nanochannels of Self-Assembled Ionic Liquid Crystal. *Sci. Adv.* **2021**, *7* (31), 669–697.

(39) Shimizu, L. S. Mini Review: Perspectives on Main-Chain Hydrogen Bonded Supramolecular Polymers. *Polym. Int.* **2007**, *56* (4), 444–452.

(40) Shimizu, L. S.; Salpage, S. R.; Korous, A. A. Functional Materials from Self-Assembled Bis-Urea Macrocycles. *Acc. Chem. Res.* **2014**, *47* (7), 2116–2127.

(41) Shimizu, L. S.; Hughes, A. D.; Smith, M. D.; Davis, M. J.; Zhang, B. P.; Zur Loye, H. C.; Shimizu, K. D. Self-Assembled Nanotubes That Reversibly Bind Acetic Acid Guests. *J. Am. Chem. Soc.* **2003**, *125* (49), 14972–14973.

(42) Bowers, C. R.; Dvoyashkin, M.; Salpage, S. R.; Akel, C.; Bhase, H.; Geer, M. F.; Shimizu, L. S. Squeezing Xenon into Phenylether Bis -Urea Nanochannels. *Can. J. Chem.* **2015**, *93* (9), 1031–1034.

(43) Kittikhunnatham, P.; Som, B.; Rassolov, V.; Stolte, M.; Würthner, F.; Shimizu, L. S.; Greytak, A. B. Fluorescence Polarization Measurements to Probe Alignment of a Bithiophene Dye in One-Dimensional Channels of Self-Assembled Phenylethynylene Bis-Urea Macrocycle Crystals. *J. Phys. Chem. C* **2017**, *121* (33), 18102–18109.

(44) Dawn, S.; Dewal, M. B.; Sobransingh, D.; Paderes, M. C.; Wibowo, A. C.; Smith, M. D.; Krause, J. A.; Pellechia, P. J.; Shimizu, L. S. Self-Assembled Phenylethynylene Bis-Urea Macrocycles Facilitate the Selective Photodimerization of Coumarin. *J. Am. Chem. Soc.* **2011**, *133* (18), 7025–7032.

(45) Salpage S. R.; Donevant, L. S.; Smith. M. D.; Bick, A.; Shimizu, L.S. Modulating the Reactivity of Chromone and Its Derivatives through Encapsulation in a Self-Assembled Phenylethynylene Bis-Urea Host. *J. Photochem. Photobiol. A* **2016**, *315*, 14-24.

(46) Geer, M. F.; Walla, M. D.; Solntsev, K. M.; Strassert, C. A.; Shimizu, L. S. Self-Assembled Benzophenone Bis-Urea Macrocycles Facilitate Selective Oxidations by Singlet Oxygen. *J. Org. Chem.* **2013**, *78* (11), 5568–5578.

(47) DeHaven, B. A.; Tokarski, J. T.; Korous, A. A.; Mentink-Vigier, F.; Makris, T. M.; Brugh, A. M.; Forbes, M. D. E.; van Tol, J.; Bowers, C. R.; Shimizu, L. S. Persistent Radicals of Self-Assembled Benzophenone Bis-Urea Macrocycles: Characterization and Application as a Polarizing Agent for Solid-State DNP MAS Spectroscopy. *Chem. - A Eur. J.* **2017**, *23* (34), 8315–8319.

(48) Goodlett, D. W.; Sindt, A. J.; Hossain, M. S.; Merugu, R.; Smith, M. D.; Garashchuk, S.; Gudmundsdottir, A. D.; Shimizu, L. S. From Incident Light to Persistent and Regenerable Radicals of Urea- Assembled Benzophenone Frameworks: A Structural Investigation. *J. Phys. Chem. A* **2021**, *125* (6), 1336–1344.

(49) Daniel, P. H.; Tannia, M.; Karl, M. K.; Kazuteru, N.; Peng, Q.; Gerrit, B.; Tore, B.; Anders, H., and; Licheng S. Tuning the HOMO and LUMO Energy Levels of Organic Chromophores for Dye Sensitized Solar Cells. *J. Org. Chem.* **2007**, *72* (25), 9550–9556..

(50) Yao, Z.; Yang, L.; Cai, Y.; Yan, C.; Zhang, M.; Cai, N.; Dong, X.; Wang, P. Rigidifying the π-Linker to Enhance Light Absorption of Organic Dye-Sensitized Solar Cells and Influences on Charge Transfer Dynamics. *J. Phys. Chem. C* **2014**, *118* (6), 2977–2986.

(51) Li, P.; Wang, Z.; Song, C.; Zhang, H. Rigid Fused π-Spacers in D–π–A Type Molecules for Dye-Sensitized Solar Cells: A Computational Investigation. *J.*

Mater. Chem. C **2017**, *5* (44), 11454–11465.

(52) Venkatraman, R.; Panneer, S. V. K.; Varathan, E.; Subramanian, V. Aromaticity–Photovoltaic Property Relationship of Triphenylamine-Based D-π-A Dyes: Leads from DFT Calculations. *J. Phys. Chem. A* **2020**, *124* (17), 3374–3385.

(53) Yang, J.; Wu, X.; Shi, J.; Tong, B.; Lei, Y.; Cai, Z.; Dong, Y. Achieving Efficient Phosphorescence and Mechanoluminescence in Organic Host–Guest System by Energy Transfer. *Adv. Funct. Mater.* **2021**, 2108072.

(54) Lei, Y.; Yang, J.; Dai, W.; Lan, Y.; Yang, J.; Zheng, X.; Shi, J.; Tong, B.; Cai, Z.; Dong, Y. Efficient and Organic Host–Guest Room-Temperature Phosphorescence: Tunable Triplet–Singlet Crossing and Theoretical Calculations for Molecular Packing. *Chem. Sci.* **2021**, *12* (19), 6518–6525.

(55) Lei, Y.; Dai, W.; Tian, Y.; Yang, J.; Li, P.; Shi, J.; Tong, B.; Cai, Z.; Dong, Y. Revealing Insight into Long-Lived Room-Temperature Phosphorescence of Host–Guest Systems. *J. Phys. Chem. Lett.* **2019**, *10* (20), 6019–6025.

(56) M, G.; AK, M.; A, M.; S, R.; PR, R.; A, D. Tuning Emission Responses of a Triphenylamine Derivative in Host-Guest Complexes and an Unusual Dynamic Inclusion Phenomenon. *J. Org. Chem.* **2016**, *81* (2), 512–521.

(57) Mandal, A. K.; Suresh, M.; Das, P.; Das, A. Restricted Conformational Flexibility of a Triphenylamine Derivative on the Formation of Host–Guest Complexes with Various Macrocyclic Hosts. *Chem. – A Eur. J.* **2012**, *18* (13), 3906–3917.

(58) Mao, L.; Zhou, M.; Shi, X.; Yang, H. B. Triphenylamine (TPA) Radical Cations and Related Macrocycles. *Chinese Chem. Lett.* **2021**.

(59) Dong, S.; Gopalakrishna, T. Y.; Han, Y.; Chi, C. Cyclobis(7,8-(Para-

Quinodimethane)-4,4′-Triphenylamine) and Its Cationic Species Showing Annulene-Like Global (Anti)Aromaticity. *Angew. Chemie Int. Ed.* **2019**, *58* (34), 11742–11746.

(60) Kurata, R.; Sakamaki, D.; Ito, A. Tetraaza[1.1.1.1]m,p,m,p-Cyclophane Diradical Dications Revisited: Tuning Spin States by Confronted Arenes. *Org. Lett.* **2017**, *19* (12), 3115–3118.

(61) Xu, X.-D.; Yao, C.-J.; Chen, L.-J.; Yin, G.-Q.; Zhong, Y.-W.; Yang, H.-B. Facile Construction of Structurally Defined Porous Membranes from Supramolecular Hexakistriphenylamine Metallacycles through Electropolymerization. *Chem. – A Eur. J.* **2016**, *22* (15), 5211–5218.

(62) Custelcean, R. Crystal Engineering with Urea and Thiourea Hydrogen-Bonding Groups. *Chem. Commun.* **2008**, No. 3, 295–307.

(63) Steed, J. W. Anion-Tuned Supramolecular Gels: A Natural Evolution from Urea Supramolecular Chemistry. *Chem. Soc. Rev.* **2010**, *39* (10), 3686–3699.

(64) Hunter, C. A. Quantifying Intermolecular Interactions: Guidelines for the Molecular Recognition Toolbox. *Angew. Chemie Int. Ed.* **2004**, *43* (40), 5310–5324.

(65) Shimizu, L. S.; Smith, M. D.; Hughes, A. D.; Shimizu, K. D. Self-Assembly of a Bis-Urea Macrocycle into a Columnar Nanotube. *Chem. Commun.* **2001**, *1* (17), 1592–1593.

(66) Jun Yang; Mahender B. Dewal, and; Shimizu, L. S. Self-Assembling Bisurea Macrocycles Used as an Organic Zeolite for a Highly Stereoselective Photodimerization of 2-Cyclohexenone. *J. Am. Chem. Soc.* **2006**, *128* (25), 8122–

8123.

(67) Moulin, E.; Niess, F.; Maaloum, M.; Buhler, E.; Nyrkova, I.; Giuseppone, N. The Hierarchical Self-Assembly of Charge Nanocarriers: A Highly Cooperative Process Promoted by Visible Light. *Angew. Chemie Int. Ed.* **2010**, *49* (39), 6974–6978.

(68) Huo, G. F.; Shi, X.; Tu, Q.; Hu, Y. X.; Wu, G. Y.; Yin, G. Q.; Li, X.; Xu, L.; Ding, H. M.; Yang, H. B. Radical-Induced Hierarchical Self-Assembly Involving Supramolecular Coordination Complexes in Both Solution and Solid States. *J. Am. Chem. Soc.* **2019**, *141* (40), 16014–16023.

(69) Hossain, M. S.; Sindt, A. J.; Goodlett, D. W.; Shields, D. J.; O'Connor, C. J.; Antevska, A.; Karakalos, S. G.; Smith, M. D.; Garashchuk, S.; Do, T. D.; et al. Effects of Self-Assembly on the Photogeneration of Radical Cations in Halogenated Triphenylamines. *J. Phys. Chem. C* **2021**, acs.jpcc.1c04933.

(70) Xiao, W.; Hu, C.; Ward, M. D. Guest Exchange through Single Crystal–Single Crystal Transformations in a Flexible Hydrogen-Bonded Framework. *J. Am. Chem. Soc.* **2014**, *136* (40), 14200–14206.

(71) Ning, G.-H.; Matsumura, K.; Inokuma, Y.; Fujita, M. A Saccharide-Based Crystalline Sponge for Hydrophilic Guests. *Chem. Commun.* **2016**, *52* (43), 7013–7015.

(72) Hicks, R. G. What's New in Stable Radical Chemistry? *Org. Biomol. Chem.* **2007**, *5* (9), 1321–1338.

(73) J. Sindt, A.; D. Smith, M.; Samuel Berens; Sergey Vasenkov; R. Bowers, C.; S. Shimizu, L. Single-Crystal-to-Single-Crystal Guest Exchange in Columnar

Assembled Brominated Triphenylamine Bis-Urea Macrocycles. *Chem. Commun.* **2019**, *55* (39), 5619–5622.

CHAPTER 2

EFFECTS OF SELF-ASSEMBLY ON THE PHOTOGENERATION OF RADICAL CATIONS IN HALOGENATED TRIPHENYLAMINES*

* Reprinted with permission from **Hossain, M. S.;** Sindt, A. J.; Goodlett, D. W.; Shields, D.; O'Connor, C.; Antevska, A.; Karakalos, S; Smith, M. D.; Garashchuk, S.; Do, T.; Gudmundsdottir, A. D.; Shimizu, L. S. *J. Phys. Chem. C* **2021**, *125*, 19991-20002.

2.0 ABSTRACT

In this chapter, we investigate the effect of assembly on charge transfer, charge recombination, and the persistence of radical cations in halogen substituted triphenylamine (TPA) dimers. A series of urea tethered TPA derivatives **1** (X = H, Cl, Br, and I) are compared, which have one phenyl group modified at the *para* position with a halogen. Ureas directed the assembly of these derivatives while halogen substituents influence the packing of the TPA units. These modifications affect the generation and persistence of TPA radical cations as monitored by electron paramagnetic resonance (EPR) spectroscopy. The formation and degradation pathways of the radical cations in solution and gas phase were probed by Ion-mobility spectrometry mass spectrometry. In contrast, supramolecular assembly enhanced the stability of these materials as well as the persistence of their photogenerated radical cations, which appear to undergo charge recombination without degradation. Greater quantities of these radical cations are observed for the bromo and non-halogenated derivatives (**1Br**, **1H**). Time-dependent density functional theory (TD-DFT) calculations on single molecules and hydrogen-bonded dimers suggest the stability of TPA radical cations largely depends on initial photoinduced charge separation and electronic coupling between assembled TPA dimers. The latter was found to be about 7 times stronger in **1I** than in **1Br** dimers, which may explain faster charge recombination and shorter lifetimes of **1I** radicals. Transient Absorption (TA) Spectroscopy and TD-DFT were able to identify the charged species for **1Br** along with the kinetic traces and measured lifetime of ~80 ns. Fluorescence quenching studies are consistent with initial charge separation and subsequent charge transfer event between nearby TPAs. Future exploration will focus on

probing the mobility and will examine application of these TPA assemblies as hole transport materials.

2.1 INTRODUCTION

Supramolecular assembly has proven to be an effective method for designing hierarchical materials.[1,2,3] Examples of self-assembled frameworks include supramolecular coordination cages,[4] covalent organic frameworks,[5] and hydrogen-bonded organic frameworks.[6,7] Precise organization of organic chromophores can afford new properties. For example, the assembly of perylene *bis*-imide dyes generates distinct optical properties[8] that can be further tailored for photoinduced energy and electron transfer.[9] The assembly of triphenylamines (TPAs) is of particular interest, as TPA and its derivatives form radical cations through chemical, electrochemical, or photoinduced oxidation.[10,11,12] These features make TPAs excellent hole transporters[13] and spin-containing magnetic materials.[14] Photoinduced processes allow TPAs to be used as a thin layer in optoelectronic devices such as perovskite-based solar cells,[15] organic solar cells,[16] organic light-emitting diodes (OLEDs),[17] and memory devices.[18] Amide substituted triarylamines from Giuseppone's group form supramolecular polymers that show exceptional transport properties.[12,19] Yang's group found the hierarchical assembly of TPA-based metallocycles could be triggered by light and the radical cations were significantly stabilized within these assemblies.[20] In all these examples, the prerequisite for stable TPA radical cation formation is that all phenyl groups contain *para* substituents. Otherwise, upon radical generation the TPA rapidly dimerizes to form benzidines or other degradation products.[21,22] Even TPAs that are incorporated into macrocycles have their *para*-positions carefully blocked.[23] Recent work suggests that supramolecular assembly has the

potential to relax this constraint.[24,19,20] This may enhance spin-spin interactions and broaden the utility of TPA-based organic radicals.[25]

The Shimizu group employs urea directed self-assembly to organize dimers and

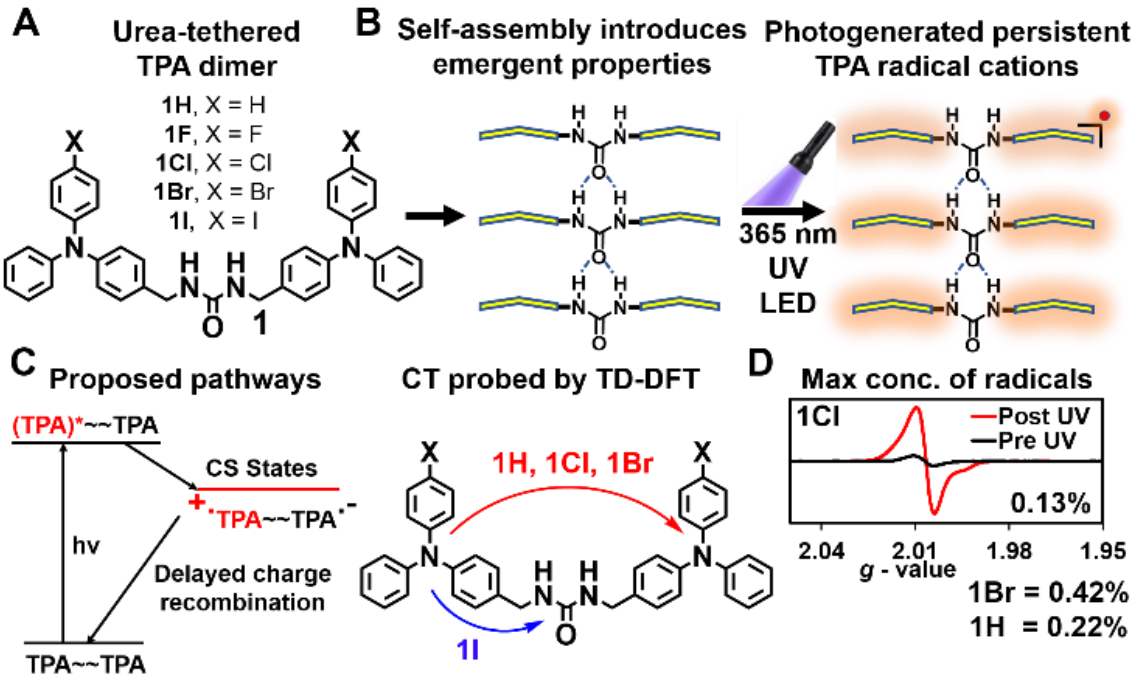

Figure 2.1. (A) The series of urea tethered halogenated TPAs investigated. (B) Schematics of tape formation guided by urea hydrogen bonding. Irradiation of the assembled structures with 365 nm UV LED forms persistent TPA radical cations as monitored by EPR. (C) Proposed pathways to charge-separated (CS) states. TD-DFT calculations suggest charge transfer between the two urea tether TPA units for 1H, 1Cl, 1Br derivatives, while 1I potentially undergoes charge transfer between the TPA and urea. (D) EPR spectra of 1Cl and summary of maximum radical concentration compared with a calibration curve of magic blue: 1Cl = 0.13%, (red spectra after 16 h of irradiation), 1Br = 0.42%, 1H = 0.22%.

macrocycles to afford robust and functional solid-state crystalline materials.[26,27] For example, UV-irradiation of unassembled TPA dimer **1Br** (Figure 1) in solution forms radical cations that degrade in minutes; however, the assembled **1Br** affords photogenerated radical cations that appear to undergo the reverse electron transfer to return to the starting material without degradation.[24] The methylene urea tethered dimers readily afford single crystals for X-ray

diffraction and radical formation in the crystals was monitored by electron paramagnetic resonance (EPR) spectroscopy. Electrochemical studies on **1Br** showed oxidation at 1.0 V versus a saturated calomel electrode (SCE). Bulk electrolysis at this potential gave a similar EPR spectrum as observed in the solid-state, suggesting a radical cation was formed in both samples. Comparison of cyclic voltammograms of **1Br** and the controls indicates that the TPA unit undergoes reduction (-1.2 V vs SCE) before the methylene urea linker or halide.[28] We hypothesize that the initial photoinduced charge separation occurs by a transfer of an electron from one TPA unit to a neighboring TPA. Here we synthesized urea tethered TPA dimers **1F**, **1Cl**, and **1I** to complete the series and compared these structures with the previously reported **1Br** and **1H**. Halogens can influence the packing structures as well as modulate electronics by enhancing the probably of spin-forbidden transitions and increasing spin-orbit coupling.[29,30] These partial *para*-substituted compounds were anticipated to degrade in solution; however, we expected that assembly and crystallization would increase their stability. Ion-mobility spectrometry mass spectrometry was used to probe degradation processes and to examine if assembled structures could be detected. The photoinduced radical formation was followed by EPR to estimate the concentration and persistence of the radical cations. The stability of these materials before and after UV-irradiation was also probed by ^{1}H NMR, X-ray photoluminescence spectrometry (XPS), absorption and emission studies. Laser flash photolysis (LFP) was performed on **1Br** to probe the initial photoinduced charged species. Time-dependent density functional theory (TD-DFT) calculations were used to analyze the frontier molecular orbitals and natural transition orbitals, and to assess the charge transfer/separation, and charge recombination on monomers and assembled dimers.

2.2 EXPERIMENTAL AND COMPUTATIONAL DETAILS

2.2.1 Characterization of Compounds

All commercially available reagents and solvents were purchased from VWR, Sigma-Aldrich, TCI America, and Alfa Aesar and were used without any further purification. Air sensitive reagents stored under nitrogen. Reactions were performed in oven-dried glassware covered with aluminum foil to protect from ambient light. ^{1}H NMR, ^{13}C NMR spectra were recorded in Bruker Avance 300 or 400 MHz spectrometers. Solvent peaks were used as a reference to report the chemical shift in ppm. High-resolution mass spectra were recorded in a direct exposure probe (DEP) in electron ionization (EI) mode on a Waters QTOF-I quadrupole time-of-flight mass spectrometer. Ion mobility mass spectrometry data of **1Br** were obtained using an Agilent 6560 IMS-QTOF instrument.

2.2.2 X-Ray Structure Determination

X-ray intensity data from a colorless needle were collected at 100(2) K using a Bruker D8 QUEST diffractometer equipped with a PHOTON-100 CMOS area detector and an Incoatec microfocus source (Mo Kα radiation, λ = 0.71073 Å). The raw area detector data frames were reduced and corrected for absorption effects using the Bruker APEX3, SAINT+, and SADABS programs.[31,32] The structure was solved with SHELXT.[33] Subsequent difference Fourier calculations and full-matrix least-squares refinement against F^2 were performed with SHELXL-2018[34] using OLEX2.[35]

2.2.3 Photophysical Properties and UV-irradiation

Samples were dried under Ar(g) and loaded in EPR tubes, which were oriented horizontally and exposed to 365 nm Waveform lighting real UV LED strips (4.5 W/ft, 3.2 ft). The photon flux was estimated as 9.78 x 10^{15} photons/sec (see SI). In solution, the absorption

spectra were recorded in Molecular Devices Spectramax M2. The diffuse reflectance of the solid sample was recorded using a Perkin Elmer Lambda 45 UV-vis spectrometer comprised of UV Winlab software and was referenced to Spectralon®. Perkin Elmer LS55 fluorescence spectrometer equipped with a pulsed high-energy source for excitation was used for emission analysis in solution, which was performed in a cuvette. Photoluminescence data in solid was collected on HORIBA Scientific Standard Microscope Spectroscopy Systems connected with iHR320 spectrometer and synchrony detector operating on Labspec 6 software. Spectra were recorded using 375 nm laser excitation source power 0.3 mW with 10xUV objective.

2.2.4 Laser Flash Photolysis (LFP) Measurements

Transient absorption measurements were performed using a commercially available laser flash photolysis instrument (LP980, Edinburgh Instruments, Inc.) with laser excitation (266 nm, 6−7 mJ, 8 mm diameter, 3−5 ns fwhm, 10 Hz) provided by a pulsed neodymium-doped yttrium aluminum garnet (Nd:YAG) laser (Surelite II, Continuum, Inc.). The details of this setup have previously been described.[36] The data were converted to a text file in the L900 software and then plotted and analyzed in the IgorPro software. Solid-state nanocrystalline suspensions were prepared following the procedure reported previously.[37] Saturated acetone solutions of **1Br** were added to a water solution in a volumetric flask placed in an ultrasound bath until the absorption at 266 nm was between 0.3 and 0.8. The resulting nanocrystalline suspension was placed inside a quartz cuvette with a 10 mm x 10 mm cross-section and analyzed. The cuvettes were capped with a rubber septum and bubbled vigorously for 5 minutes with argon or oxygen to produce argon and oxygen saturated conditions for appropriate analysis.

2.2.5 X-ray photoelectron spectroscopy (XPS) Analysis

XPS analysis was performed on a Kratos AXIS Ultra DLD XPS system with a monochromatic Al Kα source, operated at 15 keV and 150W and pressures below 10^{-9} torr. The X-rays were incident at an angle of 45° with respect to the surface normal. High-resolution core level spectra were measured with a pass energy of 40 eV and analysis of the data was performed using XPSPEAK41 software. The XPS system was equipped with a hemispherical electron analyzer and a load lock chamber for rapid introduction of samples without breaking vacuum. The XPS experiments were conducted using an electron gun, directed on the sample for charge neutralization. The UV irradiation took place in-situ, through the windows of the Ultra High Vacuum chamber.

2.2.6 Electron Paramagnetic Resonance (EPR Measurements)

EPR experiments were performed on a Bruker EMX plus equipped with a Bruker X-band microwave bridgehead and Xenon software (v 1.1b.66). The peak area was obtained by the double integration using Xenon software. Samples were sealed under argon and UV irradiated in Norell Suprasil Quartz EPR tubes (diameter 3 mm).

2.2.7 Details of the Electronic Structure Calculations and Analysis

The electronic structure calculations were performed using Q-Chem 5.3[38] and Spartan18 software[39]. Basis Set Exchange was used as a reference for selected bases.[40]
Due to practical considerations, the systems are modeled as single molecules in the gas phase. The geometry of the heavy atoms was taken from the SC-XRD data, while the positions of the hydrogen atoms were determined from the energy minimization in the gas phase employing the Density Functional Theory (DFT) at B3LYP-D3[41]/6-31G*[42] level. Theoretical UV-vis spectra and the excited state analysis are based on the time-dependent (TD) DFT calculations.

Most results reported here (Tables 2.6-9 and in Table 2.1) are obtained with the CAM-B3LYP[43] functional paired with the 6-31+G** basis set. For **1I** derivative, the iodine atom is represented using the effective core potential basis LANL2DZdp[44]. CAM-B3LYP[43], developed to improve the description of the charge-transfer excited states, is known to adequately describe the properties of dyes including the TPAs.[45] Additional TD-DFT calculations were performed using LRC–ωPBEh[46] and B3LYP-D[41] functionals (same basis sets as above) and their results were found in qualitative agreement to those based on CAM-B3LYP.

Theoretical UV-vis spectra, $g(x)$, were generated as sums of Gaussian functions broadening the spectral lines,

$$g(x) = \sqrt{\frac{1}{\pi\sigma^2}} \sum_{\mathrm{n}} f_n \, \mathrm{e}^{-\frac{(x-x_n)^2}{\sigma^2}} \qquad (2.1)$$

In Eq. (1) f_{n} and x_n represent the oscillator strength and the position of the n$^{\mathrm{th}}$ line (in nm), respectively; x is the energy variable in nm. The width of the Gaussian is controlled by the standard deviation parameter σ set to 70, 20, 20, and 110 nm for **1H**, **1Cl**, **1Br**, and **1I**, respectively, to match the broad features of the experimental spectra.

The molecular orbitals (MOs) -- the highest occupied/lowest unoccupied HOMO/LUMO -- and the natural transition orbitals – the highest occupied/lowest unoccupied natural transition orbitals HONTO/LUNTO -- were visualized with isovalue 0.04 in IQmol v2.14.0. The spin at the nuclei was computed the Rassolov-Chipman operator for RC_{R0}=0.25 a.u.[47]

Table 2.1. Vertical excitation spectra and types of transitions, energy, and oscillator strength assigned for compounds **1H**, **1Cl**, **1Br**, **1I** for the three strongest transitions, calculated with CAM-B3LYP functional paired with 6-31+G** or LANL2DZdp basis sets.

Compound	Level of theory	State	Type	ΔE, eV	f[a]	RMS electron-hole separation[b] Å	μ, D[c]	|<r_e – r_h>|[d] Å
1H	CAM-B3LYP/ 6-31+G**	S_{10}	ππ*	4.160	0.030	4.055	1.399	0.163
		S_{14}	CT ππ*	4.382	0.412	4.131	4.983	1.273
		S_{16}	CT ππ*	4.413	0.179	4.108	3.274	1.008
1Cl	CAM-B3LYP/ 6-31+G**	S_6	ππ*	4.205	0.034	4.058	1.474	0.390
		S_8	CT ππ*	4.385	0.170	4.132	3.204	1.172
		S_9	CT ππ*	4.404	0.463	4.146	5.269	1.367
1Br	CAM-B3LYP/ 6-31+G**	S_6	ππ*	4.203	0.024	4.070	1.227	0.400
		S_9	CT ππ*	4.347	0.154	4.141	3.064	1.180
		S_{10}	CT ππ*	4.365	0.528	4.149	5.650	1.282
1I	CAM-B3LYP/ LANL2DZdp	S_{14}	CT ππ*	4.175	0.088	4.250	2.358	1.434
		S_{19}	CT ππ*	4.360	0.129	4.212	2.799	1.280
		S_{20}	CT ππ*	4.384	0.186	4.245	3.352	1.627

[a]Oscillator strength. [b]Root-mean-square (RMS) electron-hole separation in angstrom. [c]μ Magnitude of transition dipole moment (TDM) in debye (D). [d]Linear electron (e) / hole (h) distance in angstrom Å. The descriptor computed from transition density matrix and state character.

2.2.8 Mass Spectrometry

The data were collected using an Agilent 6560-IMS-QTOF mass spectrometer with the methods and instrument parameters previously reported.[48]

2.3 RESULTS AND DISCUSSION

2.3.1 Urea Directed Assembly of TPA

The **1H** and **1Br** urea tether TPA derivatives were prepared as described.[24,28] Three additional halogenated TPAs were synthesized by Ullmann condensation[49] followed by a

Vilsmeier-Haack reaction (Scheme 2.1).[50] Reduction of the aldehyde[51] and treatment with phosphorus tribromide afforded the benzyl bromide,[52] which was coupled with triazinanone under basic conditions. Deprotection was performed in a mixture of 9:1 DMF/DEA (diethanolamine) at 90°C under the acidic condition to yield **1Cl**, **1I**, and **1F**. X-ray diffraction quality crystals were obtained by slow evaporation from acetonitrile solution for **1H**,[28] and **1Cl** (10 mg mL^{-1}) or from ethyl acetate solution for compound **1Br** (20 mg mL^{-1}),[24] and **1I** (10 mg mL^{-1}) respectively. The geometries of the hydrogen bonds of **1H**, **1Cl**, **1Br**, **1I** are summarized in Table 2.4. Thus far, attempts to crystallize **1F** by slow cooling, vapor diffusion, and slow evaporation have not yet yielded single crystals. We are currently screening a wider range of crystallization methods.

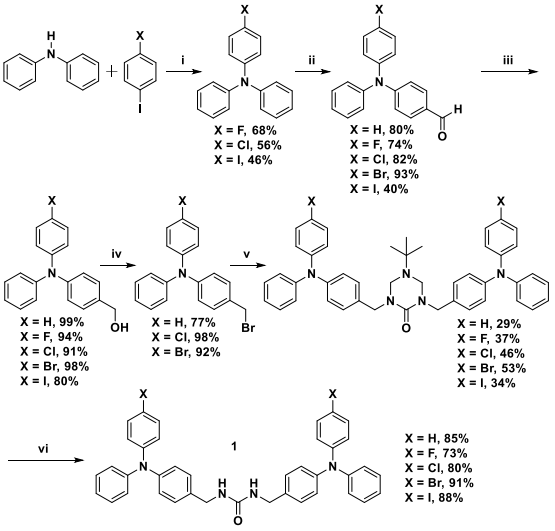

Scheme 2.1. Synthesis of 1,3-bis(4-(diphenylamino)benzyl)urea, 1,3-bis(4-((4-fluorophenyl)(phenyl)amino)benzyl)urea,1,3-bis(4-((4-chlorophenyl)(phenyl)amino)-benzyl)urea, 1,3-bis(4-((4-iodophenyl)(phenyl)amino)benzyl)urea. Reagents and conditions: i) CuI, 1,10-phenanthroline, KOH, dry toluene, 120°C, 24 h, under N_2 (X = F, Cl, I). ii) $POCl_3$, DMF, 40°C (X = H) or 60°C (X = F, Cl, Br, I). iii) $NaBH_4$ (1.108 equiv.), DCM/EtOH, RT, 12h (X = H, F, Cl, Br, I) iv) PBr_3 (0.6 equiv.), Et_2O, RT, 12h and NaH (3 equiv.), triazinanone (1 equiv.), THF, 24h (X = F, I) or PBr_3 (0.6 equiv.), Et_2O, RT, 12h (X = H, Cl, Br). v) NaH (3 equiv.), triazinanone (1 equiv.), THF, Δ, 12h (X = H, Cl, Br). vi) 9:1 DMF/DEA 1mL/mg, pH~2, 90°C, 48h (X = H, F, Cl, Br, I).

Crystals of **1I** were obtained as an ethyl acetate hemi solvate in the monoclinic space group $P2_1/c$. The asymmetric unit consists of one **1I** molecule and half of one ethyl acetate

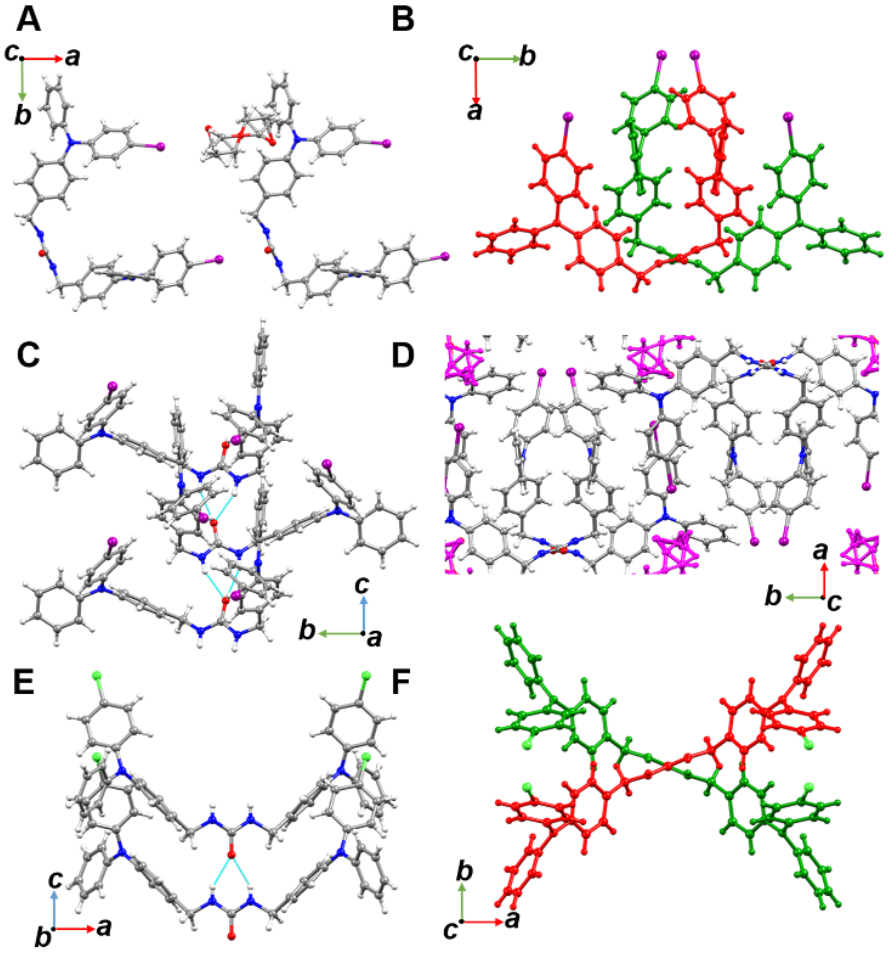

Figure 2.2. Comparison of urea tethered halogenated TPAs **1I** and **1Cl**. (A) Hemisolvated crystal structure for **1I** (B) Top down view showing a U shape for **1I**. (C) Side view of urea-urea hydrogen bonding interactions forming tapes of linked urea-tethered molecules of **1I.** (D) Packing of **1I** showing ethyl acetate solvent in the interstitial spaces between the neighboring TPAs. (E) View of linear urea hydrogen bonding interactions in **1Cl**. (F) Top down projection of the **1Cl** structure showing an X–shape.

molecule, which is disordered about a crystallographic inversion center (Figure 2.2A). The conformation of **1I** is U-shaped with the two TPA units oriented in close proximity (Figure 2.2B). The intramolecular distance between the two TPA N centers *d*(N···N) is 9.9 Å. The urea

adopts a *trans-trans* conformation and directs the assembly of infinite 1D H-bonded chains with *d*(N···O) distances of 2.887(5) and 2.891(5) Å and a twisting angle 36.28°. Figure 2.2C displays this assembly along the crystallographic *c* axis. Additional, halogen bond type interactions are observed between iodine and urea carbonyl oxygen of a neighboring molecule with C-I···O distance of 3.305(1) Å, which is less than the sum of their van der Waals radii (3.50 Å).[53] Figure 2.2D displays the crystal packing of **1I**, which reveals ethyl acetate present in the interstitial space between the neighboring TPA units. The ethyl acetate is disordered but organized through halogen bonding with a carbonyl O atom - iodine C-I···O distance of 3.442(1) Å.

In comparison, **1Br** crystallized in the orthorhombic system with the space group *Pccn*.[24] The two TPA units are stretched linearly outwards from the urea groups in contrast to the U-shape of **1I**. The ureas are in a *trans-trans* conformation and organized into chains along the crystallographic *c*-axis (Figure 2.38). The urea hydrogen bond distances are shorter (*d*(N···O) = 2.823(3) and 2.70(5) Å) with twisting angle of 51.6(1)° forming an X-shape in projection along the chain axis (Figure 2.38B). The **1Cl** is essentially isostructural to **1Br** (orthorhombic, *Pccn*). The urea hydrogen bond distances in **1Cl** are *d*(N···O) = 2.808(2) and 2.70(2) Å with a twisting angle of 47.74° (Figure 2.2E). Figure 2.2F shows the X-shape formed by the hydrogen-bonded chains of **1Cl** when viewed along crystallographic *c* axis.

The halide free **1H** crystallized in the orthorhombic system with centrosymmetric space group *Pbcn*.[28] Both TPA units extend opposite site of the disordered methylene ureas. The ureas adopt a *trans-trans* conformation with urea hydrogen bonding distances of *d*(N···O) = 2.749(8) and 2.716(8) Å and a twisting angle 16.32° (Figure 2.38C). These are the shortest H bonds and the smallest twisting angle observed in the series of compounds. Criss-crossing of

urea-tethered chains forms a cruciform pattern projected along the crystallographic *c*-axis, Figure 2.38D (right).

Simulations from the Giuseppone group on triarylamine supramolecular polymers suggest that the relative orientation of neighboring TPA is important for the photophysical

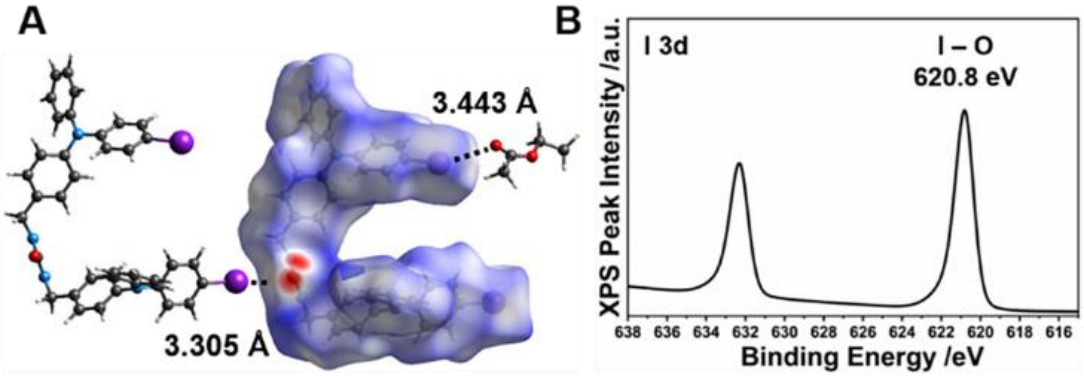

Figure 2.3. (A) Hirshfeld surface map for compound **1I** showing C-I···O interaction. (B) **I**(3d) XPS core level peaks for compound **1I** recorded with monochromatic Al Kα X-ray source.

profile of TPA.[19] Analysis of our structures (Figure 2.76-79), shows the packed TPA units of **1H**, **1Cl**, and **1Br** form similar snowflake conformations with N - N distances of 4.4 Å, supporting our comparison of these three compounds. **1I** in contrast gives a cross-flake conformation with a longer N – N distance of 13.7 Å. Further investigation of the propeller arrangement of the TPA phenyl rings within the same molecule suggests **1H**, **1Cl**, and **1Br** have a symmetrical orientation while **1I** shows a non-symmetrical conformation (Figure 2.79).

Hirshfeld surface analysis was used to further analyze intermolecular interactions in the crystal structures of **1I**, **1Br**, and **1Cl**.[54] As expected, all show the key three centered urea-urea hydrogen bonding (Figures 2.40-41A); however, only **1I** has a significant halogen bonding interaction. Figure 2.3A shows the intermolecular contact C-I···O 3.305 Å between the iodine and the carbonyl oxygen on a neighboring molecule, indicated in red. Additionally,

there is a longer, weaker interaction between iodine with the oxygen atom of ethyl acetate solvent (3.442(1) Å) as compared with the sum of their van der Waals radii 3.50 Å.[53] The surface analysis also revealed C-I···π interaction (3.538 Å) between the TPAs for compound **1I** as seen in Figure 2.41D.

X-ray photoelectron spectroscopy (XPS) was used to probe the chemical environment around a halogen by examining the binding energy (BE) of the core level electrons. The detailed XPS spectra of the **1Cl**, **1Br**, and **1I** are shown in Figures 2.39 and Figure 2.3. The core level peaks for **1Cl** (2p) 200.5 eV and **1Br** (3d) 70.5 eV are characteristic of the reported literature values for C-Cl and C-Br bonds, respectively.[55,56] This suggests there are no significant halogen bonding interactions in agreement with the XRD data. In contrast, the recorded BE core level peaks for **1I** displays I(3d) core level peaks that are significantly different than typically observed 620.8 eV versus 619 eV.[57] Similar values for the I(3d) core level peaks (620.6 eV) were observed for C-I···O halogen bond formation between pyridyl *bis*-urea macrocycle and iodobenzene,[58] confirming the value of XPS for characterizing halogen bonding interactions.

2.3.2 Absorption and Emission Spectra in Solution and Solid State

To investigate how the photophysics change with halide substitution, absorption and emission spectra were studied in argon purged dichloromethane (DCM), ethyl acetate (EtOAc), and tetrahydrofuran (THF) solution (10 μM) as seen in Figures 2.42-48. These studies are summarized in Table 2.5. All compounds displayed a similar absorption pattern ranging from 285 - 305 nm, which is attributed to strong π-π* transitions. For the emission spectra, the two bands arose with the first band around 360 nm and a second at ~450 nm with the intensity of the second band increasing with more polar solvents. Upon assembly, all

compounds displayed a sizeable red-shift (55-66 nm). The twisting angle for **1H** was 16.32° with λ_{em} = 479 nm and a greater red-shift (113 nm). Derivatives with a larger twisting angle, such as **1Br** (51.6°) exhibited a smaller red-shift (89 nm) and showed emission at a shorter wavelength, λ_{em} = 451 nm (Figure 2.49).

2.3.3 Simulations of Diffuse Reflectance by TD-DFT

The electronic structure calculations were performed for **1H**, **1Cl**, **1Br**, **1I**, and the controls **2a** and **2b** as described in Section 2.2.7. To assess the method dependence of the reported results, the excited states of **1Br** were also computed using CAM-B3LYP[43]/LANL2DZdp[44], LRC–ωPBEh[46]/6-31+G**[42], and B3LYP-D3[42]/6-31+G**[43] methods, which qualitatively yielded similar results (Table 2.10). See the supplementary information for further computational details. The frontier molecular orbitals, their energies,

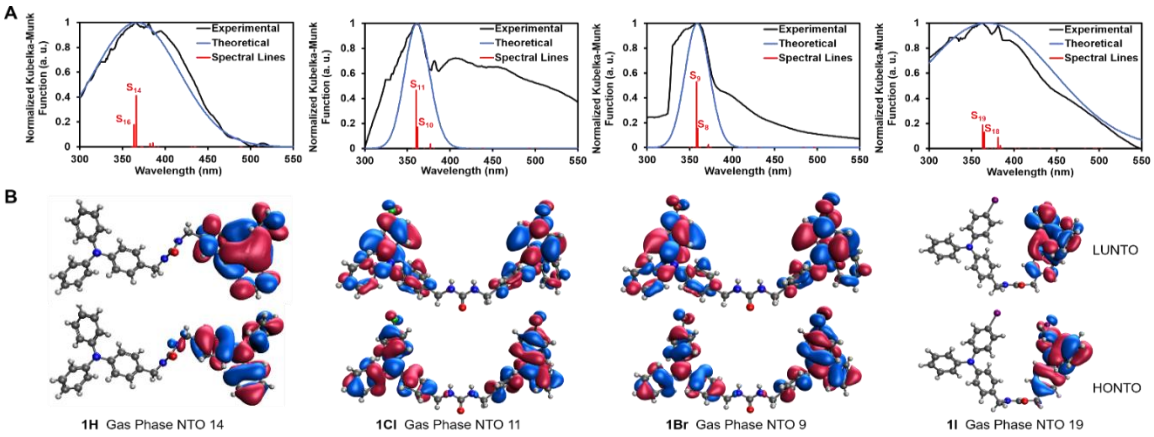

Figure 2.4. Comparison of normalized diffuse reflectance measurements of urea tethered TPAs (from left) **1H**, **1Cl**, **1Br**, **1I** with TD-DFT calculated spectra including corresponding spectral lines. From left, transition to the S_{14} state corresponds to the λ_{max} of **1H** (366 nm), transition to the S_{11} state corresponds to the λ_{max} of **1Cl** (360 nm), transition to the S_9 state corresponds to the λ_{max} of **1Br** (358 nm), transition to the S_{19} state corresponds to the λ_{max} of **1I** (363nm). (B) Natural Transition Orbitals for urea tethered TPAs (from left) **1H**, **1Cl**, **1Br**, **1I** in the gas phase. HONTO (Bottom), LUNTO (Top).

and the HOMO-LUMO gap for the six molecules are presented for comparison in figure 2.50.

Both mono-TPA controls, **2a** and **2b,** show the characteristic electron distributions where the HOMO is primarily delocalized on the lone electron pair of nitrogen (N 2pz orbital) throughout the phenyl rings. The LUMOs for **2a** and **2b** are localized or centered towards the nitrogen; there is no apparent contribution from the bromine or methylene urea. In comparison, in urea tethered TPA dimer **1H**, the HOMO is localized in one unit of the TPA while the LUMO is localized in the other unit of the urea tether TPA. This is indicative of a charge-separated state, which is usually seen in donor-acceptor systems where TPA acts as a donor connected to an acceptor through the π-conjugated bridge.[59] The Cl- and Br-substituted dimers, **1Cl** and **1Br,** show their respective HOMO and LUMO delocalized through the whole molecule. In LUMO, one of the nitrogen centers lacks electron density, which can be attributed to the formation of the charge-transfer complex.

The iodo derivative **1I** exhibits a different trend. Here, the HOMO is localized on the urea tether TPA unit, while LUMO is localized on the phenyl ring partially substituted with iodine and methylene urea. This may be indicative of charge transfer between the TPA and methylene urea for **1I** instead of two TPA units in the other derivatives. The energy gaps of the controls and TPA dimers show modest variation ranging from 6.508 eV for **1I** to 6.821 eV for **1Cl**. Typically, the presence of electron-withdrawing groups such as Cl, Br increases the HOMO levels,[60] which was not observed within the dimer series as the HOMO of **1H** (-6.419 eV) is slightly higher than **1Cl** or **1Br** (-6.783 eV). We argue that within our set of four derivatives the structural effects of the halide substitutions play a significant role. We have used the **1Br** SC-XRD structure to generate two new theoretical structures in which the bromine atoms were replaced by H or iodine. While experimentally these structures could not be tested as crystal packing would alter the geometry, the computations are straightforward.

These two structures are optimized (B3LYP-D3/6 31G*) allowing only hydrogens and the halides to move. Comparison of the HOMOs and NTOs at the strongest transitions (Figures 2.53-54) reveals that H and I incorporated into the 'scaffold' geometry of **1Br** show comparable electronic transitions. Thus, packing geometry is an important variable for controlling properties in these systems. The UV-vis spectra have been constructed from the TD-DFT energies within the random phase approximation (RPA). Since the computed energy gaps in molecules or molecular clusters tend to be larger than those in solids (as seen for example in Table S9) the calculated excitation energies of **1H**, **1Cl**, **1Br** and **1I** were multiplied by 0.773, 0.781, 0.793, and 0.779, respectively. These factors were determined by the best fit to the experimental data obtained for the crystalline samples. Once scaled, the shape of the computed absorption spectra is in good agreement with the experimental diffuse reflectance data.

For additional insight into the excited states, we have examined the natural transition orbitals (NTOs).[61] The highest occupied natural transition orbital (HONTO) and the lowest unoccupied natural transition orbital (LUNTO) were generated for the transitions of the highest oscillator strength. The frontier NTOs are presented in Figure 2.4 along with the experimental diffuse reflectance and the TD-DFT absorption spectra and spectral lines. The transitions closest to the maximum of experimental diffuse reflectance – their wavelength Indicating λ_{max} given in parenthesis -- are S_{14} (366 nm), S_{11} (360 nm), S_9 (358 nm), and S_{19} (363 nm) for **1H**, **1Cl**, **1Br**, and **1I,** respectively. According to the spatial character of the corresponding NTOs, all four transitions are of ππ* type. More specifically, while (i) similar to the frontier MOs the frontier NTOs of all four TPA derivatives lack electron density on their methylene urea moieties, (ii) in **1H** and **1I** these NTOs are localized only on one of the TPA

units where the external unsubstituted phenyl ring has less electron density and (iii) in **1Br** and **1Cl** they are delocalized over the entire molecular backbone.

The spin-density (not shown) of **1H**, **1Cl**, **1Br**, and **1I** and the corresponding radical cations, probed by EPR, is consistent with the NTO trends above: the spin-density of the radicals show the same localization patterns as HOMO-1 of the neutral species (the spin-density for the neutral species is essentially zero). Moreover, relevant to the EPR measurements, spin on the nuclei is asymmetrically distributed between the TPA units in the cases of **1Cl** and **1Br**, and is nearly equally split between the two units of **1H** and **1I**. The absolute values of the electron spins at the nuclei summed over the left/right TPA units are 0.000/0.333, 0.183/0.183, 0.177/ 0.187, and 0.445/0.000 for **1H**, **1Cl**, **1Br**, and **1I**, respectively. The maximum spin values are seen on the nitrogen atoms of the TPA centers; their values for the left/right TPA units in order of {**1H**, **1Cl**, **1Br**, **1I**} are 0/0.099, 0.051/0.051, 0.049/0.052 and 0.126/0.000. (Table 2.15) Altogether, the analyses of the orbitals and spin-density confirm the charge localization trend.

For more quantitative analysis of the charge transfer (CT) character in **1H**, **1Cl**, **1Br**, and **1I** upon UV-vis excitation, the RMS electron-hole separation,[62] the transition dipole moment (TDM) in debye (μ), and the linear electron-hole (e/h) distance in angstrom, encoded in the transition density matrix analysis[63,64], are listed in Tables 2.1 and 2.6-9 for the optically active transitions. The RMS e/h separations, which represent the exciton 'size', characterize the dynamic charge separation. Electronic transitions associated with changes of the localized electron density and TDM are characterized by the transition type, which is either ππ* or CT ππ. The former describes a localized excitation (ππ*, small linear e/h separation); the latter describes the charge transfer state with the larger e/h separation.

These electron/hole descriptors were used to assign the transition type to the excited states. For **1H,** the states S_{14} and S_{16} with oscillator strength of 0.412, and 0.179 with RMS e/h distances of 4.131, and 4.108 show the highest change in TDM (4.983 D, 3.274 D) and e/h separation (1.273 Å, 1.008 Å); these states are identified as CT ππ* transitions. In contrast, the S_{10} state (TDM of 1.399 D and e/h separation of 0.163 Å) is assigned as ππ*. The rest of the states are similar to S_{10} and are identified as ππ* transitions. Visualization of the NTOs further supports the argument as S_{14}, and S_{16} states show similar electron density distribution. For **1Cl**, **1Br**, and **1I** states (S_8, S_9), (S_9, S_{10}), and (S_{14}, S_{19}, S_{20}) respectively assigned as CT ππ* transitions while the rest of the states assigned as ππ* transitions following similar trends as described earlier. Based on the NTO and transition density matrix analyses, we conclude that the urea tethered TPA derivatives have CT characteristics at specific transition.

2.3.4 MASS SPECTROMETRY

UV irradiation of compound **1Br** generates radicals that are persistent in the solid state; however, the molecule quickly degrades in solution.[24] We turned to ion-mobility spectrometry mass spectrometry to investigate the radical cation formation and its degradation products. The full ESI mass spectrum of **1Br** at 50 μM in 25:75 v/v ACN:H_2O with 0.1% FA (formic acid) and the ion mobility data of the monomeric species are shown in Figure 2.5A, B, respectively. The solution was exposed to room light during the analysis process. Intact oligomers as large as the trimer (*m/z* 2190*)* were observed. The arrival time distribution in panel B reveals that there are two distinct monomeric species whose exact masses are consistent with a radical cation *(*$M^{\bullet+}$, *m/z* = 730) and protonated species ($[M+H]^+$, *m/z* = 731). Panels C and D highlight additional species detected in the low *vs.* high mass region. Notably, *m/z* 336 is the most abundant fragment, which was identified as a Br-TPA radical cation

(Figure S47A). Its isotope pattern is consistent with a Br-containing molecule (Br has two isotopes; ^{79}Br and ^{81}Br). Another interesting fragment is *m/z* 585 (Figure 2.55), corresponding to a radical cation degraded from a covalent dimer of **1Br**. This result is consistent with the

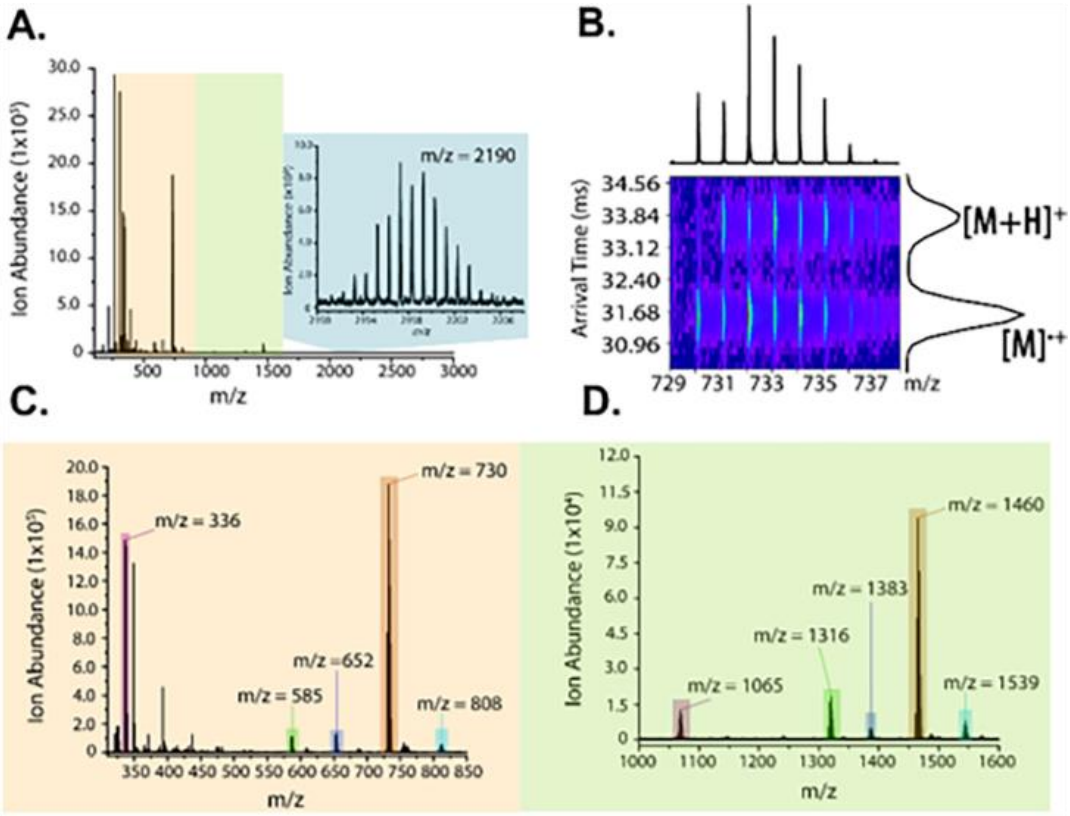

Figure 2.5. (A) A full ESI mass spectrum of **1Br** with the trimer in the inset. (B) The 2D plot of *m/z* vs. arrival time for the monomers, where the radical and protonated species can be distinguished based on monoisotopic masses. The isotopic peak distribution and arrival times indicate the existence of two distinct species. (C) Partial mass spectrum showing monomer (*m/z* = 730) and its fragments. (D) Partial mass spectrum containing the dimer (*m/z* = 1460) and radical-recombined byproducts.

fact that radical cations of **1Br** can degrade in minutes and a minor population of covalent dimers may exist in solution. Interestingly, in the high mass region, we observed mass spectral peaks corresponding to the recombined byproducts (*m/z* 1065, 1316, 1383, and 1539) of the radical cations (*m/z* 336, 585, 652, and 808) and **1Br**. For example, the Br-TPA fragment (*m/z* 335) combines with the **1Br** monomer (exact mass = 730 amu), to form a new species at *m/z*

1065. The byproducts are low abundance and color-coded in panels C, D based on their precursors. This result highlights the high propensity for the radical fragments to recombine with the abundant monomer. Finally, despite the radical fragments, the intact assembled oligomers (n = 2, 3) were still the dominant species during our experiments, indicating that assembled **1Br** is stable and can resist degradation.

2.3.5 EPR Experiments to Quantify Radical Generation

In the solid-state, no degradation of crystalline **1Br** was detected by SC-XRD, PXRD and solution-state NMR even after 10 h of UV-irradiation using a Hanovia 450 W medium

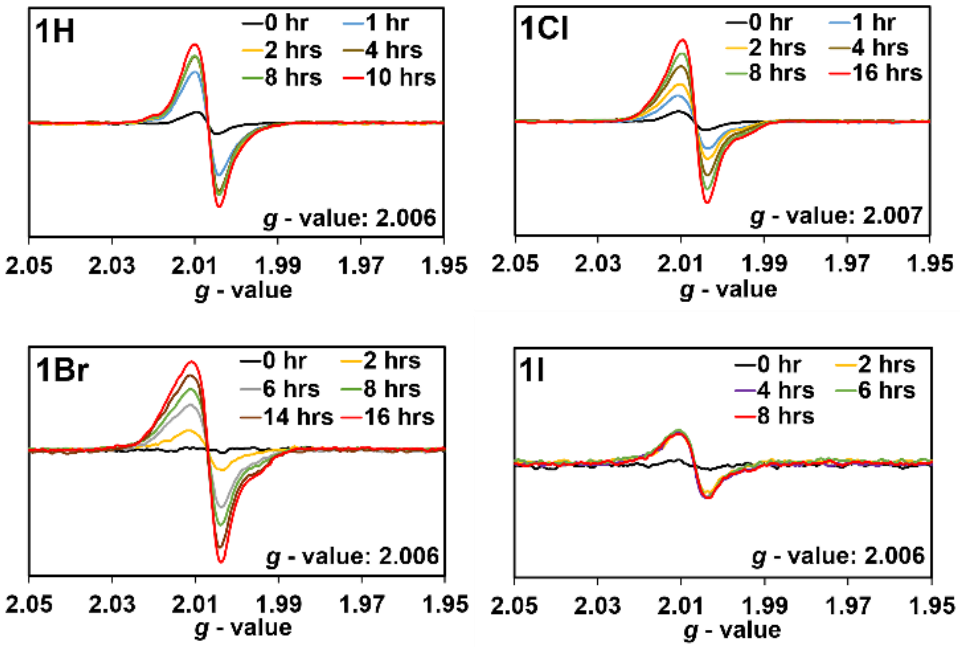

Figure 2.6. EPR studies of urea tethered TPA derivatives at room temperature in solid-state. EPR signal pre- and post-UV irradiation (hr) of compound **1H**, **1Cl**, **1Br**, **1I** with corresponding *g*-values.

pressure Hg arc lamp.[24] Prior work showed lower intensity 365 nm LED's gives identical EPR spectra for **1Br** versus the mercury lamp, although longer irradiation time is required.[28] Some broadening of the aryl and carbonyl resonances was observed in the solid-state MAS ^{13}C NMR

of **1Br**, which further indicated the delocalization of the electron density.[28] To examine the effect of the halogen heavy atom on the stability of the radicals, we turned to X-band EPR spectroscopy. Freshly recrystallized samples were filtered, dried under Ar (g) at room temperature, placed in quartz EPR tubes and irradiated with 365 nm LEDs. The samples were then evaluated for radical generation, radical persistence, the maximum concentration of radicals, and lifetime at room temperature. The TPA dimer **1Br** (6.8 mg), and **1Cl** (10.5 mg) were triply recrystallized and showed good agreement between their EPR studies. The **1H** (8.1 mg) and **1I** (9.1 mg) samples were doubly recrystallized and showed good agreement. Figure 2.6 compares the EPR signals before and after UV irradiation on an incremental timescale for **1H**, **1Cl**, **1Br**, and **1I**. While pre-UV irradiation shows little to no EPR signal, post-UV irradiation dramatically increases

Table 2.2. Analysis of radical generation induced by UV-irradiation

Compound	Maximum radical concentration	Half-lives (Days)
1H	0.22%	3
1Cl	0.13%	6
1Br	0.42%	7[a]
1I	0.06%	<1

[a]Values taken from reference.[10] A standard deviation of 0.04% and 0.01% was found for the average of three trials each for **1Br** and **1I** respectively.

the signal. **1H** and **1I** exhibit a broad, axial powder pattern shape EPR signal. **1Cl** and **1Br** show more anisotropy while retaining the powder pattern shape. The corresponding *g*-values for these urea tethered TPA derivatives are 2.006 (**1H**, **1Br**, **1I**), and 2.007 (**1Cl**), which are close to the *g*-value of TPA radical cations in solution (2.002-2.005).[65] This suggests that radical cations were formed in the supramolecular assembly.

To estimate the concentration of radicals generated, the double integration of the EPR spectra was plotted as a function of UV irradiation time (Figure 2.56). Next, the concentration

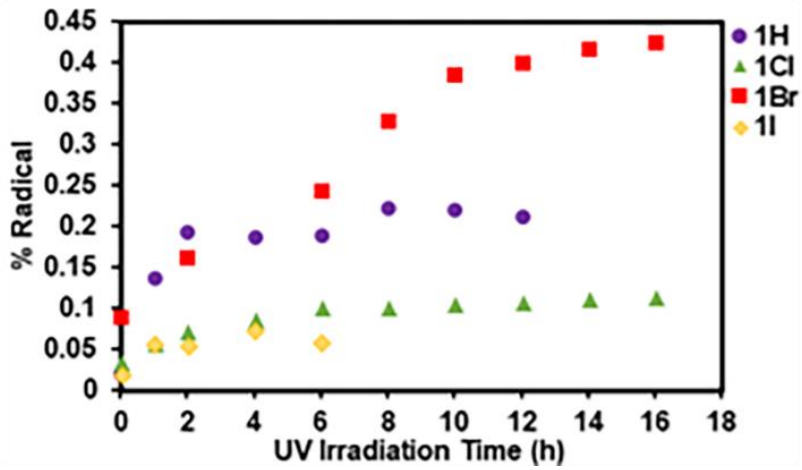

Figure 2.7. EPR studies of radical formation as a function of irradiation time for urea tethered TPAs. Double integration of the EPR spectra over time of UV irradiation and later compared with the calibration curve of magic blue.

of the radicals was approximated by comparing the data with a calibration of Magic Blue solutions in dry DCM (Figure 2.59). This comparison gives a qualitative estimate of radicals generated in solid state. In each case, the percentage of radicals increased with longer irradiation time until reaching a plateau or maximum concentration, which can be seen in Figure 2.7. At these time points (~16 h (**1Cl**, **1Br**), ~10 h (**1H**), ~2 h (**1I**)), we estimate the maximum concentration of radicals from the same number of radicals seen in 100 μL of a 0.30 mM (**1H**), 0.21 mM (**1Cl**), 0.20 mM (**1Br**), 0.07 mM (**1I**) solution of magic blue. Accounting for the sample weight, the maximum concentrations of radicals followed the order of **1Br** > **1H** > **1Cl** > **1I** and ranged from a high of 0.42% ±0.04% for **1Br** to very low, near our detection limit for **1I** (~0.06% ±0.01%). We repeated the experiments two more times for both **1I** and **1Br** to estimate the error in these experiments as seen in Figures 2.56 and S58. The low radical concentration observed for **1I** could also be related to its solvate structure. Previously, we

observed that host:guest complexes of TPA macrocycles with polar solvents exhibited lower radical concentrations.[28] Overall, parent **1H** and the chloro derivative **1Cl** showed similar, percentages of radicals 0.22±0.04% and 0.13±0.04% respectively. This was surprising as the heavy atom containing **1Cl** was expected to have a faster ISC rate in comparison to **1H**, which lacks a heavy atom.

Next, the persistence of photogenerated TPA radicals was probed by a dark-decay study. After being irradiated to their maximum radical concentrations, the samples were stored in the dark at room temperature under argon, and EPR spectra recorded over time. Figure 2.8A shows the EPR spectra recorded periodically for **1H**, and **1Cl** (for **1I** see Figure 2.60). Again, the EPR signals were doubly integrated to obtain the area and plotted over time in Figure 2.8B. Fluctuations in the observed EPR signal intensity are likely due to the alignment of the crystals

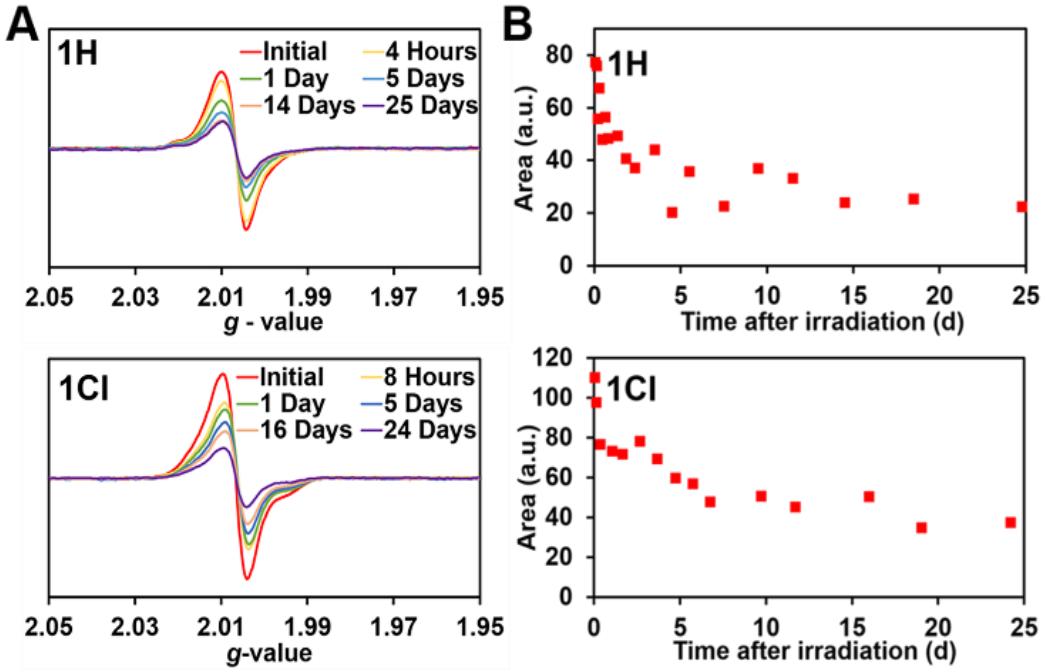

Figure 2.8. Dark decay EPR study on urea tethered TPAs in solid-state after UV-irradiation to their maximum radical concentration. (A) EPR spectra generated after decay over time. (left) (B) The double integration of the EPR spectra over time of UV irradiation. (right)

with respect to the applied field of the EPR instrument during measurements.[66,67] Half-lives were estimated by comparing the area at the maximum concentration of radicals until the area reaches half. As seen in Table 2, half-lives of the radicals were estimated ~7 days for **1Br**,[24] ~6 days for **1Cl**, ~3 days for **1H**, respectively.

Previous studies on **1Br** showed that radicals can be observed even after 1 month and can be regenerated to re-exposure to light.[24] We continuously monitored the EPR signal for **1H** and **1Cl** to check the stability of these urea tethered TPA derivatives. Even after 25 days (**1H**) and 24 days (**1Cl**) no change in the line shape of EPR spectra or corresponding *g*-value were observed, which demonstrates the stability of these derivatives and remarkable persistence of the TPA radical cation.

2.3.6 Transient Absorption Spectroscopy

LFP was used to identify charge-separated species formed during UV irradiation in solid-state. For the experiment, we prepared 1.4 μM nanocrystalline suspension of **1Br** in water in oxygen, air, and argon purged environments. Figure 2.9 shows the transient absorption (TA) spectra of nanocrystal suspension of **1Br** in degassed water (argon purged). The TA spectra of the **1Br** compound taken from 10 – 210 ns are broad with a peak around 650 nm (Figure 2.9A). The fact that the lifetimes were virtually unchanged in comparison to the error associated with kinetic measurements was unexpected as the triplet state should show lifetime quenching in presence of oxygen. However, these crystalline materials are close-packed without pores, and triplet quenching would be expected to be primarily a surface phenomenon.[37] The rest of the wavelengths fit this general trend, and almost all lifetimes fell between 60 – 90 ns with mono-exponential fits. According to the TD-DFT simulation of the TA absorption of **1Br**, the intense electronic transition at around 650 nm (Figure 2.9C) is

ascribed to the presence of a radical cation and in the range previously seen in solution.[68] The triplet transition is predicted to occur at 885 nm, which is outside the window for detection.

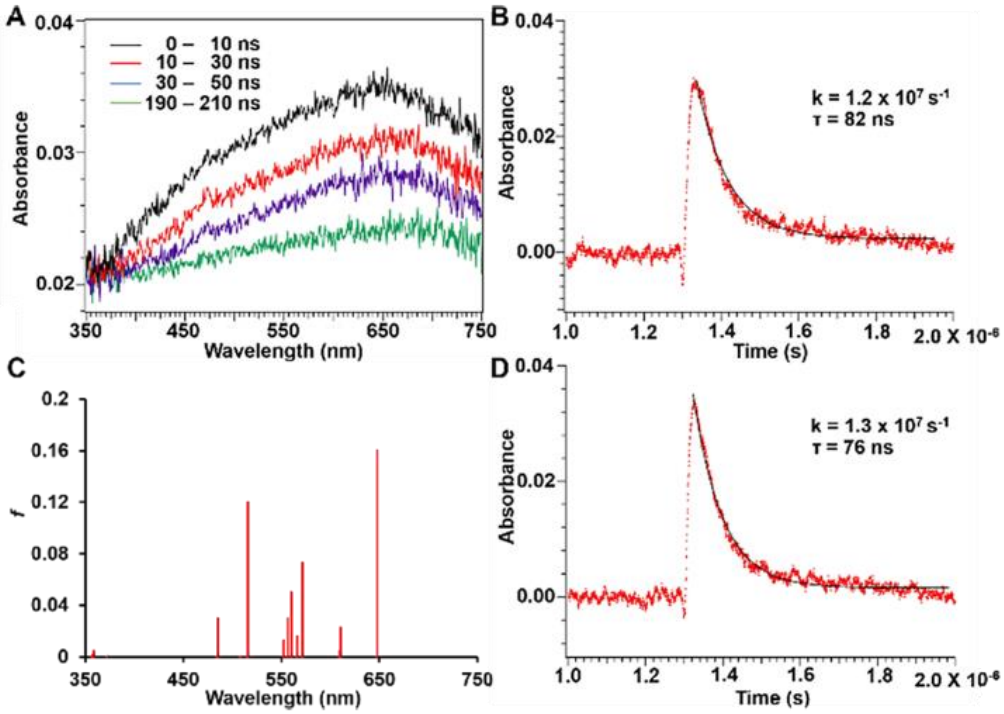

Figure 2.9. Transient absorption data, kinetic traces, and the TD-DFT spectral lines for **1Br** compounds: (A) transient absorption spectra from 10 – 210 ns of argon degassed nanocrystalline suspensions in water upon 266 nm pulsed laser excitation; (B) kinetic traces at 650 nm argon degassed nanocrystalline suspensions in water; (C) spectral lines from the TD-DFT calculation of the excited states at the LRC-ωPBEh/6-31+G** level. SC-XRD data was used for the calculation; (D) kinetic traces at 650 nm oxygen degassed nanocrystalline.

2.3.7 Solid-state Photoluminescence and Electronic Structure Analysis

A fluorescence quenching study was conducted to gain insight into the evolution of our systems after the initial formation of the charged species. The solid-state samples of the TPA derivatives were UV-irradiated for 6 h and the fluorescence intensity (λ_{exc} = 375 nm) was compared pre-UV and post-UV irradiation. The same single crystal was used for both measurements. Upon UV irradiation (6h), the fluorescence intensity of all these derivatives is

reduced to about a quarter of the initial intensity (Figure 2.75). Since fluorescence quenching is expected after the initial formation of a CT complex,[69] these results suggest that the initial charge separation, facilitated by the organization and geometry of the TPAs, is followed by the rapid charge transfer between neighboring TPAs and, subsequently, by slower charge recombination. Slow recombination rate would be manifested in the unusual stability of the urea tethered TPA radical cations in solid-state.

In support of the explanation above, we have focused on the particularly long-lived **1Br** radicals and examined the properties of the monomer, and hydrogen-bonded dimer and trimer, the latter two 'stacked' to mimic their arrangement in a crystal according to the crystallographic data. Because of the extended system size (234 atoms for a trimer), the electronic structure calculations were performed using a semiempirical method detailed in SI; the results are summarized in Tables 2.11-13. The hypothesis is that in solid-state UV irradiation of the **1Br** samples leads to the intramolecular charge separation $2(\text{TPA-TPA})^{*} \rightarrow (\text{TPA-TPA})^{+}+(\text{TPA-TPA})^{-}$ and the ions are long-lived due to small electronic coupling between the monomers in the ground state.

The computed energy differences of the charged monomers with respect to the ground state, E^0, and with respect to the UV-vis-populated excited state, E*, of the neutral species,

$\Delta = E^{+}+E^{-}-2E^{0}$ and $\Delta = E^{+}+E^{-}-2E^{*}$

show that the cation/anion pairs become energetically more stable for larger aggregates: Δ decreases from 674 to 557 kJ/mol while $|\Delta^{*}|$ increases from 138 to 225 kJ/mol as we go from the isolated monomer to the trimer model. More accurate DFT calculation for the monomer, yielding lower Δ and higher $|\Delta^{*}|$ compared to the semiempirical results, suggests even larger stabilization of the charge-separated pairs due to the crystalline environment. The electronic

couplings in the ground state, related to the charge recombination, have been estimated using Koopman's theorem as described in SI (Table 2.12). As summarized in Table 2.12 for the **1Br** and **1I** dimers, the electron coupling in the **1I** model is about 7 times stronger than that for **1Br** model, while the hole coupling is about 4 times stronger. This suggests that the charge recombination is more efficient in **1I** than in **1Br**, which is consistent with the longer radical lifetimes observed for **1Br**. Moreover, examination of the frontier orbitals (Figure 2.52) shows that the LUMO of **1Br** is delocalized over the two units, while the LUMO of **1I** is largely localized on one unit, which suggests that **1Br** is more likely to undergo intra-molecular charge separation upon the UV-vis excitation, compared to **1I**. This is consistent with the higher intensity of the radical generation in **1Br**. To summarize, (i) the intra-molecular (intra-unit) charge transfer upon UV irradiation is feasible; (ii) the charge recombination in the ground state is less likely for **1Br** than for **1I**; (iii) larger model size representing solid-state increases the stability of the charged (radical) pairs relative to the neutral pairs and reduces the excitation gap.

2.4 SUMMARY AND CONCLUSION

While introducing steric substituents on TPAs is a common method to stabilize radical cations in solution,[20,70] our work suggests self-assembly is a viable alternative strategy. The urea tethered TPA dimers studied here lack typical electron acceptors and have unsubstituted *para* positions. As expected, these compounds form radical cations upon UV-irradiation in solution, which are not stable. Intriguingly, ion mobility spectroscopy mass spectroscopy also suggests that self-assembly stabilizes radicals. These MS studies on **1Br** were performed under exposure to light to detect radical degradation and recombination products produced from radical fragments recombining with the abundant monomers. Yet, assembled dimers and

trimers were the dominant species, indicating that assembly is likely stabilizing even in the solution and gas phase.

Urea-guided assembly afforded single crystals for four of the structures, which enabled exploration of the effects of halogen substituents (heavy atoms) on photophysics and radical cation formation within a series of similar assembled structures. The structures of **1H**, **1Cl**, and **1Br** adopted anti-parallel extended TPA conformations with an average TPA N···N distance of approximately 14 Å. The N···N separation was slightly longer in **1H** (14.1 Å) as compared with ~13.9 Å in **1Cl** and **1Br**. In contrast, **1I**, which alone crystallized as a solvate, adopts a U-shaped structure with a shorter N···N distance of 9.9 Å. **1I** exhibited both halogen and hydrogen bonding interactions.

In the solid-state, the anti-parallel extended TPA conformations of **1H**, **1Cl**, **1Br** exhibited increased photogenerated radicals versus the U-shaped structure in the **1I** solvate. The **1Br** derivative displayed the highest efficiency of radical generation (maximum radical ~ 0.42%) and longest lifetime/ slowest recombination (half-life ~7 days). Surprisingly, the **1H** derivative also generated large amounts of persistent TPA radical cations, despite lacking the heavy atom to facilitate spin-orbit coupling as well as containing four unsubstituted *para* positions that would typically speed degradation processes in solution. Analysis of frontier molecular orbitals indicates that two TPA groups tethered by methylene urea are necessary for the formation of a charge-separated state as compared with the untethered TPA.

Detailed TD-DFT studies were performed on monomers and assembled dimers of **1Br**, **1I**, and for **1Br** trimer. These studies suggest that UV generated CT is feasible, favoring an intramolecular process for **1Br** versus **1I**. Further, the electronic coupling leads to charge recombination roughly 7 times faster in **1I** as compared to **1Br**. Therefore, the observation that

1Br displays both larger quantity and longer lifetime of radicals is reasonable as charge recombination in its ground state is less likely than in **1I**. Computations on larger models, i.e. dimers and trimers used to represent assemblies and solid-state structures, show that although the neutral systems are energetically more favorable, the relative stability of the radical pairs increases with the size of the molecular model, providing support for the experimentally observed stabilization of radicals in the solid-state. Currently, we are probing the rate of charge recombination and charge transport within both thin films and crystals of **1Br**, **1I**, and related derivatives to investigate if these charged radical pairs are mobile or if they represent unproductive, with respect to mobility, trapped states. A better understanding of how structure affects charge separation and mobility in assembled TPAs will promote the use of these materials as hole transporting layers for optoelectronic devices.

2.5 EXPERIMENTAL

2.5.1 Synthesis and characterization of compounds

General procedure for urea tethered halogenated TPA synthesis

Step i: Procedure followed for **X = F, Cl, I**

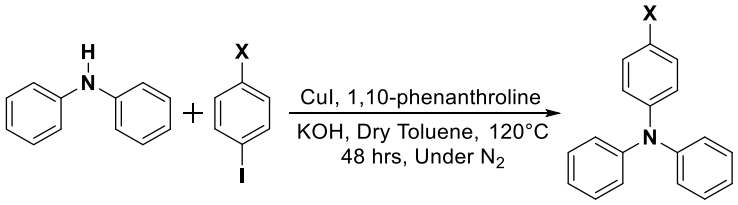

The compounds were synthesized as reported previously.[49] In a Schlenk flask commercially available 1-halo-4-iodobenzene (21.27 mmol, 1.2 equiv.), diphenylamine (17.73 mmol, 1 equiv.), copper (I) iodide (4.60 mmol, 0.26 equiv.), 1,10-phenanthroline (4.96 mmol, 0.28 equiv.), potassium hydroxide (70.92 mmol, 4 equiv.) were added and mixed in dry toluene (1 x 20 mL). The mixture was degassed using freeze-pump-thaw (3

times) and was heated at 120 °C under N_2 atmosphere for 48 h. Then the reaction mixture cooled to room temperature and quenched with H_2O (1 x 30 mL). The organics were extracted with methylene chloride (3 x 30 mL) and dried over anhydrous $MgSO_4$. The solvent was removed by rotary evaporation, and the crude material was further purified by column chromatography using silica and 100% hexane as eluent. The final product was obtained as a white solid.

Step ii: Procedure followed for **X = F, Cl, Br, I**

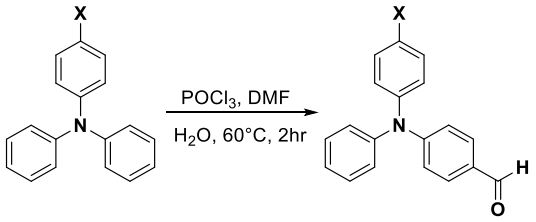

This step was followed according to the previous literature procedure.[50] Additional personal protective equipment and elevated flow rate in the hood were used for safety. In a round bottom flask, phosphoryl chloride (3.845 mmol, 1.125 equiv.) was added dropwise to N, N-dimethylformamide (4.614 mmol, 1.35 equiv.) at 0 °C. Then the reaction mixture stirred for 20 min at room temperature. Next, 4-halo-N, N-diphenylaniline (3.417 mmol, 1 equiv.) was dissolved in a minimum amount of N, N-dimethylformamide and added dropwise to the reaction mixture. The reaction mixture was heated for 2 h at 60 °C, cooled to room temperature, carefully quenched with ice-cold H_2O (1 x 20 mL) and neutralized by adding saturated $NaHCO_3$ until pH ~7. Then the mixture was extracted with chloroform (3 x 20 mL), washed with water (1 x 10 mL), and brine (1 x 20 mL) and dried over anhydrous $MgSO_4$. After removing the solvent by rotary evaporation, the crude material

was further purified by column chromatography using 95:05 = Hexane: Ethyl Acetate as eluent. The product was obtained as yellow solid.

Step iii: Procedure followed for **X = H, F, Cl, Br, I**

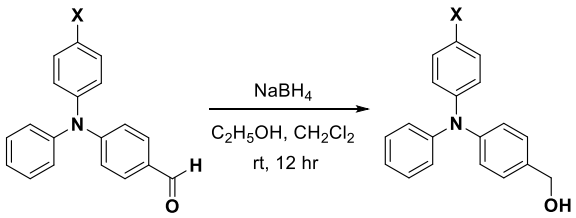

This step was followed according to previous literature procedures.[51] In an oven-dried round bottom flask, the product from step **ii** (1.79 mmol, 1 equiv.) was added and dissolved in 30 mL of 3:1 mixture of dry methylene chloride and ethanol. The mixture was stirred for 5 minutes at room temperature. Then sodium borohydride (1.99 mmol, 1.108 equiv.) was added and let the reaction mixture stirred for 12 hours at room temperature in the dark. Then the reaction was quenched by adding 50 mL H_2O, and the organics were extracted with (3 x 25 mL) methylene chloride and dried over anhydrous $MgSO_4$. The solvent was subsequently removed under reduced pressure and the product obtained as sticky solid.

Step iv: Procedure followed for **X = H, F, Cl, Br, I**

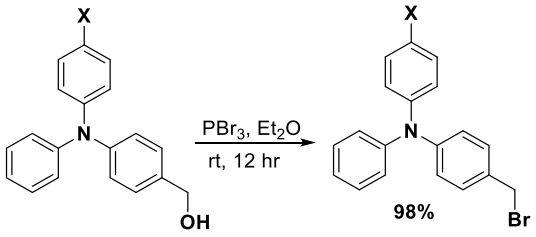

Compounds were synthesized according to the previous procedure.[52] In an oven-dried round bottom flask, the product from the step **iii** (1.68 mmol, 1 equiv.) was dissolved in 14 mL of dry diethyl ether placed in an ice bath. Then phosphorus tribromide (0.996

mmol, 0.6 equiv.) was added as a solution in 10 mL dry diethyl dropwise to the reaction mixture over 5 minutes. The reaction mixture was stirred in the dark at room temperature for 12 hours. Then 25 mL ice-cold H_2O and 13 mL of saturated $NaHCO_3$ has been added to quench the reaction. Then the organics were extracted with (1 x 12 mL) methylene chloride and washed with brine (3 x 12 mL) and dried over anhydrous $MgSO_4$. Then the solvent was removed by rotary evaporation. The final product was obtained as sticky solid. Notes: The products for **X = F, I** were not stable and the crude material was used without any further purifications.

Step v: Procedure followed for **X = H, F, Cl, Br, I**

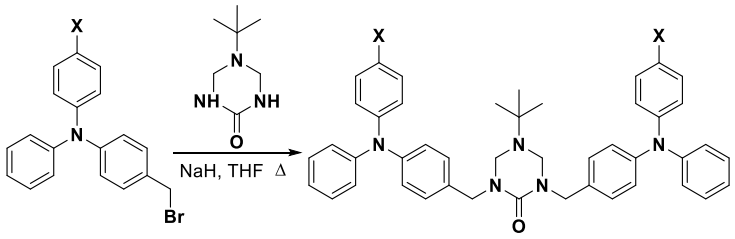

This step was carried out according to the previous literature procedure.[24] Initially, 5-(tert-butyl)-1,3,5-triazinan-2-one (0.602 mmol, 1 equiv.) sodium hydride (1.86 mmol, 3 equiv.) were added in 10 mL of dry tetrahydrofuran and was stirred for 10 minutes. Then the product from step **iv** (1.25 mmol, 2 equiv.) dissolved in 10 mL dry tetrahydrofuran, added to the reaction mixture and stirred overnight at reflux. The next day, the reaction was cooled to room temperature and 2.8 mL of both 1N HCl and H_2O were added to quench the reaction. The organics were extracted with methylene chloride (3 x 30 mL) and then washed with brine (1 x 30 mL) and dried over anhydrous $MgSO_4$. The solvent was removed in rotary evaporation and the crude material was purified by column chromatography using 1:1 = Hexane: Ethyl Acetate as an eluent. The final product was obtained as sticky solid.

Step vi: Procedure followed for **X = H, F, Cl, Br, I**

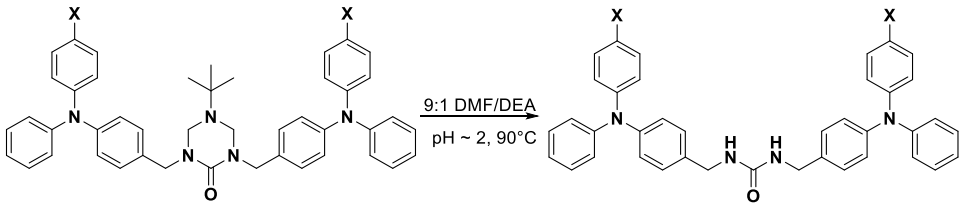

The deprotection was carried out according to the previous procedures.[24] Product from step **v** (0.216 g, 0.306 mmol) were suspended in 108 mL of 9:1 mixture of dimethylformamide and diethanolamine and pH was adjusted to 2 by using conc. HCl and set the reaction at 90°C for 2 days. The reaction mixture pH was readjusted in every 12 hours interval. After the reaction cooled to the room temperature, $NaHCO_3$ added to neutralize the mixture, and 1 x 200 mL of H_2O was added and put in the refrigerator for 2 hours. Precipitant was collected by suction filtration and washed with 50 mL of H_2O and dried under vacuum yield white solid.

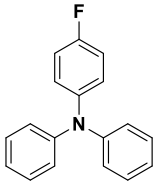

68%

4-fluoro-N, N-diphenylaniline: The final product was obtained as a white solid (3.156 g, 68%). The obtained spectra matched as previously reported.[71] ^{1}H NMR (400 MHz, $CDCl_3$): δ (ppm) 7.26-7.19 (m, 4H), 7.10−7.01 (m, 6H), 7.10−6.92 (m, 4H), 7.03−6.99 (m, 4H); ^{13}C NMR (101 MHz, $CDCl_3$): δ (ppm) 158.9 (d, *J* = 242.5 Hz), 147.9, 143.8, 129.2, 126.4 (d, *J* = 7.7 Hz), 123.5, 122.5, 116.0 (d, *J* = 22.0 Hz); HRMS-APCI (+) $[M+H]^+$: calculated, 264.1183; found: 264.1176.

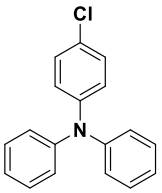

56%

4-chloro-N, N-diphenylaniline: The final product was obtained as a white solid (0.920 g, 56%). The obtained spectra matched as previously reported.[72] ^{1}H NMR (400 MHz, $CDCl_3$): δ (ppm) 6.99 (d, *J* = 8.8 Hz, 2H), 7.02 (t, *J* = 7.2 Hz, 2H), 7.05 (d, *J* = 8.4 Hz, 4H), 7.17 (d, *J* = 8.8 Hz, 2H), 7.24 (t, *J* = 7.8 Hz, 4H); EI-MS: m/z 279 (M^+, 100%), 281(M^++2, 34%).

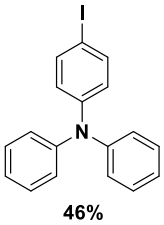

46%

4-iodo-N, N-diphenylaniline: The final product was obtained as a white solid (0.995 g, 46%). The obtained spectra matched as reported previously.[49] ^{1}H NMR (300 MHz, $CDCl_3$): δ (ppm) 7.58 (d, 2H), 7.28 (m, 4H), 7.08 (m, 6H), 6.83 (d, 2H). MS (ESI): m/z, calculated, 371.21; found, 372.02 $[m + H]^+$

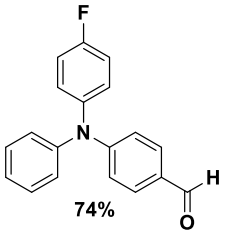

74%

4-((4-fluorophenyl)(phenyl)amino)benzaldehyde: The product was obtained as yellow solid (0.721 g, 74%). ^{1}H NMR (300 MHz, $CDCl_3$): δ (ppm) 9.81 (s, 1H), 7.68 (d, *J* = 8.6 Hz, 2H), 7.34 (t, *J* = 7.8 Hz, 2H), 7.21 – 7.12 (m, 5H), 7.05 (t, *J* = 8.5 Hz, 2H), 6.97

(d, *J* = 8.7 Hz, 2H). ^{13}C NMR (75 MHz, $CDCl_3$): δ (ppm) 190.64, 161.87, 158.61, 153.47, 146.07, 142.18, 142.14, 131.55, 129.91, 129.08, 128.47, 128.36, 126.13, 125.31, 118.92, 116.95, 116.65. HRMS (EI): calculated, 291.1059; found: 291.1060.

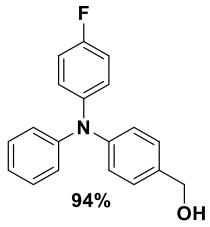

(4-((4-fluorophenyl)(phenyl)amino)phenyl)methanol: the product obtained as sticky solid (0.493 g, 94%). ^{1}H NMR (300 MHz, $(CD_3)_2SO$): δ (ppm) 7.29 – 7.23 (m, 4H), 7.14 (t, *J* = 8.8 Hz, 2H), 7.04 – 6.92 (m, 7H), 5.11 (t, *J* = 5.7 Hz, 1H), 4.43 (d, *J* = 5.7 Hz, 2H). ^{13}C NMR (75 MHz, $(CD_3)_2SO$): δ (ppm) 159.73, 156.54, 147.51, 145.93, 143.74, 143.71, 137.33, 129.44, 127.91, 126.08, 125.97, 123.55, 122.65, 122.33, 116.40, 116.10, 62.59. HRMS (EI): [M+] calculated, 293.1216; found: 293.1218.

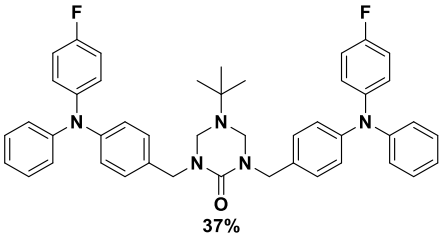

5-(tert-butyl)-1,3-bis(4-((4-fluorophenyl)(phenyl)amino)benzyl)-1,3,5-triazinan-2-one: The final product was obtained as sticky solid (0.216 g, 37%). ^{1}H NMR (300 MHz, $(CD_3)_2CO$): δ (ppm) 7.32 (d, *J* = 8.5 Hz, 4H), 7.29 – 7.23 (m, 4H), 7.07 (d, *J* = 6.7 Hz, 8H), 7.02 – 6.97 (m, 10H), 4.49 (s, 4H), 4.33 (s, 4H), 1.01 (s, 9H). ^{13}C NMR (75 MHz, $(CD_3)_2CO$): δ (ppm) 161.22, 158.02, 156.61, 148.80, 147.74, 145.03, 144.99, 134.36, 130.54, 130.17, 127.13, 127.02, 124.59, 124.05, 123.39, 116.99, 116.69, 62.26, 54.82, 48.41, 28.71. HRMS (ES): [M+] calculated, 708.3508; found: 708.3514.

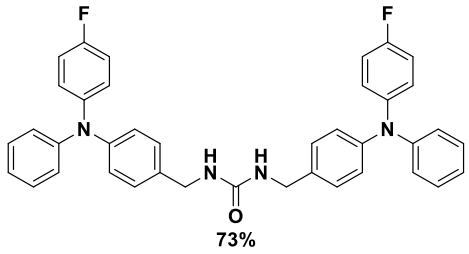

73%

1,3-bis(4-((4-fluorophenyl)(phenyl)amino)benzyl)urea: The final product obtained as white solid (0.135 g, 73%). ^{1}H NMR (300 MHz, (CD_2Cl_2): δ (ppm) 7.26 – 7.12 (m, 8H), 7.06 – 6.92 (m, 18H), 4.67 (t, *J* = 5.5 Hz, 2H), 4.31 (d, *J* = 5.9 Hz, 4H). ^{13}C NMR (75 MHz, (CD_2Cl_2): δ (ppm) 161.09, 158.51, 157.88, 148.38, 147.54, 144.47, 144.43, 134.32, 129.80, 128.80, 127.02, 126.91, 124.06, 124.04, 123.14, 116.67, 116.37, 44.40. HRMS (ES): [M+] calculated, 611.2617; found: 611.2611.

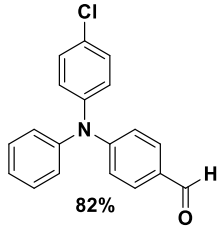

82%

4-((4-chlorophenyl)(phenyl)amino)benzaldehyde: The final product obtained as yellow solid (0.827 g, 82%). ^{1}H NMR (300 MHz, $(CD_3)_2CO$): δ (ppm) 9.85 (s, 1H), 7.76 (d, *J* = 8.8 Hz, 2H), 7.43 (t, *J* = 8.1 Hz, 4H), 7.28 – 7.18 (m, 5H), 7.02 (d, *J* = 8.7 Hz, 2H). ^{13}C NMR (75 MHz, $(CD_3)_2CO$): δ (ppm) 190.71, 153.67, 146.87, 146.08, 131.87, 130.84, 130.65, 128.30, 127.29, 126.35, 120.40. HRMS (EI): [M+] calculated, 307.0764; found: 307.0767.

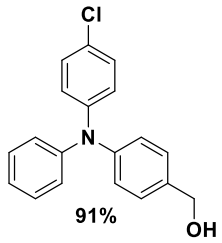

(4-((4-chlorophenyl)(phenyl)amino)phenyl)methanol: The final product obtained as sticky solid (0.370 g, 91%). ^{1}H NMR (300 MHz, $(CD_3)_2SO$): δ (ppm) 7.33 – 7.25 (m, 6H), 7.07 – 6.89 (m, 7H), 5.14 (t, *J* = 5.7 Hz, 1H), 4.45 (d, *J* = 5.7 Hz, 2H). ^{13}C NMR (75 MHz, $(CD_3)_2SO$): δ (ppm) 146.96, 146.41, 145.41, 138.05, 129.56 129.23, 127.97, 125.79, 124.39, 124.04, 123.77, 123.16, 62.58. HRMS (EI): [M+] calculated, 309.0920; found: 309.0918.

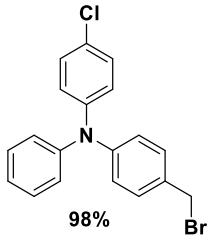

4-(bromomethyl)-N-(4-chlorophenyl)-N-phenylaniline: The final product obtained as sticky solid (0.400 g, 98%). ^{1}H NMR (300 MHz, (CD_2Cl_2): δ (ppm) 7.31 – 7.19 (m, 6H), 7.11 – 6.96 (m, 7H), 4.51 (s, 2H). ^{13}C NMR (75 MHz, (CD_2Cl_2): δ (ppm) 148.16, 147.53, 146.65, 132.33, 130.72, 130.04, 129.85, 128.38, 126.02, 125.44, 124.33, 123.69, 34.62. HRMS (EI): [M+] calculated 371.0076; found: 371.0085.

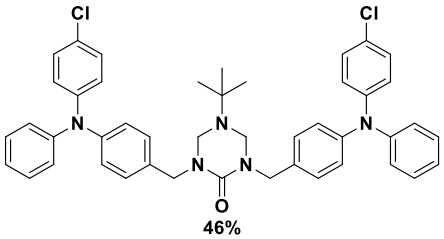

5-(tert-butyl)-1,3-bis(4-((4-chlorophenyl)(phenyl)amino)benzyl)-1,3,5-triazinan-2-one: The final product obtained as white solid (0.179 g, 46%). ^{1}H NMR (300 MHz, (CD_2Cl_2): δ (ppm) 7.27 – 7.16 (m, 12H), 7.05 – 6.95 (m, 14H), 4.45 (s, 4H), 4.24 (s, 4H), 0.99 (s, 9H). ^{13}C NMR (75 MHz, (CD_2Cl_2): δ (ppm) 156.45, 147.98, 147.15, 147.04, 134.09, 129.98, 129.85, 129.64, 127.50, 125.13, 125.09, 124.69, 123.64, 62.19, 54.68, 48.62, 28.64. HRMS (ESI): [M+] calculated 740.2917; found: 740.2924.

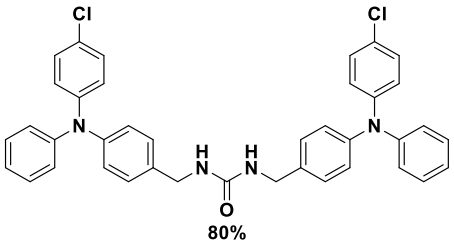

80%

1,3-bis(4-((4-chlorophenyl)(phenyl)amino)benzyl)urea: The final product obtained as white solid (0.116 g, 80%). ^{1}H NMR (300 MHz, (CD_2Cl_2): δ (ppm) 7.29 – 7.14 (m, 12H), 7.07 – 6.93 (m, 14H), 4.68 (t, *J* = 5.5 Hz, 2H), 4.32 (d, *J* = 5.9 Hz, 4H). ^{13}C NMR (75 MHz, (CD_2Cl_2): δ (ppm) 158.56, 147.93, 147.09, 147.07, 135.00, 129.92, 129.71, 128.87, 127.68, 125.29, 124.87, 124.86, 123.80, 44.37. HRMS (ESI): [M+] calculated 643.2026; found: 643.2025.

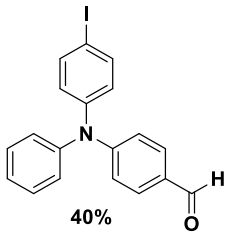

40%

4-((4-iodophenyl)(phenyl)amino)benzaldehyde: The final product obtained as yellow solid (0.224 g, 40%). ^{1}H NMR (300 MHz, $CDCl_3$): δ(ppm) 9.83 (s, 1H), 7.69 (d, J = 8.7 Hz, 2H), 7.62 (d, J = 8.7 Hz, 2H), 7.35 (t, J = 7.8 Hz, 2H), 7.17 (dt, J = 8.7, 7.4 Hz,

3H), 7.04 (d, J = 8.7 Hz, 2H), 6.91 (d, J = 8.7 Hz, 2H). ^{13}C NMR (75 MHz, $CDCl_3$): δ (ppm) 190.31, 152.68, 146.06, 145.74, 138.67, 131.32, 129.90, 129.71, 127.57, 126.31, 125.44, 120.09, 88.36. HRMS (EI): [M+] calculated, 399.0120; found: 399.0109.

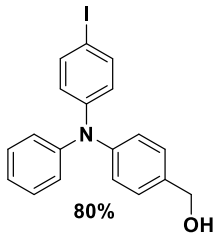

(4-((4-iodophenyl)(phenyl)amino)phenyl)methanol: The final product obtained as sticky solid (0.170 g, 80%). ^{1}H NMR (300 MHz, $(CD_3)_2SO$): δ(ppm) 7.56 (d, *J* = 8.7 Hz, 2H), 7.33 – 7.24 (m, 4H), 7.09 – 6.95 (m, 5H), 6.73 (d, *J* = 8.7 Hz, 2H), 5.14 (t, *J* = 5.7 Hz, 1H), 4.45 (d, *J* = 5.7 Hz, 2H). ^{13}C NMR (75 MHz, CD_2Cl_2): δ (ppm) 148.23, 147.69, 147.04, 138.56, 136.84, 129.95, 128.81, 125.66, 125.10, 125.00, 123.97, 85.19, 64.96. HRMS (EI): [M+] calculated, 401.0277; found: 401.0270.

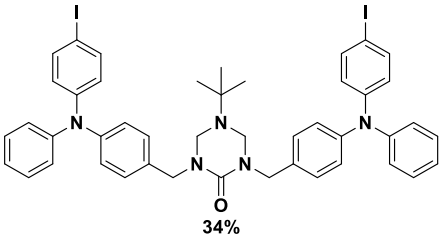

5-(tert-butyl)-1,3-bis(4-((4-iodophenyl)(phenyl)amino)benzyl)-1,3,5-triazinan-2-one: The final product obtained as white solid (0.112 g, 34%). ^{1}H NMR (300 MHz, CD_2Cl_2): δ(ppm) 7.49 (d, *J* = 8.8 Hz, 4H), 7.24 (q, *J* = 6.8, 6.1 Hz, 8H), 7.04 (dd, *J* = 7.7, 5.4 Hz, 10H), 6.79 (d, *J* = 8.8 Hz, 4H), 4.45 (s, 4H), 4.24 (s, 4H), 0.99 (s, 9H). ^{13}C NMR (75 MHz CD_2Cl_2): δ(ppm) 156.41, 148.30, 147.74, 146.80, 138.50, 134.30, 130.01,

129.88, 125.46, 125.34, 124.96, 124.44, 123.87, 84.90, 62.18, 48.61, 28.65. HRMS (ESI): [M+] calculated 924.1630; found: 924.1628.

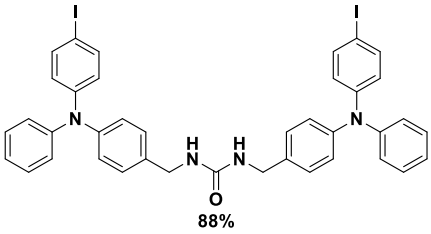

88%

1,3-bis(4-((4-iodophenyl)(phenyl)amino)benzyl)urea: The final product obtained as white solid (0.082 g, 88%). ^{1}H NMR (300 MHz, CD_2Cl_2): δ(ppm) 7.49 (d, *J* = 8.8 Hz, 4H), 7.28 – 7.16 (m, 8H), 7.07 – 6.99 (m, 10H), 6.78 (d, *J* = 8.8 Hz, 4H), 4.68 (t, *J* = 5.8 Hz, 2H), 4.32 (d, *J* = 5.8 Hz, 4H). ^{13}C NMR (75 MHz, (CD_2Cl_2): δ(ppm) 158.53, 148.27, 147.71, 146.83, 138.57, 135.24, 129.95, 128.88, 125.62, 125.14, 124.64, 124.01, 44.36. HRMS (ESI): [M+] calculated 827.0728; found: 827.0743148.

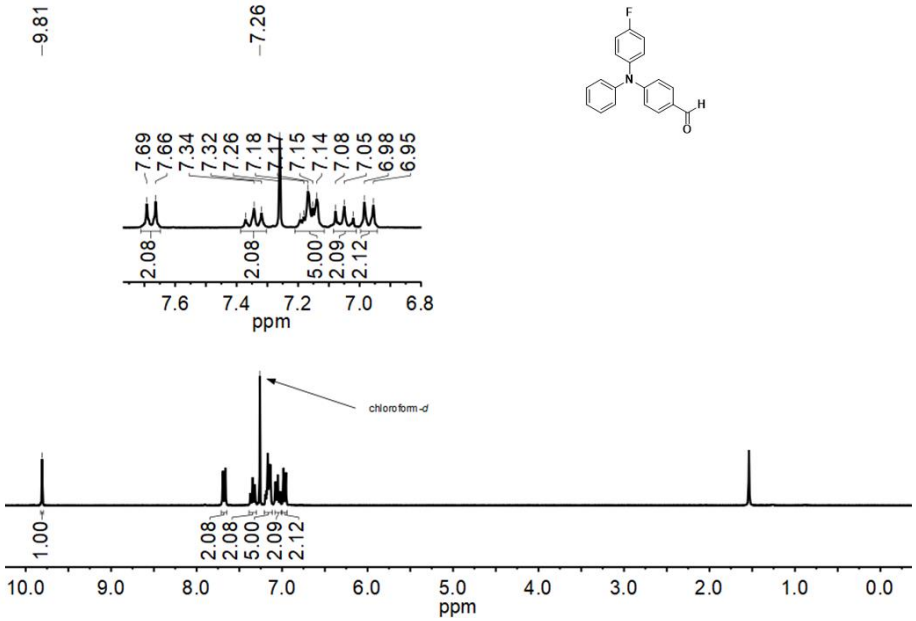

Figure 2.10. ^{1}H NMR ($CDCl_3$, 300 MHz).

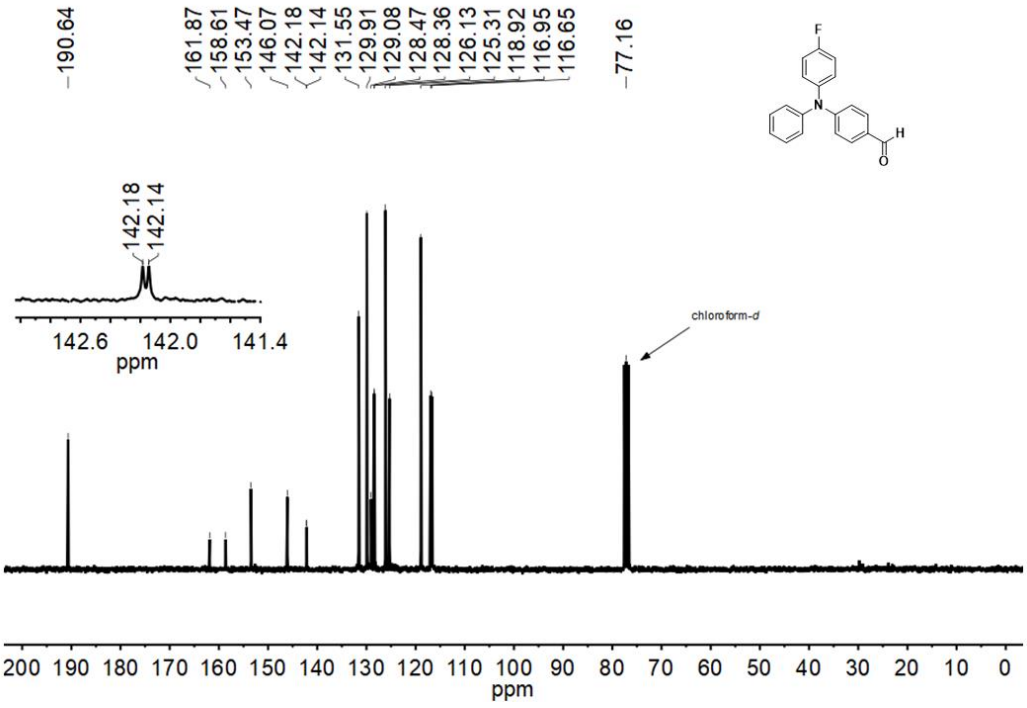

Figure 2.11. ^{13}C NMR ($CDCl_3$, 75 MHz).

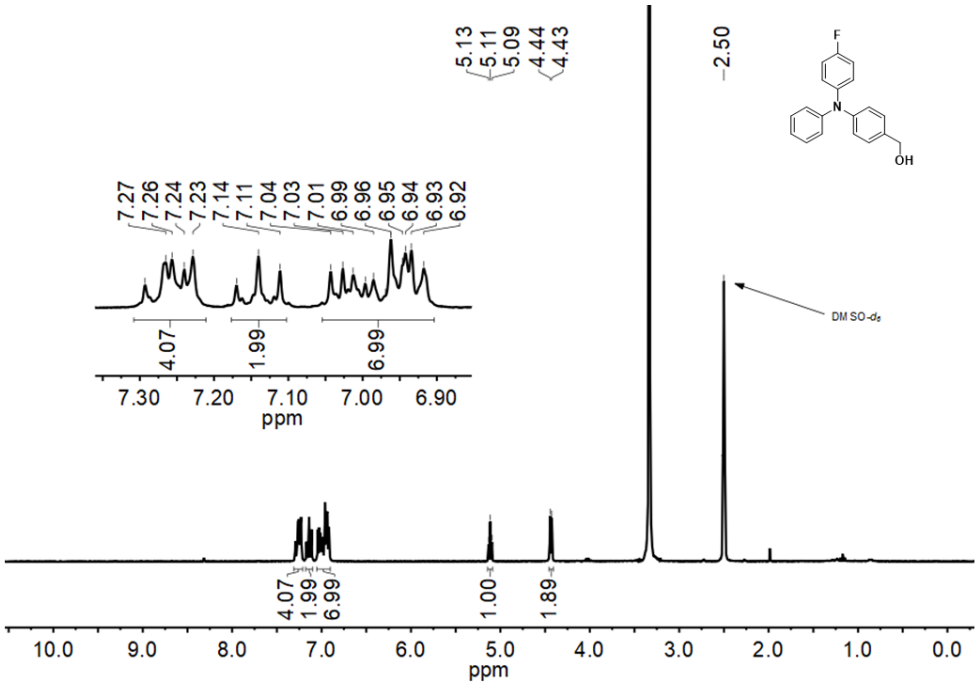

Figure 2.12. ^{1}H NMR ($(CD_3)_2SO$, 300 MHz).

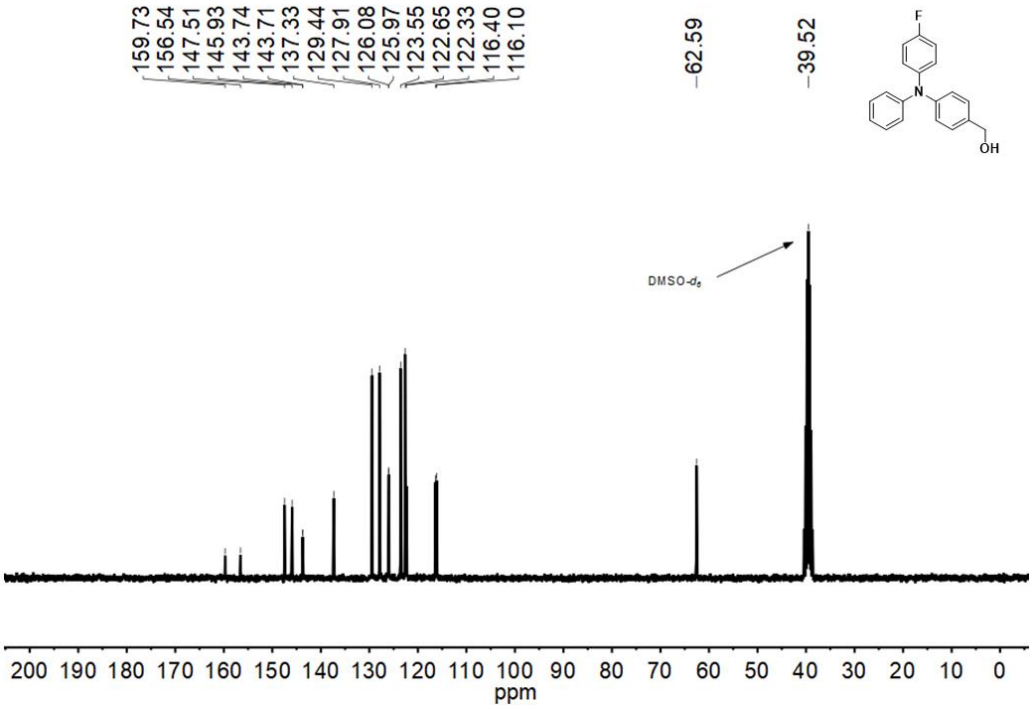

Figure 2.13. ^{13}C NMR ($(CD_3)_2SO$, 75 MHz).

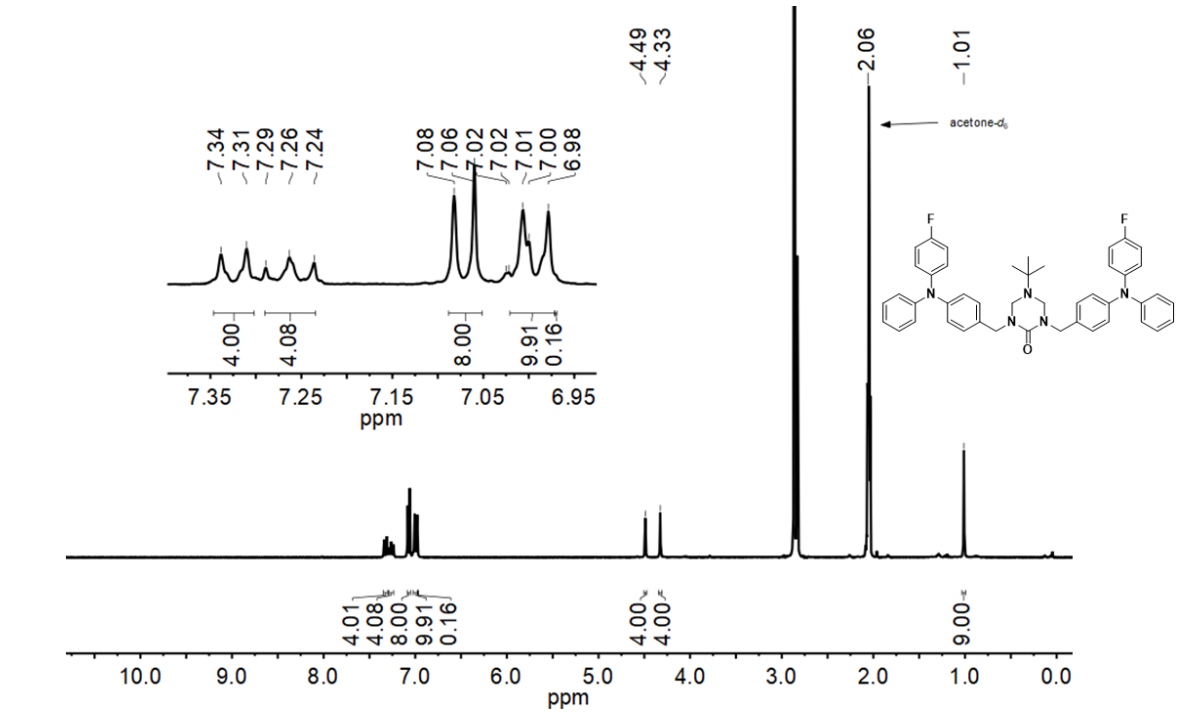

Figure 2.14. ^{1}H NMR ($(CD_3)_2CO$, 300 MHz).

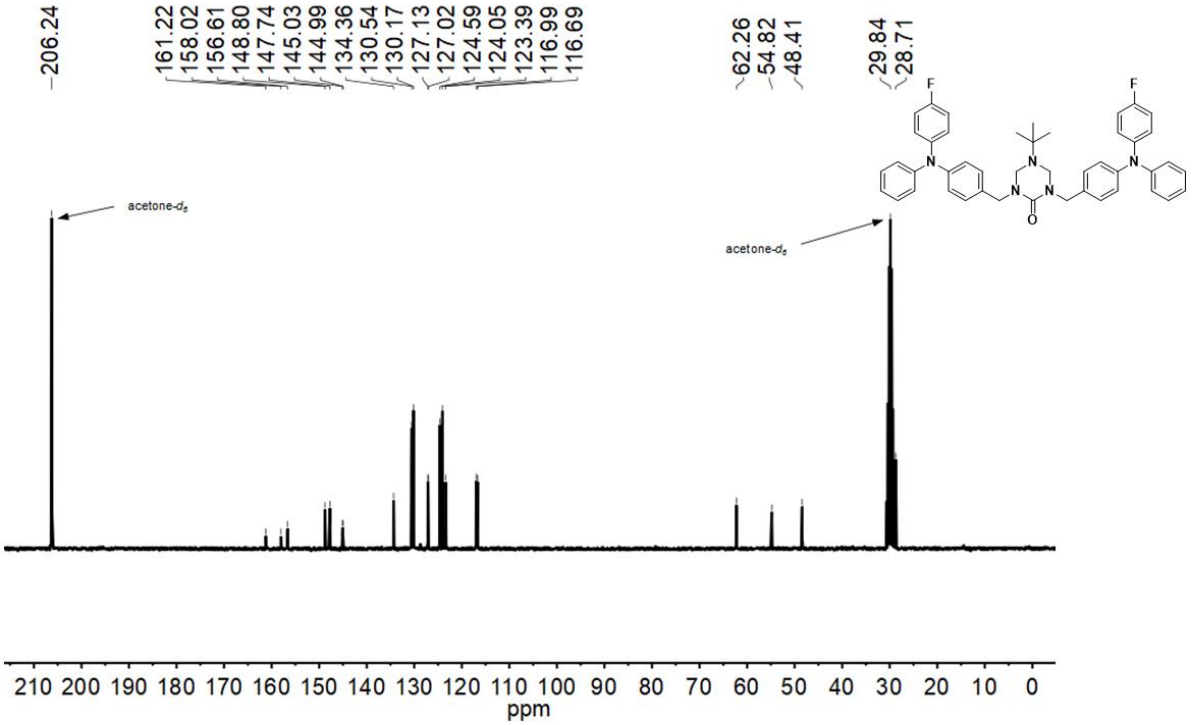

Figure 2.15. ^{13}C NMR ($(CD_3)_2CO$, 75 MHz).

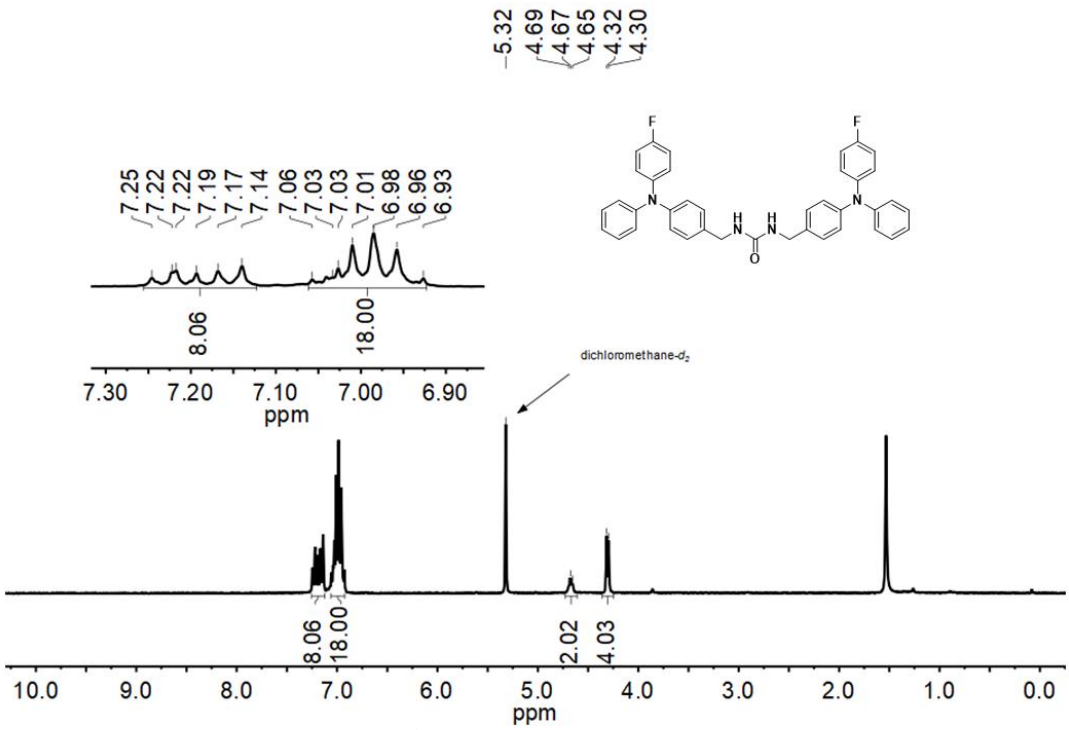

Figure 2.16. ^{1}H NMR (CD_2Cl_2, 300 MHz).

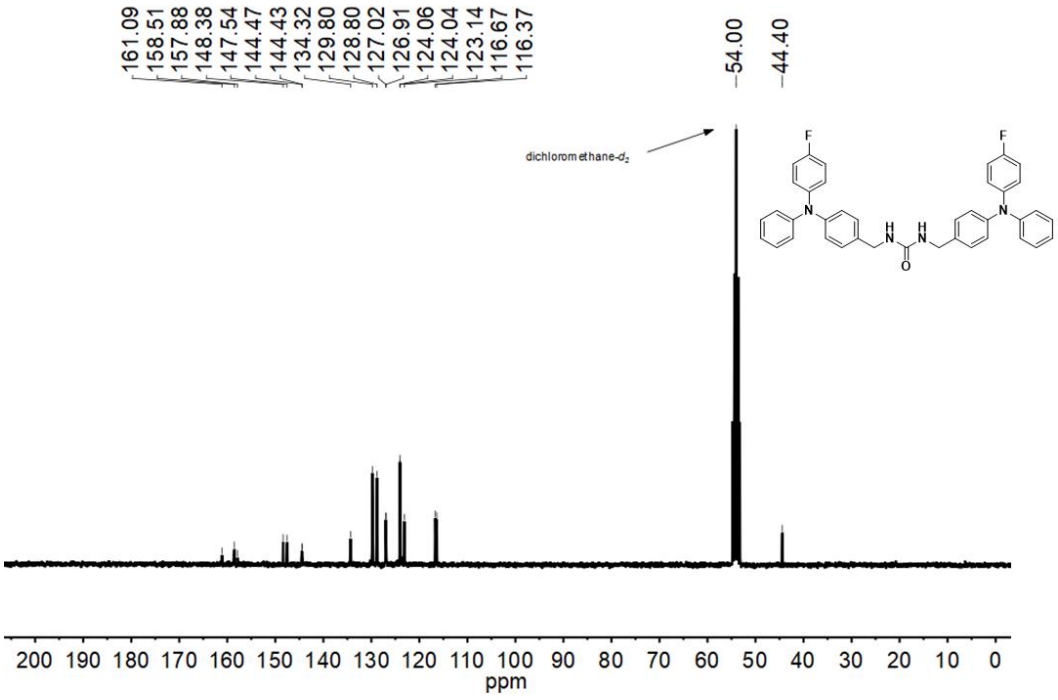

Figure 2.17. ^{13}C NMR (CD_2Cl_2, 75 MHz).

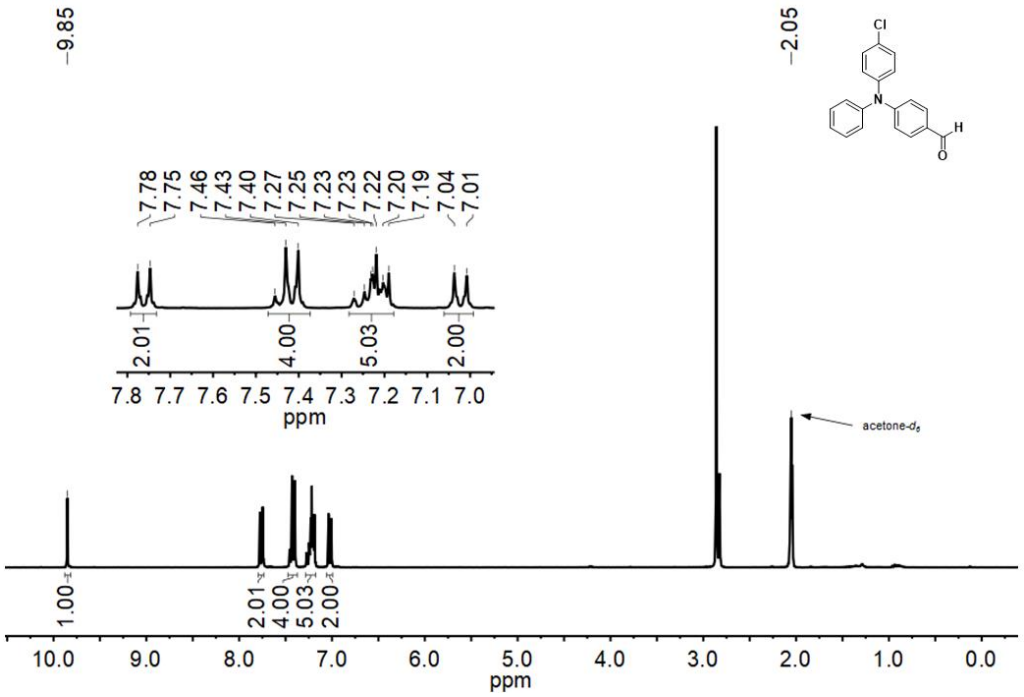

Figure 2.18. ^{1}H NMR ($(CD_3)_2CO$, 300 MHz).

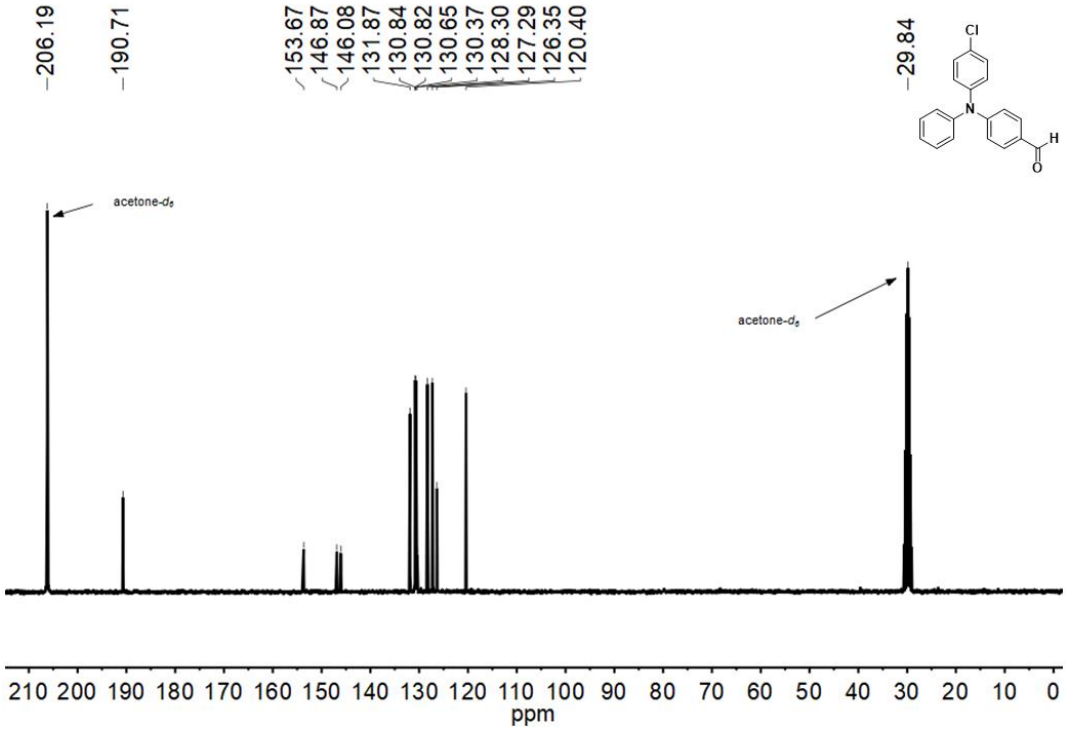

Figure 2.19. ^{13}C NMR ($(CD_3)_2CO$, 75 MHz).

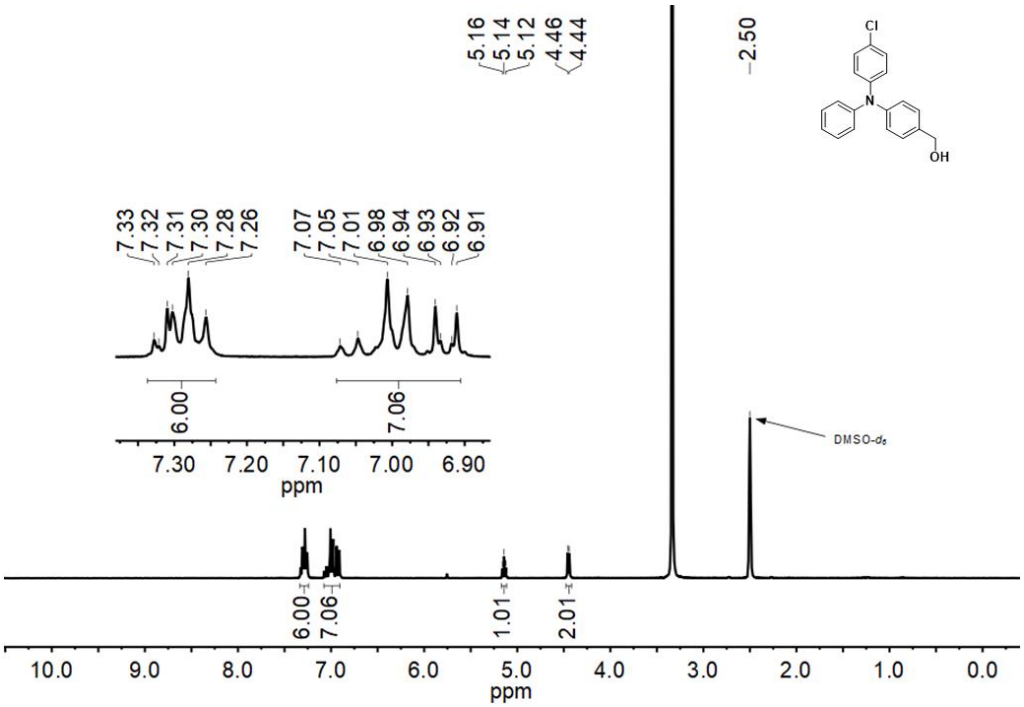

Figure 2.20. ^{1}H NMR ($(CD_3)_2SO$, 300 MHz).

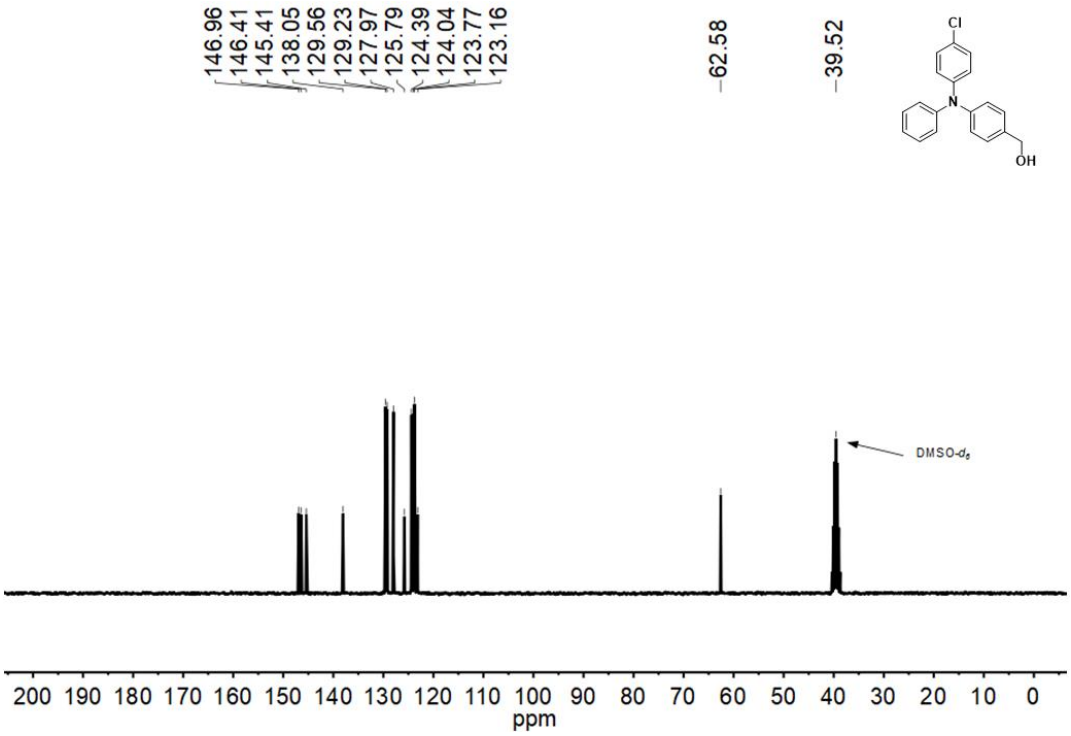

Figure 2.21. ^{13}C NMR ($(CD_3)_2SO$, 75 MHz).

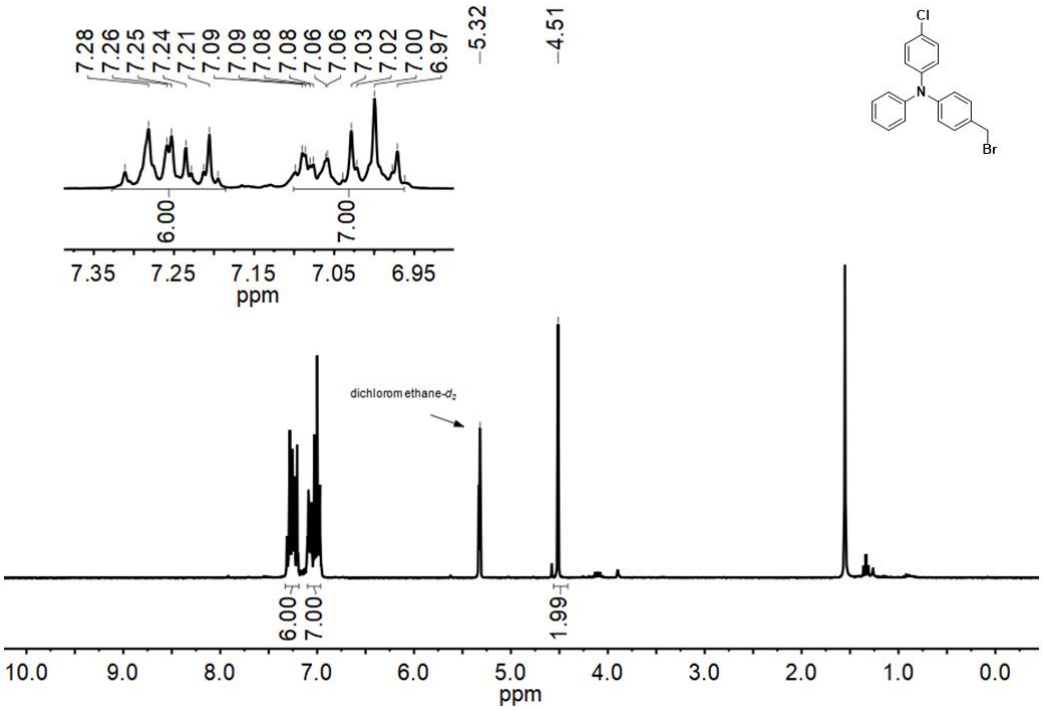

Figure 2.22. ^{1}H NMR (CD_2Cl_2, 300 MHz).

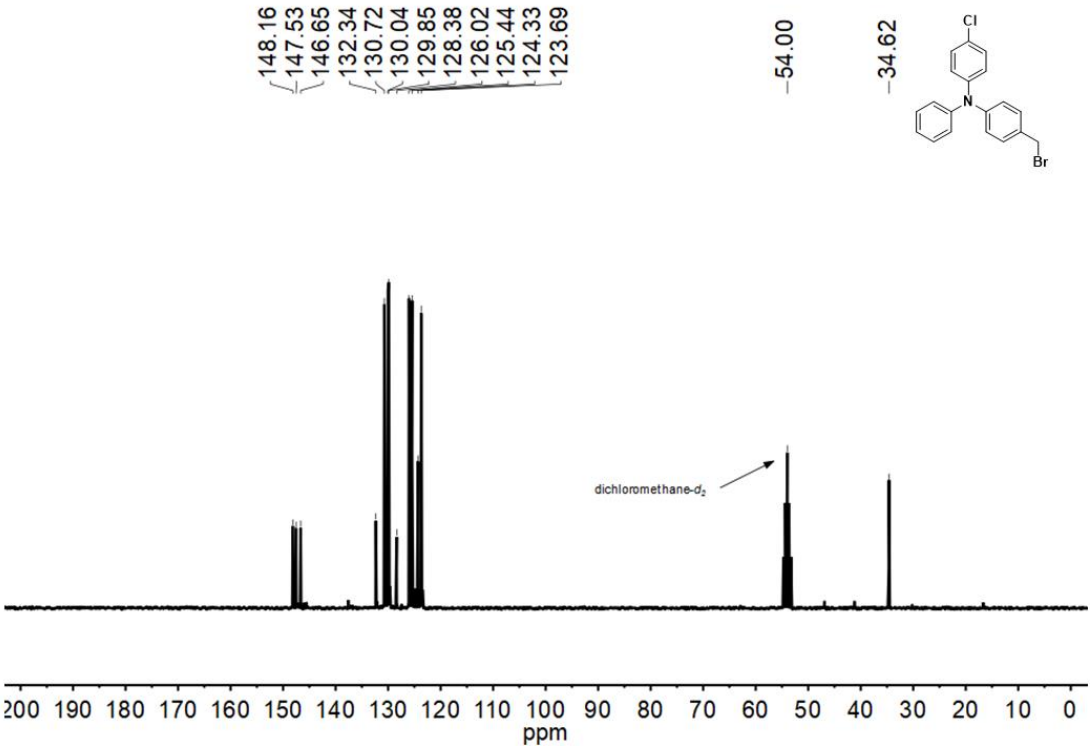

Figure 2.23. ^{13}C NMR (CD_2Cl_2, 75 MHz).

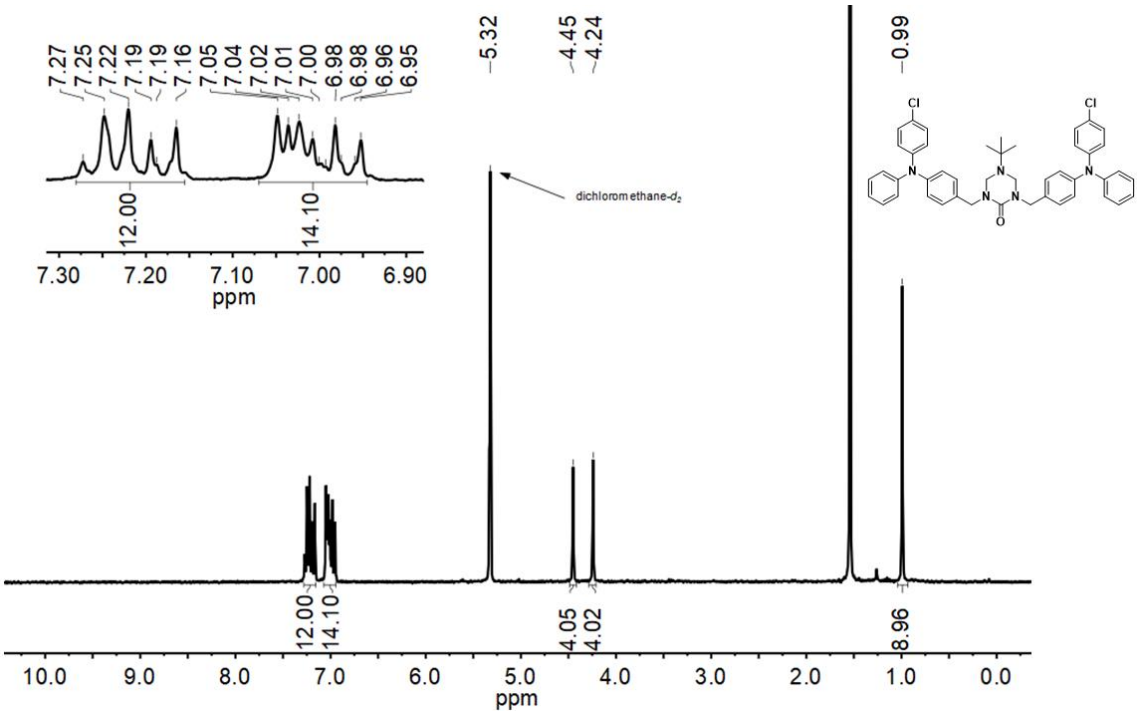

Figure 2.24. ^{1}H NMR (CD_2Cl_2, 300 MHz).

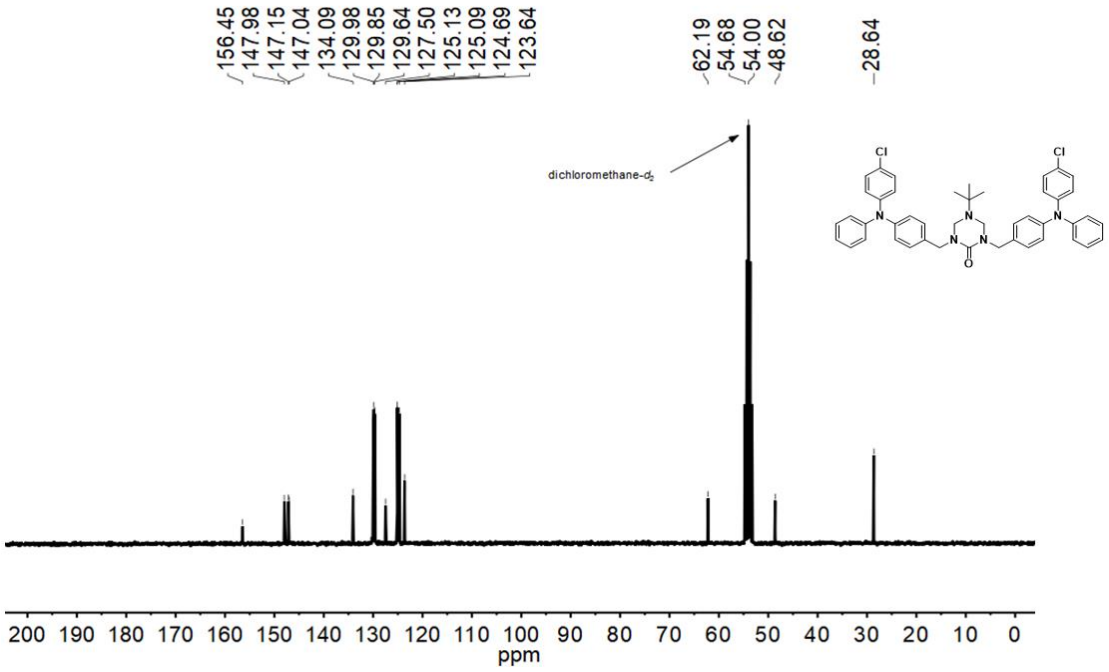

Figure 2.25. ^{13}C NMR (CD_2Cl_2, 75 MHz).

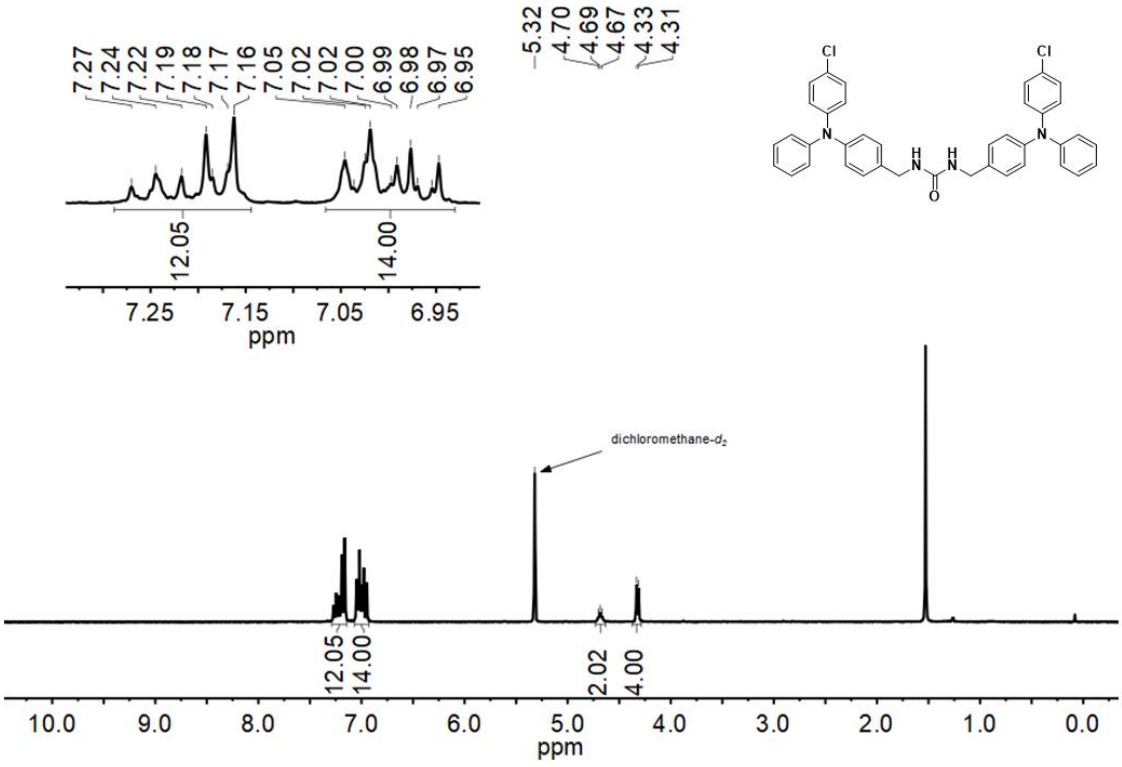

Figure 2.26. ^{1}H NMR (CD_2Cl_2, 300 MHz).

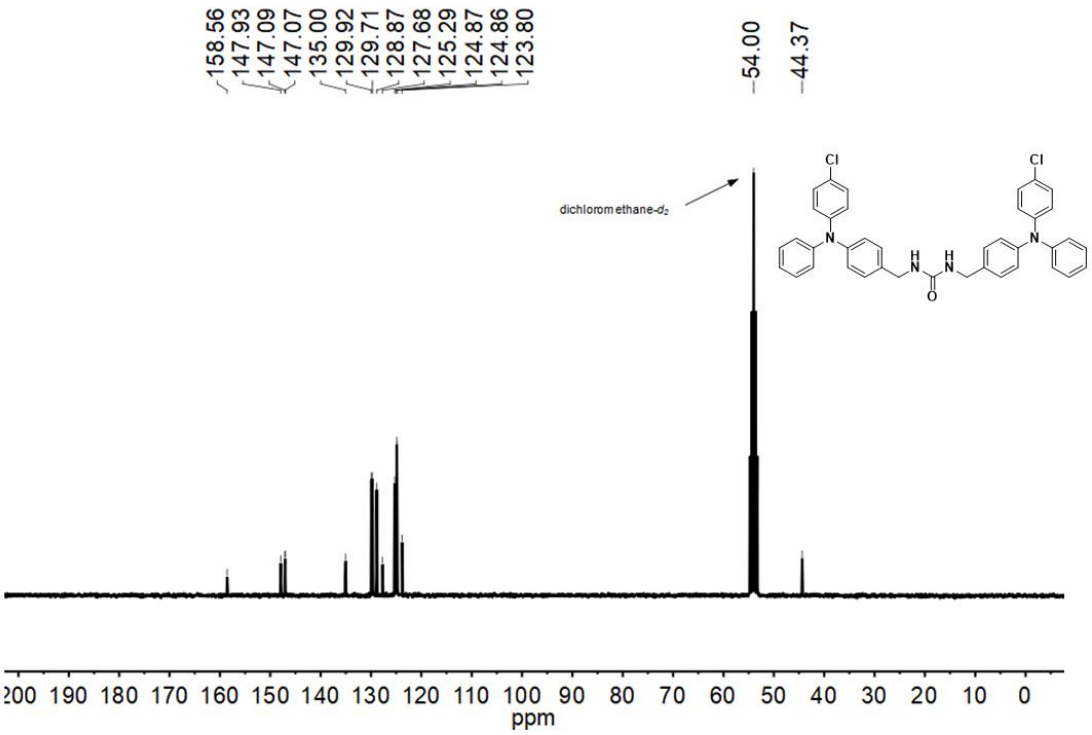

Figure 2.27. ^{13}C NMR (CD_2Cl_2, 75 MHz).

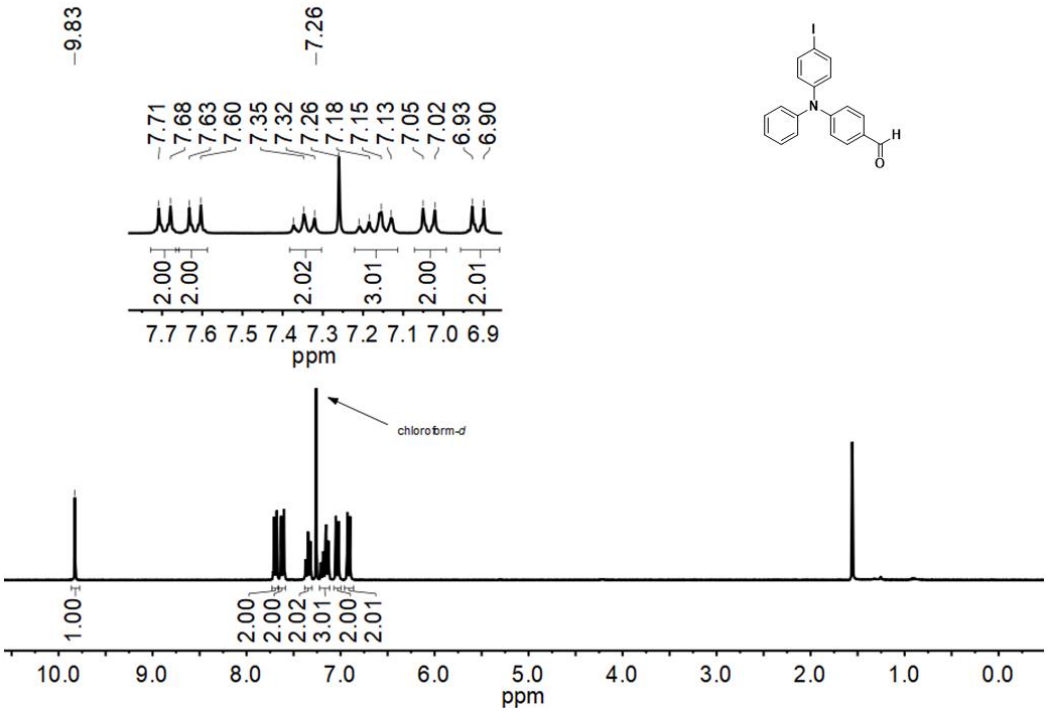

Figure 2.28. ^{1}H NMR ($CDCl_3$, 300 MHz).

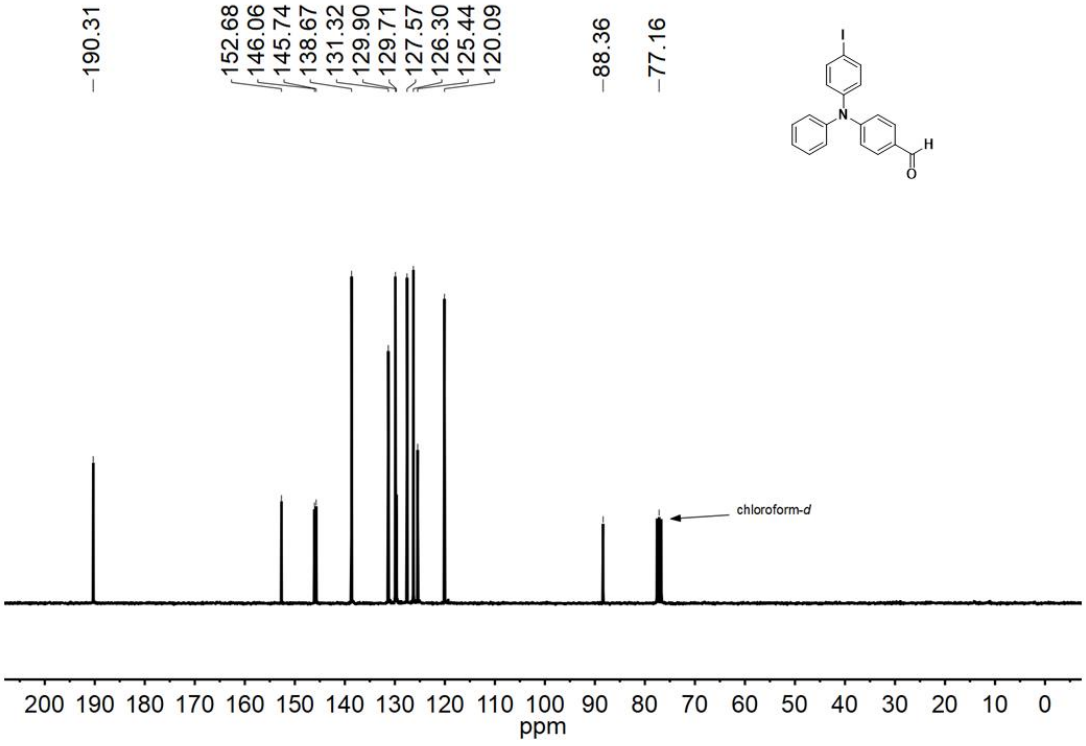

Figure 2.29. ^{13}C NMR ($CDCl_3$, 75 MHz).

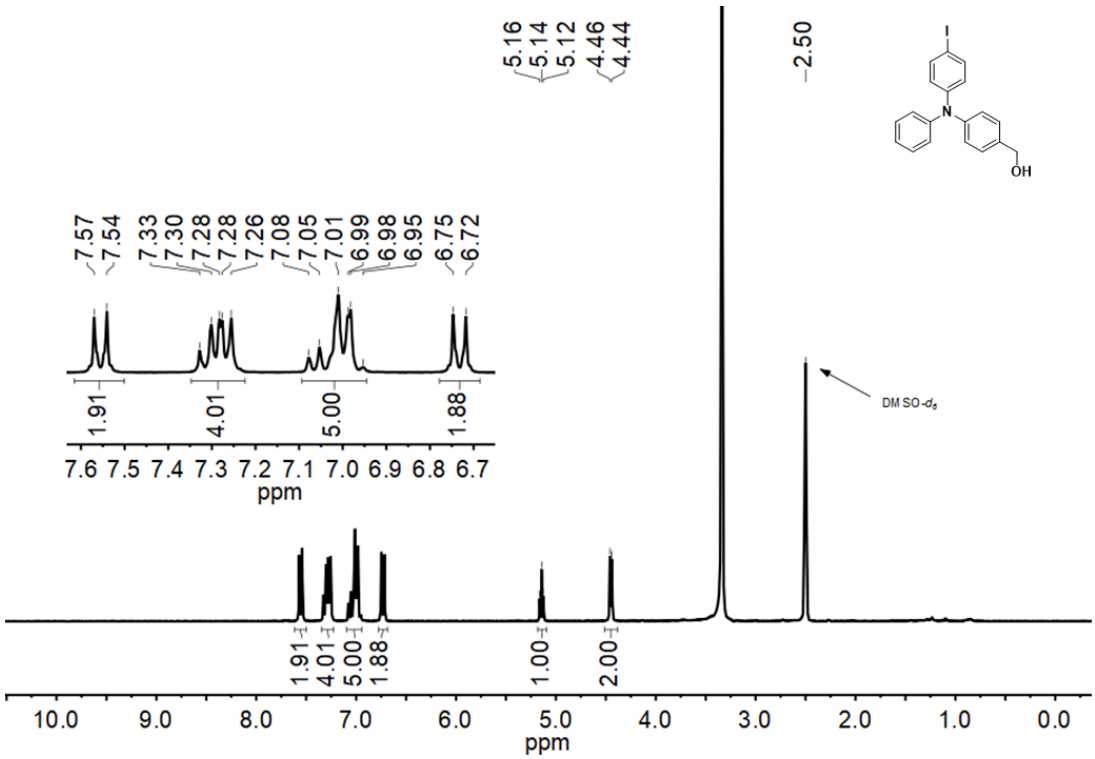

Figure 2.30. ^{1}H NMR ($(CD_3)_2SO$, 300 MHz)

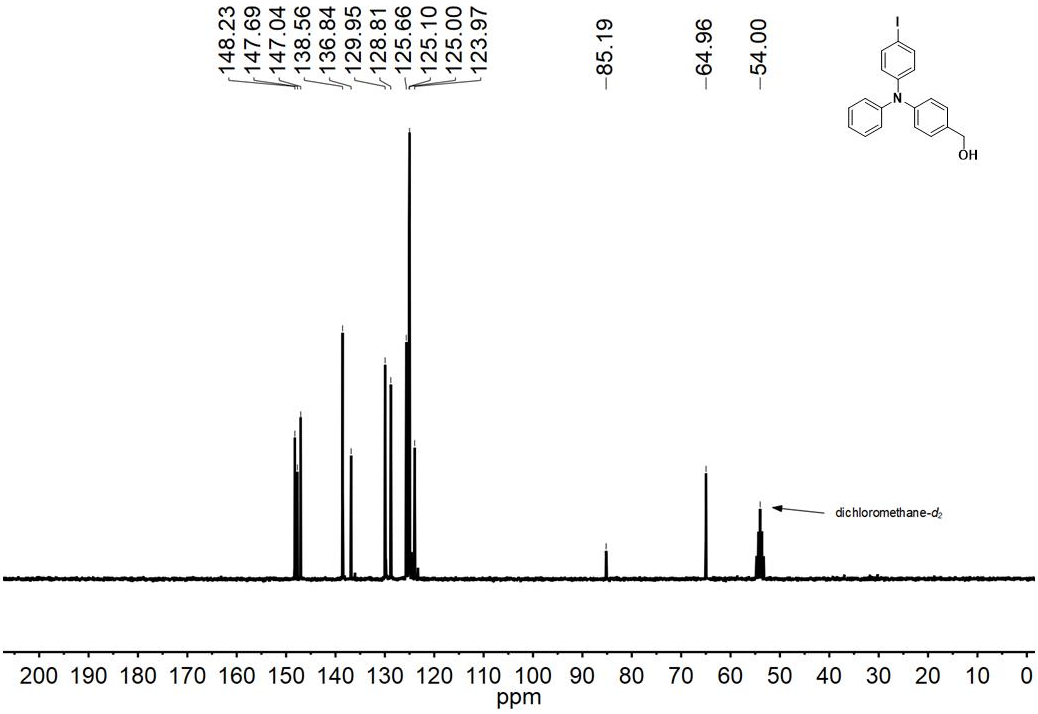

Figure 2.31. ^{13}C NMR (CD_2Cl_2, 75 MHz).

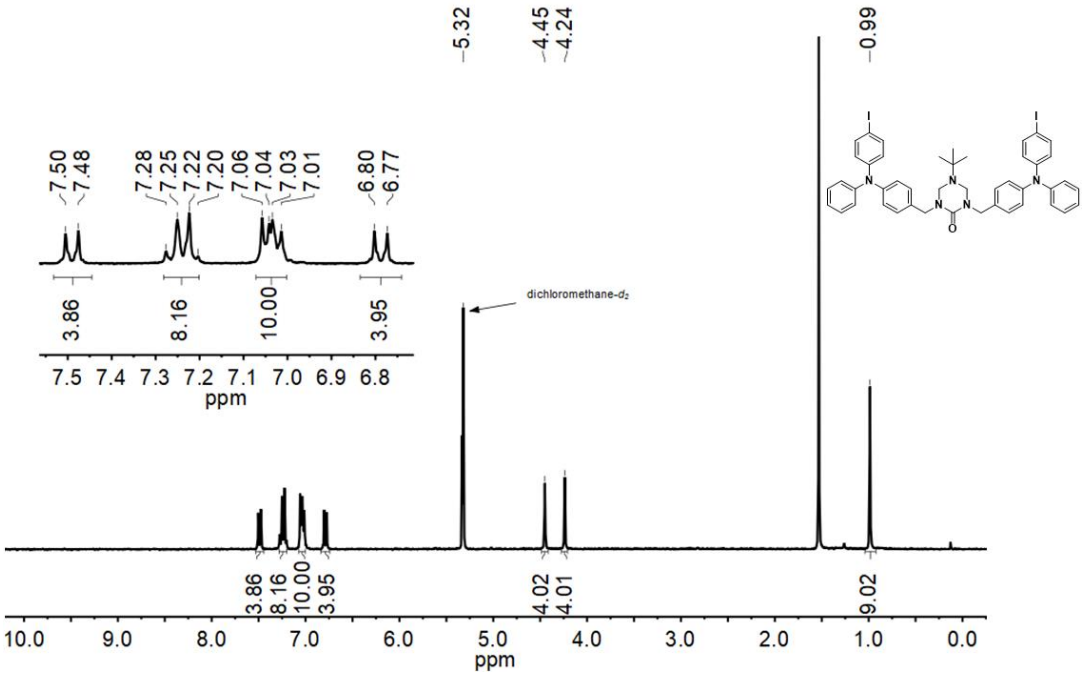

Figure 2.32. ^{1}H NMR (CD_2Cl_2, 300 MHz).

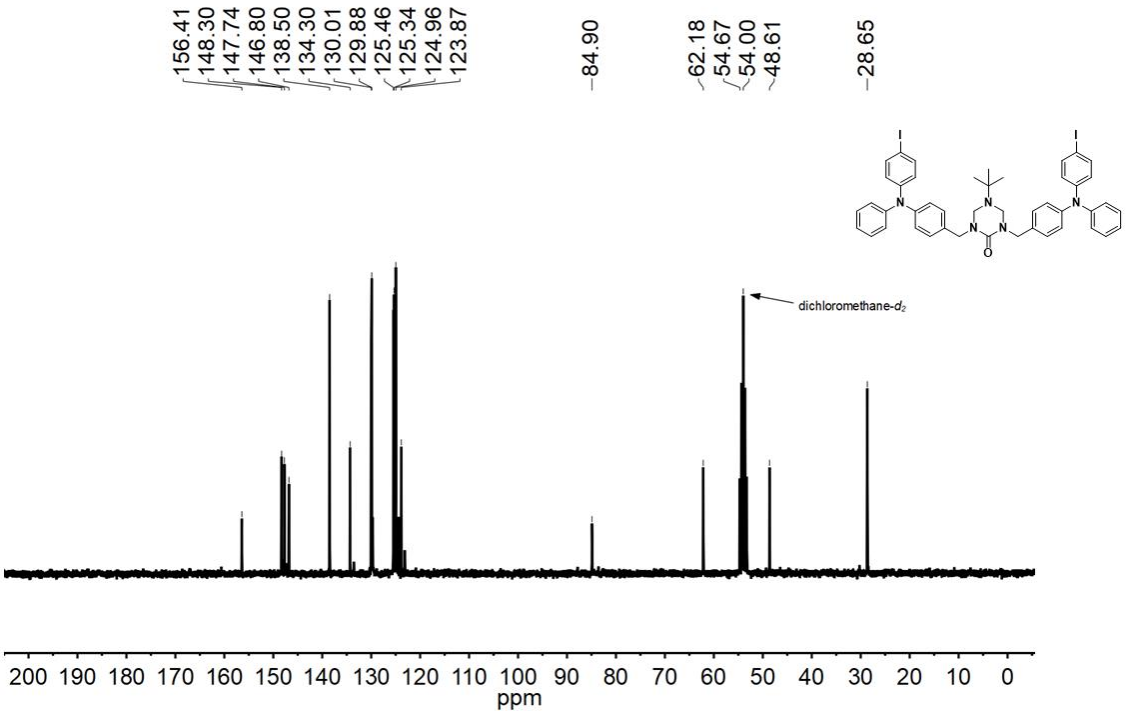

Figure 2.33. ^{13}C NMR (CD_2Cl_2, 75 MHz).

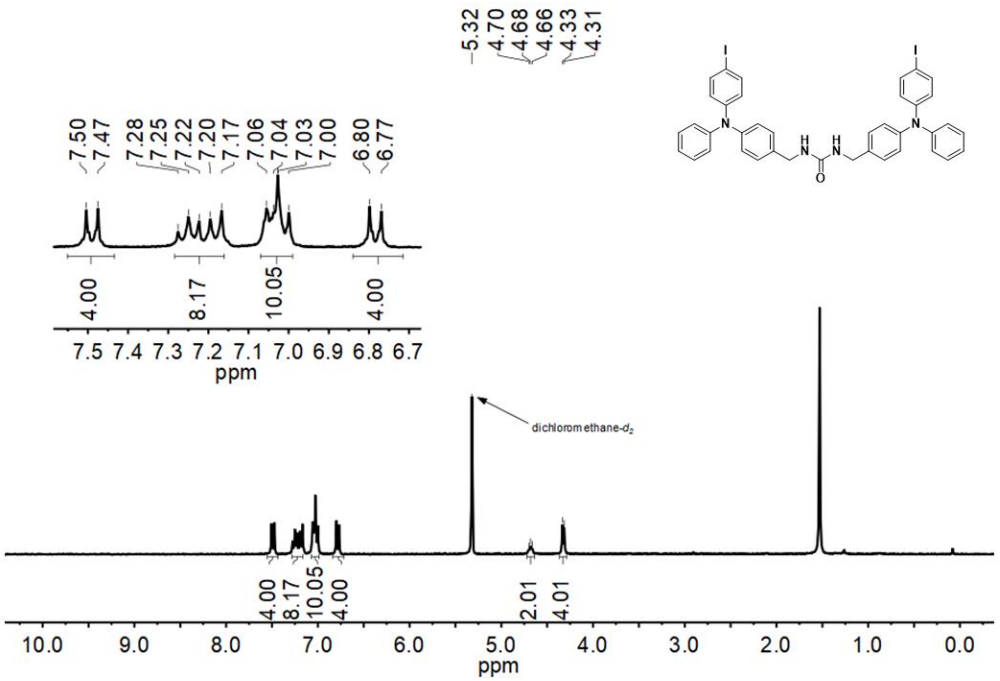

Figure 2.34. ^{1}H NMR (CD_2Cl_2, 300 MHz).

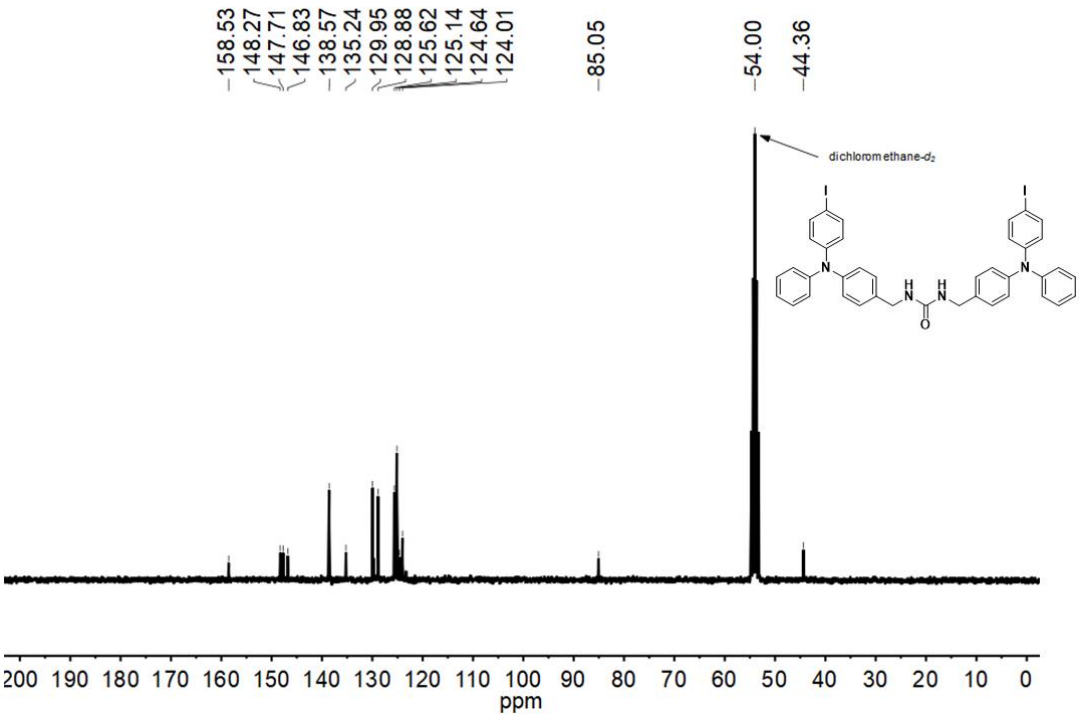

Figure 2.35. ^{13}C NMR (CD_2Cl_2, 75 MHz).

1

2.5.2 Crystal data and structure refinement

Structure 1I

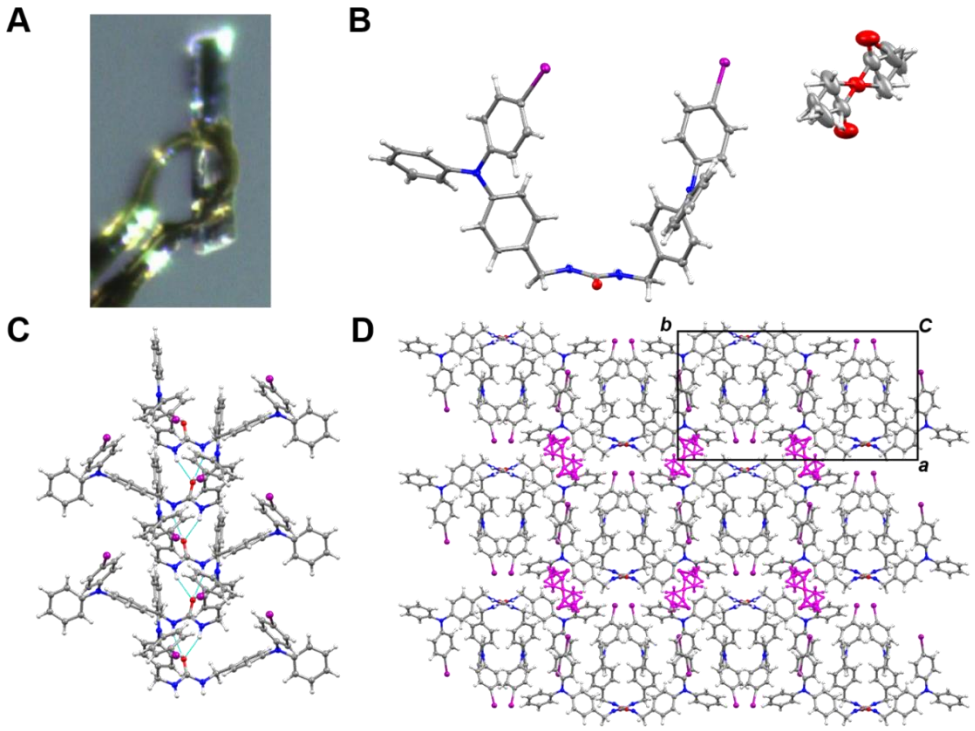

Figure 2.36. Different crystalline arrangement of urea tethered TPA **1I**. (A) Data crystal. (B) Asymmetric unit of the crystal Displacement ellipsoids drawn at the 50% probability level. The ethyl acetate is disordered about a crystallographic inversion center and half is present per $C_{39}H_{32}I_2N_4O$ molecule. (C) Hydrogen-bonded strands run along the crystallographic *c* axis direction. (D) Crystal packing along *c* axis. Disordered ethyl acetate molecules highlighted in magenta.

The compound crystallizes in the monoclinic system. The pattern of systematic absences in the intensity data was consistent the space group $P2_1/c$, which was confirmed by structure solution. The asymmetric unit consists of one $C_{39}H_{32}I_2N_4O$ molecule and half of one ethyl acetate molecule, which is disordered about a crystallographic inversion center. The ethyl acetate was refined with half-occupancy, with the aid of C-C and C-O distance restraints. All non-hydrogen atoms were refined with anisotropic displacement

parameters. SHELX DELU and SIMU restraints were applied to the ethyl acetate carbon and oxygen atoms to maintain physically reasonable displacement ellipsoids. Hydrogen atoms bonded to carbon were placed in geometrically idealized positions and included as riding atoms with *d*(C-H) = 0.95 Å and *U*iso(H) = 1.2*U*eq(C) for arene hydrogen atoms, *d*(C-H) = 0.99 Å and *U*iso(H) = 1.2*U*eq(C) for methylene hydrogen atoms and *d*(C-H) = 0.98 Å and *U*iso(H) = 1.5*U*eq(C) for methyl hydrogens. Hydrogen atoms bonded to nitrogen were located and refined with *d*(N-H) = 0.85(2) distance restraints and *U*iso(H) = 1.2*U*eq(N). The largest residual electron density peak in the final difference map is 0.90 $e^-/Å^3$ located 0.99 Å from I1.

Structure 1Cl

The compound crystallizes in the orthorhombic system. The pattern of systematic absences in the intensity data was uniquely consistent with the space group *Pccn*, which was verified by structure solution. The asymmetric unit consists of half of one molecule, which is located on a two-fold axis of rotation. The structure is disordered. After routine location and anisotropic refinement of the unique half of the molecule, a large residual electron density peak (magnitude 1.1 e-/$Å^3$) was observed in a chemically implausible site, *ca*. 2.0 Å from Cl1. After ruling out data processing errors (crystal slippage, poor integration parameters, absorption correction, *e.g.*) the peak was eventually interpreted as the chlorine atom of a minor 'whole-molecule' disorder component. Other peaks could be picked from difference Fourier maps to complete the unique half of the minor disorder component, also located on the two-fold axis. The carbonyl C and O atoms are common to both disorder components. 1,2- and 1,3-distances in the minor disorder component (atoms label suffixes "B") were restrained to be similar to those in the major component (atom

label suffixes "A") *via* a SHELX SAME instruction. Anisotropic displacement parameters

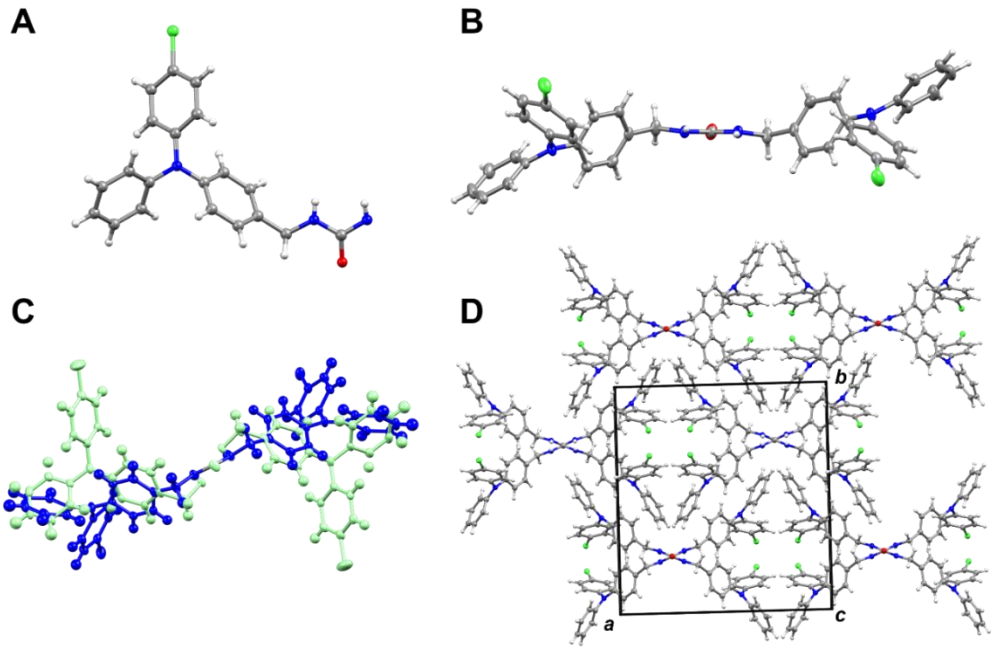

Figure 2.37. Different crystalline arrangement of linear analog **1Cl**. (A) Molecular structure for urea tethered TPA **1Cl** (B) Displacement ellipsoid plot of the major component. Displacement ellipsoids drawn at the 50% probability level. (C) Whole-molecule disorder throughout the crystal. Both disorder components located on a C_2 axis of rotation. Displacement ellipsoids drawn at the 50% probability level. Major disorder component (blue) population is 95%. (D) Crystal packing along the *c*-axis.

for atoms which are overlapped were held equal. Additional FLAT instructions were necessary for rings C9B-C14B and C15B-C20B, and Cl1B was restrained to be equidistant from C11B and C13B. The disorder fractions were constrained to sum to one and refined to A/B = 0.945(1) / 0.055(1). A previously solved bromine analog showed similar disorder, but with a minor component fraction of 9%. As in that compound, no sign of the disorder was evident in the diffraction frames, and no resolving twin law was found by using the TwinRotMat program.[73] The disorder model suggests a deviation from ideal C_2 point symmetry in approximately 5% of molecules throughout the crystal. All non-hydrogen

atoms were refined with anisotropic displacement parameters. Hydrogen atoms bonded to carbon were placed in geometrically idealized positions and included as riding atoms with *d*(C-H) = 0.95 Å and *U*iso(H) = 1.2*U*eq(C) for aromatic hydrogen atoms, and *d*(C-H) = 0.99 Å and *U*iso(H) = 1.2*U*eq(C) for methylene hydrogen atoms. One unique position for the hydrogen atoms bonded to the urea nitrogen was located. It was refined isotropically with distances to both N1A and N1B restrained to be 0.84(2) Å. The largest residual electron density peak in the final difference map is 0.27 $e^-/Å^3$, located 0.68Å from H11B. A model neglecting the whole-molecule disorder gave *R*1/*wR*2 = 0.057/0.176 with difference map extrema of +1.07/-0.47 $e^-/Å^3$

Comparison of solid-state assembly of 1Br, and 1H

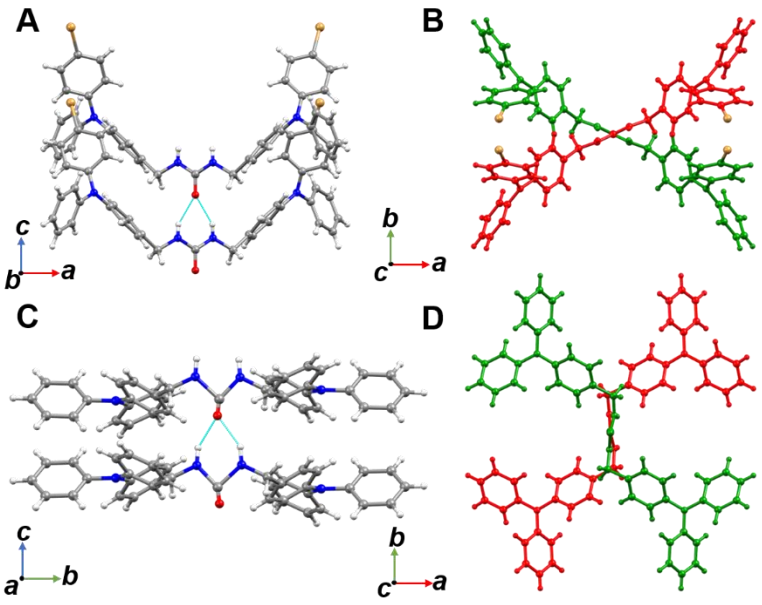

Figure 2.38. Comparison of urea-tethered halogenated TPAs **1Br** and **1H**. (A) Urea-urea hydrogen bonding interactions in **1Br** forming a tape. (B) Top down projection of a **1Br** chain showing a X-shape. (C) Urea stacking for **1H.** (D) Top down view of **1H** form a cruciform pattern.

Table 2.3. Data Collection and Refinement for urea tethered TPA derivatives

Identification code	**1Cl**	**1I**
Empirical formula	$C_{39}H_{32}Cl_2N_4O$	$C_{41}H_{36}I_2N_4O_2$
Formula weight	643.58	870.54
Temperature/K	100(2)	100(2)
Crystal system	orthorhombic	monoclinic
Space group	Pccn	$P2_1/c$
a/Å	18.4725(12)	14.8483(10)
b/Å	19.8765(13)	26.8994(18)
c/Å	8.9785(6)	9.0681(6)
α/°	90	90
β/°	90	97.5310(10)
γ/°	90	90
Volume/$Å^3$	3296.6(4)	3590.7(4)
Z	4	4
$\rho_{calc}g/cm^3$	1.297	1.610
μ/mm^{-1}	0.235	1.793
F(000)	1344.0	1728.0
Crystal size/mm^3	0.24 × 0.08 × 0.06	0.28 × 0.05 × 0.02
Radiation	MoKα (λ = 0.71073)	MoKα (λ = 0.71073)
2Θ range for data collection/°	3.01 to 52.836	2.766 to 52.85
Index ranges	-23 ≤ h ≤ 23, -24 ≤ k ≤ 24, -11 ≤ l ≤ 11	-18 ≤ h ≤ 18, -33 ≤ k ≤ 33, -11 ≤ l ≤ 11
Reflections collected	62942	51827
Independent reflections	3378 [R_{int} = 0.0661, R_{sigma} = 0.0199]	7388 [R_{int} = 0.0541, R_{sigma} = 0.0295]
Data/restraints/parameters	3378/72/286	7388/47/472
Goodness-of-fit on F^2	1.033	1.195
Final R indexes [I>=2σ (I)]	R_1 = 0.0418, wR_2 = 0.1028	R_1 = 0.0468, wR_2 = 0.1038
Final R indexes [all data]	R_1 = 0.0562, wR_2 = 0.1131	R_1 = 0.0570, wR_2 = 0.1079
Largest diff. peak/hole / e $Å^{-3}$	0.27/-0.38	0.90/-0.94

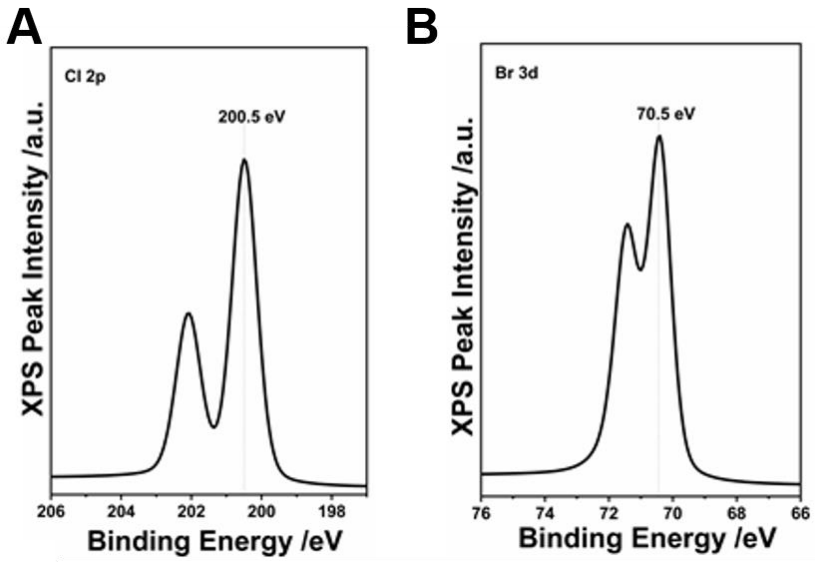

Figure 2.39. XPS analysis for **1Cl** and **1Br** respectively recorded with monochromatic Al Kα X-ray source. (A) Cl(2p) XPS core level peaks. (B) Br(3d) XPS core level peaks.

Hirshfeld Surface Map

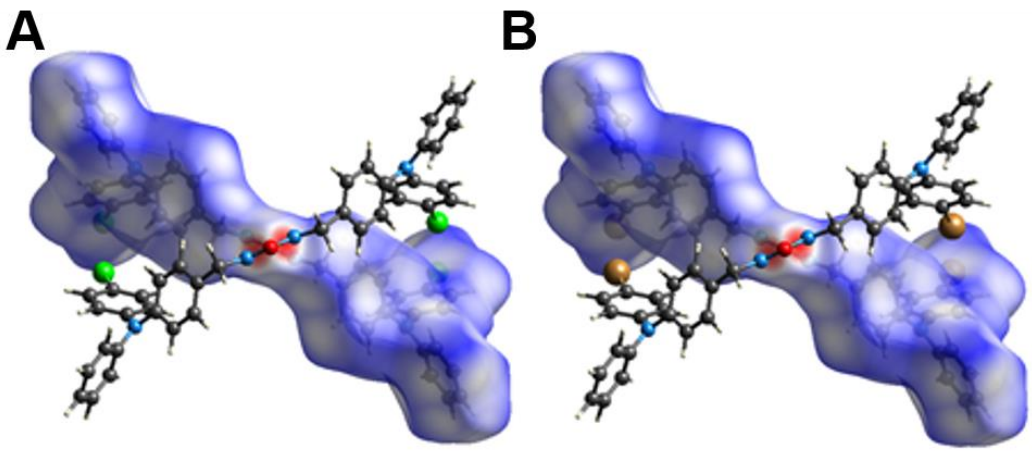

Figure 2.40. Hirshfeld surface map generated by crystal explorer.[54] Red region corresponds strong interaction, white region corresponds to weak interaction and blue region corresponds to no significant interaction. (A) Hirshfeld surface map for **1Cl**. (B) Hirshfeld surface map for **1Br**. In both cases, only the 3 centered urea hydrogen bonding was identified as the strong interactions.

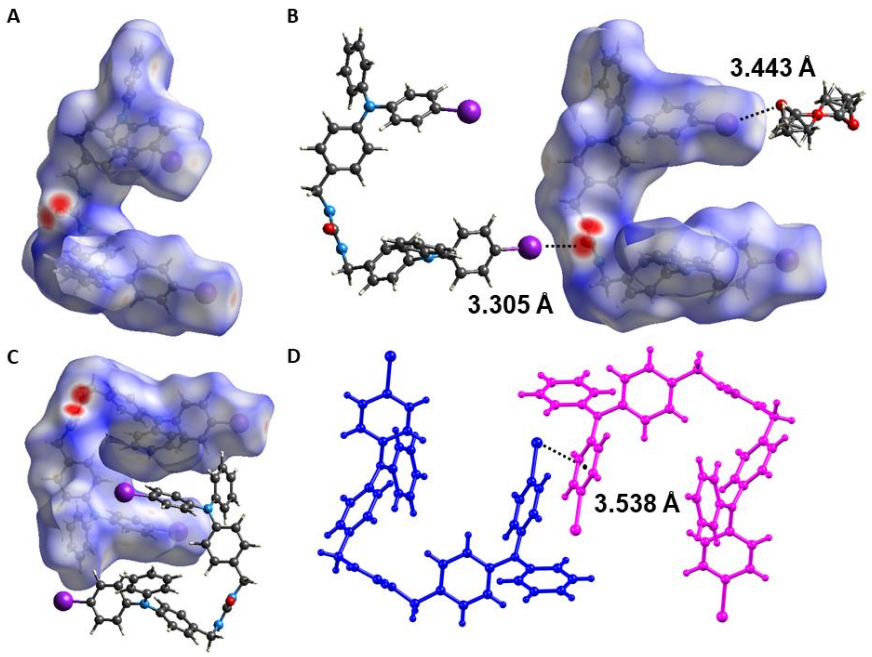

Figure 2.41. Hirshfeld surface analysis.[54] (A) Hirshfeld surface map for **1I**. Red region corresponds strong interaction, white region corresponds to weak interaction and blue region corresponds to no significant interaction. (B) Possible I···CO(O) (urea) interaction 3.305 Å and I···O(EtOAc) interaction 3.443 Å less than sum of the van der waals radii of I···O, 3.5 Å.[10] (C) Possible C-I···π s interaction in Hirshfeld surface analysis. (D) Crystal views of compound **1I** showing C-I···π interaction 3.538 Å. Distance measured from the centroid of the phenyl to the plane of the iodine atom.

Table 2.4. Geometry of the hydrogen bonds of the urea tethered triphenylamines.

Compound (X)	D—H···A	*d* (D···A) (Å)	∠(DHA) (°)	Twisting angle (°)
1H[a]	N1—H1···O1	2.749(8)	148.12	16.32
	N2—H2···O1	2.716(8)	143.07	--
1Cl	N1—H1···O1	2.808(2)	151.18	47.74
	N2—H2···O1	2.808(2)	151.18	--
1Br[b]	N1—H1···O1	2.823(3)	153.07	51.6
	N2—H2···O1	2.700(5)	153.07	--
1I	N1—H1···O1	2.887(5)	152.79	36.28
	N2—H2···O1	2.892(5)	153.64	--

[a] Crystal data taken from reference[28], [b]Crystal data taken from reference[24]

Table 2.5. Measured photophysical properties for compounds **1H**, **1F**, **1Cl**, **1Br**, **1I**.

Compound	Solvent	λ_{abs} (nm)[c]	ε ($\times 10^4$ M^{-1} cm^{-1})	λ_{ems} (nm)[d]
1H	DCM	300	4.26	365, 500
1F		300	4.13	371
1Cl		300	5.53	373, 445
1Br[a]		303[a]	5.20[a]	366, 449[a]
1I		305	4.86	364, 442
1H	EtOAc	298	4.36	358, 472
1F		295	4.26	370
1Cl		300	4.72	374, 478
1Br[a]		301[a]	5.53[a]	364, 453[a]
1I		300	4.63	362,480
1H	THF	299	4.52	362, 470
1F		285	4.95	369
1Cl		300	2.58	372, 475
1Br[a]		302[a]	5.22[a]	367, 457[a]
1I		300	5.00	361
1H solid[b]		366		479
1Cl solid		360		451
1Br solid[a]		358		451
1I solid		363		459

[a] Data taken from reference 24. [b] Data taken from reference 28 [c] Peak position at the largest absorption band. [d] Peak position at the largest emission bands in nanometers (largest denoted with * if applicable, excited at λ_{abs}).

2.5.3 Absorbance Measurements

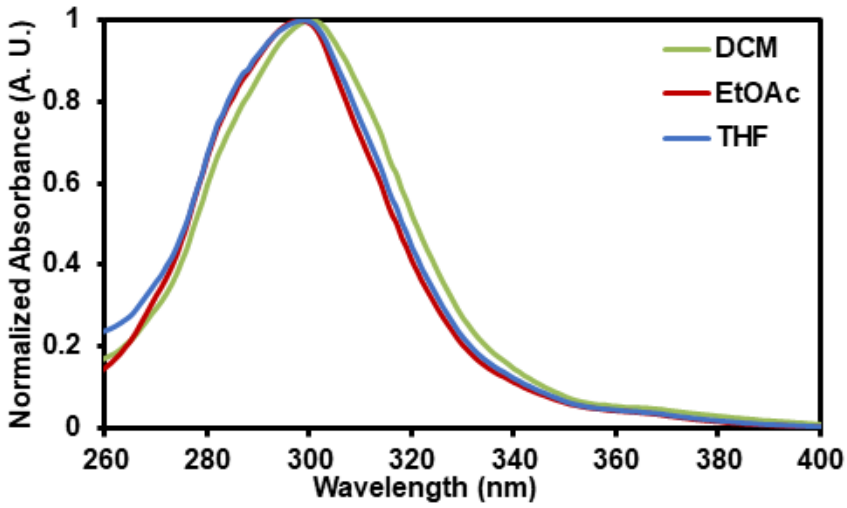

Figure 2.42. UV/Vis absorption spectrum of compound **1H** in DCM, EtOAc and THF.

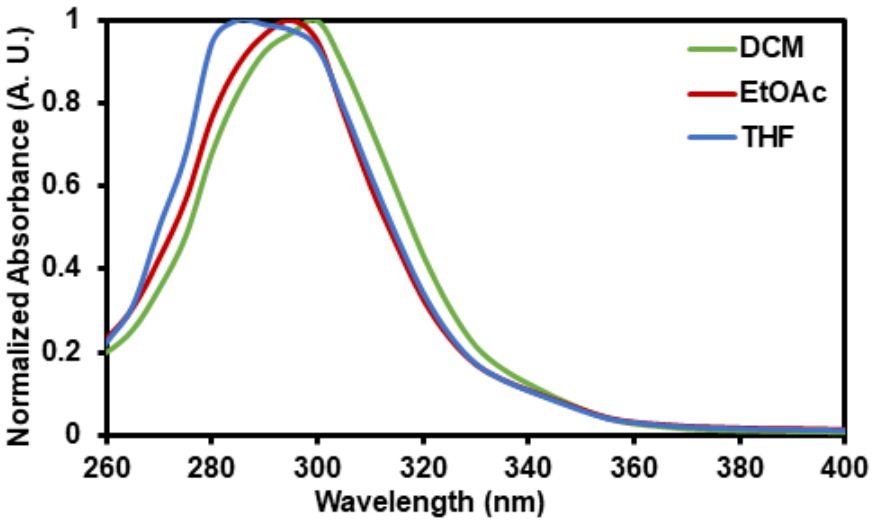

Figure 2.43. UV/Vis absorption spectrum of compound **1F** in DCM, EtOAc and THF.

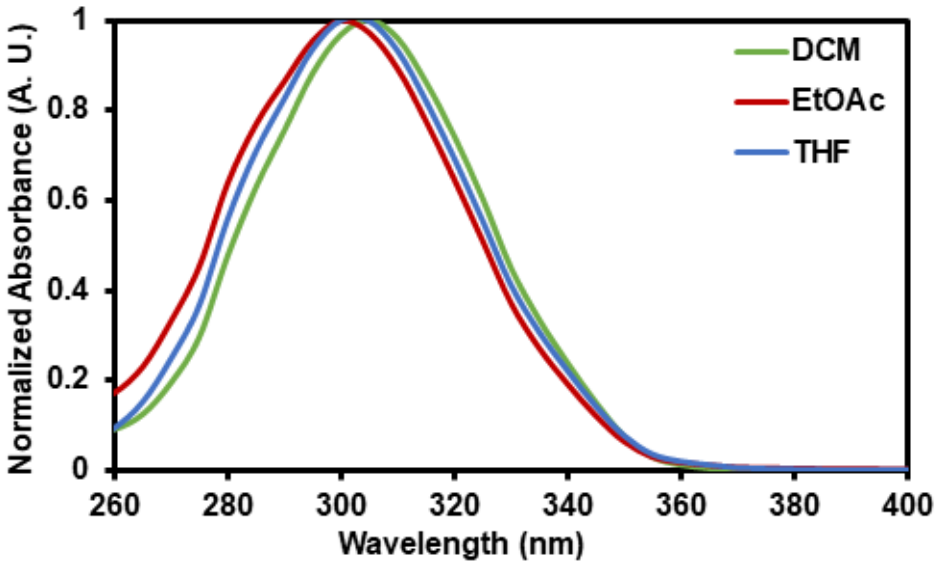

Figure 2.44. UV/Vis absorption spectrum of compound **1I** in DCM, EtOAc and THF.

2.5.4 Emission Measurements

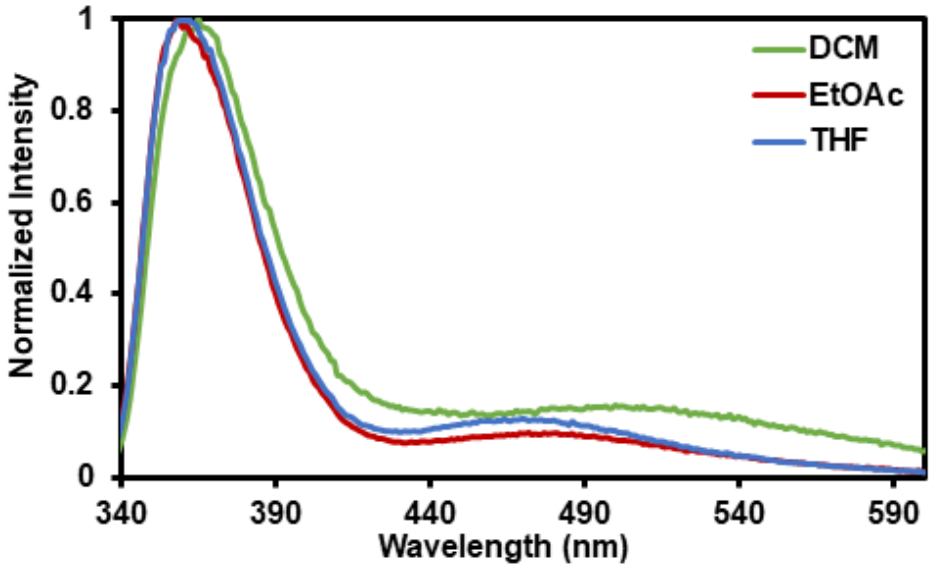

Figure 2.45. UV/Vis emission spectrum of compound **1H** in DCM, EtOAc, THF.

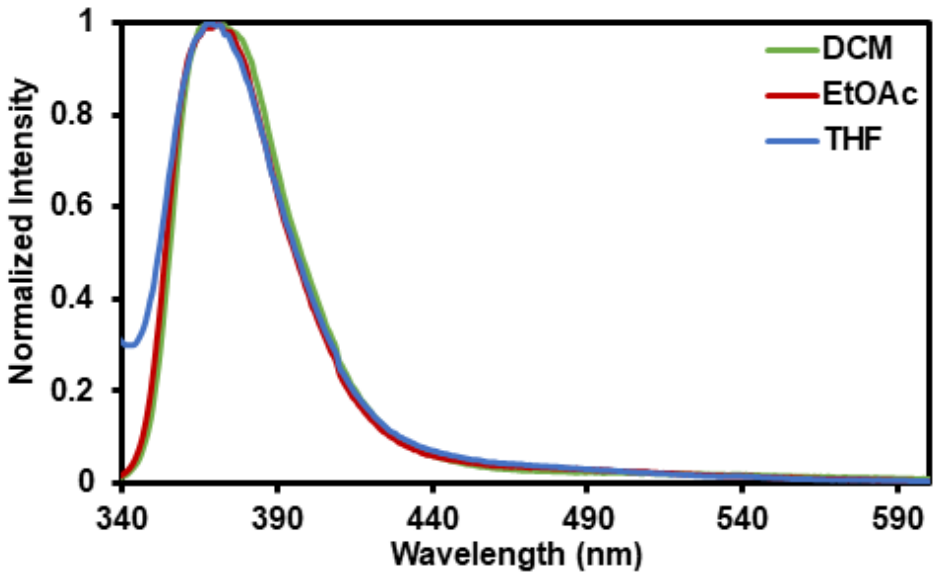

Figure 2.46. UV/Vis emission spectrum of compound **1F** in DCM, EtOAc, THF.

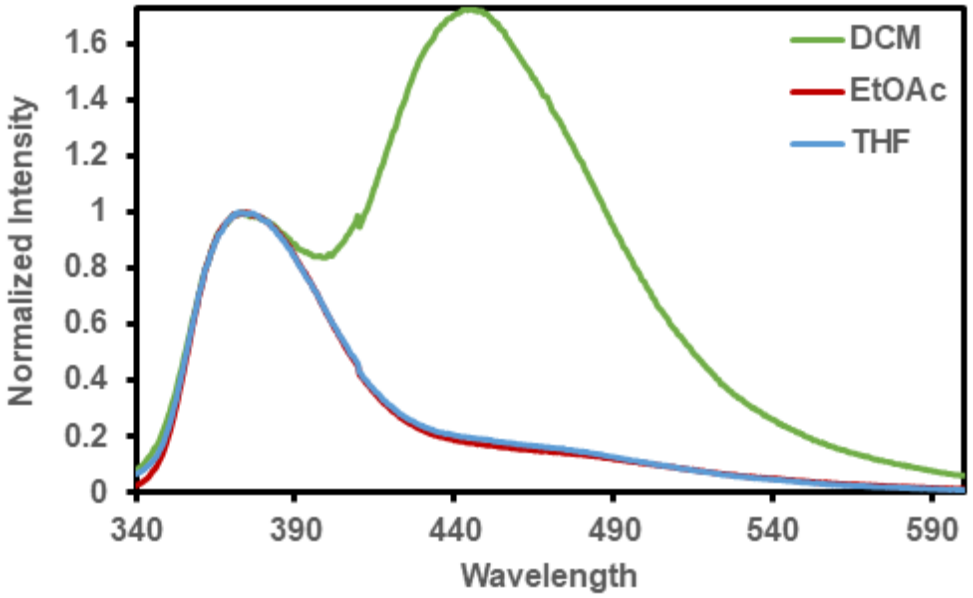

Figure 2.47. UV/Vis emission spectrum of compound **1Cl** in DCM, EtOAc, THF.

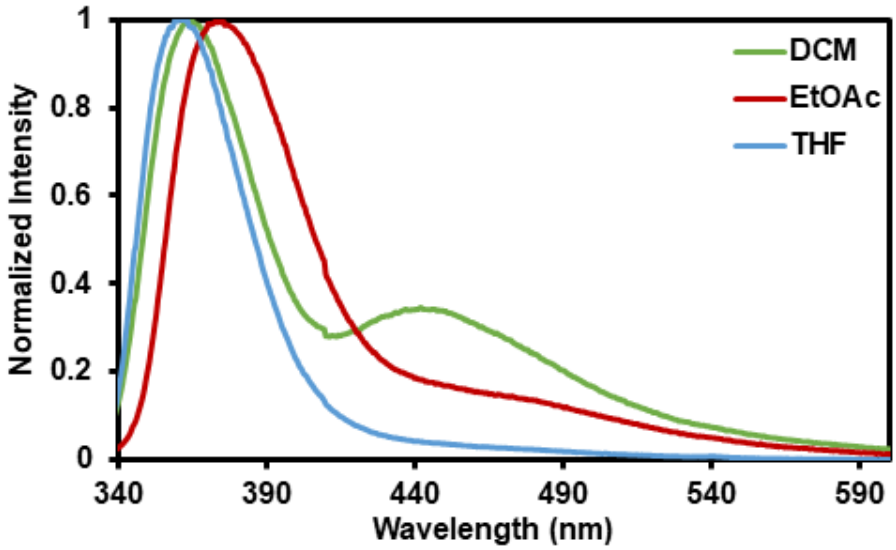

Figure 2.48. UV/Vis emission spectrum of compound **1I** in DCM, EtOAc, THF.

2.5.5 Diffuse reflectance and Emission spectrum

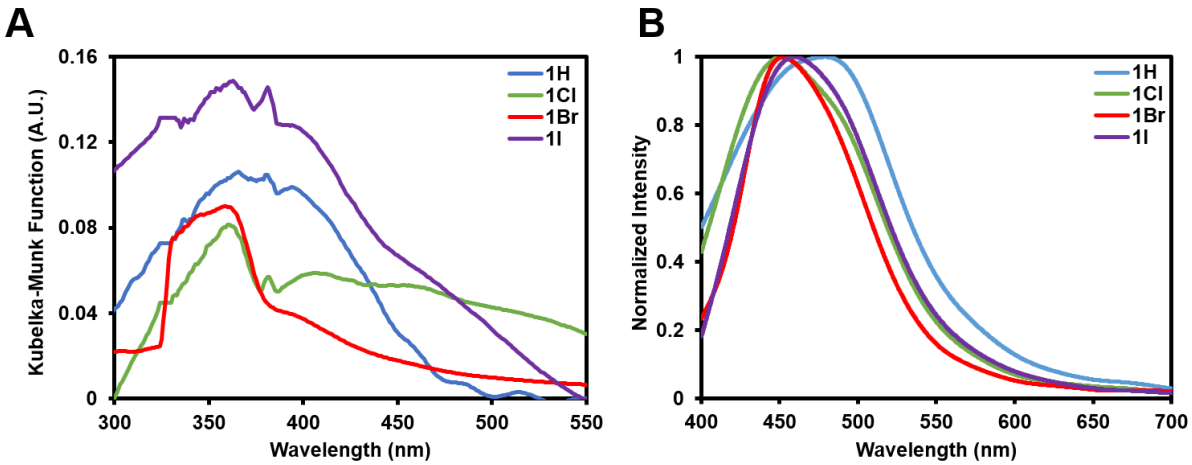

Figure 2.49. Diffuse reflectance and emission spectra of urea tethered derivatives in solid state at room temperature. (A) Diffuse reflection spectra for compound **1H**,[28] **1Cl**, **1Br**,[24] and **1I**. (B) Normalized emission spectra of single crystal for compound **1H**, **1Cl**, **1Br**, and **1I**.

2.5.6 Frontier molecular orbitals

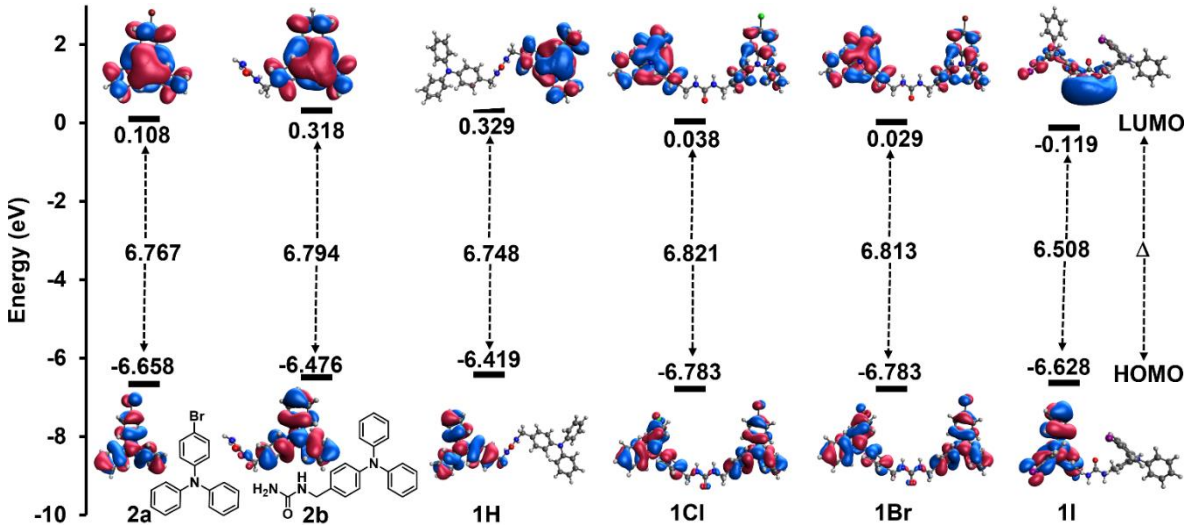

Figure 2.50. Frontier molecular orbitals of urea tethered **1H**, **1Cl**, **1Br**, **1I** and untethered **2a**, **2b** derivatives in gas phase.

Table 2.6. Excited state transitions in gas phase obtained by TD-DFT based on CAM-B3LYP[43]/6-31+G**.[42] SC-XRD data of **1H** were used as coordinates of the heavy atoms. The energies were scaled by multiplying with 0.773 which were used to assign the spectral lines shown in Figure 2.4.

State	Energy (nm)	Oscillator Strength (f_{osc})	RMS Electron-hole separation[a] Å	μ, D[b]	|<r_e - r_h>|[c] Å
S_1	509	1.148E-07	2.899	0.003	0.228
S_2	504	9.4E-08	2.900	0.002	0.225
S_3	489	4.44E-08	2.865	0.001	0.364
S_4	488	2.381E-07	2.851	0.004	0.355
S_5	435	6.26E-08	3.439	0.002	0.094
S_6	435	3.51E-08	2.598	0.001	0.048
S_7	434	2.051E-07	2.548	0.003	0.056
S_8	430	7.8E-09	3.502	0.007	0.099
S_9	392	1.865E-07	3.302	0.003	0.443
S_{10}	387	1.057E-07	3.305	0.002	0.427
S_{11}	385	0.0309213	4.055	1.399	0.163
S_{12}	382	0.0243833	4.055	1.237	0.177
S_{13}	373	9.635E-07	3.479	0.007	0.987
S_{14}	371	4.922E-07	3.453	0.005	0.936
S_{15}	366	0.4126832	4.131	4.983	1.273
S_{16}	364	6.887E-07	3.116	0.006	0.351
S_{17}	364	1.07E-05	3.104	0.025	0.310
S_{18}	363	0.1794871	4.108	3.274	1.008
S_{19}	361	8.325E-07	3.050	0.007	0.212
S_{20}	361	7.829E-05	3.052	0.068	0.256

[a]Root-mean-square (RMS) electron-hole separation in angstrom. [b]μ Magnitude of transition dipole moment in debye (D). [c]Linear electron (e) / hole (h) distance in angstrom Å.

Table 2.7. Excited state transitions in gas phase obtained by TD-DFT based on CAM-B3LYP[43]/6-31+G**.[42] SC-XRD data of **1Cl** were used as coordinates of the heavy atoms. The energies were scaled by multiplying with 0.781 which were used to assign the spectral lines shown in Figure 2.4.

State	Energy (nm)	Oscillator Strength (f_{osc})	RMS Electron-hole separation[a] Å	μ, D[b]	|<r_e - r_h>|[c] Å
S_1	499	4.18E-08	2.896	0.001	0.144
S_2	499	2.78E-08	2.894	0.001	0.147
S_3	493	3.73E-07	2.849	0.005	0.127
S_4	493	1.4E-07	2.847	0.003	0.127
S_5	438	1.45E-06	2.518	0.010	0.045
S_6	438	3.66E-08	2.521	0.001	0.044
S_7	423	2.74E-08	3.574	0.001	0.237
S_8	422	7.68E-08	3.572	0.002	0.236
S_9	381	8.95E-08	3.347	0.002	0.200
S_{10}	381	2.19E-07	3.347	0.003	0.200
S_{11}	377	0.034659	4.058	1.474	0.390
S_{12}	376	0.01186	4.065	0.861	0.392
S_{13}	369	3.85E-08	3.314	0.001	0.671
S_{14}	369	1.51E-07	3.314	0.003	0.672
S_{15}	361	0.170785	4.132	3.204	1.172
S_{16}	360	0.463809	4.146	5.269	1.367
S_{17}	359	2.71E-07	3.084	0.004	0.368
S_{18}	359	1.41E-06	3.083	0.009	0.365
S_{19}	356	5.84E-06	3.031	0.018	0.125
S_{20}	356	1.72E-06	3.043	0.010	0.128

[a]Root-mean-square (RMS) electron-hole separation in angstrom. [b]μ Magnitude of transition dipole moment in debye (D). [c]Linear electron (e) / hole (h) distance in angstrom Å.

Table 2.8. Excited state transitions in gas phase obtained by TD-DFT based on CAM-B3LYP[43]/6-31+G**.[42] SC-XRD data of **1Br** were used as coordinates of the heavy atoms. The energies were scaled by multiplying with 0.793 which were used to assign the spectral lines shown in Figure 2.4.

State	Energy (nm)	Oscillator Strength (f_{osc})	RMS Electron-hole separation[a] Å	μ, D[b]	|<r_e - r_h>|[c] Å
S_1	496	5.79E-08	2.938	0.002	0.250
S_2	496	3.82E-07	2.937	0.005	0.250
S_3	483	6.39E-07	2.862	0.007	0.219
S_4	483	1.02E-07	2.862	0.002	0.219
S_5	430	1.37E-07	2.578	0.003	0.064
S_6	430	8.85E-08	2.578	0.002	0.064
S_7	417	5.41E-08	3.559	0.001	0.265
S_8	417	1.21E-07	3.557	0.002	0.265
S_9	375	3.49E-07	3.347	0.004	0.130
S_{10}	375	8.96E-07	3.347	0.007	0.130
S_{11}	371	0.02403	4.070	1.227	0.400
S_{12}	371	0.017029	4.071	1.033	0.402
S_{13}	362	3.21E-06	3.334	0.014	0.349
S_{14}	362	4.6E-07	3.334	0.005	0.353
S_{15}	359	0.154865	4.141	3.064	1.180
S_{16}	358	0.528491	4.149	5.650	1.282
S_{17}	354	1.41E-06	3.074	0.009	0.340
S_{18}	354	9.37E-06	3.074	0.023	0.340
S_{19}	350	3.95E-05	3.055	0.048	0.222
S_{20}	350	9.91E-06	3.055	0.024	0.221

[a]Root-mean-square (RMS) electron-hole separation in angstrom. [b]μ Magnitude of transition dipole moment in debye (D). [c]Linear electron (e) / hole (h) distance in angstrom Å.

Table 2.9. Excited state transitions in gas phase obtained by TD-DFT based on CAM-B3LYP[43]/LANL2DZdp.[44] SC-XRD data of **1I** were used as coordinates of heavy atoms. The energies were scaled by multiplying with 0.779 which were used to assign the spectral lines shown in Figure 2.4.

State	Energy (nm)	Oscillator Strength (f_{osc})	RMS Electron-hole separation[a] Å	μ, D[b]	|<r_e - r_h>|[c] Å
S_1	503	5.06E-07	2.894	0.006	0.209
S_2	496	4.25E-07	2.930	0.005	0.348
S_3	493	6.44E-07	2.853	0.007	0.271
S_4	483	4.89E-07	2.743	0.006	0.238
S_5	445	1.68E-07	2.593	0.003	0.077
S_6	443	4.98E-07	2.384	0.006	0.086
S_7	431	2.64E-07	3.490	0.004	0.286
S_8	416	2.28E-07	3.560	0.003	0.148
S_9	406	5.4E-07	3.521	0.006	1.004
S_{10}	401	1.57E-07	3.373	0.003	0.793
S_{11}	386	7.88E-07	3.359	0.007	0.143
S_{12}	383	0.022809	4.060	1.204	0.306
S_{13}	381	4.41E-08	3.523	0.001	0.719
S_{14}	381	0.088101	4.250	2.358	1.434
S_{15}	377	3.65E-08	3.270	0.001	0.075
S_{16}	374	2.7E-07	3.293	0.004	0.507
S_{17}	368	3.85E-06	3.102	0.015	0.345
S_{18}	366	5.17E-06	3.357	0.017	0.754
S_{19}	365	0.12957	4.212	2.799	1.280
S_{20}	363	0.186869	4.245	3.352	1.627

[a]Root-mean-square (RMS) electron-hole separation in angstrom. [b]μ Magnitude of transition dipole moment in debye (D). [c]Linear electron (e) / hole (h) distance in angstrom Å.

Table 2.10. Excited state transitions in gas phase obtained by TD-DFT calculations using different set of functional and basis. SC-XRD data of **1Br** were used as initial coordinates of heavy atoms.

Functional	Basis set	State	Oscillator Strength (f_{osc})	RMS Electron-hole separation[a] Å	μ, D[b]	|<r_e - r_h>|[c] Å
CAM-B3LYP[43]	6-31+G**[42]	S_{11}	0.024	4.070	1.227	0.400
		S_{15}	0.154	4.141	3.064	1.180
		S_{16}	0.528	4.149	5.650	1.282
CAM-B3LYP	LANL2DZdp[44]	S_{12}	0.030	4.055	1.386	0.397
		S_{15}	0.146	4.214	2.991	1.237
		S_{16}	0.542	4.205	5.738	1.313
B3LYP-D3[41]	6-31+G**	S_{11}	0.010	4.649	2.695	1.763
		S_{14}	0.445	4.627	5.509	1.785
		S_{17}	0.578	4.682	6.152	1.079
LRC-wPBEh[46]	6-31+G**	S_{12}	0.029	3.974	1.352	0.409
		S_{17}	0.155	4.054	1.546	1.193
		S_{18}	0.576	4.061	2.922	1.273

[a]Root-mean-square (RMS) electron-hole separation in angstrom. [b]μ Magnitude of transition dipole moment in debye (D). [c]Linear electron (e) / hole (h) distance in angstrom Å.

2.5.7 Computational details and the electronic structure analysis

For practical reasons – the largest model contains 234 atoms – the positions of the hydrogen atoms were optimized using a semiempirical method PM3 (Parametric Method 3)[74,75] implemented in Spartan18[39] software. The optimization was performed for the ionic and neutral structures of monomer, hydrogen-bonded dimer, and trimer. The excited-state energy E^* for the neutral systems was estimated from the electronic excitations (computed using time-dependent DFT based on B3LYP/6-31G* method[76-79] at the neutral system geometries. The lowest excitation energy with non-negligible oscillator strength was taken in the case of monomer and trimer; in the case of the dimer, the four lowest states were averaged due to their close spacing and comparable oscillator strength. In all cases, the energy of the charge-separated species, summarized in Table 2.11, lies between the ground and excited state energies of the

neutral system. The energy differences of the charged monomers with respect to the ground state E^0 and the UV/Vis populated excited state E^* of the neutral species are defined as

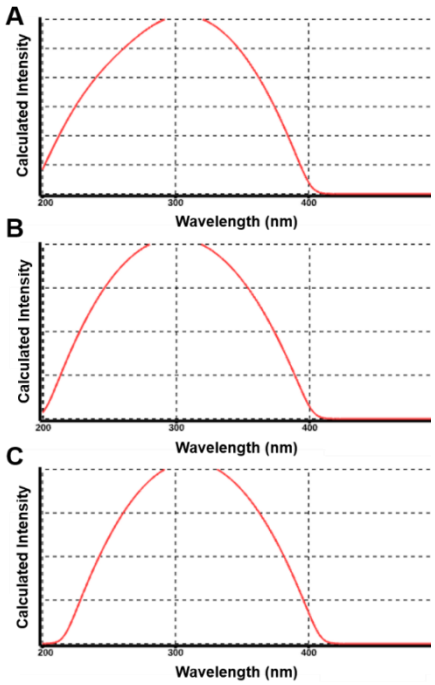

Figure 2.51. UV/Vis of **1Br** at PM3 geometry using 20 excited states computed at B3LYP/6-31G* in spartan A) Monomer. B) Hydrogen bonded dimer. C) Hydrogen bonded trimer.

$$\Delta = E^+ + E^- - 2E^0,\ \Delta^* = E^+ - E^- - 2E^*. \qquad (2.2)$$

In the case of monomer Δ and Δ^* computed at the DFT level are also listed.

Table 2.11. H atoms are optimized with PM3 method. The results are given for geometries obtainedby optimizing H-atom positions for the neutral species at PM3 level.

method	units	Δ [kJ/mol]	Δ^* [kJ/mol]	UVvis [eV]
PM3	3	557.08	-225.42	4.055 [a]
PM3	2	608.00	-187.81	4.124
PM3	1	674.17	-137.85	4.208
B3LYP/6-31G*	1	615.92	-196.10	4.208
B3LYP/6-31+G*	1	588.58	-189.37	4.031

[a] values obtained at B3LYP/6-31G* level are used in PM3 estimates

The electronic couplings in the ground state affecting the radical lifetimes are estimated for a dimer model by invoking Koopmans' theorem (Table 2.12). For two equivalent molecules, the LUMO+1/LUMO energy splitting is associated with the electron conductivity, whereas the HOMO/HOMO-1 energy splitting is associated with the hole conductivity.[80-82] The $E^{LUMO+1} - E^{LUMO}$ energy gap of the neutral system is proportional to twice the coupling V_c between the initial/final states of an anionic dimer upon electron transfer, and likewise $E^{HOMO} - E^{HOMO-1}$ gap is related to the coupling for the hole transfer in the cationic dimer. These estimates work for the Hartree-Fock theory implemented without

Table 2.12. The HOMO and LUMO gaps in eV for the hydrogen bonded dimer **1I**, and **1Br** systems computed within the Hartree-Fock theory.

system	basis	HOMO gap [eV]	LUMO gap [eV]
1Br	LANL2DZ	0.0354	0.0299
1Br	def2-SVP	0.0272	0.0218
1I	LANL2DZ	1.0041	0.2095
1I	def2-SVP	0.9878	0.1442

the diffuse basis functions. Thus, we compare **1Br** and **1I** dimer models based on the energy gaps computed using the valence and polarized bases, LANL2DZ and def2-SVP, respectively, with the matching effective core potentials.[83,84]

Table 2.13. The fragment charge difference for the **1Br** dimer models.

method	dQ [a.u.]
HF/6-31+G	0.244
lrc-ωPBEh/6-31+G	0.279
CAM-B3LYP/6-31+G	0.308
CAM-B3LYP/6-31+G*	0.349
CAM-B3LYP/6-31+G**	0.341
[a] CAM-B3LYP/def2-SVP	0.430/**0.871**

[a] 6-31+G* is used for non-halogen atoms; the value in bold is for **1I**

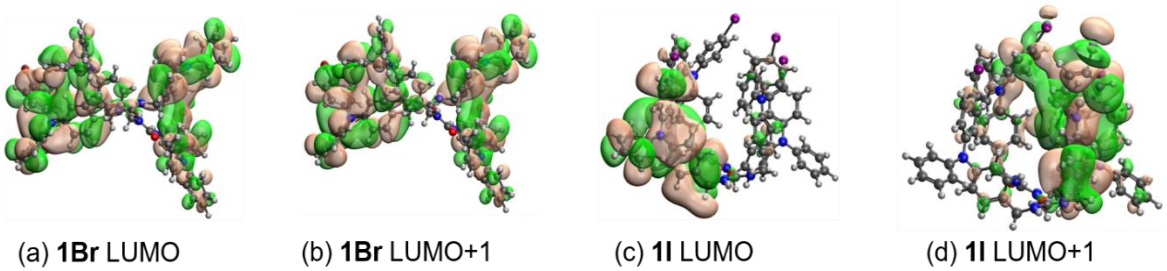

Figure 2.52. The frontier orbitals obtained at HF/def2-SVP level, for the **1Br** (a,b) and **1I** (c,d) hydrogen bonded dimer.

To evaluate the feasibility of the charge separation upon irradiation, we have computed the fragment charge difference (FCD)[85], with the fragments defined as charged units within the dimer model using CAM-B3LYP and for comparison lrc-ωPBEh, density functionals suited to capture the charge separation. The FCD, obtained using 30 excited singlet states, is listed (Table 2.13). For **1Br** all methods give non-zero FCD in the range of $dQ \approx 0.3-0.4$ a.u. For comparison, the FCD was computed for **1I** and **1Br** employing effective core potential def2-ECP paired with def2-SV and diffuse basis 6-31+G* for the non-halogen atoms: the value for **1I** is twice larger than that for **1Br**. Thus, the generation of radical pairs upon UV irradiation is feasible for both species. We note, however, that the oscillator strength is higher for **1Br** than for **1I**, which may contribute to a higher maximum radical concentration for **1Br** compared to **1I**.

2.5.8 Geometry dependence calculation: 1Br

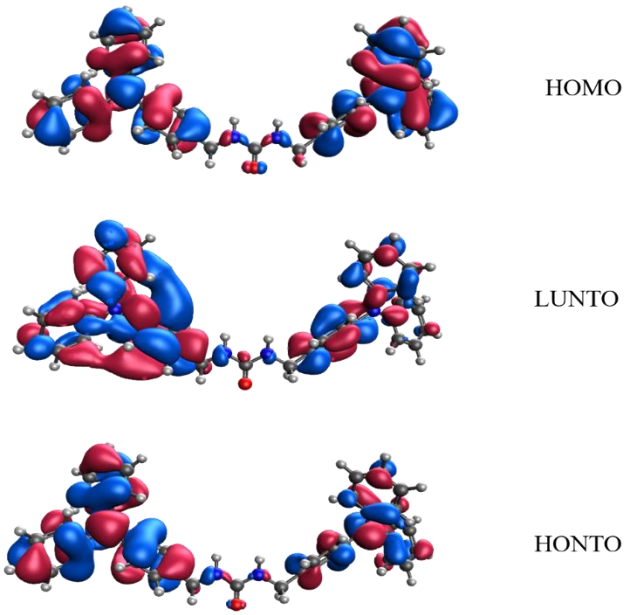

Gas phase NTO 17

Figure 2.53. Frontier molecular orbitals and gas phase NTO 17.

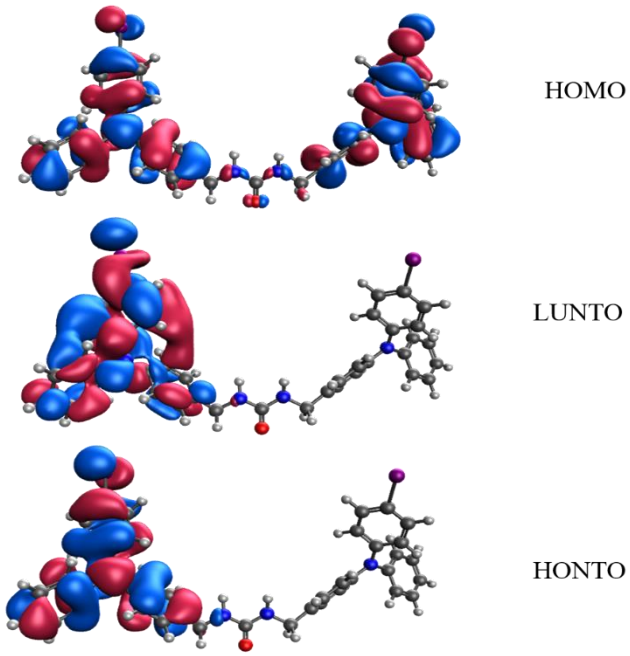

Gas phase NTO 18

Figure 2.54. Frontier molecular orbitals and gas phase NTO 18.

Single crystal .cif structure taken and Bromine atom replaced by hydrogen. Then the positions of hydrogen atoms were optimized at B3LYP-D3/6-31G* level. Then the frontier orbitals and NTOs were generated using CAM-B3LYP/6-31+G** methods in gas phase.

2.5.9 Mass Spectrum Data

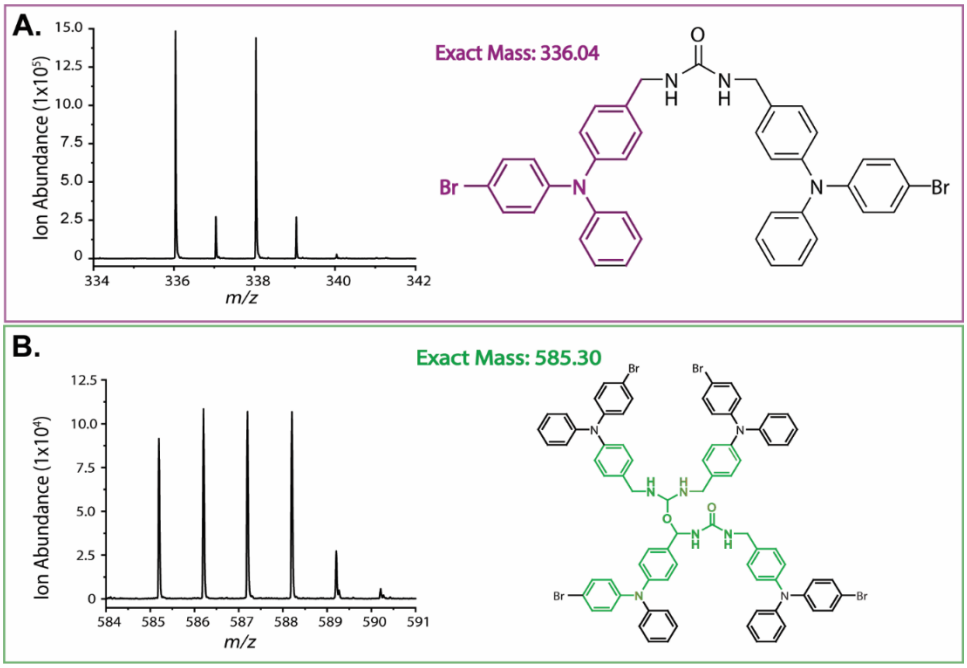

Figure 2.55. Partial mass spectrum of **1Br** and chemdraw of exact mass (in color). (A) m/z 336 most abundant fragment identified as Br-TPA radical cation consistent with the isotope pattern. (B) m/z 585 radical cation degraded from the covalent dimer.

2.5.10 EPR Data

EPR data following the change in concentration of radicals with increased irradiation time.

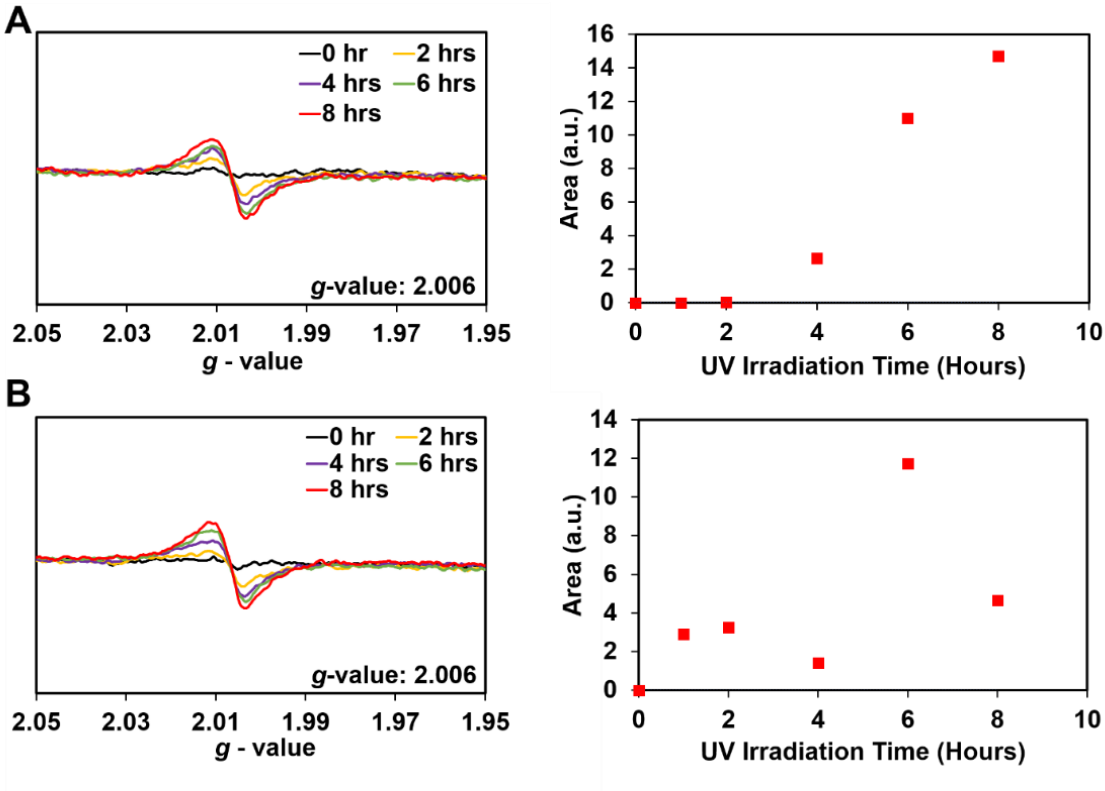

Figure 2.56. EPR data for the urea tethered TPA **1I**. EPR spectra over time (left). EPR spectra were doubly integrated to obtain the area plotted vs the time of UV irradiation using 365 nm UV LED source (right). **Trial 1:** (Figure 11 in main paper) A maximum radical concentration of 0.06% was found for 9.1 mg of **1I** by averaging the last three data points. (A) **Trial 2:** A maximum radical concentration of 0.08% was found for 5.6 mg of **1I** by averaging the last three data points. (B) **Trial 3:** A maximum radical concentration of 0.07% was found for 5.5 mg of **1I** by averaging the last three data points. A standard deviation 0.008 % was found from these three trials.

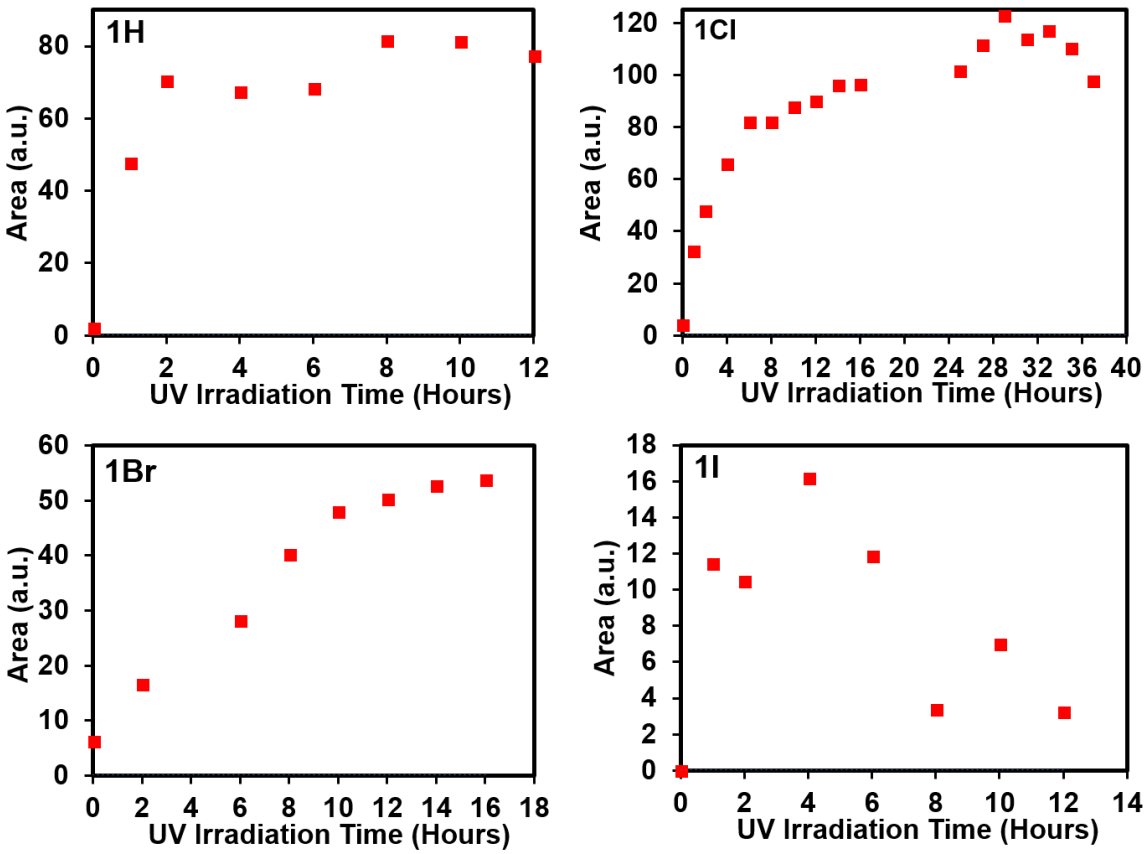

Figure 2.57. EPR data for the urea tethered TPA derivatives of compound **1H**, **1Cl**, **1Br**, and **1I**. EPR spectra were doubly integrated to obtain the area plotted vs the time of UV irradiation using 365 nm UV LED source.

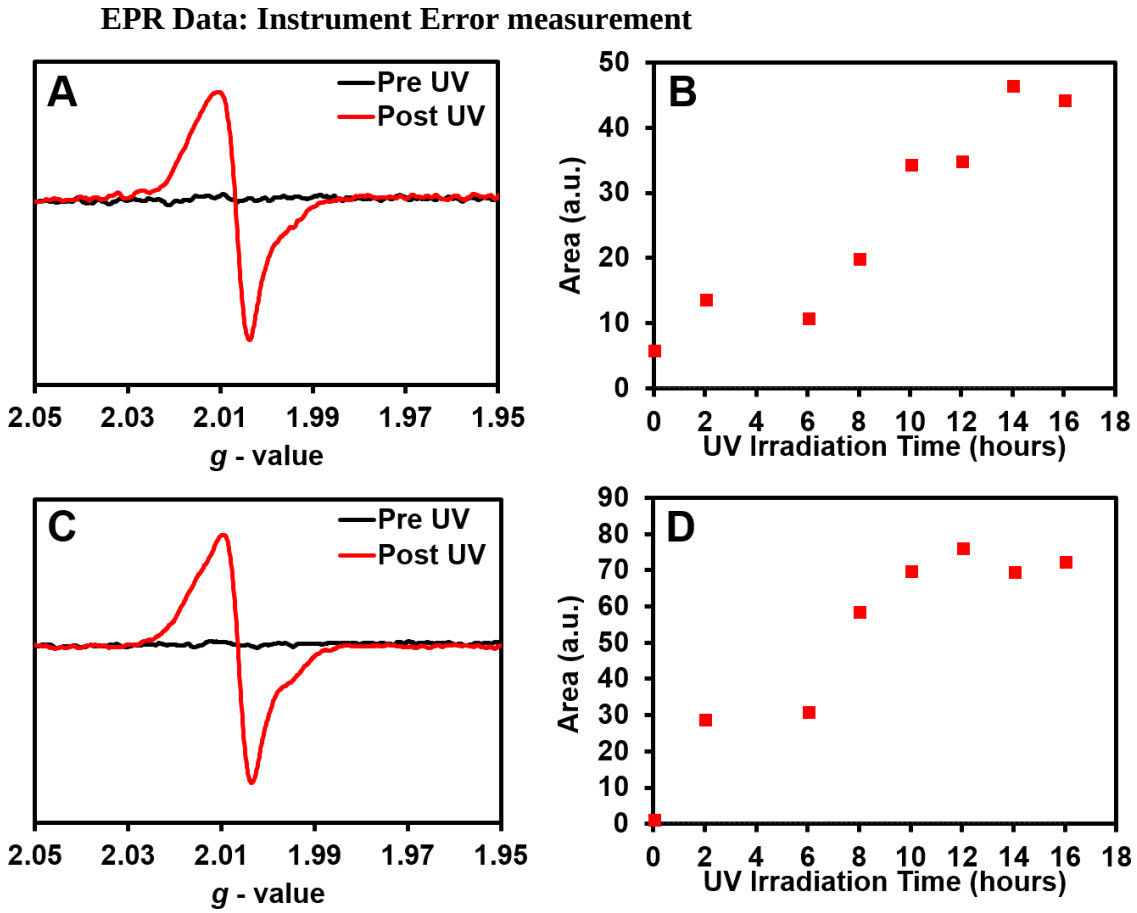

Figure 2.58. EPR data of **1Br**. (A) EPR spectra of pre- and post-UV irradiation. (B) EPR spectra were doubly integrated to obtain the area over time of UV irradiation. A maximum radical concentration of 0.33% was found for 3.8 mg of **1Br** by averaging the last three data points. (C) Second trial of EPR spectra of pre and post UV irradiation. (D) EPR spectra were doubly integrated to obtain the area over time of UV irradiation. A maximum radical concentration of 0.44% was found for 4.7 mg of **1Br** by averaging the last three data points. A standard deviation 0.04 % was found from these three trials (third trial included in Figure S45).

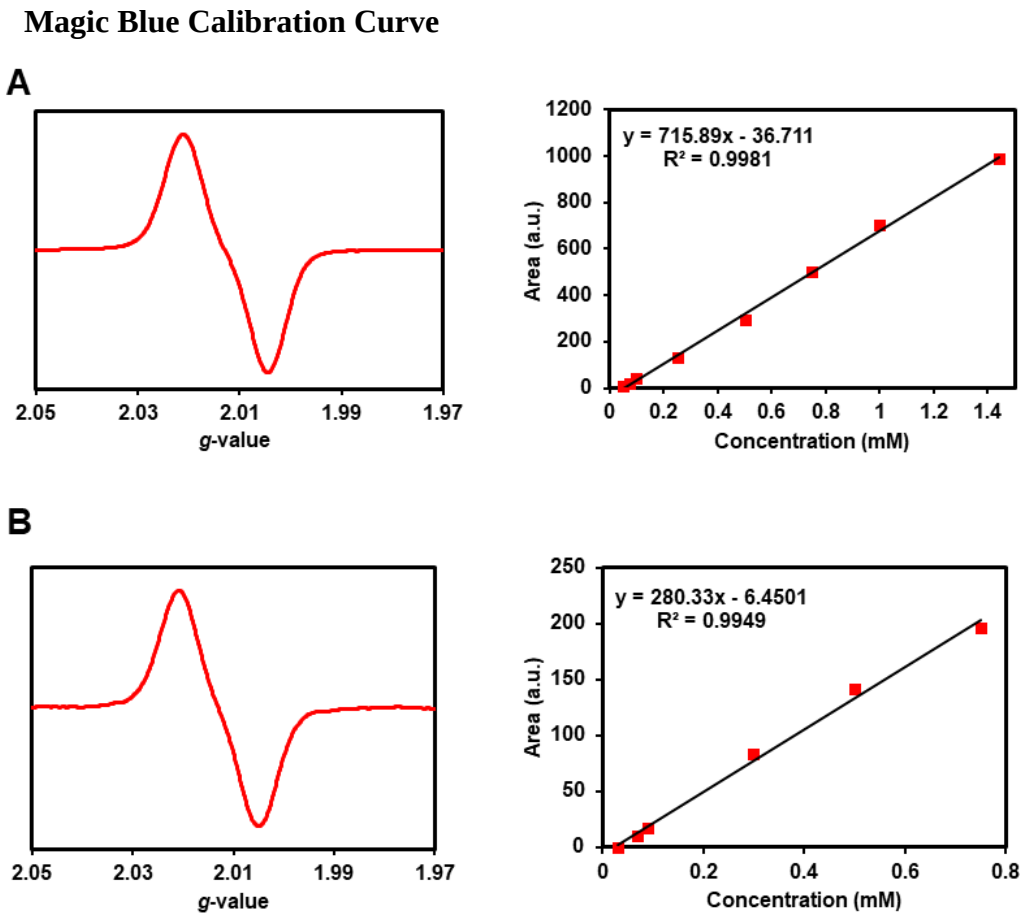

Figure 2.59. EPR data and calibration curve of magic blue to determine the radical concentration. (A) EPR spectra for 1 mM solution of magic blue in degassed dry dichloromethane (left) and calibration curve (right). (B) EPR spectra for 0.75 mM solution of magic blue in degassed dry dichloromethane (left) and calibration curve (right). Calibration curve A was taken from reference 16. It should be noted that the calibration curve (A) was used to determine the radical concentration for compound **1Cl**, which was measured at that time. Then the EPR spectrometer went under maintenance. Then the calibration curve (B) was prepared in the time of the experiment to determine radical concentration for compound **1H**, **1Br**, and **1I.**

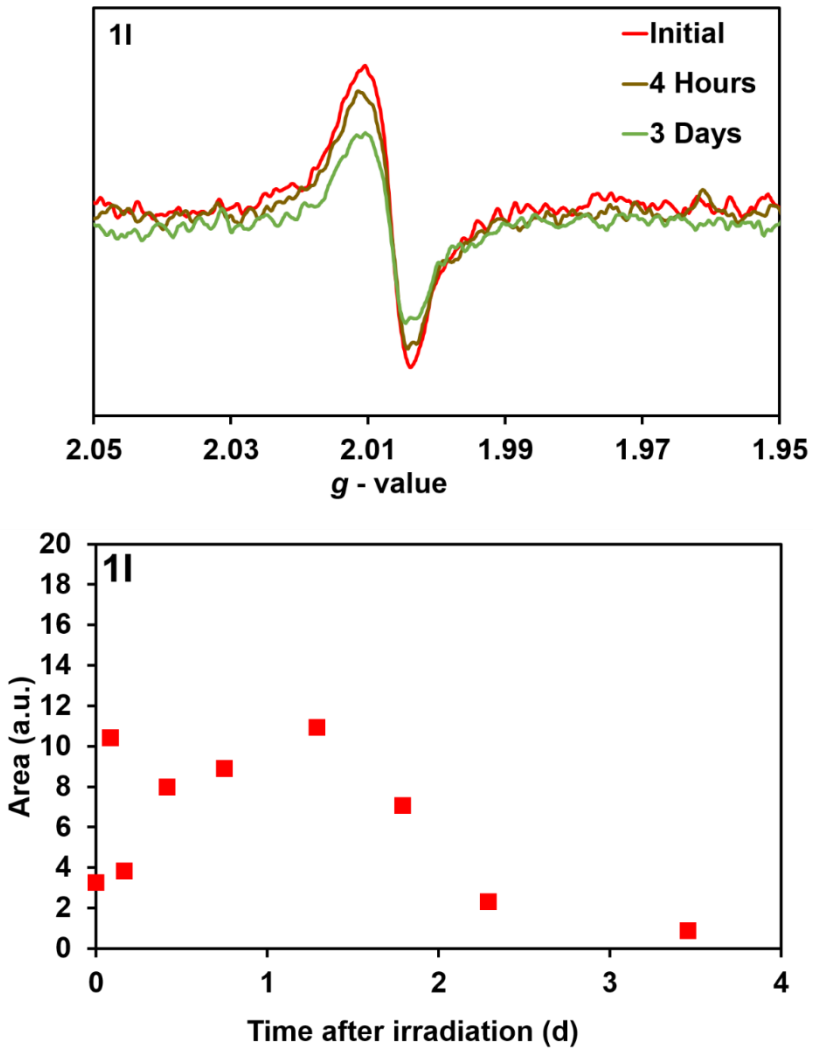

Figure 2.60. EPR data for the urea tethered TPA **1I**. EPR Spectra over time (Top) by keeping the UV irradiated sample under dark. EPR spectra were doubly integrated to obtain the area plotted vs time.

2.5.11 NMR Spectra Pre and Post-UV

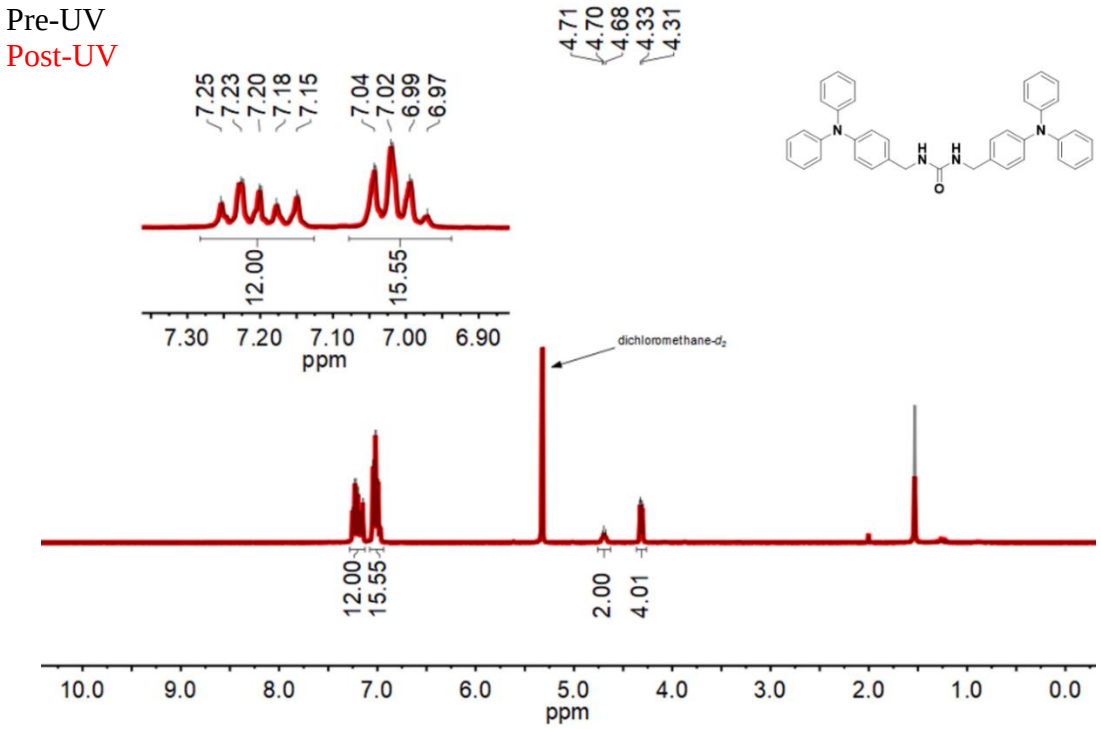

Figure 2.61. ^{1}H NMR spectra of compound **1H** after EPR studies (CD_2Cl_2-d_2, 300 MHz) (red). ^{1}H NMR spectra of freshly synthesized compound **1H** (black). Sample was re-dissolved in NMR solvent before measurement taken. No changes were seen on the parent resonances in NMR before and after UV irradiation. Peaks and integrals are for the **1H** compound after EPR studies.

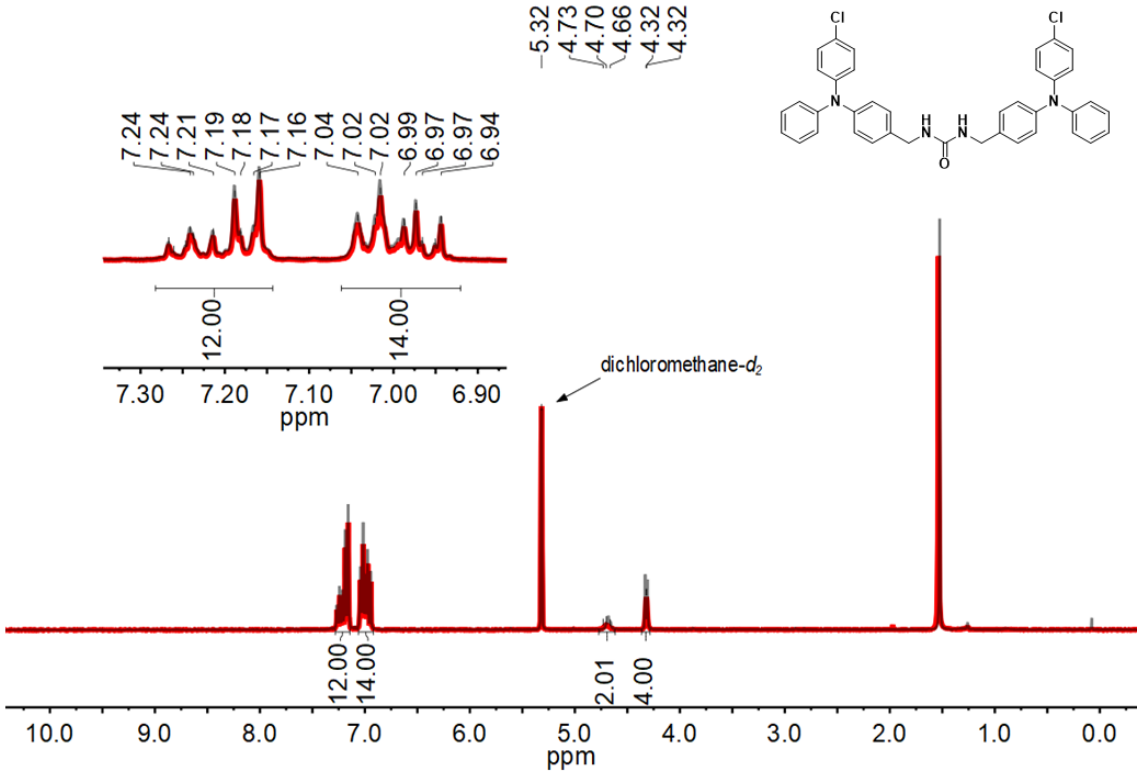

Figure 2.62. ^{1}H NMR spectra of compound **1Cl** after EPR studies (CD_2Cl_2-d_2, 300 MHz) (red). ^{1}H NMR spectra of freshly synthesized compound **1Cl** (black). Sample was re-dissolved in NMR solvent before measurement taken. No changes were seen on the parent resonances in NMR before and after UV irradiation. Peaks and integrals are for the **1Cl** compound after EPR studies.

Pre-UV
Post-UV

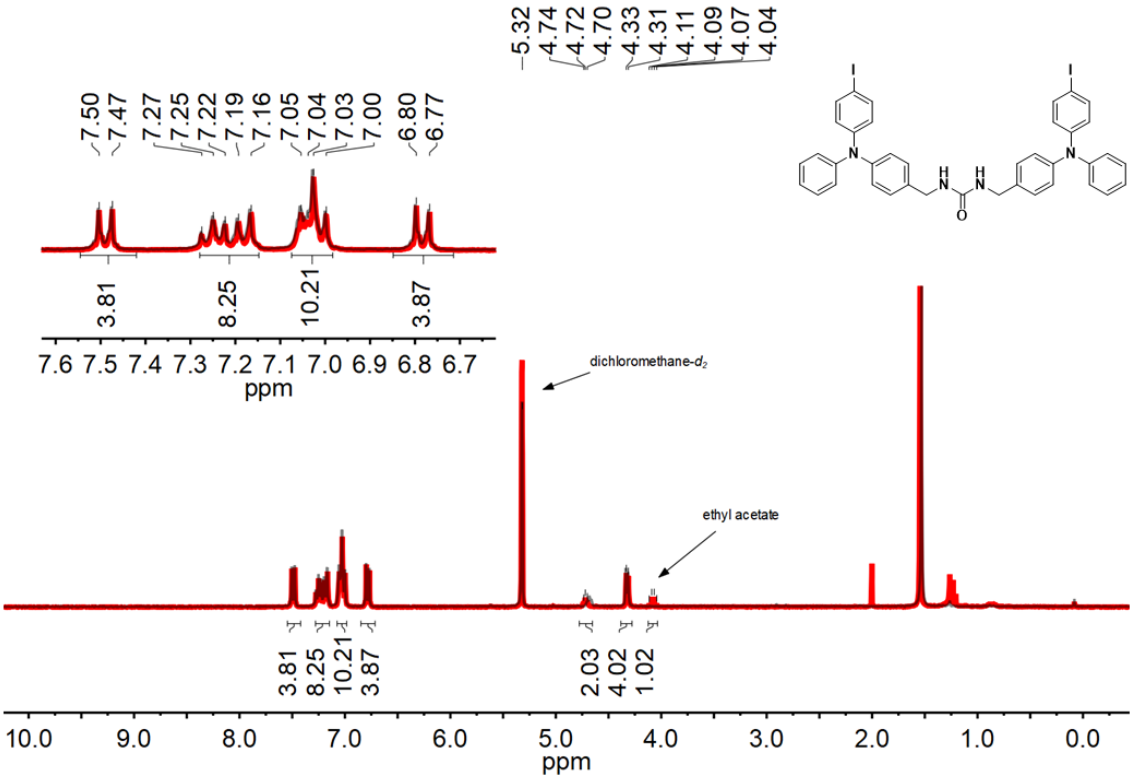

Figure 2.63. ^{1}H NMR spectra of compound **1I** after EPR studies (CD_2Cl_2-d_2, 300 MHz) (red). ^{1}H NMR spectra of freshly synthesized compound **1I** (black). Sample was re-dissolved in NMR solvent (dichloromethane) before measurement taken. Peaks and integrals are for the **1I** compound after EPR studies. No changes were seen on the parent resonances in NMR before and after UV irradiation. We observed the presence of ethyl acetate with a ratio of **1I** : ethyl acetate = 2:1 which further correlate hemi solvated crystals of **1I.**

2.12.4 High Resolution Mass Spectrometry analysis Pre and Post-UV irradiation

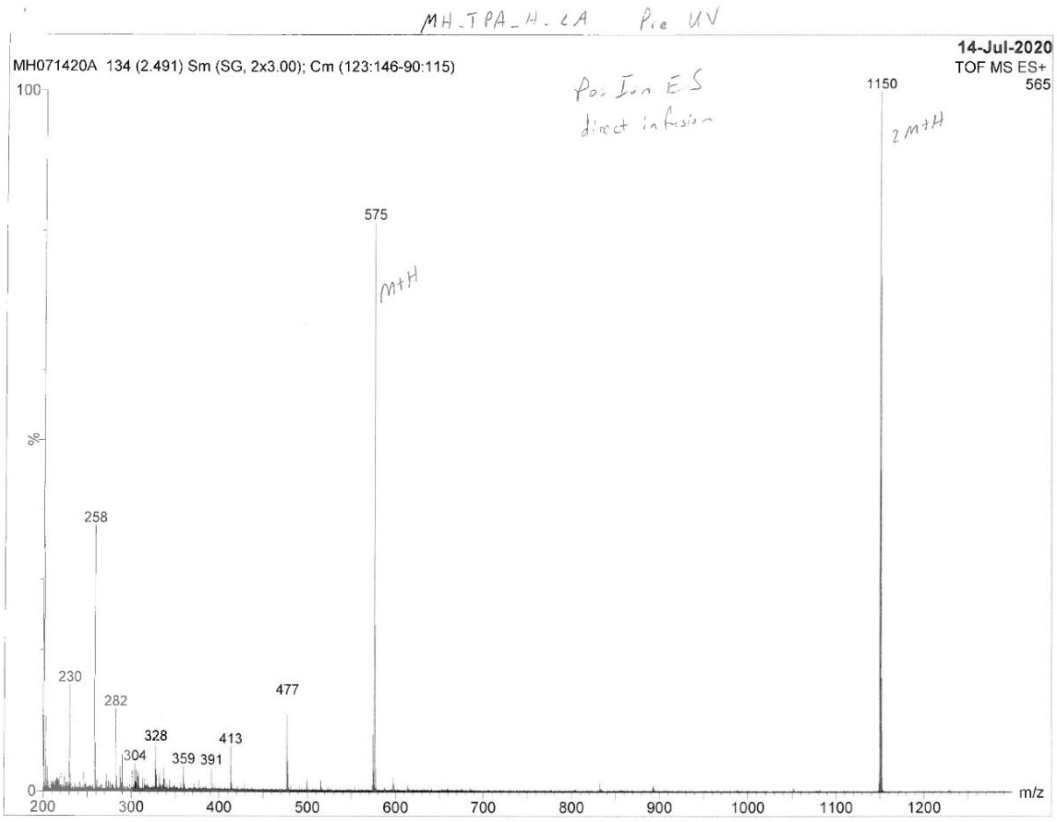

Figure 2.64. Positive-ion electrospray mass spectroscopy (direct infusion) of **1H** prior to UV irradiation. The peak at 575 m/z is consistent with [M + H]+ of **1H** whereas the peak at 1150 m/z is consistent with [2M + H] a potential dimer of **1H**.

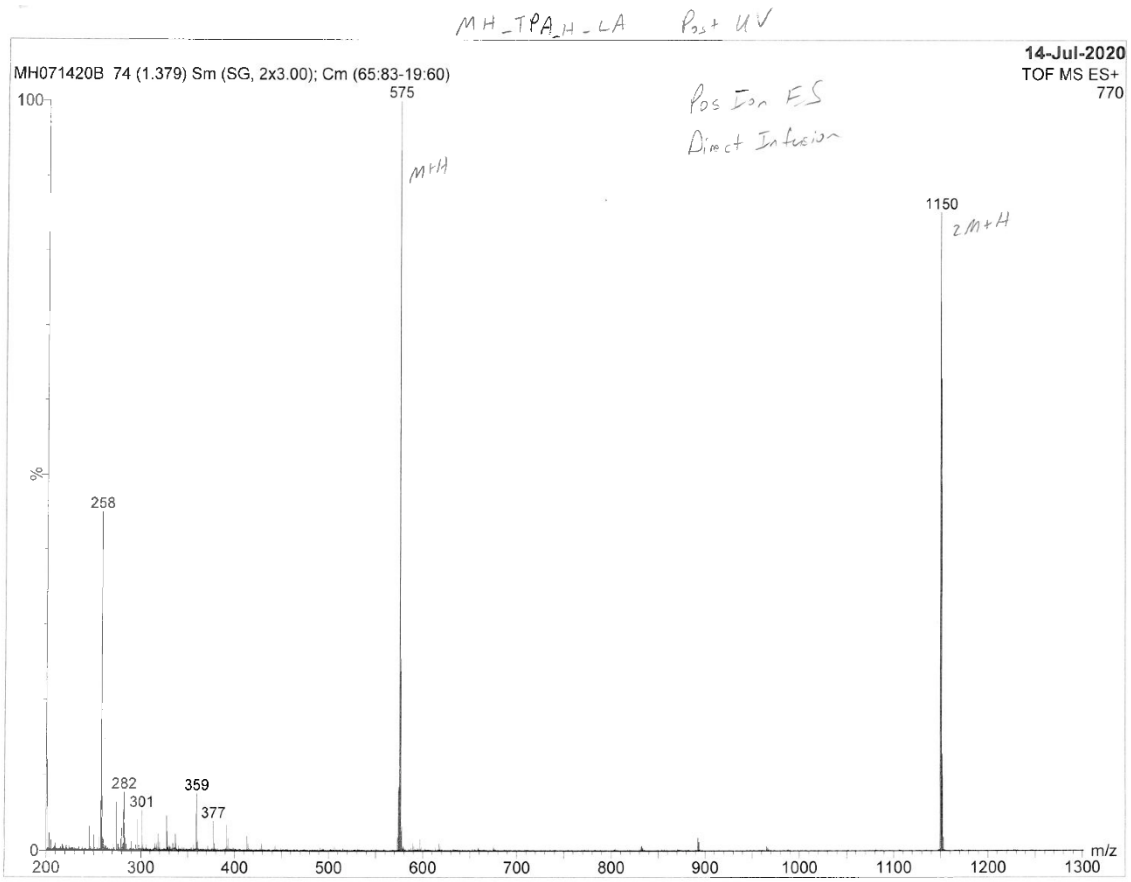

Figure 2.65. Positive-ion electrospray mass spectroscopy (direct infusion) of **1H** after UV irradiation (after EPR measurements). The peak at 575 m/z is consistent with [M + H]+ of **1**H whereas the peak at 1150 m/z is consistent with [2M + H] a potential dimer of **1H**. No significant changes were observed pre and post UV-irradiation.

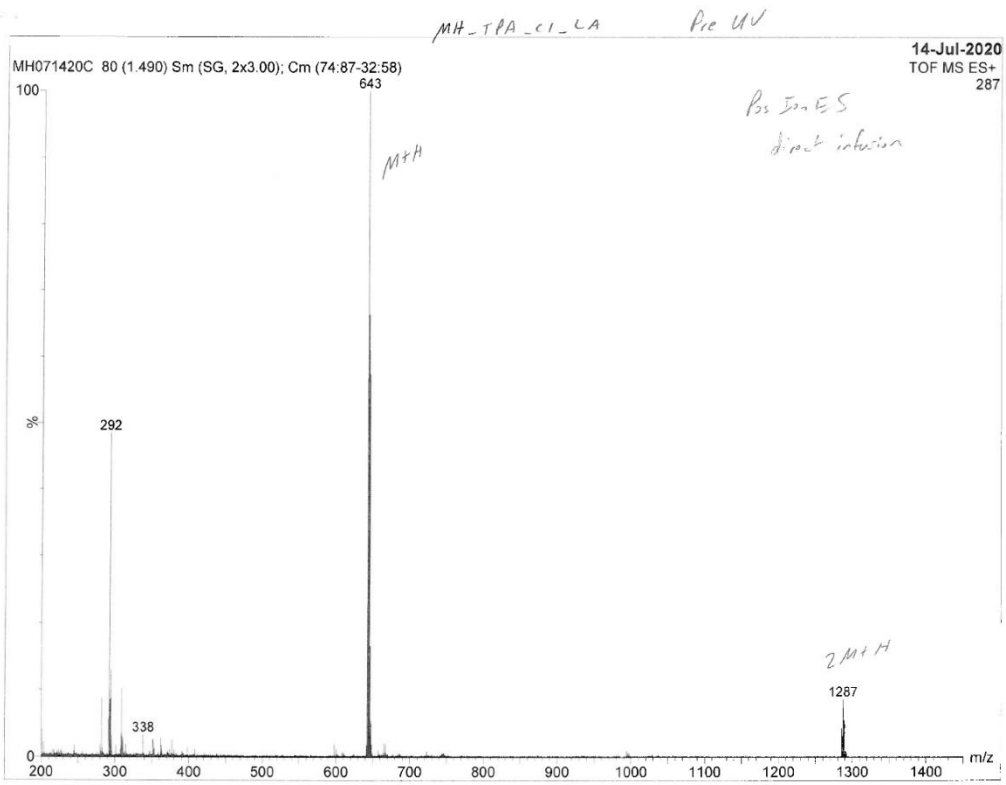

Figure 2.66. Positive-ion electrospray mass spectroscopy (direct infusion) of **1Cl** prior to UV irradiation. The peak at 643 m/z is consistent with [M + H]+ of **1Cl** whereas the peak at 1287 m/z is consistent with [2M + H] a potential dimer of **1Cl**.

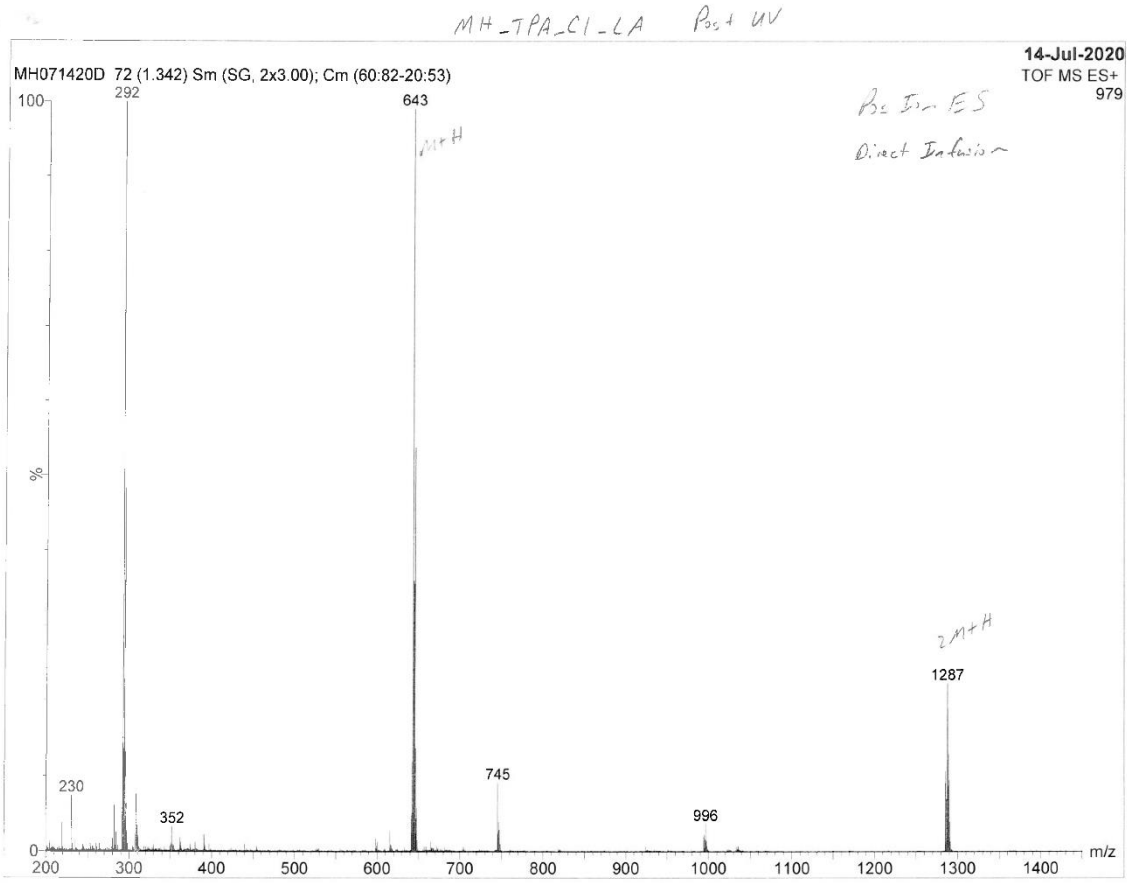

Figure 2.67. Positive-ion electrospray mass spectroscopy (direct infusion) of **1Cl** after UV irradiation (after EPR measurements). The peak at 643 m/z is consistent with [M + H]+ of **1**Cl whereas the peak at 1287 m/z is consistent with [2M + H] a potential dimer of **1Cl**. No significant changes were observed pre and post-UV irradiation.

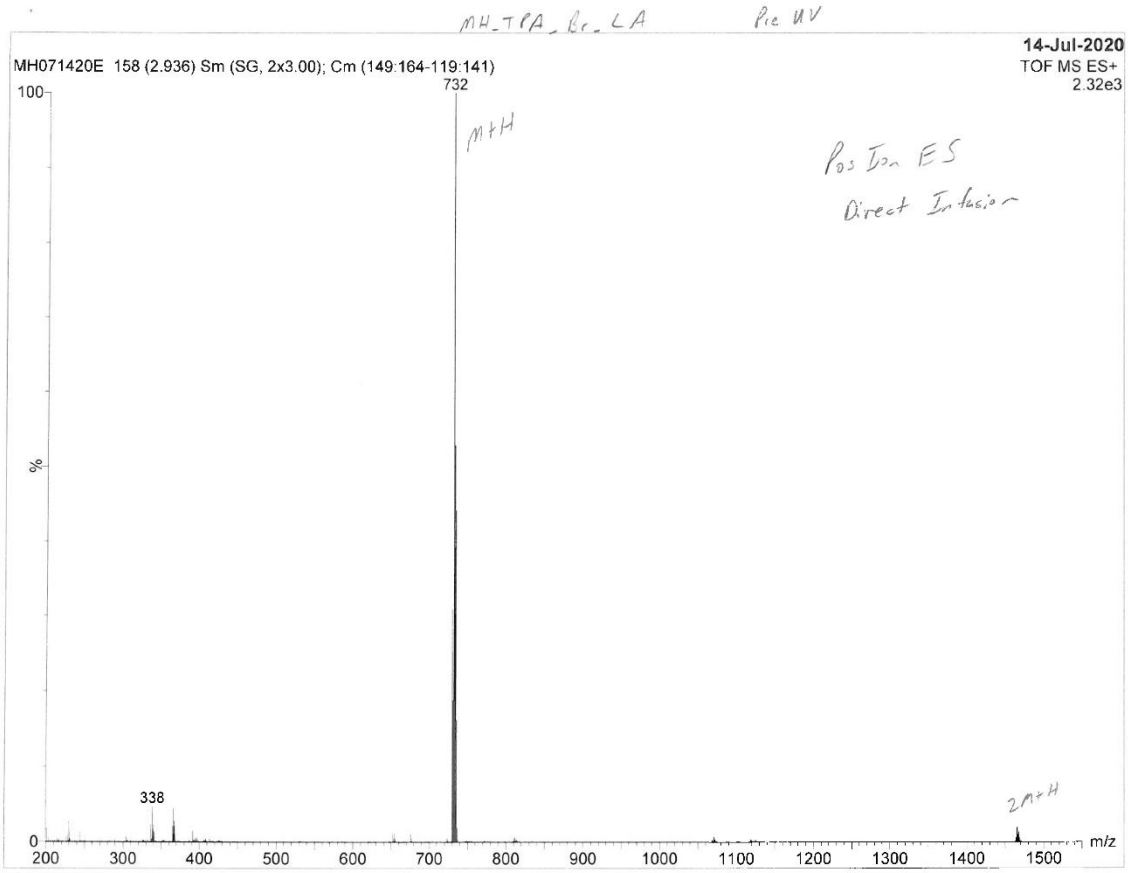

Figure 2.68. Positive-ion electrospray mass spectroscopy (direct infusion) of **1Br** prior to UV irradiation. The peak at 732 m/z is consistent with [M + H]+ of **1Br** whereas the peak at 1465 m/z is consistent with [2M + H] a potential dimer of **1Br**.

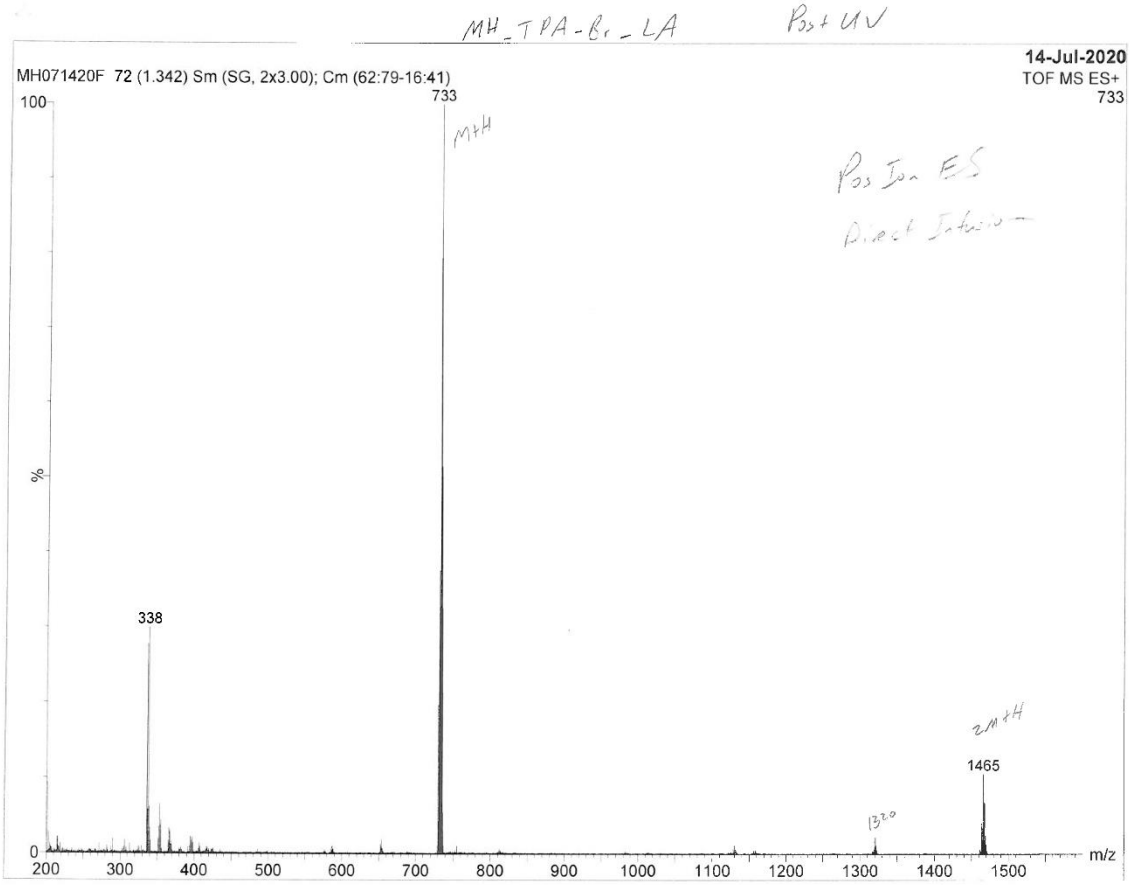

Figure 2.69. Positive-ion electrospray mass spectroscopy (direct infusion) of **1Br** after UV irradiation (after EPR measurements). The peak at 733 m/z is consistent with [M + H]+ of **1**Br whereas the peak at 1465 m/z is consistent with [2M + H] a potential dimer of **1Br**. No significant changes were observed pre and post UV-irradiation.

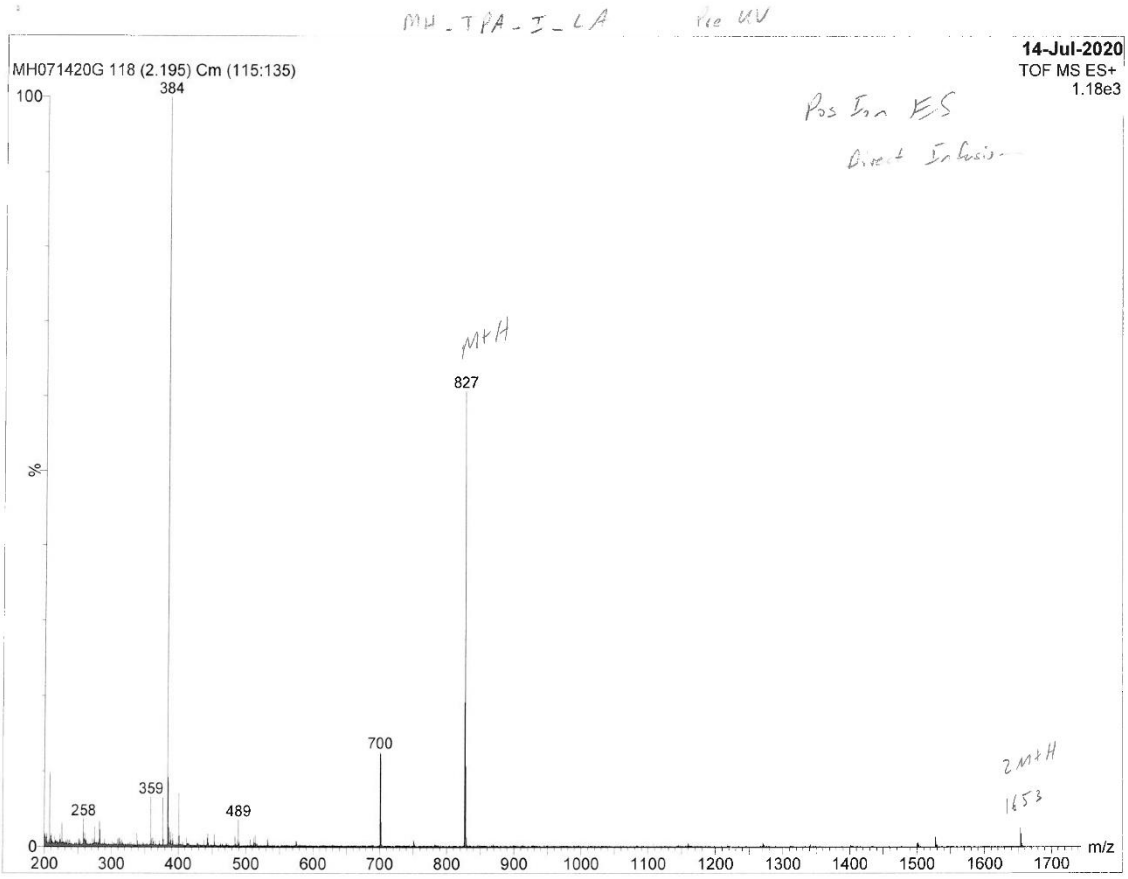

Figure 2.70. Positive-ion electrospray mass spectroscopy (direct infusion) of **1I** prior to UV irradiation. The peak at 827 m/z is consistent with [M + H]+ of **1I** whereas the peak at 1653 m/z is consistent with [2M + H] a potential dimer of **1I**.

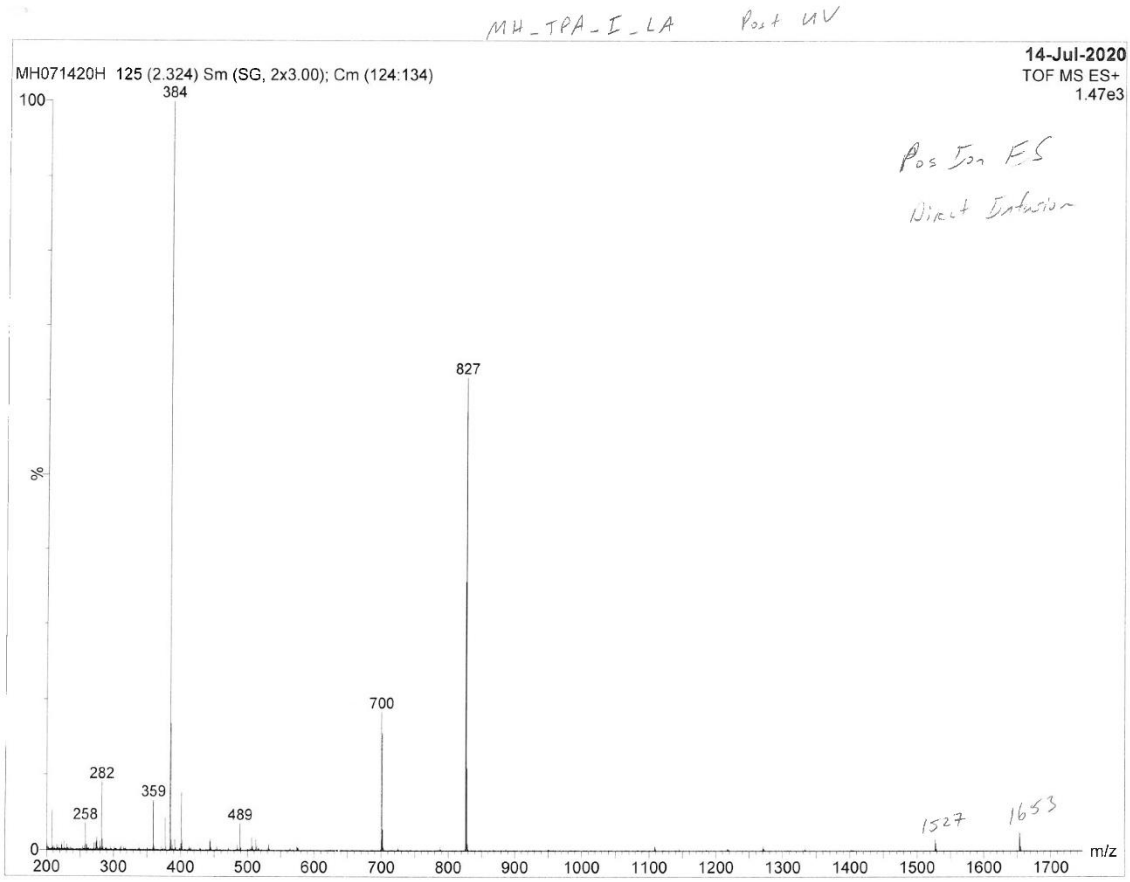

Figure 2.71. Positive-ion electrospray mass spectroscopy (direct infusion) of **1I** after UV irradiation (after EPR measurements). The peak at 827 m/z is consistent with [M + H]+ of **1I** whereas the peak at 1653 m/z is consistent with [2M + H] a potential dimer of **1I**. No significant changes were observed pre and post-UV irradiation.

2.5.12 XPS Analysis Pre and Post UV irradiation

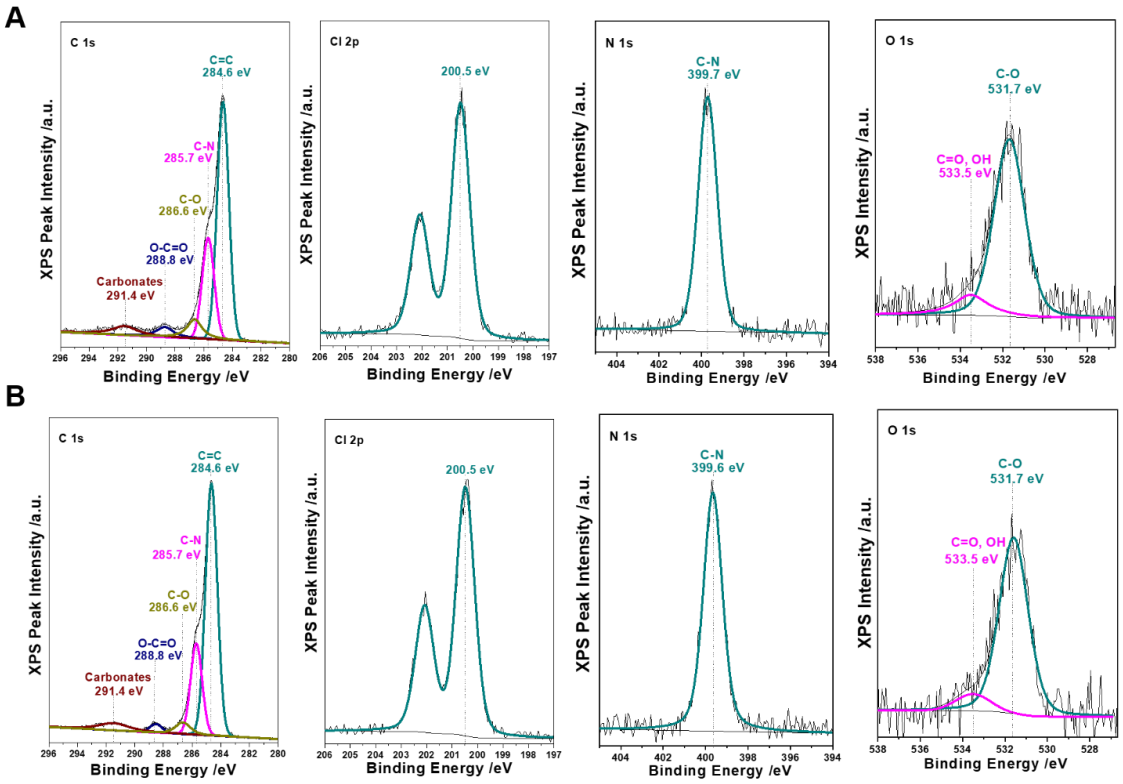

Figure 2.72. XPS analysis of crystalline **1Cl** pre and post (24 hours) UV irradiation. UV irradiation was performed in situ (A) Binding energy of XPS core level peaks (from left) C 1s, Cl 2p, N 1s, O 1s pre-UV irradiation. (B) Binding energy of XPS core level peaks (from left) C 1s, Cl 2p, N 1s, O 1s post-UV irradiation. No changes were observed in the binding energy of the core level peaks which can be attributed to the stability of the crystalline **1Cl** during UV irradiation.

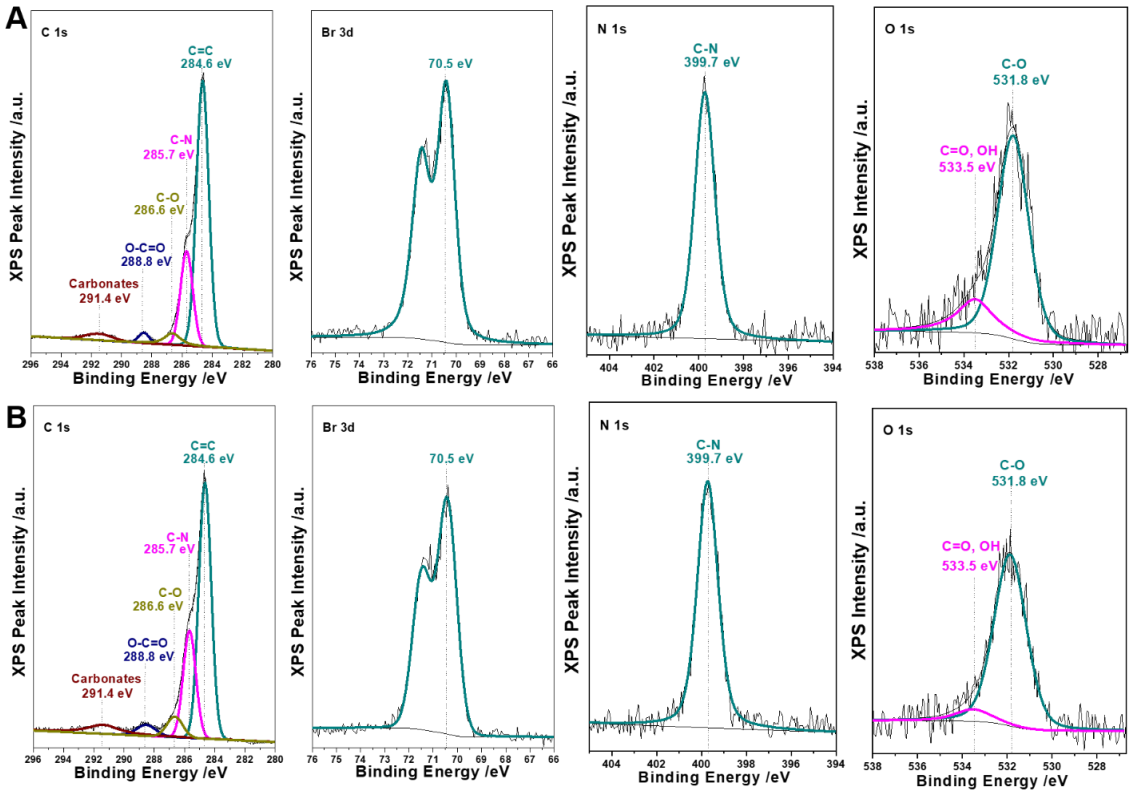

Figure 2.73. XPS analysis of crystalline **1Br** pre and post (24 hours) UV irradiation. UV irradiation was performed in situ (A) Binding energy of XPS core level peaks (from left) C 1s, Br 3d, N 1s, O 1s pre-UV irradiation. (B) Binding energy of XPS core level peaks (from left) C 1s, Br 3d, N 1s, O 1s post UV irradiation. No changes were observed in the binding energy of the core level peaks pre and post-UV irradiation which can be attributed to the stability of the crystalline **1Br** during UV irradiation.

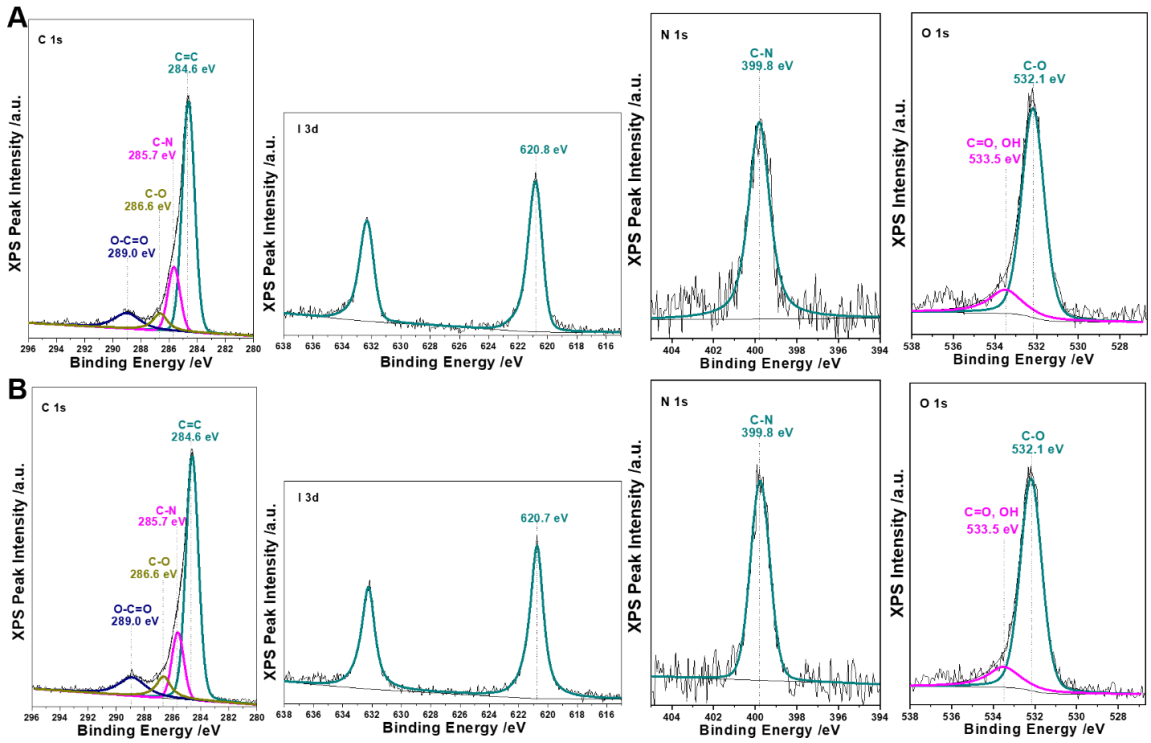

Figure 2.74. XPS analysis of crystalline **1I** pre and post (24 hours) UV irradiation. UV irradiation was performed in situ (A) Binding energy of XPS core level peaks (from left) C 1s, I 3d, N 1s, O 1s pre-UV irradiation. (B) Binding energy of XPS core level peaks (from left) C 1s, I 3d, N 1s, O 1s post UV irradiation. No changes were observed in the binding energy of the core level peaks pre and post-UV irradiation which can be attributed to the stability of the crystalline **1I** during UV irradiation.

2.5.13 Photoluminescence Quenching Study

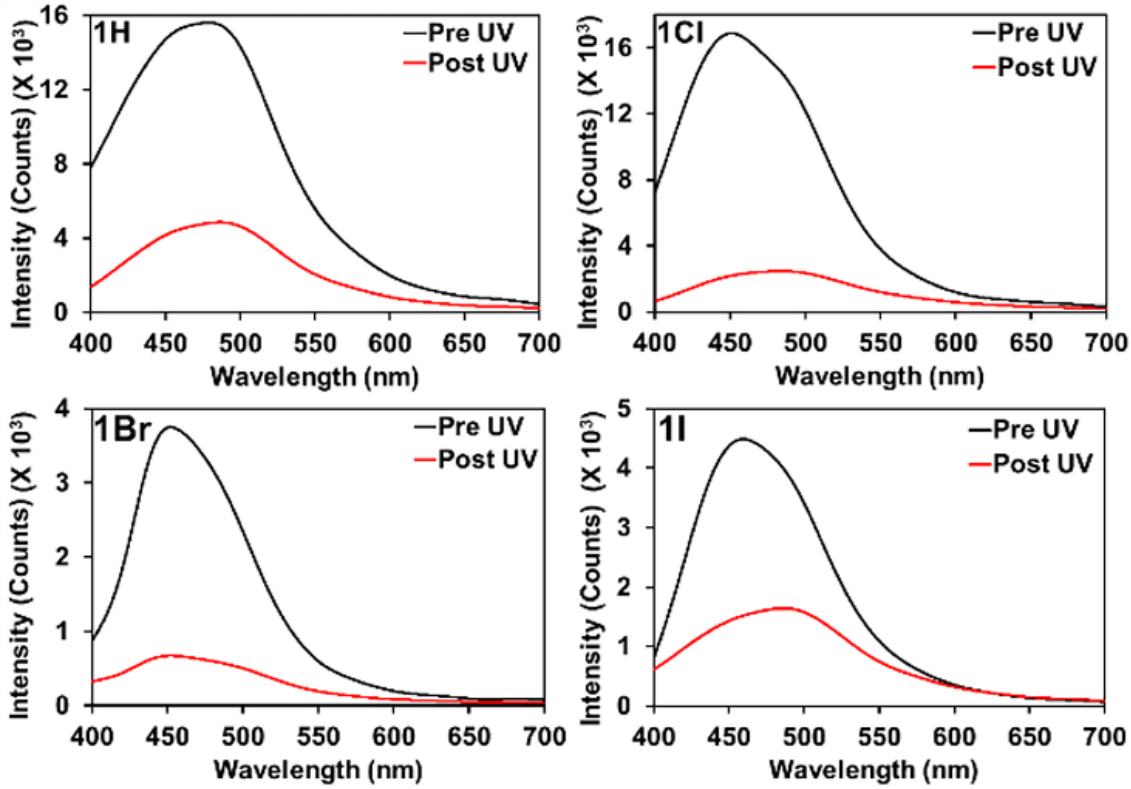

Figure 2.75. Emission spectra of pre-UV (black line) and post-UV irradiation (red line) for 6 Hours for compound **1H** (top left), **1Cl** (top right), **1Br** (bottom left), **1I** (bottom right) respectively. 375 nm laser excitation source was used. Same single crystals were used for the measurement.

2.15 Light Flux of 365 nm UV LEDs

Table 2.14. Photon flux measurements

Sample	Measured Current (amps)
Background	4.1×10^{-11}
LED 1	2.13×10^{-6}
LED 2	2.29×10^{-6}
LED 3	2.25×10^{-6}
LED 4	2.04×10^{-6}
LED 5	2.40×10^{-6}
Average	2.22×10^{-6}
Background subtracted average	2.22×10^{-6}
Multiplied by number of LEDs in photoreactor (120)	2.67×10^{-4}

FDS100 photodiode from ThorLabs were used to measure the photon flux of the 365 nm UV LEDs photoreactor. Individuals LEDs current were measured at the same distance from the photodiode as the sample distance in the photoreactor (3.5 cm). Ambient light background was subtracted from the average current measured for 5 LEDs and multiplied by the number of LEDs in the photoreactor (120). Power of the LED strip in watts was calculated by dividing the current value by the responsivity of the photodiode (0.05 amps/watt at 365 nm) at the sample distance in the photoreactor (5.33 x 10^{-3}).

Solving for E in the equation for photon energy ($E = \frac{hc}{\lambda}$) with λ = 365 nm, gives a photon energy value of 5.45 x 10^{-19} J. Division of the measured wattage by the photon energy gives a photon flux value of 9.78 x 10^{15} photons/second delivered to the sample for all persistent radical studies.

2.5.14 Symmetry and Assembly of TPA units

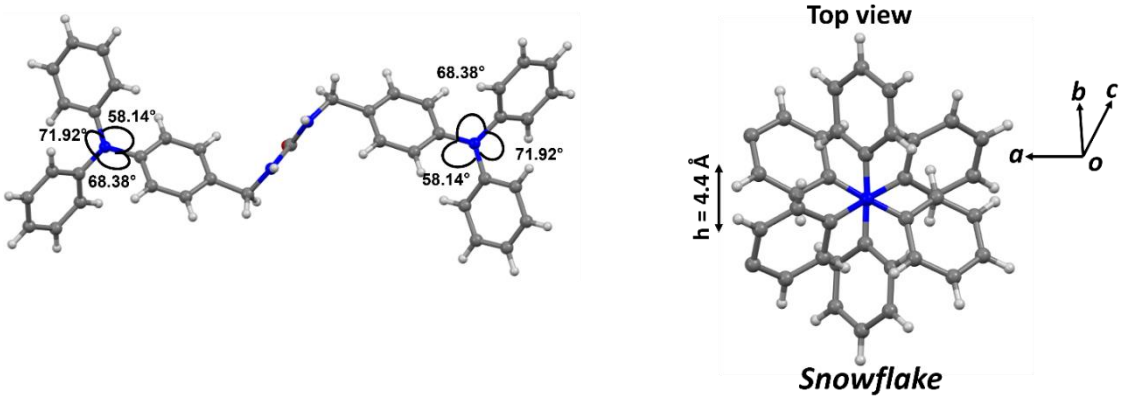

Figure 2.76. Structure and orientation of the TPA units (**1H**). Chiral propeller conformations of TPA unit of the opposite side of the urea tethered TPA (Left). Snowflake conformation of TPA units (Right), the distance measured from N – N center.

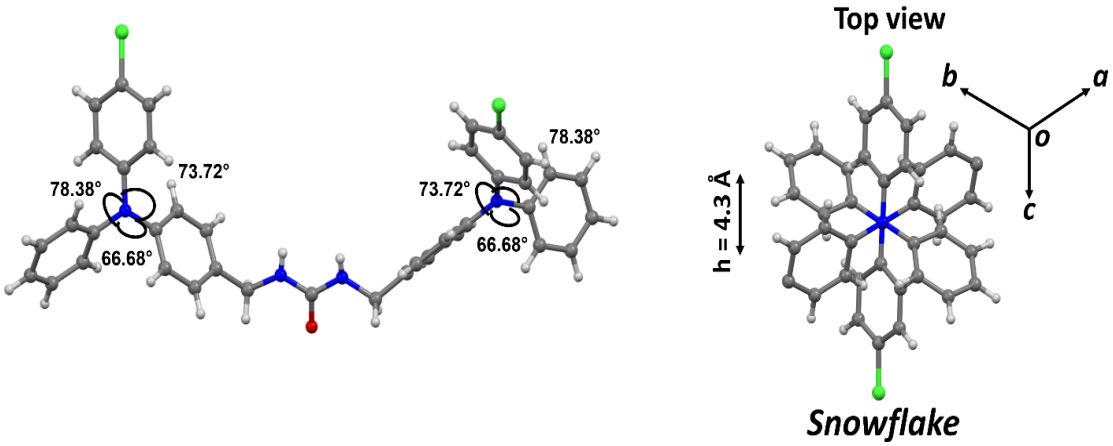

Figure 2.77. Structure and orientation of the TPA units (**1Cl**). Chiral propeller conformations of TPA unit of the opposite side of the urea tethered TPA (Left). Snowflake conformation of TPA units (Right), the distance measured from N – N center.

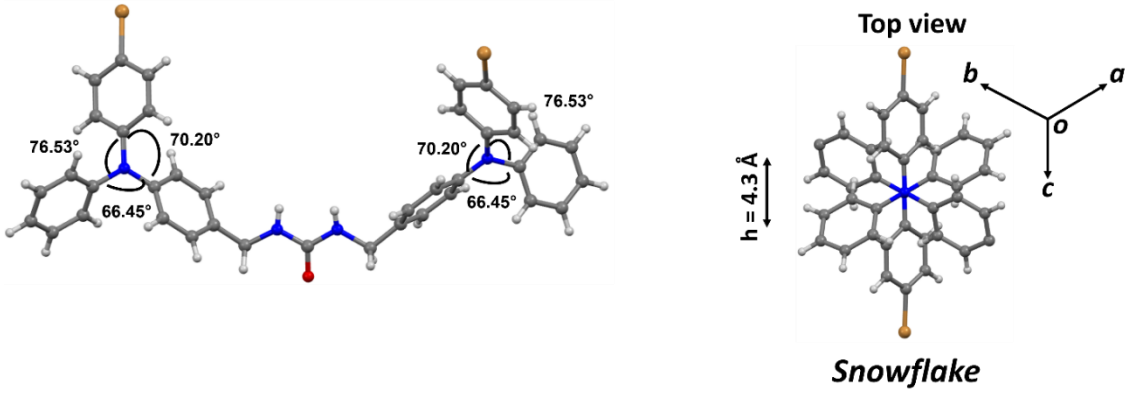

Figure 2.78. Structure and orientation of TPA unit (**1Br**). Chiral propeller conformations of TPA unit of the opposite side of the urea tethered TPA (Left). Snowflake conformation of TPA units (Right), the distance measured from N – N center.

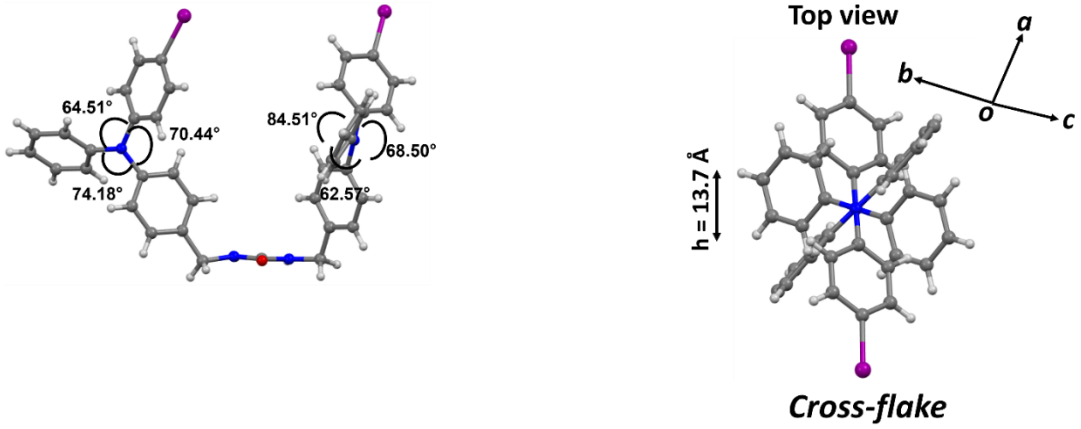

Figures 2.79. Structure and orientation of TPA unit (**1I**). Don't observe the chiral propeller shape of TPA units of the opposite side of the urea tethered TPA. (Left) Cross-flake conformation of TPA units (Right), the distance measured from N – N center.

Table 2.15. Values of the spin at the nuclei in **1H**, **1Cl**, **1Br**, and **1I**. The atoms of the left/right TPA units are listed sequentially; the bridge atoms are omitted. Computed by using Rassolov-Chipman operator for RC_R0 = 0.25 a.u.

1H		**1Cl**		**1Br**		**1I**	
Atomic Number	**Nuclear Spins**	**Atomic Number**	**Nuclear Spins**	**Atomic Number**	**Nuclear Spins**	**Atomic Number**	**Nuclear Spins**
7	0.0000029	17	0.0020215	35	0.0011474	53	0
6	0.0000014	7	0.0510088	7	0.0491371	7	0.1256291
6	0.0000033	6	0.0091972	6	0.0085198	6	0.0136394
1	0.0000012	6	-0.005655	6	-0.005422	6	-0.007522
6	0.0000055	1	0.0005852	1	0.0005511	1	0.0009544
1	0.0000009	6	0.0067937	6	0.0065449	6	0.017028
6	-0.000005	1	-0.001008	1	-0.000952	1	-0.001478
6	0.0000046	6	-0.009431	6	-0.009147	6	-0.018737
1	0.0000007	6	0.007053	6	0.0066023	6	0.0153478
6	-0.000005	1	-0.001004	1	-0.00094	1	-0.001142
1	0.0000007	6	-0.006324	6	-0.005825	6	-0.009118
6	0.0000138	1	0.000625	1	0.0005913	1	0.0009485
6	0.0000165	6	-0.008951	6	-0.008822	6	-0.020511
1	0.0000024	6	0.0064052	6	0.006092	6	0.0159179
6	0.0000155	1	-0.00073	1	-0.000736	1	-0.001072
1	0.0000021	6	-0.004108	6	-0.00441	6	-0.006943
6	0.0000134	1	0.0004964	1	0.0005125	1	0.0010448
1	0.0000016	6	0.0064723	6	0.0073734	6	0.0118817
6	0.0000147	6	-0.00385	6	-0.004176	6	-0.005837
1	-0.000002	1	0.0005205	1	0.0005285	1	0.0008149
6	0.0000155	6	0.0063727	6	0.0063106	6	0.0175643
1	0.0000022	1	-0.00076	1	-0.000802	1	-0.001177
6	0.0000034	6	-0.00937	6	-0.009006	6	-0.025128
6	0.0000036	6	0.0071117	6	0.0067347	6	0.0226317
1	0.0000004	1	-0.000905	1	-0.000843	1	-0.002744
6	0.0000032	6	-0.005038	6	-0.004755	6	-0.019566
1	0.0000004	1	0.0005713	1	0.0005391	1	0.0015259
6	0.0000035	6	0.0075134	6	0.0069972	6	0.0301613
1	0.0000005	1	-0.001171	1	-0.001092	1	-0.003718
6	0.0000032	6	-0.005111	6	-0.004707	6	-0.019373
1	0.0000005	1	0.000648	1	0.0006063	1	0.0014643
6	0.0000033	6	0.0067835	6	0.0063499	6	0.0231466
1	0.0000005	1	-0.00086	1	-0.000804	1	-0.002833
7	0.099055	17	0.002019	35	0.0012154	53	0
6	0.0217205	7	0.0510563	7	0.0518743	7	0.000012

6	0.0120533	6	0.0092047	6	0.0090009	6	0.0000128
1	0.0011838	6	-0.00567	6	-0.005738	6	-2.2E-06
6	0.0160205	1	0.0005866	1	0.0005838	1	-4E-07
1	0.0019406	6	0.0067809	6	0.0069233	6	0.0000007
6	0.0198807	1	-0.001012	1	-0.001011	1	-1E-07
6	0.0144446	6	-0.009438	6	-0.009678	6	-5E-07
1	-0.002286	6	0.0070857	6	0.0070244	6	0.0000031
6	0.0129818	1	-0.001003	1	-0.000992	1	0.0000002
1	0.001471	6	-0.006323	6	-0.006154	6	0.0000029
6	0.0216851	1	0.0006255	1	0.0006257	1	-1E-07
6	0.016243	6	-0.008943	6	-0.009328	6	-1.7E-06
1	0.0021124	6	0.0063569	6	0.0064501	6	0.0000013
6	0.0127031	1	-0.00073	1	-0.000778	1	-2E-07
1	0.0013686	6	-0.004112	6	-0.004655	6	-1.3E-06
6	0.0166106	1	0.0004964	1	0.0005418	1	0.0000001
1	0.0026099	6	0.0064639	6	0.0077702	6	0.0000016
6	0.0119053	6	-0.003838	6	-0.004406	6	-8E-07
1	0.0013432	1	0.0005195	1	0.0005582	1	0
6	0.0155738	6	0.0063813	6	0.0066829	6	0.0000008
1	0.0022291	1	-0.000758	1	-0.000848	1	-1E-07
6	0.0186372	6	-0.009368	6	-0.00953	6	-1.9E-06
6	0.0133465	6	0.0071602	6	0.0071631	6	0.0000016
1	0.0013657	1	-0.000901	1	-0.000889	1	-1E-07
6	0.0069973	6	-0.005006	6	-0.005006	6	-1.3E-06
1	0.00105	1	0.0005723	1	0.00057	1	0.0000001
6	0.0099261	6	0.0074788	6	0.0073676	6	0.0000021
1	-0.001556	1	-0.001166	1	-0.00115	1	-3E-07
6	-0.006975	6	-0.005098	6	-0.004972	6	-1.4E-06
1	0.0009569	1	0.0006393	1	0.0006398	1	0.0000001
6	0.0136178	6	0.0067006	6	0.0066721	6	0.0000017
1	0.0013914	1	-0.00086	1	-0.000852	1	-2E-07

2.6 REFERENCES

(1) Stupp, S. I.; Palmer, L. C. Supramolecular Chemistry and Self-Assembly in Organic Materials Design. *Chem. Mater.* **2014**, *26*, 507–518.

(2) Lehn, J. M. Toward Complex Matter: Supramolecular Chemistry and Self-Organization. *Proc. Natl. Acad. Sci. U. S. A.* **2002**, *99*, 4763–4768.

(3) Adhikari, B.; Lin, X.; Yamauchi, M.; Ouchi, H.; Aratsu, K.; Yagai, S. Hydrogen-Bonded Rosettes Comprising π-Conjugated Systems as Building Blocks for Functional One-Dimensional Assemblies. *Chem. Commun.* **2017**, *53*, 9663–9683.

(4) Datta, S.; Saha, M. L.; Stang, P. J. Hierarchical Assemblies of Supramolecular Coordination Complexes. *Acc. Chem. Res.* **2018**, *51*, 2047–2063.

(5) Waller, P. J.; Gándara, F.; Yaghi, O. M. Chemistry of Covalent Organic Frameworks. *Acc. Chem. Res.* **2015**, *48*, 3053–3063.

(6) Luo, J.; Wang, J. W.; Zhang, J. H.; Lai, S.; Zhong, D. C. Hydrogen-Bonded Organic Frameworks: Design, Structures and Potential Applications. *CrystEngComm* **2018**, *20*, 5884–5898.

(7) Lin, R. B.; He, Y.; Li, P.; Wang, H.; Zhou, W.; Chen, B. Multifunctional Porous Hydrogen-Bonded Organic Framework Materials. *Chem. Soc. Rev.* **2019**, *48*, 1362–1389.

(8) Chen, Z.; Baumeister, U.; Tschierske, C.; Würthner, F. Effect of Core Twisting on Self-Assembly and Optical Properties of Perylene Bisimide Dyes in Solution and Columnar Liquid Crystalline Phases. *Chem. - A Eur. J.* **2007**, *13*, 450–465.

(9) Würthner, F.; Saha-Möller, C. R.; Fimmel, B.; Ogi, S.; Leowanawat, P.; Schmidt, D. Perylene Bisimide Dye Assemblies as Archetype Functional Supramolecular Materials. *Chem. Rev.* **2016**, *116*, 962–1052.

(10) Quinton, C.; Alain-Rizzo, V.; Dumas-Verdes, C.; Miomandre, F.; Clavier, G.; Audebert, P. Redox-Controlled Fluorescence Modulation (Electrofluorochromism) in Triphenylamine Derivatives. *RSC Adv.* **2014**, *4*, 34332–34342.

(11) Saha, A.; Chen, M.; Lederer, M.; Kahnt, A.; Lu, X.; Guldi, D. M. Sulfur Rich Electron Donors-Formation of Singlet versus Triplet Radical Ion Pair States Featuring Different Lifetimes in the Same Conjugate. *Chem. Sci.* **2017**, *8*, 1360–1368.

(12) Moulin, E.; Armao, J. J.; Giuseppone, N. Triarylamine-Based Supramolecular Polymers: Structures, Dynamics, and Functions. *Acc. Chem. Res.* **2019**, *52*, 975–983.

(13) Agarwala, P.; Kabra, D. A Review on Triphenylamine (TPA) Based Organic Hole Transport Materials (HTMs) for Dye Sensitized Solar Cells (DSSCs) and Perovskite Solar Cells (PSCs): Evolution and Molecular Engineering. *J. Mater. Chem. A* **2017**, *5*, 1348–1373.

(14) Roquet, S.; Cravino, A.; Leriche, P.; Alévêque, O.; Frère, P.; Roncali, J. Triphenylamine-Thienylenevinylene Hybrid Systems with Internal Charge Transfer as Donor Materials for Heterojunction Solar Cells. *J. Am. Chem. Soc.* **2006**, *128*, 3459–3466.

(15) Petrus, M. L.; Schutt, K.; Sirtl, M. T.; Hutter, E. M.; Closs, A. C.; Ball, J. M.; Bijleveld, J. C.; Petrozza, A.; Bein, T.; Dingemans, T. J.; et al. New Generation

Hole Transporting Materials for Perovskite Solar Cells: Amide-Based Small-Molecules with Nonconjugated Backbones. *Adv. Energy Mater.* **2018**, *8*, 1801605.

(16) Labrunie, A.; Gorenflot, J.; Babics, M.; Alévêque, O.; Dabos-Seignon, S.; Balawi, A. H.; Kan, Z.; Wohlfahrt, M.; Levillain, E.; Hudhomme, P.; et al. Triphenylamine-Based Push-Pull σ-C60 Dyad As Photoactive Molecular Material for Single-Component Organic Solar Cells: Synthesis, Characterizations, and Photophysical Properties. *Chem. Mater.* **2018**, *30*, 3474–3485.

(17) Zhao, J.; Yang, Z.; Chen, X.; Xie, Z.; Liu, T.; Chi, Z.; Yang, Z.; Zhang, Y.; Aldred, M. P.; Chi, Z. Efficient Triplet Harvesting in Fluorescence-TADF Hybrid Warm-White Organic Light-Emitting Diodes with a Fully Non-Doped Device Configuration. *J. Mater. Chem. C* **2018**, *6*, 4257–4264.

(18) Wu, J. H.; Liou, G. S. Substituent and Charge Transfer Effects on Memory Behavior of the Ambipolar Poly(Triphenylamine)S. *ACS Appl. Mater. Interfaces* **2015**, *7*, 15988–15994.

(19) Moulin, E.; Niess, F.; Maaloum, M.; Buhler, E.; Nyrkova, I.; Giuseppone, N. The Hierarchical Self-Assembly of Charge Nanocarriers: A Highly Cooperative Process Promoted by Visible Light. *Angew. Chemie Int. Ed.* **2010**, *49*, 6974–6978.

(20) Huo, G. F.; Shi, X.; Tu, Q.; Hu, Y. X.; Wu, G. Y.; Yin, G. Q.; Li, X.; Xu, L.; Ding, H. M.; Yang, H. B. Radical-Induced Hierarchical Self-Assembly Involving Supramolecular Coordination Complexes in Both Solution and Solid States. *J. Am. Chem. Soc.* **2019**, *141*, 16014–16023.

(21) Ito, A.; Ino, H.; Tanaka, K.; Kanemoto, K.; Kato, T. Facile Synthesis, Crystal Structures, and High-Spin Cationic States of All-*Para*-Brominated Oligo(N-Phenyl-m-Aniline)s. *J. Org. Chem.* **2002**, *67*, 491–498.

(22) Yano, M.; Sato, K.; Shiomi, D.; Ichimura, A.; Abe, K.; Takui, T.; Itoh, K. Synthesis of 1,3-Bis(Diarylamino)Benzenes as Model Precursors for One-Dimensional Organic Ferromagnetic Metals; Characterization of the Dications by Cyclic Voltammetry and Electron Spin Transient Nutation Spectroscopy. *Tetrahedron Lett.* **1996**, *37*, 9207–9210.

(23) Mao, L.; Zhou, M.; Shi, X.; Yang, H. B. Triphenylamine (TPA) Radical Cations and Related Macrocycles. *Chinese Chem. Lett.* **2021**.

(24) Sindt, A. J.; Dehaven, B. A.; McEachern, D. F.; Dissanayake, D. M. M. M.; Smith, M. D.; Vannucci, A. K.; Shimizu, L. S. UV-Irradiation of Self-Assembled Triphenylamines Affords Persistent and Regenerable Radicals. *Chem. Sci.* **2019**, *10*, 2670–2677.

(25) Miller, J. S. Magnetically Ordered Molecule-Based Materials. *Chem. Soc. Rev.* **2011**, *40*, 3266–3296.

(26) Shimizu, L. S.; Salpage, S. R.; Korous, A. A. Functional Materials from Self-Assembled Bis-Urea Macrocycles. *Acc. Chem. Res.* **2014**, *47*, 2116–2127.

(27) Dehaven, B. A.; Goodlett, D. W.; Sindt, A. J.; Noll, N.; De Vetta, M.; Smith, M. D.; Martin, C. R.; González, L.; Shimizu, L. S. Enhancing the Stability of Photogenerated Benzophenone Triplet Radical Pairs through Supramolecular Assembly. *J. Am. Chem. Soc.* **2018**, *140*, 13064–13070.

(28) Sindt, A. J.; DeHaven, B. A.; Goodlett, D. W.; Hartel, J. O.; Ayare, P. J.; Du, Y.; Smith, M. D.; Mehta, A. K.; Brugh, A. M.; Forbes, M. D. E.; et al. Guest Inclusion Modulates Concentration and Persistence of Photogenerated Radicals in Assembled Triphenylamine Macrocycles. *J. Am. Chem. Soc.* **2020,** *142*, 502–511.

(29) Turro, J. N.; Ramamurthy, V.; Scaiano C. J. *Modern Molecular Photochemistry of Organic Molecules*; University Science Books, Sausalito, CA, 2010.

(30) Zhao, J.; Xu, K.; Yang, W.; Wang, Z.; Zhong, F. The Triplet Excited State of Bodipy: Formation, Modulation and Application. *Chem. Soc. Rev.* **2015**, *44*, 8904–8939.

(31) APEX III, Version 2016.5-0 and SAINT+, Version 8.37A; Bruker AXS, Inc., Madison, Wisconsin, USA, 2016.

(32) Krause, L.; Herbst-Irmer, R.; Sheldrick, G. M.; Stalke, D. Comparison of Silver and Molybdenum Microfocus X-Ray Sources for Single-Crystal Structure Determination. *J. Appl. Crystallogr,* **2015**, *48*, 3–10.

(33) Sheldrick, G. M. SHELXT – Integrated Space-Group and Crystal-Structure Determination. *Acta Crystallogr. A* **2015**, *71*, 3–8.

(34) Sheldrick, G. M. Crystal Structure Refinement with SHELXL. *Acta Crystallogr. C* **2015**, *71*, 3–8.

(35) Dolomanov, O. V.; Bourhis, L. J.; Gildea, R. J.; Howard, J. A. K.; Puschmann, H. OLEX2: A Complete Structure Solution, Refinement and Analysis Program. *J. Appl. Crystallogr.* **2009**, *42*, 339–341.

(36) Sarkar, S. K.; Upul Ranaweera, R. A. A.; Merugu, R.; Abdelaziz, N. M.; Robinson, J.; Day, H. A.; Krause, J. A.; Gudmundsdottir, A. D. Comparison of the

Photochemistry of Acyclic and Cyclic 4-(4-Methoxy-Phenyl)-4-Oxo-but-2-Enoate Ester Derivatives. *J. Phys. Chem. A* **2020**, *124*, 7346–7354.

(37) Simoncelli, S.; Kuzmanich, G.; Gard, M. N.; Garcia-Garibay, M. A. Photochemical Reaction Mechanisms and Kinetics with Molecular Nanocrystals: Surface Quenching of Triplet Benzophenone Nanocrystals. *J. Phys. Org. Chem.* **2010**, *23*, 376-381.

(38) Shao, Y.; Gan, Z.; Epifanovsky, E.; Gilbert, A. T. B.; Wormit, M.; Kussmann, J.; Lange, A. W.; Behn, A.; Deng, J.; Feng, X.; et al. Advances in Molecular Quantum Chemistry Contained in the Q-Chem 4 Program Package. *Mol. Phys.* **2015**, *113*, 184–215.

(39) Spartan'18, version 1.4.4; Wavefunction, Inc. Irvine, CA, 2019

(40) Pritchard, B. P.; Altarawy, D.; Didier, B.; Gibson, T. D.; Windus, T. L. New Basis Set Exchange: An Open, Up-to-Date Resource for the Molecular Sciences Community. *J. Chem. Inf. Model.* **2019**, *59*, 4814–4820.

(41) Devlin, F. J.; Finley, J. W.; Stephens, P. J.; Frisch, M. J. Ab Initio Calculation of Vibrational Absorption and Circular Dichroism Spectra Using Density Functional Force Fields: A Comparison of Local, Nonlocal, and Hybrid Density Functionals. *J. Phys. Chem.* **1995**, *99*, 16883–16902.

(42) Ditchfield, R.; Hehre, W. J.; Pople, J. A. Self-Consistent Molecular-Orbital Methods. IX. An Extended Gaussian-Type Basis for Molecular-Orbital Studies of Organic Molecules. *J. Chem. Phys.* **1971**, *54*, 720–723.

(43) Yanai, T.; Tew, D. P.; Handy, N. C. A New Hybrid Exchange-Correlation Functional Using the Coulomb-Attenuating Method (CAM-B3LYP). *Chem. Phys.*

Lett. **2004**, *393*, 51–57.

(44) Hay, P. J.; Wadt, W. R. Ab Initio Effective Core Potentials for Molecular Calculations. Potentials for the Transition Metal Atoms Sc to Hg. *J. Chem. Phys.* **1985**, *82*, 270–283.

(45) Bernini, C.; Zani, L.; Calamante, M.; Reginato, G.; Mordini, A.; Taddei, M.; Basosi, R.; Sinicropi, A. Excited State Geometries and Vertical Emission Energies of Solvated Dyes for DSSC: A PCM/TD-DFT Benchmark Study. *J. Chem. Theory Comput.* **2014**, *10*, 3925–3933.

(46) Rohrdanz, M. A.; Martins, K. M.; Herbert, J. M. A Long-Range-Corrected Density Functional That Performs Well for Both Ground-State Properties and Time-Dependent Density Functional Theory Excitation Energies, Including Charge-Transfer Excited States. *J. Chem. Phys.* **2009**, *130*, 054112.

(47) Rassolov, V. A.; Chipman, D. M. New Operators for Electronic Density Calculation. I. Derivations and Formal Analysis. *J. Chem. Phys.* **1998**, *105*, 1470.

(48) Link, B. A.; Sindt, A. J.; Shimizu, L. S.; Do, T. D. Selective Host-Guest Chemistry, Self-Assembly and Conformational Preferences of: M -Xylene Macrocycles Probed by Ion-Mobility Spectrometry Mass Spectrometry. *Phys. Chem. Chem. Phys.* **2020**, *22*, 9290–9300.

(49) Wang, L.; Shi, Y.; Zhao, Y.; Liu, H.; Li, X.; Bai, M. Push-Pull 1,8-Naphthalic Anhydride with Multiple Triphenylamine Groups as Electron Donor. *J. Mol. Struct.* **2014**, *1056–1057*, 339–346.

(50) Li, Z.; Dong, Q.; Xu, B.; Li, H.; Wen, S.; Pei, J.; Yao, S.; Lu, H.; Li, P.; Tian, W. New Amorphous Small Molecules - Synthesis, Characterization and Their

Application in Bulk Heterojunction Solar Cells. *Sol. Energy Mater. Sol. Cells* **2011**, *95*, 2272–2280.

(51) Tian, H.; Yang, X.; Chen, R.; Zhang, R.; Hagfeldt, A.; Sun, L. Effect of Different Dye Baths and Dye-Structures on the Performance of Dye-Sensitized Solar Cells Based on Triphenylamine Dyes. *J. Phys. Chem. C* **2008**, *112*, 11023–11033.

(52) Dubinina, G. G.; Price, R. S.; Abboud, K. A.; Wicks, G.; Wnuk, P.; Stepanenko, Y.; Drobizhev, M.; Rebane, A.; Schanze, K. S. Phenylene Vinylene Platinum(II) Acetylides with Prodigious Two-Photon Absorption. *J. Am. Chem. Soc.* **2012**, *134*, 19346–19349.

(53) Bondi, A. Van Der Waals Volumes and Radii. *J. Phys. Chem.* **1964**, *68*, 441–451.

(54) Spackman, M. A.; Jayatilaka, D. Hirshfeld Surface Analysis. *CrystEngComm* **2009**, *11*, 19–32.

(55) Barthos, R.; Méhn, D.; Demortier, A.; Pierard, N.; Morciaux, Y.; Demortier, G.; Fonseca, A.; Nagy, J. B. Functionalization of Single-Walled Carbon Nanotubes by Using Alkyl-Halides. *Carbon N. Y.* **2005**, *43*, 321–325.

(56) Ehlert, C.; Unger, W. E. S.; Saalfrank, P. C K-Edge NEXAFS Spectra of Graphene with Physical and Chemical Defects: A Study Based on Density Functional Theory. *Phys. Chem. Chem. Phys.* **2014**, *16*, 14083–14095.

(57) Moulder, J. F.; Stickle, W. F.; Sobol, P. E.; Bomben, K. D.; Chastain, J. *Handbook of X-Ray Photoelectron Spectroscopy*; Perkin-Elmer: Eden Prairie, MN, 1992

(58) Som, B.; Salpage, S. R.; Son, J.; Gu, B.; Karakalos, S. G.; Smith, M. D.; Shimizu, L. S. Pillars of Assembled Pyridyl Bis-Urea Macrocycles: A Robust Synthon to Organize Diiodotetrafluorobenzenes. *CrystEngComm* **2017**, *19*, 484–491.

(59) Leliege, A.; Blanchard, P.; Rousseau, T.; Roncali, J. Triphenylamine/Tetracyanobutadiene-Based D-A-D π-Conjugated Systems as Molecular Donors for Organic Solar Cells. *Org. Lett.* **2011**, *13*, 3098–3101.

(60) Cias, P.; Slugovc, C.; Gescheidt, G. Hole Transport in Triphenylamine Based OLED Devices: From Theoretical Modeling to Properties Prediction. *J. Phys. Chem. A* **2011**, *115*, 14519–14525.

(61) Martin, R. L. Natural Transition Orbitals. *J. Chem. Phys.* **2003**, *118*, 4775–4777.

(62) Mewes, S. A.; Plasser, F.; Dreuw, A. Communication: Exciton Analysis in Time-Dependent Density Functional Theory: How Functionals Shape Excited-State Characters. *J. Chem. Phys.* **2015**, *143*, 171101.

(63) Plasser, F.; Wormit, M.; Dreuw, A. New Tools for the Systematic Analysis and Visualization of Electronic Excitations. I. Formalism. *J. Chem. Phys.* **2014**, *141*, 024106.

(64) Plasser, F.; Bäppler, S. A.; Wormit, M.; Dreuw, A. New Tools for the Systematic Analysis and Visualization of Electronic Excitations. II. Applications. *J. Chem. Phys.* **2014**, *141*, 024107.

(65) Forrester, A. R.; Hay, J. M.; Thompson, R. H. *Organic Chemistry of Stable Free Radicals*; Academic Press: New York, 1968.

(66) Žilić, D.; Rakvin, B.; Dalal, N. S. Study of the Local Field Distribution on a Single-Molecule Magnet by a Single Paramagnetic Crystal: A DPPH Crystal on the Surface of an Mn12-Acetate Crystal. *J. Appl. Phys.* **2011**, *110*, 093909.

(67) Yano, J.; Sauer, K.; Girerd, J.-J.; Yachandra, V. K. Single Crystal X- and Q-Band EPR Spectroscopy of a Binuclear Mn $_2$ (III, IV) Complex Relevant to the Oxygen-Evolving Complex of Photosystem II. *J. Am. Chem. Soc.* **2004**, *126*, 7486–7495.

(68) Pinzon, J. R.; Gasca, D. C.; Sankaranarayanan, S. G.; Bottari, G.; Torres, T.; Guldi, D. M.; Echegoyen, L. Photoinduced Charge Transfer and Electrochemical Properties of Triphenylamine Ih-Sc3N@C80 Donor-Acceptor Conjugates. *J. Am. Chem. Soc.* **2009**, *131*, 7727–7734.

(69) Doose, S.; Neuweiler, H.; Sauer, M. Fluorescence Quenching by Photoinduced Electron Transfer: A Reporter for Conformational Dynamics of Macromolecules. *ChemPhysChem* **2009**, *10*, 1389–1398.

(70) Schaub, T. A.; Mekelburg, T.; Dral, P. O.; Miehlich, M.; Hampel, F.; Meyer, K.; Kivala, M. A Spherically Shielded Triphenylamine and Its Persistent Radical Cation. *Chem. – A Eur. J.* **2020**, *26*, 3264–3269.

(71) Inoue, F.; Kashihara, M.; Yadav, M. R.; Nakao, Y. Buchwald-Hartwig Amination of Nitroarenes. *Angew. Chemie Int. Ed.* **2017**, *56*, 13307–13309.

(72) Chen, C.; Yang, L. M. Arylation of Diarylamines Catalyzed by Ni(II)-PPh3 System. *Org. Lett.* **2005**, *7*, 2209–2211.

(73) Spek, A. L. Structure Validation in Chemical Crystallography. *Acta Crystallogr. Sect. D Biol. Crystallogr.* **2009**, *65*, 148–155.

(74) Stewart, J. J. P. Optimization of Parameters for Semiempirical Methods I. Method. *J. Comput. Chem.* **1989**, *10*, 209–220.

(75) Stewart, J. J. P. Optimization of Parameters for Semiempirical Methods. III Extension of PM3 to Be, Mg, Zn, Ga, Ge, As, Se, Cd, In, Sn, Sb, Te, Hg, Tl, Pb,

and Bi. *J. Comput. Chem.* **1991**, *12*, 320–341.

(76) Burke, K.; Werschnik, J.; Gross, E. K. U. Time-Dependent Density Functional Theory: Past, Present, and Future. *J. Chem. Phys.* **2005**, *123*, 62206.

(77) Lee, C.; Yang, W.; Parr, R. G. Development of the Colle-Salvetti Correlation-Energy Formula into a Functional of the Electron Density. *Phys. Rev. B* **1988**, *37*, 785–789.

(78) Becke, A. D. Density-Functional Thermochemistry. III. The Role of Exact Exchange. *J. Chem. Phys.* **1993**, *98*, 5648–5652.

(79) Rassolov, V. A.; Ratner, M. A.; Pople, J. A.; Redfern, P. C.; Curtiss, L. A. 6-31G* Basis Set for Third-Row Atoms. *J. Comput. Chem.* **2001**, *22*, 976–984.

(80) Yang, C. H.; Hsu, C. P. The Dynamical Correlation in Spacer-Mediated Electron Transfer Couplings. *J. Chem. Phys.* **2006**, *124*, 244507.

(81) You, Z. Q.; Shao, Y.; Hsu, C. P. Calculating Electron Transfer Couplings by the Spin-Flip Approach: Energy Splitting and Dynamical Correlation Effects. *Chem. Phys. Lett.* **2004**, *390*, 116–123.

(82) You, Z. Q.; Hsu, C. P.; Fleming, G. R. Triplet-Triplet Energy-Transfer Coupling: Theory and Calculation. *J. Chem. Phys.* **2006**, *124*, 74105.

(83) Wadt, W. R.; Hay, P. J. Ab Initio Effective Core Potentials for Molecular Calculations. Potentials for Main Group Elements Na to Bi. *J. Chem. Phys.* **1985**, *82*, 284–298.

(84) Peterson, K. A.; Figgen, D.; Goll, E.; Stoll, H.; Dolg, M. Systematically Convergent Basis Sets with Relativistic Pseudopotentials. II. Small-Core Pseudopotentials and Correlation Consistent Basis Sets for the Post-d Group 16-

18 Elements. *J. Chem. Phys.* **2003**, *119*, 11113–11123.

(85) Voityuk, A. A.; Rösch, N. Fragment Charge Difference Method for Estimating Donor-Acceptor Electronic Coupling: Application to DNA π-Stacks. *J. Chem. Phys.* **2002**, *117*, 5607–5616.

CHAPTER 3

STRUCTURE PROPERTY INVESTIGATIONS IN UREA TETHERED IODINATED TRIPHENYLAMINES

3.0 ABSTRACT

Herein, we report conductive studies on urea-directed self-assembled iodinated triphenylamine (TPA) derivatives. Despite numerous reports of conductive TPAs, the challenges of correlating its solid-state assembly with properties hinders the efficient design of new materials. Recent work demonstrates that urea directed solid-state assembly can afford well-organized TPA derivatives. Modified *para* positions on the TPAs can further facilitate closed packing of TPA units. In this chapter, we compare the assembled structures of methylene urea bridged dimer of di-iodo TPA (**3**), the corresponding methylene urea di-iodo TPA monomer (**2**) with a di-iodo mono aldehyde (**1**) control. These modifications lead to needle shape crystals that are organized by hydrogen bonding and halogen bonding. Specifically, the assembly of **2** and **3** is directed by urea hydrogen bonds motif, π···π stacking, I···I, and I···π interactions as determined by SC-XRD, Hirshfeld surface analysis, and X-ray photoelectron spectroscopy (XPS). The stable long needle shape crystal were robust enough to measure the conductivity by two contact probe methods with TPA **2** exhibiting higher conductivity values (6.44E-07 S/cm) compared **1 (**1.65E-08 S/cm). Upon UV-irradiation, both compounds formed low quantities of radicals with TPA **3** shows higher concentration and prolonged stability of the radicals compared to **1**. Tentatively, radical formation in these systems may indicate trapped states, although more studies are needed. TD-DFT calculation suggests that electron transfer occurs through the urea stacks and that hole mobilities proceed through the closed-packed TPA units. Future exploration will be focused on probed the conductivity in thin-film and potential application in optoelectronic devices.

3.1 INTRODUCTION

Intentional design of the supramolecular framework can lead to the emerging property of the molecules ranging from magnetism[1], dichroism[2], and conductivity[3]. Triphenylamine (TPA) is one of the most promising organic molecules due to its ability of

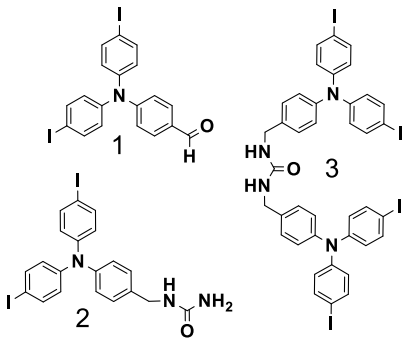

Figure 3.1. Comparison of TPA structures investigated. TPA without assembly motif urea **1**. TPA tethered to one side of urea **2**. TPA tethered to both side of urea **3**.

electron or hole transfer, which can have application in dye-sensitized solar cells[4], perovskite solar cells[5], organic light-emitting diodes (OLEDs)[6], fluorescence imaging[7], magnetic materials[8]. Most of these modified TPA systems largely focused on either incorporating different electron acceptor molecules through π conjugation or tethering two or more TPA units. This structural modification leads to increased efficiency of electron or hole transfer of TPA and further enhances the potential of these TPA derivatives. Indeed, study of these systems contribute to improved next-generation TPA-based hole transporters. However, the electron transport capability intrinsic to TPA is still under explored. A greater understanding of how TPA structure and their controlled assembly correlate with functions is still in progress. One difficulty is controlling and fully characterizing the solid-state assembly of TPA derivatives. Herein, urea tethered di-iodinated TPA **2** and a tetra-iodinated TPA **3** were synthesized and crystallized where the *para* positions of the external phenyl rings were modified by iodine. While urea guides the

assembly, the close packing of TPA units is further tailored by I – I, π – π, and I – π interactions. These materials form low levels of radicals upon UV-irradiation in crystals. We examine their photophysics, conductivity, and ion mobility in crystals, and their ability of electron transport was explored by computational approach.

Flexibility and tunability are the two main feature that makes an electron transportable organic chromophore attractive compared to inorganic counterparts. Specifically, the non-covalent interaction responsible for crystal packing can be tuned to design functional materials with properties ranging from semiconductor, insulator, and conductor.[9,10] TPA is redox-active organic molecule that can generate electron/hole pairs has been widely used as a hole transporter in the semiconductor industry.[11] In TPA, the phenyl rings arranged in propeller shapes, make halo-effects of the π orbitals electrons results in the transfer of the electrons or charge carriers.[12] This effect can be extended through π interactions or hetero atom halogens. These modifications also increase the solution processability of TPA derivatives in thin-film and structural information can be obtained by electronic microscopic (EM) and atomic force microscopic (AFM) techniques (transmission EM, scanning EM).[13,14] However useful structural information, for instance, π stacking, halogen-π, halogen-halogen interactions which are key to the coupling and charge transfer is difficult to obtain with these techniques. Single crystal X-ray Diffraction (SC-XRD) techniques can be utilized to extract useful structural information correlated with functional features. Osman and his coworkers recently crystallized TPA-based spiro-OMeTAD by the anti-solvent method which is used as a hole transfer layer in perovskite solar cells. They have observed mesoscale ordering driven by discontinuous π-π stacking interactions between the fluorene plane of adjacent spiro-OMeTAD is the key for

transporting the charges.[15] Giuseppone group crystallized TPA derivatives where all the *para* positions were modified by amide groups.[16] SC-XRD data suggest the formation of equidistant snowflake conformations packed via intercolumnar hydrogen bonds. They have observed higher mobilities of charges in the crystal due to the tight packing of the aromatic cores between stacked dimers.

Shimizu group utilizes urea to guide the assembly to afford needle shape crystals which are readily available for structural information by SC-XRD.[17,18] Previously we have synthesized and crystallized a series of urea tethered TPA derivatives where one of the *para* positions of the phenyl groups were modified by halogen.[19] In the solid-state, these materials can generate stable radicals with variable quantities. While the bromo derivative generates the highest amount of radicals surprisingly iodo derivative forms the least amount of radicals. TD-DFT calculation suggests electrical coupling in the hydrogen-bonded dimers of the iodo derivative was 7 times stronger compared to the bromo derivative. It is expected that complete iodine substitution on the external phenyl rings will help to closely pack the TPA units and hence increase the electrical coupling. To test our hypothesis urea tethered di-iodinated TPA **2** and tetra-iodinated **3** were synthesized and crystallized. Their SC-XRD determined structures were compared with untethered TPA **1** to investigate the effect of urea tethering and iodine substitution on the 3-dimensional structures. Hirshfeld surface analysis and XPS studies suggest while urea guides the assembly TPA unit into tapes, which then closely packed via C-I$\cdots\pi$, I-I interactions. The conductivity of a single crystal was measured by the two-contact probe method. Finally, TD-DFT was used to investigate the electron transfer mechanism within hydrogen-bonded stacks.

3.2 SYNTHESIS AND CRYSTALLIZATION

Urea tethered iodinated TPAs **2** and **3** were synthesized in six steps following established procedures (Scheme 3.1).[19] A Vilsmeier-Haack reaction converted

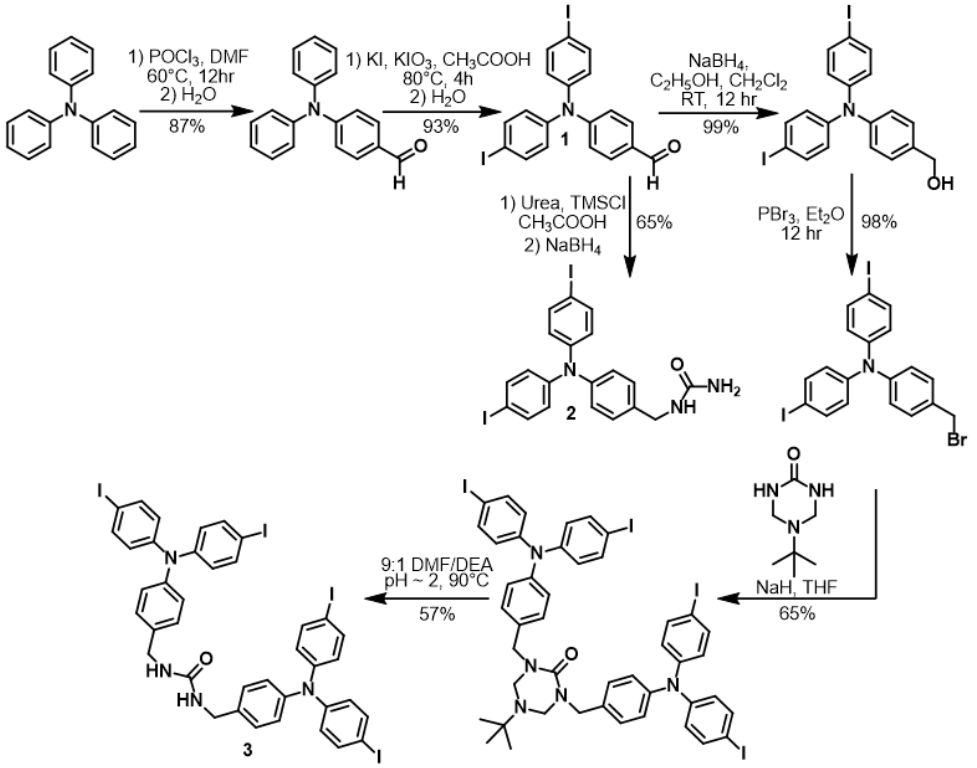

Scheme 3.1. Synthesis of **1** and urea tethered iodinated **2**, and **3**.

commercial TPA to its' mono aldehyde.[20] Iodination of *para* positions of the remaining phenyl rings was carried out with potassium iodide and potassium iodate yield **1**.[21] A modified reductive amination with urea yields a singly TPA tethered to methylene urea **2**. Alternatively, the aldehyde was reduced to alcohol.[22] Bromination followed by subsequent reaction with triazinanone under basic conditions yields the urea tethered dimer.[23] Deprotection was performed in a mixture of 9:1 DMF/DEA (diethanolamine) in acidic media to yield **3**. X-ray diffraction quality ethyl acetate or methanol solvated crystals of **3** were obtained by slow evaporation either from ethyl acetate (2.5 mg/mL) or a 1:1 mixture of DCM:methanol solution (5 mg/mL).

Solvent-free crystals of **2** were obtained by slow evaporation from ethyl acetate (2.5 mg/mL). The yellow plate crystals of **1** were obtained by slow evaporation of 1:1 = DCM:Hexane (5 mg/mL).

3.3 UREA DIRECTED ASSEMBLY OF TPA

Both the ethyl acetate and methanol solvated crystals of **3** are isostructural, crystallizing in the triclinic space group *P*-1 (No. 2). The asymmetric unit consists of half each of two crystallographically independent TPA **3** molecules. A region of disordered ethyl acetate or methanol molecules is located on a crystallographic inversion center as shown in Figure 3.13-3.14. Overall, crystal consists of a 50/50 disorder of chains with urea groups pointing up or down while the rest of the group atoms remains the same. The TPAs on the opposite side of the urea arranged themselves in inverted fashion with TPA N···N distances of 13.82 Å and 14.26 Å for two independent molecules, slightly higher compared with the series of related compounds reported previously.[19] The ureas adopts the *trans-trans* conformation and typical three centered urea-urea hydrogen bonding directs the assembly with d(N···O) distances from 2.915(10) - 3.152(12), Å and a twisting angle 27.16° (Figure 3.18a). The twisted chains of the ureas forming a skewed shape if viewed along with the crystallographic *c* – axis (Figure 3.18b). Infinite 1D chains of H-bonded urea organizes into columnar tubes that encapsulate ethyl acetate or methanol in a host-guest ratio of 1:0.72 and 1:2 respectively as seen in Figure 3.2c-d and Figure 3.18c. The channel diameter of the interior cross-section is 7.18 x 3.64 Å centroid to centroid (Figure 3.2e). Multiple face-to-face intermolecular π-stacking and C-I···π interactions are present within the channel (Figure 3.20-21). The

neighboring tubes are held together by weak I···I halogen bonds (I···I distance 3.874 Å), slightly less than the sum of van der Waals radii (3.96 Å) of iodine (Figure 3.22).[24]

The methylene urea **2** also crystallized in the triclinic space group *P*-1 (No.2)

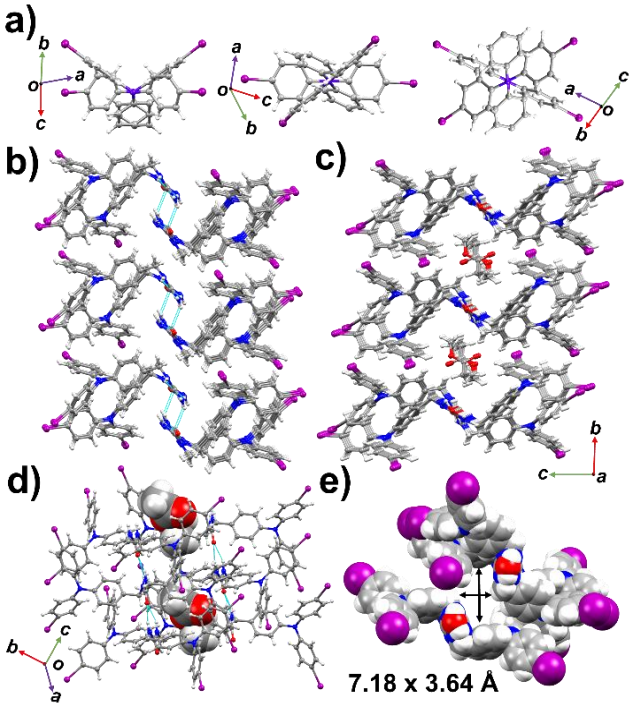

Figure 3.2. Comparison of crystals of **1**, urea tethered solvent free crystal **2**, and urea tethered solvated crystal **3**. Disorder omitted for clarity. a) Packing of TPA units in **1** (left), **2** (middle), **3** (right). b) Assembly of **2** through hydrogen-bonded urea tape. Inter-chain H-bonds links two strands (top down view). c) Packing of **3** through hydrogen-bonded urea tape. H-bonded urea chains encapsulate ethyl acetate. d) A view of bifurcated H-bond chain running parallel to crystallographic *a* axis in **3**. Ethyl acetate molecules are shown in the spacefill model. e) Spacefill model of **3** showing the cross-sectional area of the channel. (vdW radii subtracted)

with two crystallographically independent but chemically identical molecules in the asymmetric unit (Figure 3.15). Again, the ureas adopt the *trans-trans* conformation and urea hydrogen bonding directs the assembly with d(N···O) distances from 2.921(2) - 3.252(2) Å and a twisting angle of 17.81° (Figure 3.19). In addition, one urea NH hydrogen forms another hydrogen bond with a neighboring carbonyl

oxygen (d(N···O) = 3.068(3)) Å to link two chains together (Figure 3.2b). The individual chains are held together with weak I···I halogen bond distance 3.854 Å less than the sum of van der Waals radii (3.96 Å) as seen in Figure 3.24. The control TPA **1** aldehyde, with no hydrogen bonding groups, crystallized in the monoclinic system with the monoclinic space group *Pc*. The structure is disordered with the formyl group and iodines scrambled together on two separate sites (Figure 3.16).

The Giuseppone group and others, hypothesize that it is the relative orientation of TPA units are important for conductivity and photophysical properties of TPA supramolecular polymers.[25,26] Giuseppone group observed stacking of TPA units with favourable snowflake or Mercedes-Benz conformation with N···N distances 4.8 Å to 5 Å. Therefore, the packing of TPA units was analysed from this perspective. Aldehyde **1** (Figure 3.2a, left) forms a butterfly shape with TPA N···N distances 7.05 Å. The TPA units of **2** organized into a cross-flake conformation (Figure 3.2a, middle) with TPA N···N distances 14.557 Å. In both solvated crystal forms of **3**, the TPAs adopts slightly rotated snowflake conformation (Figure 3.2a, right) with TPA N-N distance 11.70 Å. The phenyl rings of **1** shows a less rotated conformation (51.76° - 62.11°) compared to **2** (71.54° - 93.55°), and **3** (64.06° - 75.56°) as seen in Figure 3.17.

Hirshfeld surface analysis was utilized to further investigate the non-covalent interaction promoting the packing of the crystals of **2** and **3**.[27] Hirshfeld surface map (Figure 3.3) of **2** and **3** shows the key urea hydrogen bonding interaction indicated in red. We observed offset π stacking interactions in **2** with distances 3.023 Å and 3.597 Å measured from H - centroid. There are C-I···π (3.881 Å), and offset π

stacking (3.135 Å) interactions in **3** suggested by the Hirshfeld surface analysis. X-ray photoelectron spectroscopy (XPS) was further utilized to probe the chemical

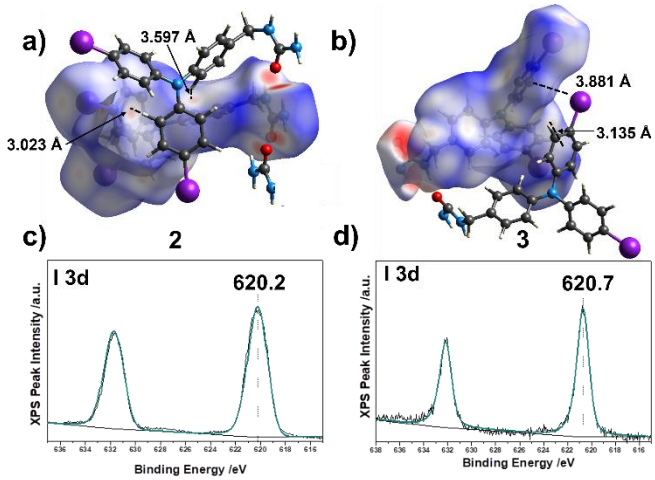

Figure 3.3. Hirshfeld surface map (Isovalue 0.05) and **I**(3d) XPS core level peaks recorded with a monochromatic Al Kα X-ray source of the asymmetric unit of **2** and **3**. a) Hirshfeld surface map of **2** showing offset π stacking interactions. b) Hirshfeld surface map of **3** showing C-I···π, and offset π stacking interactions. c) **I**(3d) XPS core level peaks for compound **2**. d) **I**(3d) XPS core level peaks for compound **3** (ethyl acetate solvated).

environment around the iodine. A shift in the binding energy of the core level electrons of I(3d) would be expected due to the interactions of C-I···π and I···I halogen bond. Indeed, a shift was observed in binding energy I(3d) from 619 eV to 620.7 eV, 620.2 eV for **3** (ethyl acetate solvated), and **2** respectively (Figure 3.3).[28] These results suggest urea directed assembly was further promoted by closed packing of TPA units.

3.4 PHOTOPHYSICAL PROPERTIES

To probe how assembly and packing of TPA units effects the photophysics in the solid-state, diffuse reflectance and photoluminescence experiments were performed for each sample (Table 3.1). Diffuse reflectance experiments on bulk crystals (Figure 3.25) show that the absorbance of urea containing materials **2** and **3** were shifted to the lower

Table 3.1. Measured photophysical properties for compounds **1, 2**, and **3.**

Compound	λ_{abs} (nm)[a]	λ_{ems} (nm)[b]
1 in solid	445	478
2 in solid	367	503
3 in solid	361	451
3 (in Methylene chloride)	309	365, 440
3 (in thin films)	321	

[a]Peak position at the largest absorption band. In solid diffuse reflectance experiments performed in bulk crystals. [b]Peak position at the largest emission bands in nanometers using 375 nm laser excitation source for solid and 300 nm excitation source for solution (10 μM) and in thin films. In solid photoluminescence experiments performed in single crystals.

wavelength 367 nm and 361 nm respectively as compared to **1** at 445 nm. The absorbance of **3** was also studied in thin films and in solution (argon purged methylene chloride) at room temperature (Figure 3.26). The absorbance was observed at shorter wavelength at 321 nm (thin films) and 309 nm (solution) as compared to the bulk crystals. A photoluminescence study was done on single crystals of **1-3** using λ_{EXC} = 375 nm (Figure 3.27). The emission bands ranged from 451-503 nm with **2** exhibiting the longest wavelength emission λ_{Em} = 503 and largest Stokes shift (136 nm) as compared to **3** λ_{Em} = 451 nm (Stokes shift ~ 90 nm). The aldehdye **1** in comparison showed λ_{Em} = 478 nm with a Stokes shift of 33 nm. Packing has been shown to influence the photophysics in dihalogenated methylene ureas derivatives with smaller twisting angle shows higher stokes shift.[19] Higher, red-shifted emissions were also observed for the formation of excimer due to closely packed TPA units.[29] The emission study of **3** in solution (10 μM in dry CH_2Cl_2) displayed two bands at 365 nm and 440 nm, while a quenching study in oxygen purged solution suggest the both the band may arise due to fluorescence (Figure 3.28).

3.5 CONDUCTIVITY MEASUREMENT

The intrinsic electrical conductivity of the single crystal of **2** and **3** were measured using the 2-contact probe method in dark at room temperature (Figure 3.4). For the measurement, triply recrystallized samples were used (See experimental section for further details of the experimental setup). By parking two probe voltage or current was supplied or measured. The total resistance was obtained by fitting the linear region of a current-voltage (I-V) curve using Ohm's law. Current was measured at 10 V bias and the calculated electrical conductivity of three different trials of single crystals of **2** and **3** tabulated in Table 3.3-3.4. The highest electrical conductivity of a single crystal of **3** is 1.65E-08 S/cm and in a range of 1.41E-09 – 1.65E-08 S/cm. TPA **2** shows a higher conductivity value compared to **3** with the highest conductivity 6.44E-07 S/cm and in a range of 6.44E-07 S/cm to 2.93E-10 S/cm. Dimensions and morphology (cracked or twisted) of the crystal can influence the conductivity as in the case of **2** with much thinner crystals shows very low conductivity. It should be noted that most of the higher conductivity values for the TPA derivatives were observed in thin films, which was attributed to close packing and enhanced stacking interaction of phenyl rings.

Previous evidence on halogen-substituted urea tethered TPA derivatives suggest the formation of variable percent of radicals upon UV irradiation.[19] However, the partial iodine substituted urea tethered TPA derivative showed the least radical formation and highest electrical coupling. We expected that complete iodine substitution would further enhance electrical coupling as facilitated by close packing of TPA units. To further investigate the effect of light, the conductivity of **2** and **3** were measured upon UV irradiation (Table 3.5-3.6). For the experiments, 365 nm UV LED was used (photon flux)

and conductivity was measured at a time interval. Upon UV-irradiation a reduction of conductivity was observed for both **2** and **3** which plateaued at 5 hours. Single crystal of **3** shows higher sensitivity upon UV irradiation as the conductivity decrease from 1.65E-08

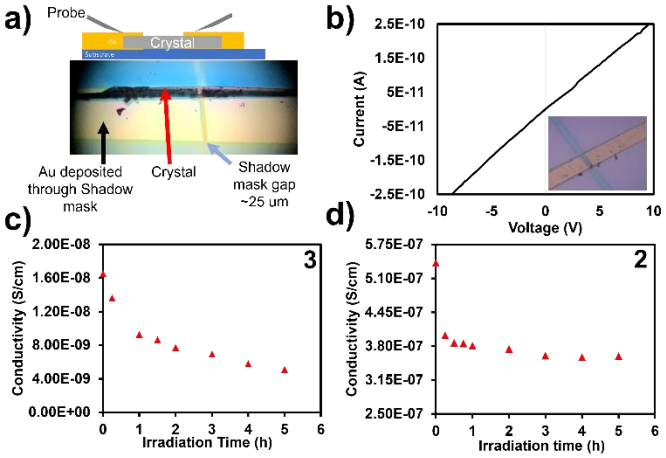

Figure 3.4. Electrical conductivity measurement under dark and UV-irradiation at room temperature. a) two contact probe setup used to measure the conductivity of a single crystal. b) I-V curve for a trial of **3** under dark at room temperature by measuring the sum of resistance of the material, wires, and contacts using two contact probe method. Inset shows a single crystal setup. c, d) changes in electrical conductivity under UV-irradiation using 365 nm UV sources at room temperature.

to 5.12E-09 compared to **2** (5.39E-07 to 3.60E-07). To further investigate if the conductivity of crystal **3** regain back to its initial state we continuously monitored the conductivity in dark after initial 5 hours of UV irradiation (Table 3.7). We observe no significant changes or rises in the conductivity value of **3** to its initial state as seen in Figure 3.29. Our hypothesis is that the unpaired spins or the charge carriers generated through UV-irradiation are long-lived. The continuous C-I···π, and π···π interactions helps to delocalize the charges, which might be detrimental for charge transport or hole mobilities and hence decrease the electrical conductivity.[15,30]

3.6 EPR EXPERIMENTS

To further understand the consistent drop of the conductivity and how UV irradiation would affect the overall properties of the crystals X-band EPR spectroscopy was utilized to measure radical formation in **2** and **3**. Figures 3.5 shows sample **3** display a

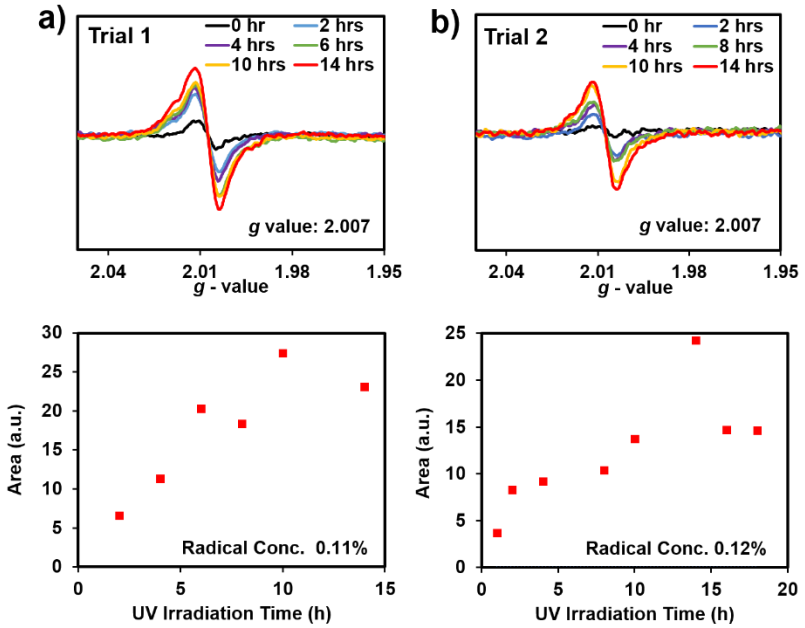

Figure 3.5. EPR data for the urea tethered TPA **3**. EPR spectra over time of UV irradiation (top). EPR spectra were doubly integrated to obtain the area plotted vs time of UV irradiation using 365 nm UV LED (bottom). a) Trial 1: A maximum radical concentration of 0.11% was obtained for 8.1 mg of triply recrystallized material by averaging last 3 data points. b) A maximum radical concentration of 0.12% was obtained for 7.7 mg of triply recrystallized material by averaging last 3 data points.

powder pattern shape EPR signal with corresponding *g* value 2.007. The radical is characterized as a TPA radical cation suggested by the previous work of our group for a similar series of derivatives.[19] Further details of the EPR experiment and methods used to estimate the radical concentration can be found in experimental section. Although the radicals generated by **3** are low in quantity (0.11%, 0.12%), we observe comparable EPR spectra even after 22 days without UV irradiation (Figure 3.31). Compound **2** did not show any significant changes in the pre- and post-UV irradiated EPR spectra (Figure 3.33). These

results suggest that reverse electron transfer is much slower for **3** as compared to **2**. The extensive π···π stacking interactions in **3** helps to delocalize the charges and may hinder charge transport manifested by lower conductivity values upon UV irradiation.

3.7 TD-DFT TO UNDERSTAND ELECTRON TRANSFER

Next, we turned to TD-DFT calculation to understand the electron transfer in the ground state. CAM-B3LYP[31] functional paired with LANL2DZdp[32] basis set were used, which is proven to be effective to describe the electronic transition for the similar series of derivatives. Further computational details were given in

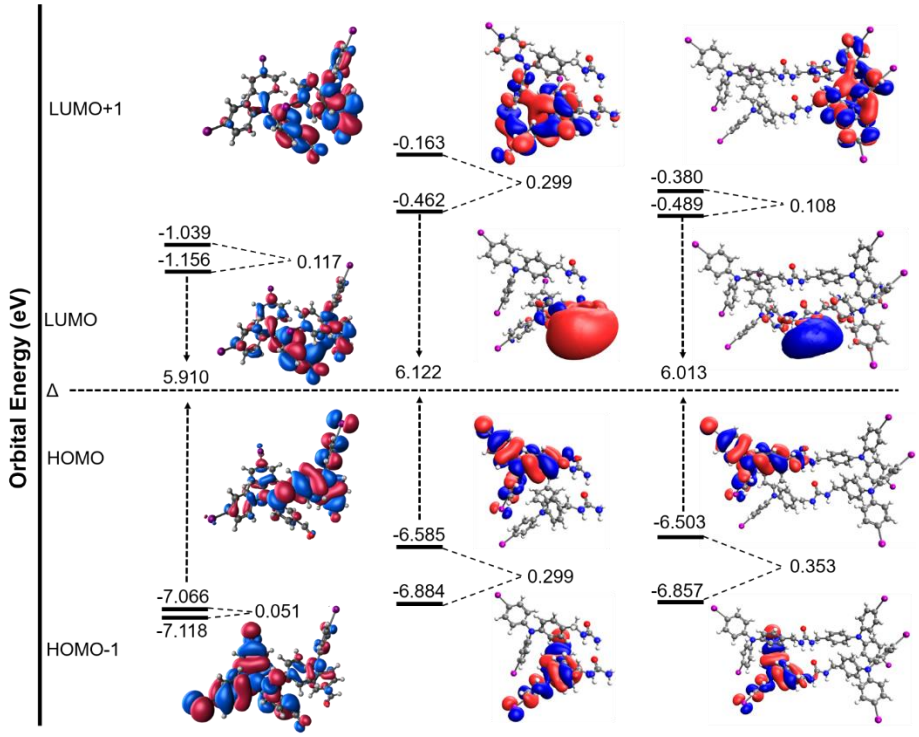

Figure 3.6. From left, Frontier molecular orbitals, their energies, and gap of dimer of **1** with no hydrogen bonded groups and hydrogen bonded dimer of **2**, **3**. Frontier molecular orbitals generated using CAM-B3LYP/LANL2DZdp methods in the gas phase visualized at Isovalue 0.04.

experimental section 3.15. The frontier orbitals (HOMOs/LUMOs), their energies, and gap for **1**, **2**, and **3** were generated and compared, and given in figure 3.6.

First, we compare the energy levels to investigate the relationship between the molecular structure and electronic properties. Introduction of urea motif increases the HOMO (-6.585 eV, -6.503 eV) and LUMO (-0.462 eV, 0.489 eV) energy for **2**, **3** respectively compared to control **1**, -7.066 eV (HOMO) and -1.156 eV (LUMO). Overall, the HOMO-LUMO energy gap was higher in **2** (6.122 eV), and **3** (6.013 eV) compared to **1** (5.910 eV). In addition, the frontier orbitals of **1** demonstrated the electron density delocalization over the entire molecular skeleton. The electron density distribution in the hydrogen-bonded dimer of **2** and **3** suggest the localized density in either of the TPA units in HOMO-1 and HOMO as seen in Figure 3.6. In the case of LUMO and LUMO+1, the electron density localized on the same TPA unit and methylene urea for **2** while in **3** the electron density delocalized on both TPA unit and a single unit of urea. In summary, these electron density distributions suggest the hole mobility through the HOMOs promoted by closely packed TPA units and electron mobility through the hydrogen-bonded urea motif.

For additional insight into the excited state, TD-DFT was employed to construct the UV-vis spectra both in solution and solid-state within random phase approximation (RPA). CAM-B3LYP/LANL2DZdp methods have been chosen to simulate experimental diffuse reflectance spectra as this method was sufficient to reproduce the absorption spectra in solution. Further computational details can be found in the experimental section. The computed absorption spectra were in good match with experimental diffuse reflectance spectra and the highest occupied natural transition orbital (HONTO), lowest unoccupied natural transition orbital (LUNTO)

was generated at the λ_{max} at the transition with the highest oscillator strength. The electronic transitions and the corresponding wavelength are **1** (S_{14}, 445 nm), **2** (S_{27}, 367 nm), **3** (S_{30}, 361 nm) which can be seen in Figure 3.7. The nature of spatial overlap of the NTOs suggests these transitions raised by $\pi\pi^*$ excitation. The key differences between these NTOs that **1** with no hydrogen bonding groups the electron density only delocalized on one of the TPA units. TPA **2** which forms an interchain hydrogen bond and a bifurcated hydrogen bond shows electron density in one of the TPA units which partially overlaps with the neighboring TPA. TPA **3**

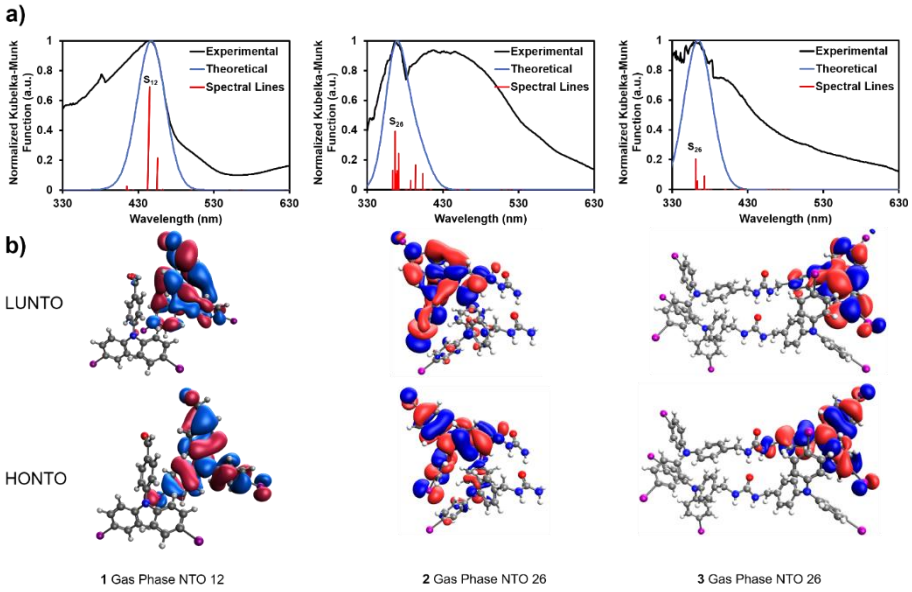

Figure 3.7. Comparison of normalized diffuse reflectance measurements, TD-DFT simulated spectra, and corresponding spectral lines. a) From left, transitions to the S_{12} state corresponds to the λ_{max} of 1 at 445 nm, transitions to the S_{26} state corresponds to the λ_{max} of 2 at 367 nm, transitions to the S_{26} state corresponds to the λ_{max} of 3 at 361 nm. b) Natural transition orbitals of 1, 2, and 3 in gas phase.

with TPA on both sides of urea shows delocalization of electron density only one of the TPA units. Both **2** and **3** lack electron density on the hydrogen bond motif urea.

3.8 CONCLUSION

While much effort has been made to design and synthesize TPA-based conductors, true rational design remains a challenge due to a lack of understanding of the relationship between the supramolecular structure and properties. TPA derivatives have an intrinsic tendency of forming glasses that prevent important structural information. To remove this constrain, our group has incorporated ureas, a directional hydrogen bonding motif that directs the self-assembly of the TPA into ordered crystalline structures. These structures afford needle shape single crystals readily available for SC-XRD analysis. This gives us valuable structural information which can be utilized to probe the relation between structure and functions as well as facilitate modeling of ordered small oligomers with TD-DFT.

In this chapter, two urea tethered TPA derivatives were synthesized and crystallized. While urea guide the assembly, close packing of the TPA units were promoted by halogen bonding and aryl stacking interactions (I···I, I···π, π···π interactions). Comparison with control **1**, which contains no urea group, suggests that the urea tethering influences the photophysics and these derivatives absorb at a lower wavelength exhibiting higher stokes shifts. The conductivity of TPA **2** and **3** was measured by two contact probe methods where **2** shows higher conductivity values compared to **3**. Photoirradiation effects the overall properties of the crystals and generates detectable thought minor quantities of radicals. We also observed in a decrease in conductivity values upon UV irradiation much larger in **3** compared to **1**. TD-DFT calculation suggests urea-directed assembly is important for transferring the electrons while the closed-packing of TPA units promote hole mobilities. We hypothesize that continuous π stacking interactions helps to delocalize

the charges which can restrict charge transport by hopping or other electron transfer pathways. Future work will be focused on probing the conductivity of the urea tethered TPA derivatives in thin-film and potential applications in optoelectronic devices.

3.9 EXPERIMENTAL

3.9.1 General Methods

Both commercially available reagents and solvents were purchased from VWR, Sigma-Aldrich, TCI America and, Alfa Aesar and used in synthesis without any further purification. Reagents that are air-sensitive stored under the protection of nitrogen. The round bottom flask was oven-dried for reactions. ^{1}H NMR, ^{13}C NMR spectra were recorded in Bruker Avance 300 or 400 MHz spectrometers. To report the chemical shift in ppm, solvent peaks were used as a reference. High-resolution mass spectra were recorded in a direct exposure probe (DEP) in electron ionization (EI) mode on a waters QTOF-I quadrupole time-of-flight mass spectrometer.

3.9.2 Photophysical Properties

Commercially Waveform Lighting real UV 365 nm LEDs were used for UV irradiation. UV/Vis absorption spectra in solution were recorded in Molecular Devices Spectramax M2. Diffuse reflectance experiment of the solid sample was performed by using a Perkin Elmer Lambda 45 UV/vis spectrometer comprised of UV Winlab software and was referenced to Spectralon®. Emission experiment in solution (cuvette) was performed by using Perkin Elmer LS55 fluorescence spectrometer equipped with a pulsed high-energy source for excitation. Photoluminescence experiment of the solid sample was performed in HORIBA Scientific Standard Microscope Spectroscopy Systems connected with iHR320 spectrometer and synchrony detector operating on Labspec 6 software. 375

nm laser excitation source was used to record the spectra with power delivery 0.3 mW comprised with 10xUV objective.

3.9.3 EPR Studies

Bruker EMX plus equipped with a Bruker X-band microwave bridgehead and Xenon software (v 1.1b.66) were used for EPR experiments. Double integration of the area under the curve of the EPR spectra was performed using Xenon software to obtain peak area. Norell Suprasil Quartz tubes were used for UV irradiation and EPR experiments and were sealed under the protection of argon.

3.9.4 XPS Analysis

Kratos AXIS Ultra DLD XPS system with a monochromatic Al Ka source, operated at 15 keV and 150W and at pressures below 10^{-9} torr was used for XPS analysis. The X-rays were incident at an angle of 45° with respect to the surface normal. High resolution core level spectra were measured with a pass energy of 40 eV and analysis of the data was carried out using XPSPEAK41 software. The XPS system was equipped with a hemispherical electron analyzer and a load lock chamber for rapid introduction of samples without breaking vacuum. The XPS experiments were conducted using an electron gun, directed on the sample for charge neutralization. The UV irradiation took place in-situ, through the windows of the Ultra High Vacuum chamber.

3.10 EXPERIMENTAL PROCEDURE

Synthesis of 4-(diphenylamino)benzaldehyde

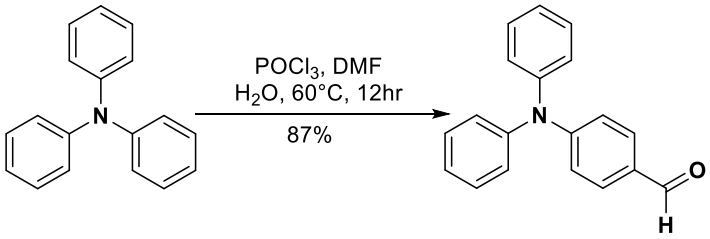

The compound was synthesized according to the previous literature procedures. In an oven-dry round bottom flask, phosphoryl chloride (1.055 mL, 11.34 mmol, 1 equiv.) was added dropwise to N, N-dimethylformamide (0.875 mL, 11.34 mmol, 1 equiv.) at 0°C and the mixture stirred for 20 minutes at room temperature. For proper safety, an elevated flow rate in the hood and acid glove was used. Next, commercially available triphenylamine (1 g, 4.10 mmol, 0.36 mmol) was dissolved in 10 mL of N, N-dimethylformamide and added to the reaction mixture dropwise and the reaction mixture heated at 40°C for 12 hours. After completion, the reaction mixture was cooled to room temperature, 30 mL ice-cold H_2O was added and the solution left in the refrigerator for 2 hours. The resulting precipitant was collected by suction filtration and recrystallized from a minimum amount of ethanol. The final product was obtained as a yellow solid (yield 0.9617 g, 87%). The obtained spectra matched with previous reports.[33] ^{1}H NMR (400 MHz, $CDCl_3$): δ (ppm) d 9.81(s, 1H), 7.68 (d, J = 8.4 Hz, 2H), 7.34 (t, 4H), 7.17-7.19 (m, 6H), 7.02 (d, J = 8.5 Hz, 2H). HRMS (EI): [M+] calculated 273.1154, found, 273.1155

Synthesis of 4-(bis(4-iodophenyl)amino)benzaldehyde

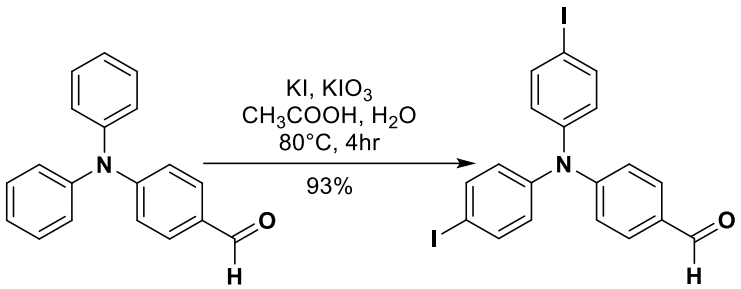

The compound was synthesized according to the previous literature procedure. In a 100 mL round bottom flask, 4-(diphenylamino)benzaldehyde (0.7213 g, 2.638 mmol, 1 equiv.) and potassium iodide (0.591 g, 3.562 mmol, 1.35 equiv.) was added in 10 mL of 9:1 mixture of acetic acid and H_2O. The mixture heated until it reached 80°C. Then

potassium iodate (0.565 g, 2.64 mmol, 1 equiv.) was added and the mixture heated at 80°C for 4 hours. After completion, the solution was cooled to room temperature and neutralized with $NaHCO_3$. Then the resulting solution was washed with methylene chloride (3 X 30 mL), washed with aqueous saturated $Na_2S_2O_3$ (3 X 30 mL), and dried over anhydrous $MgSO_4$. The solvent was removed by rotary evaporation and the crude material was purified by column chromatography using 3:1 = Hexane: Ethyl Acetate as eluent. The final product was obtained as a yellow solid (1.29 g, 93%). The obtained spectra matched previous reports.[33] ^{1}H NMR (600 MHz, CDCl3): δ (ppm) 9.84 (s, 1H), 7.71 (d, J = 8.3 Hz, 2H), 7.63 (d, J = 8.5 Hz, 4H), 7.05 (d, J = 8.3 Hz, 2H), 6.89 (d, J = 8.4 Hz, 4H). 13C NMR (150 MHz, CDCl3): δ (ppm)190.35, 152.17, 145.69, 138.85, 131.34, 130.31, 127.60, 120.75, 88.75. MS (FAB): m/z = 524.91 [M+H]+

Synthesis of 1-(4-(bis(4-iodophenyl)amino)benzyl)urea

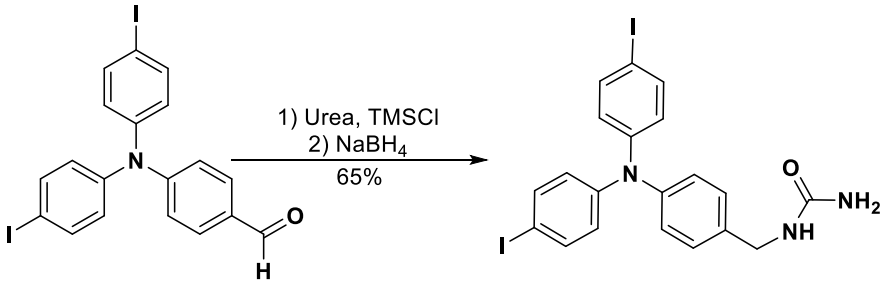

Compound was synthesized according to the previous literature procedure. The previous aldehyde (1.619 g, 3.083 mmol) and urea (1.86 g, 30.83 mmol) were dissolved in 50 mL acetic acid and trimethylsilyl chloride (0.58 mL, 4.624 mmol) added. The resulting mixture was stirred at room temperature for 12 hours. Then sodium borohydride (0.174 g, 4.624 mmol) was added and the solution stirred for 2 hours. After completion 500 mL of water was added and resulting precipitate collected by filtration. The final product was obtained as beige solid by column chromatography using 1:1 = CH_2Cl_2:ethyl acetate as

eluent (1.138 g, 65%). ^{1}H NMR (300 MHz, (CD_2Cl_2): δ (ppm) 7.52 (d, *J* = 8.8 Hz, 4H), 7.21 (d, *J* = 8.3 Hz, 2H), 7.02 (d, *J* = 8.5 Hz, 2H), 6.80 (d, *J* = 8.8 Hz, 4H), 4.86 (s, *J* = 5.8 Hz, 1H), 4.35 (s, *J* = 5.9 Hz, 2H), 4.29 (d, *J* = 5.9 Hz, 2H). ^{13}C NMR (75 MHz, $(CD_3)_2SO$-*d*$_6$) δ (ppm) 158.62, 146.70, 144.62, 138.08, 137.13, 128.60, 125.20, 125.08, 86.08, 42.32. HRMS (ES): [M+] calculated 568.9461; found: 568.9475

Synthesis of (4-(bis(4-iodophenyl)amino)phenyl)methanol

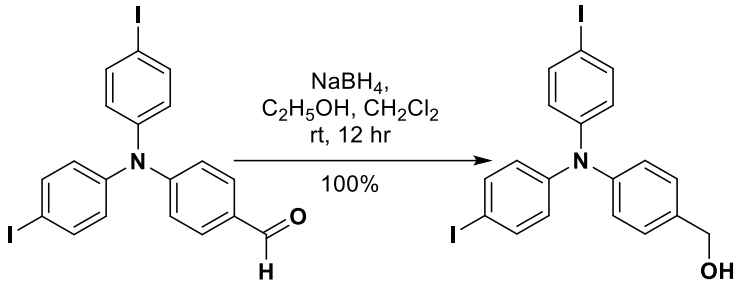

Compound was synthesized according to the previous procedure. Product from the previous step (1.917 g, 3.65 mmol, 1 equiv.) was dissolved in 60 mL of 3:1 mixture of dry CH_2Cl_2 and ethanol and stirred for 5 minutes at room temperature. Then sodium borohydride (0.16 g, 4.01 mmol, 1.1 equiv.) was added to the reaction mixture and stirred for 12 hours at room temperature in the dark. After completion, the reaction mixture was quenched by adding 90 mL of H_2O and the organics were extracted with CH_2Cl_2 (3 X 35 mL) and dried over anhydrous $MgSO_4$. Then the solvent was removed under reduced pressure and the final product was obtained as a sticky white solid (1.921 g, 99 %). The obtained spectra matched with previous reports.[33] ^{1}H NMR (400 MHz, $CDCl_3$) δ(ppm): 7.52 (d, J = 8.8 Hz, 4H), 7.27 (d, J = 7.9 Hz, 2H), 7.05 (d, J = 8.4 Hz, 2H), 6.81 (d, J = 8.8 Hz, 4H), 4.65 (s, 2H).

Synthesis of 4-(bromomethyl)-N,N-bis(4-iodophenyl)aniline

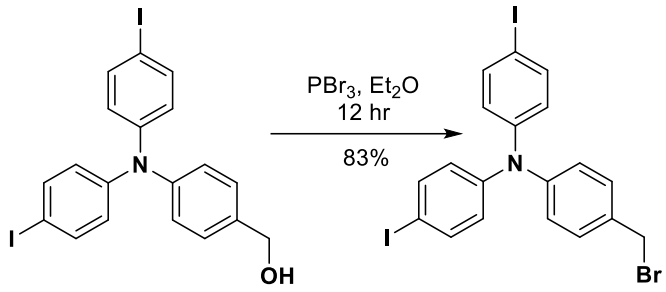

Compound was synthesized according to the previous procedure. The previous alcohol (1.921 g, 3.645 mmol, 1 equiv.) was dissolved in 40 mL of dry diethyl ether and cooled to 0°C in an ice bath. Then phosphorus tribromide (0.652 g, 2.406 mmol, 230 μl, 0.66 equiv.) was added dropwise as a solution in 10 mL dry diethyl ether to the reaction mixture over 5 minutes and the reaction stirred at room temperatures in dark for 12 hours. Once finished, 55 mL ice old H_2O and (3 X 20 mL) of saturated $NaHCO_3$ were added to the reaction mixtures. Then the organics were extracted with CH_2Cl_2 (1 x 55 mL), further washed with brine (3 x 20 mL) and dried over anhydrous $MgSO_4$. Then the solvent was reduced by using rotary evaporation and the final product was obtained as a sticky solid (2.12 g, 98%). The obtained spectra matched with previous reports.[33] ^{1}H NMR (400 MHz, $CDCl_3$) δ(ppm): 7.54 (d, J = 8.7 Hz, 4H), 7.34 (d, J = 6.4 Hz, 2H), 7.03 (d, J = 8.3 Hz, 2H), 6.79 (d, J = 8.7 Hz, 4H), 4.20 (s, 2H).

Synthesis of 1,3-bis(4-(bis(4-iodophenyl)amino)benzyl)-5-(tert-butyl)-1,3,5-triazinan-2-one

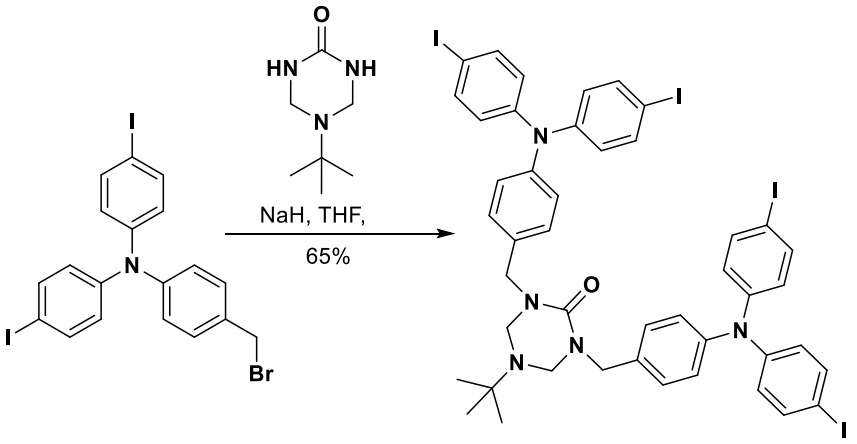

In an oven-dry round bottom flask, 5-(tert-butyl)-1,3,5-triazinan-2-one (0.274 g, 1.74 mmol, 1 equiv.) sodium hydride (0.214 g, 5.34 mmol, 3 equiv.) were added to 27 mL of dry tetrahydrofuran and the solution was stirred for 10 minutes. Then the previous bromide (2.12 g, 3.6 mmol, 2 equiv.) was dissolved in 27 mL of dry tetrahydrofuran and added to the reaction mixtures under the protection of N_2. The reaction mixture was heated at refluxed in the dark for 24 hours. After completion, the reaction mixture was cooled to room temperature and 8 mL of both 1N HCl and H_2O were added to quench the reaction. Then the organics were extracted with CH_2Cl_2 (3 x 80 mL) and washed with brine (1 x 80 mL) and dried over anhydrous $MgSO_4$. Then the solvent was reduced in rotary evaporation and the crude material was further purified by column chromatography using = Hexane: Ethyl Acetate as an eluent. The final product was obtained as a yellow solid (1.370 g, 65%). ^{1}H NMR (300 MHz, (CD3)2CO): δ (ppm) 7.59 (d, J = 8.3 Hz, 8H), 7.37 (d, J = 7.8 Hz, 4H), 7.06 (d, J = 7.8 Hz, 4H), 6.83 (d, J = 8.2 Hz, 8H), 4.51 (s, 4H), 4.33 (s, 4H), 1.00 (s, 9H). ^{13}C NMR (75 MHz, Chloroform-d) δ (ppm) 156.07, 147.03, 145.83, 138.26, 133.81,

129.76, 125.60, 125.04, 85.85, 61.60, 54.41, 48.30, 28.41. HRMS (ES): [M+] calculated 1175.9563; found: 1175.9552.

Synthesis of 1,3-bis(4-(bis(4-iodophenyl)amino)benzyl)urea

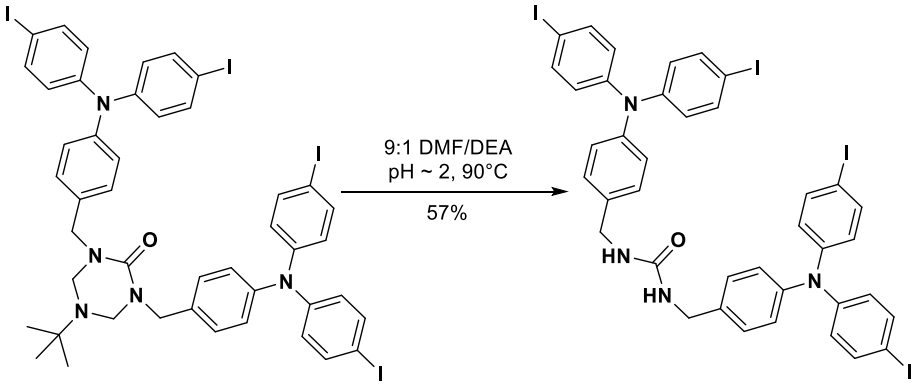

The protected urea from the previous step (0.284 g, 0.241 mmol) was suspended in mL of 9:1 mixture of dimethylformamide and diethanolamine while adjusting the pH at 2 using conc. HCl. Then the reaction was heated at 90°C for 2 days and readjust the pH for every 12 hours interval. After completion, the solution was cooled to room temperature and the the pH adjusted to neutral using $NaHCO_3$. Next, 200 mL of ice-cold H_2O was added and keep in the refrigerator for 2 hours. Then the precipitant was collected by suction filtration and dried under vacuum. The final product was obtained as a white solid (0.148 g, 57%). ^{1}H NMR (300 MHz, (CD_2Cl_2): δ (ppm) 7.52 (d, *J* = 8.8 Hz, 8H), 7.19 (d, *J* = 8.5 Hz, 4H), 7.01 (d, *J* = 8.5 Hz, 4H), 6.79 (d, *J* = 8.8 Hz, 8H), 4.71 (t, *J* = 5.8 Hz, 2H), 4.33 (d, *J* = 5.9 Hz, 4H). HRMS (ES): [M+] calculated 1078.8671; found: 1078.8672.

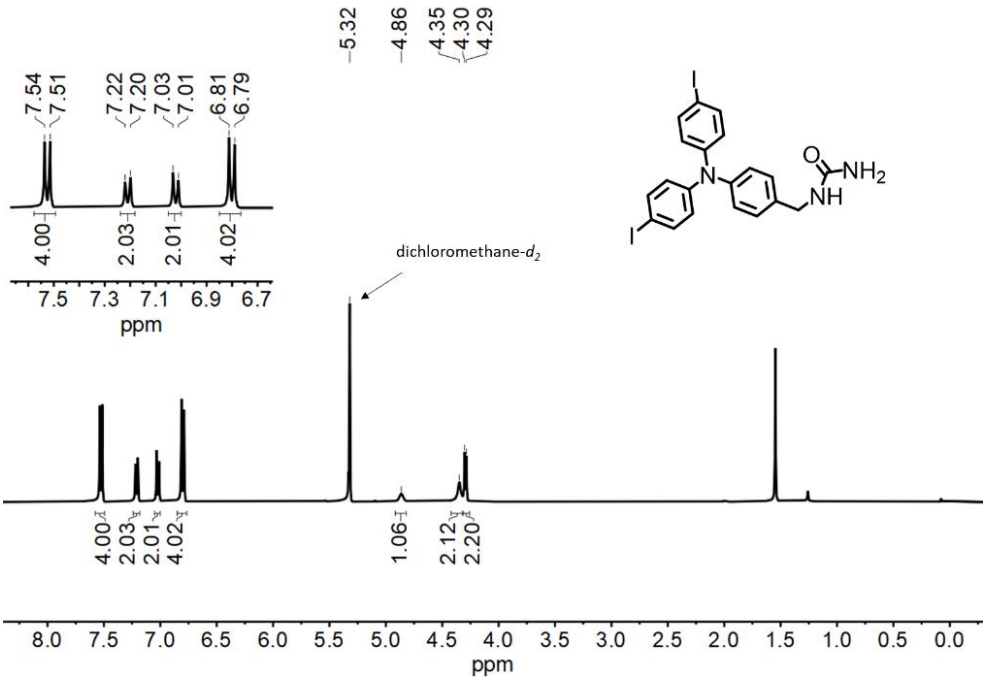

Figure 3.8. ^{1}H NMR (CD_2Cl_2, 300 MHz)

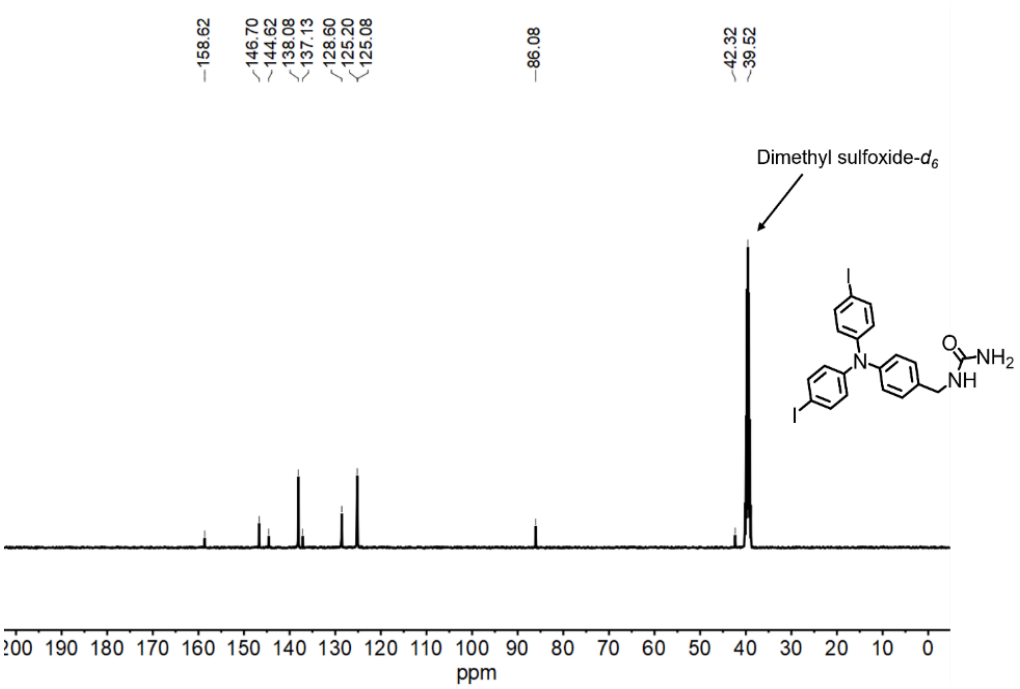

Figure 3.9. ^{13}C NMR ($(CD_3)_2SO$), 75 MHz)

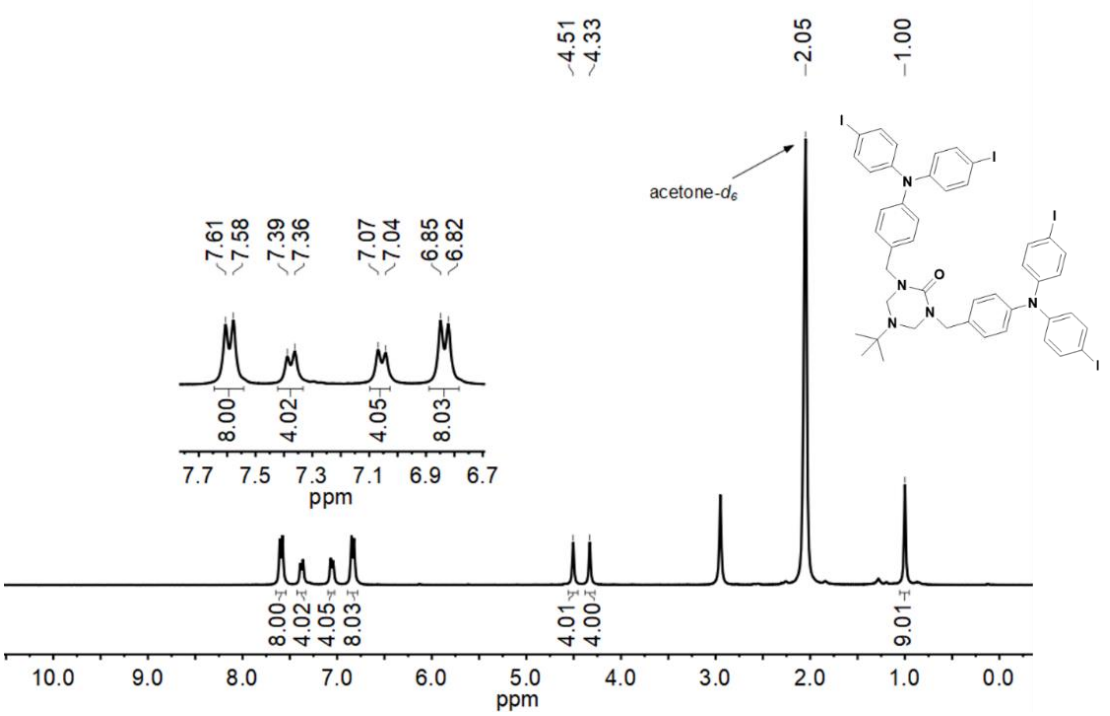

Figure 3.10. ^{1}H NMR ($(CD_3)_2CO$, 300 MHz)

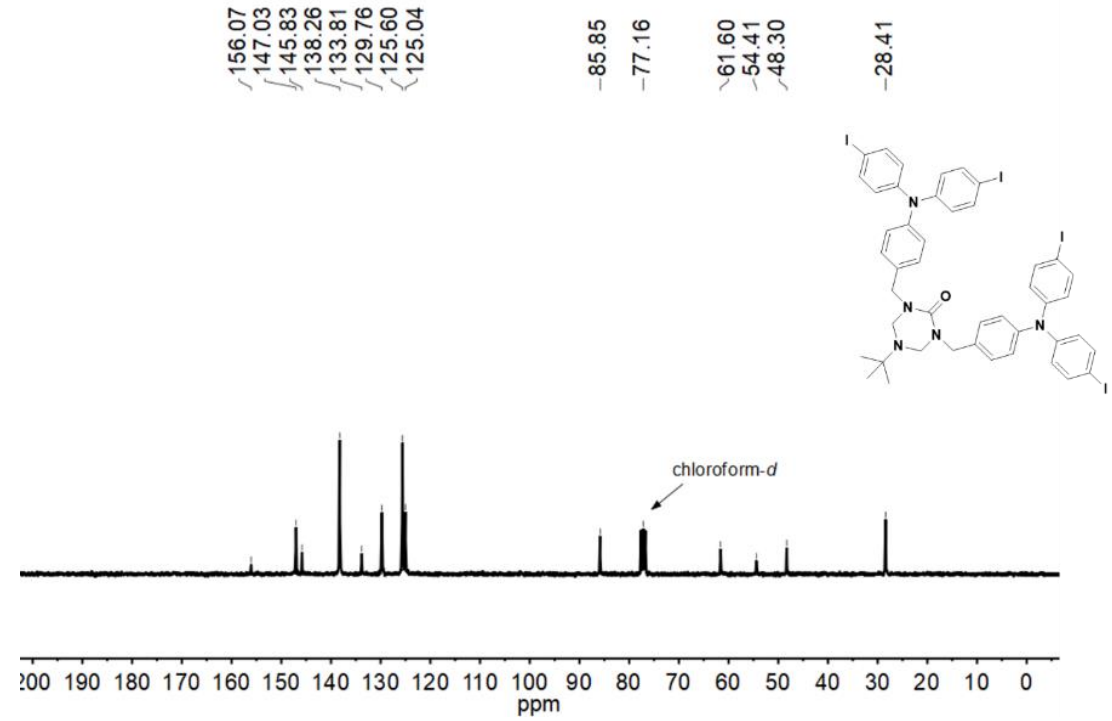

Figure 3.11. ^{13}C NMR ($CDCl_3$, 75 MHz)

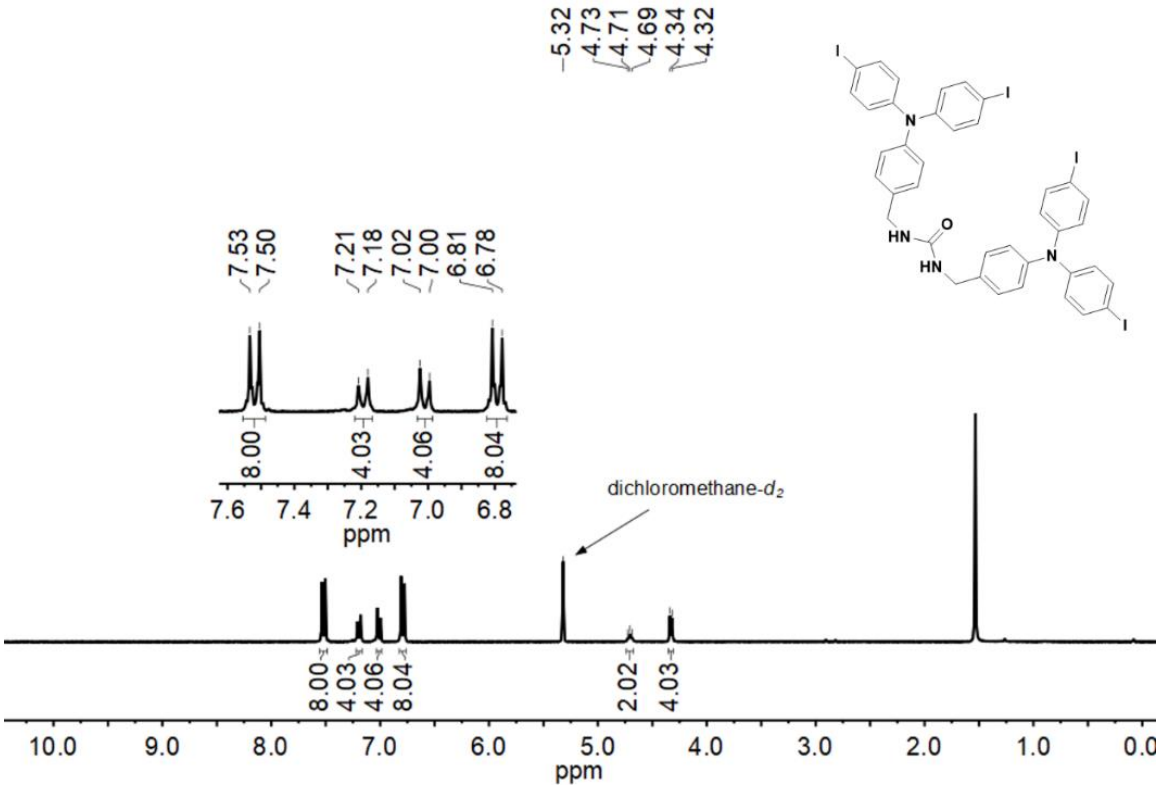

Figure 3.12. ^{1}H NMR (CD_2Cl_2, 300 MHz)

3.11 CRYSTAL DATA AND STRUCTURE REFINEMENT

Single Crystal X-Ray Diffraction (SC-XRD) for Structure Determination, $C_{39}H_{30}I_4N_4O\cdot(C_4H_8O_2)_{0.72(1)}$ (3)

X-ray intensity data from a colorless needle were collected at 100(2) K using a Bruker D8 QUEST diffractometer equipped with a PHOTON-100 CMOS area detector and an Incoatec microfocus source (Mo Kα radiation, λ = 0.71073 Å). The raw area detector data frames were reduced and corrected for absorption effects using the Bruker APEX3, SAINT+ and SADABS programs.[34,35] The structure was solved with SHELXT.[36] Subsequent difference Fourier calculations and full-matrix least-squares refinement against F^2 were performed with SHELXL-2018[37] using OLEX2.[38]

The compound crystallizes in the triclinic system. The space group *P*-1 (No. 2) was confirmed by structure solution. The asymmetric unit consists of half each of two crystallographically independent $C_{39}H_{30}I_4N_4O$ molecules and a region of disordered ethyl acetate (EtOAc) molecules. Both$C_{39}H_{30}I_4N_4O$ molecules are located on crystallographic inversion centers. The central urea group in each is inconsistent with centrosymmetry and

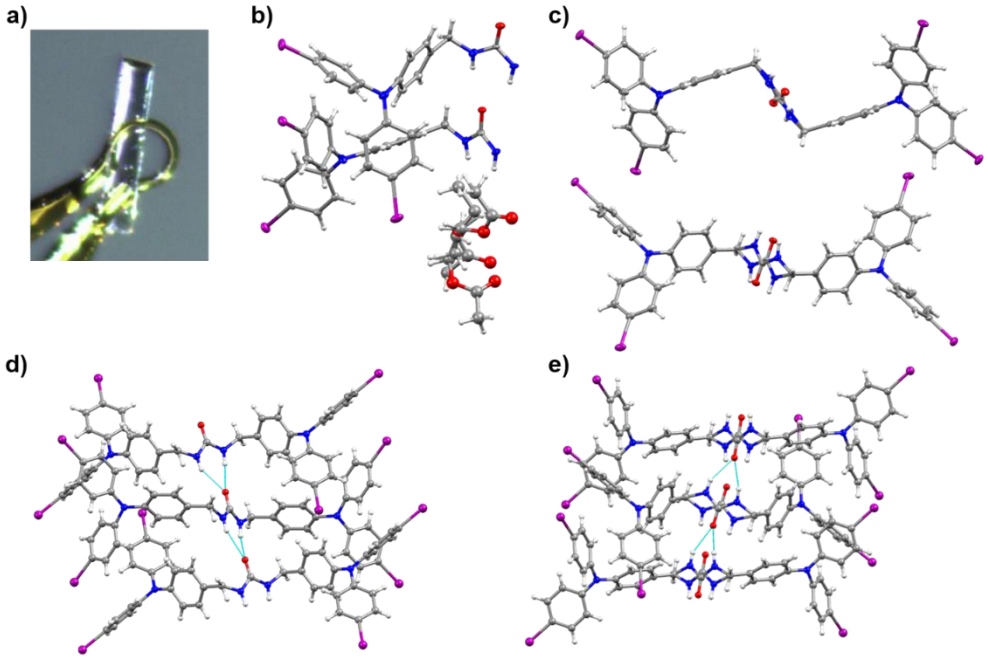

Figure 3.13. **a)** Data crystal **3** (ethyl acetate solvated) b) Asymmetric unit of the crystal. Displacement ellipsoid drawn at the 50% probability level. c) The urea group in each independent molecule is disordered across an inversion center. Each urea component is 50% occupied. Displacement ellipsoids drawn at the 50% probability level. d) Disorder model. Crystal consists of 50/50 disorder of chains with urea groups pointing "up" e) chains with urea groups pointing "down". The average throughout the crystal of the two is shown in the right image. Only the urea group atoms are affected; the remaining atoms of each molecule are common to the two urea components.

is therefore disordered across the inversion center in both independent molecules. Only the urea group atoms are disordered; the remainder of each molecule remains invariant regardless of urea group orientation. The disorder was also observed in the acentric space group *P*1 (No. 1) and therefore is not imposed by incorrectly high space group symmetry.

The urea group atoms (O1/N1/N2/C1 and O2/N4/N5/C21) were refined with half-occupancy. Similar C-N distance restraints (SHELX SADI) were applied, and the C=O distances were restrained to 1.20(1) Å. The EtOAc disorder was modeled using three independent molecular components of variable occupancy. All are further disordered about a crystallographic inversion center. Occupancies refined to 0.202(6), 0.269(5) and 0.251(5) for the three components. Appropriate 1,2- and 1,3- C-C and C-O distance restraints (DFIX) were applied to maintain reasonable EtOAc molecular geometries. All EtOAc carbon and oxygen atoms were refined with a common isotropic displacement parameter. All other non-hydrogen atoms were refined with anisotropic displacement parameters. Hydrogen atoms bonded to carbon were located in difference Fourier maps before being placed in geometrically idealized positions and included as riding atoms with *d*(C-H) = 0.95 Å and *U*iso(H) = 1.2*U*eq(C) for aromatic hydrogen atoms, *d*(C-H) = 0.96 Å and *U*iso(H) = 1.2*U*eq(C) for methylene hydrogen atoms and *d*(C-H) = 0.98 Å and *U*iso(H) = 1.5*U*eq(C) for methyl hydrogens. The largest residual electron density peak in the final difference map is 0.84 $e^-/Å^3$, located 0.92 Å from I2.

Single Crystal X-Ray Diffraction (SC-XRD) for Structure Determination, $C_{39}H_{30}I_4N_4O \cdot 2(CH_3OH)$ (3)

X-ray intensity data from a colorless plate were collected at 100(2) K using a Bruker D8 QUEST diffractometer equipped with a PHOTON-100 CMOS area detector and an Incoatec microfocus source (Mo Kα radiation, λ = 0.71073 Å). The raw area detector data frames were reduced and corrected for absorption effects using the Bruker APEX3, SAINT+ and SADABS programs. The structure was solved with SHELXT.

Subsequent difference Fourier calculations and full-matrix least-squares refinement against F^2 were performed with SHELXL-2018 using OLEX2.

The compound crystallizes in the triclinic system. The space group *P*-1 (No. 2) was confirmed by structure solution. The asymmetric unit consists of half each of two

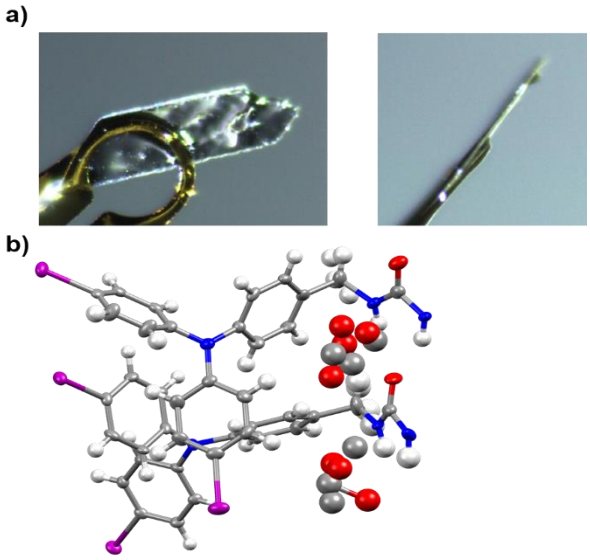

Figure 3.14. a) Data crystal **3** (methanol solvated). b) Asymmetric unit of the crystal. Displacement ellipsoid drawn at the 50% probability level.

crystallographically independent $C_{39}H_{30}I_4N_4O$ molecules and a region of severely disordered molecules which were modeled as methanol. Both $C_{39}H_{30}I_4N_4O$ molecules are located on crystallographic inversion centers. The central urea group in each is inconsistent with centrosymmetry and is therefore disordered across the inversion center in both independent molecules. Only the urea group atoms are disordered; the remainder of each molecule remains invariant regardless of urea group orientation. The disorder was also observed in the acentric space group *P*1 (No. 1) and therefore is not imposed by incorrectly high space group symmetry. The urea group atoms (O1/N1/N2/C1 and O2/N4/N5/C21) were refined with half-occupancy. Similar C-N distance restraints (SHELX SADI) were applied, and the C=O distances were restrained to 1.20(1) Å. The methanol disorder was

modeled using seven independent components of variable occupancy. Refined occupancies ranged from C1S/O1S = 0.460(9) to C7S/O7S = 0.16(1). Constraints were applied such that the sum of atomic occupancies of independent disorder components within van der Waals radii of each other was less than one. Methanol C-O distances were restrained to 1.45(1) Å using DFIX instructions. All methanol carbon and oxygen atoms were refined with a common isotropic displacement parameter. All other non-hydrogen atoms were refined with anisotropic displacement parameters. Hydrogen atoms bonded to carbon were located in difference Fourier maps before being placed in geometrically idealized positions and included as riding atoms with *d*(C-H) = 0.95 Å and *U*iso(H) = 1.2*U*eq(C) for aromatic hydrogen atoms and *d*(C-H) = 0.96 Å and *U*iso(H) = 1.2*U*eq(C) for methylene hydrogen atoms. No hydrogen atoms were located or calculated for the methanol species. The largest residual electron density peak in the final difference map is 1.01 $e^-/Å^3$, located 0.71 Å from I2.

X-Ray Structure Determination, $C_{20}H_{17}I_2N_3O$ (2)

X-ray intensity data from a colorless plate were collected at 100(2) K using a Bruker D8 QUEST diffractometer equipped with a PHOTON-II area detector and an Incoatec microfocus source (Mo Kα radiation, λ = 0.71073 Å). The raw area detector data frames were reduced, scaled and corrected for absorption effects using the Bruker APEX3, SAINT+ and SADABS programs.[1,2] The structure was solved with SHELXT.[3] Subsequent difference Fourier calculations and full-matrix least-squares refinement against F^2 were performed with SHELXL-2018[3] using OLEX2.[4]

The compound crystallizes in the triclinic system. The space group *P*-1 (No. 2) was confirmed by structure solution. The asymmetric unit consists of two crystallographically independent but chemically identical molecules. All non-hydrogen atoms were refined

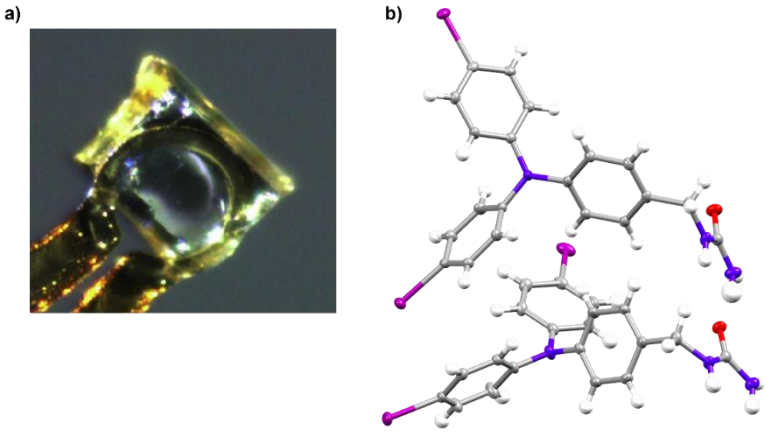

Figure 3.15. a) Data crystal 2. b) Asymmetric unit of the crystal. Displacement ellipsoids drawn at the 50% probability level. Twin crystallographically independent but chemically identical molecules.

with anisotropic displacement parameters. All hydrogen atoms were located in difference Fourier maps. Those bonded to carbon were placed in geometrically idealized positions and included as riding atoms with *d*(C-H) = 0.95 Å and *U*iso(H) = 1.2*U*eq(C) for arene hydrogen atoms and *d*(C-H) = 0.99 Å and *U*iso(H) = 1.2*U*eq(C) for methylene hydrogen atoms. Hydrogen atoms bonded to nitrogen were located and refined isotropically with *d*(N-H) = 0.86 Å distance restraints. The largest residual electron density peak in the final difference map is 0.95 $e^{-}/Å^{3}$, located 0.73 Å from I1.

Single Crystal X-Ray Diffraction (SC-XRD) for Structure Determination, $C_{39}H_{30}I_4N_4O\cdot(C_4H_8O_2)_{0.72(1)}$ (1)

X-ray intensity data from a pale yellow plate were collected at 100(2) K using a Bruker D8 QUEST diffractometer equipped with a PHOTON-II area detector and an Incoatec microfocus source (Mo Kα radiation, λ = 0.71073 Å). The raw area detector data

frames were reduced, scaled and corrected for absorption effects using the Bruker APEX3, SAINT+ and SADABS programs.[1,2] The structure was solved with SHELXT.[3] Subsequent difference Fourier calculations and full-matrix least-squares refinement against F^2 were performed with SHELXL-2018[3] using OLEX2.[4]

The compound crystallizes in the monoclinic system. The pattern of systematic absences in the intensity data was consistent with the space groups *Pc* and *P*2/*c*. The acentric group *Pc* was found by the solution program XT, and was confirmed by obtaining a reasonable and stable structural model. The space group choice was further verified with

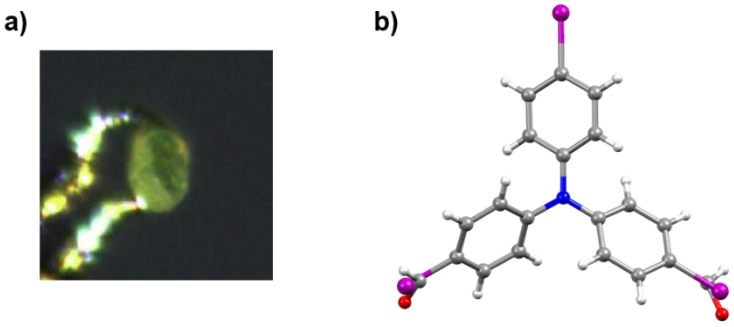

Figure 3.16. a) Data Crystal 1. b) disordered with the formyl group and iodines scrambled together on two separate sites.

ADDSYM, which found no missed symmetry elements.[5] A hypothetical non-disordered structure was used to enable the ADDSYM search. The asymmetric unit in *Pc* consists of one molecule. The structure is disordered, with the formyl group and iodine ligands I2 and I3 scrambled together on two separate sites. This was identified by observation of abnormally large iodine displacement parameters when I2 and I3 were refined with full occupancies, and also by difficulty in locating the formyl group atoms. Trial refinements of the I2 and I3 occupancies resulted in significant reduction from 100% along with a large decrease in *R*-values. Subsequently, difference Fourier peaks corresponding to formyl group carbon and oxygen atoms were observed near the partially occupied I2 and I3 sites.

The formyl group scrambled with I3 is further disordered over two orientations C20A/O2A and C20B/O2B. The occupancy of iodine site I1 refined to 100% iodine, and is not disordered with a formyl group. For the final cycles, *d*(C-C) = 1.47(2) Å and *d*(C-O) = 1.25(2) Å distance restraints were used. The disorder fractions at each substituent site refined to: I2/C19-O1 = 0.745(2)/0.255(2) and I3/C20A-O20A/C20B-O20B = 0.256(2)/0.342(3)/0.402(3). All non-hydrogen atoms were refined with anisotropic displacement parameters except for the disordered formyl group atoms (isotropic). Hydrogen atoms bonded to carbon were in general located in difference Fourier maps before being placed in geometrically idealized positions and included as riding atoms with *d*(C-H) = 0.95 Å and *U*iso(H) = 1.2*U*eq(C). The largest residual electron density peak in the final difference map is 0.94 $e^-/Å^3$, located 0.45 Å from H19. The absolute structure (Flack) parameter after the final refinement cycle was 0.019(11).

Table 3.2. X-ray structure refinement data

Empirical formula	$C_{41.89}H_{35.78}I_4N_4O_{2.44}$	$C_{41}H_{30}I_4N_4O_3$	C20H17I2N3O	C19H13I2NO
Formula weight	1141.92	1134.29	569.17	525.10
Temperature/K	100(2)	100(2)	100(2)	100(2)
Crystal system	triclinic	triclinic	triclinic	monoclinic
Space group	P-1	P-1	P-1	Pc
a/Å	9.5202(4)	9.4847(12)	9.4579(4)	9.7182(3)
b/Å	10.0356(4)	9.8569(13)	9.9193(4)	8.0639(2)
c/Å	23.9703(9)	23.787(3)	23.4761(9)	11.5611(3)
α/°	92.092(2)	91.327(3)	90.9100(10)	90
β/°	100.214(2)	100.187(3)	99.539(2)	107.3914(9)
γ/°	114.586(2)	114.405(3)	114.9540(10)	90
Volume/$Å^3$	2033.89(14)	1981.7(4)	1960.13(14)	864.59(4)
Z	2	2	4	2
$\rho_{calc}g/cm^3$	1.865	1.901	1.929	2.017
μ/mm^{-1}	3.106	3.188	3.223	3.641
F(000)	1093.0	1080.0	1088.0	496.0
Crystal size/mm^3	0.34 × 0.06 × 0.02	0.54 × 0.22 × 0.02	0.3 × 0.22 × 0.12	0.12 × 0.07 × 0.05
Radiation	MoKα (λ = 0.71073)	MoKα (λ = 0.71073)	MoKα (λ = 0.71073)	MoKα (λ = 0.71073)
2Θ range for data collection/°	4.498 to 52.798	4.564 to 53.404	4.55 to 66.376	4.392 to 56.576
Index ranges	-11 ≤ h ≤ 11, -12 ≤ k ≤ 11, -29 ≤ l ≤ 29	-11 ≤ h ≤ 11, -12 ≤ k ≤ 12, -29 ≤ l ≤ 30	-14 ≤ h ≤ 14, -15 ≤ k ≤ 15, -36 ≤ l ≤ 36	-12 ≤ h ≤ 12, -10 ≤ k ≤ 10, -15 ≤ l ≤ 15
Reflections collected	46016	39928	76938	24434
Independent reflections	8313 [R_{int} = 0.0452, R_{sigma} = 0.0303]	8311 [R_{int} = 0.0637, R_{sigma} = 0.0474]	14982 [R_{int} = 0.0437, R_{sigma} = 0.0358]	4193 [R_{int} = 0.0280, R_{sigma} = 0.0213]
Data/restraints/parameters	8313/50/528	8311/35/517	14982/6/494	4193/11/225
Goodness-of-fit on F^2	1.242	1.035	1.021	1.160
Final R indexes [I>=2σ (I)]	R_1 = 0.0362, wR_2 = 0.0745	R_1 = 0.0373, wR_2 = 0.0721	R_1 = 0.0275, wR_2 = 0.0512	R_1 = 0.0275, wR_2 = 0.0644
Final R indexes [all data]	R_1 = 0.0455, wR_2 = 0.0771	R_1 = 0.0610, wR_2 = 0.0818	R_1 = 0.0442, wR_2 = 0.0553	R_1 = 0.0296, wR_2 = 0.0662
Largest diff. peak/hole / e $Å^{-3}$	0.83/-0.68	1.01/-1.03	0.95/-1.08	0.95/-0.76

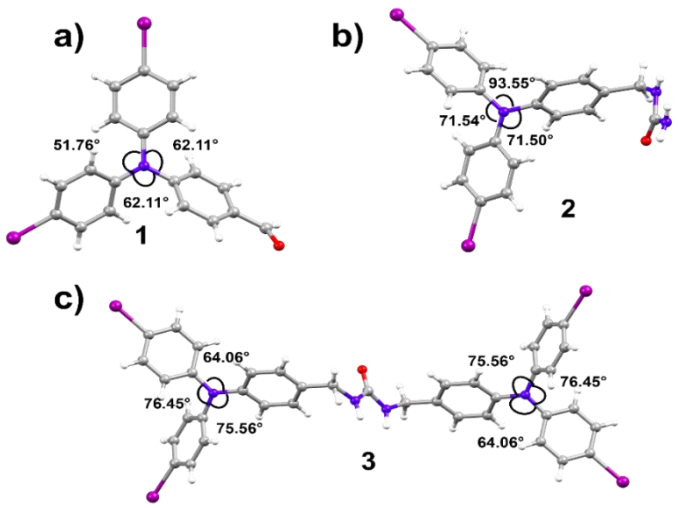

Figure 3.17. Structure and orientation of TPA unit. a) propeller conformations of TPA unit for **1**. b) propeller conformations of TPA unit for **2**. C) chiral propeller conformation of TPA unit for **3**. Symmetric orientation observed on both side of the TPA units.

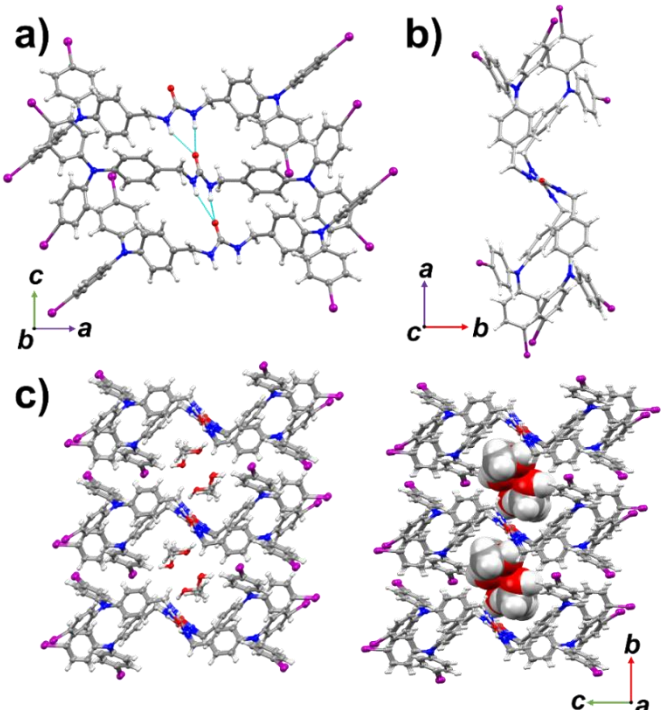

Figure 3.18. Views from the urea tethered solvated crystal of **3**. a) side view of crystal **3** showing hydrogen bonded urea tape. b) urea chains formed a skewed shape if viewed along crystallographic *c* – axis. c) H-bonded urea chains encapsulate solvent (methanol shown left). Methanol solvent in spacefill model (right).

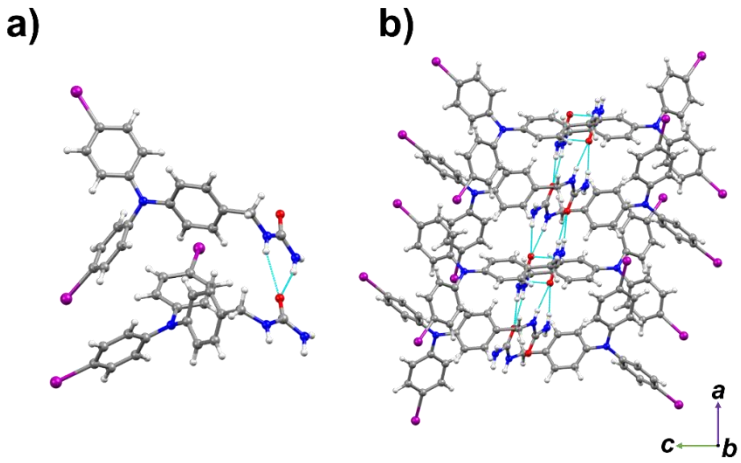

Figure 3.19. Views from the X-ray structure of **2**. a) Assembly through hydrogen bonded urea tape. b) Inter-chain H-bonds links two strands (side view).

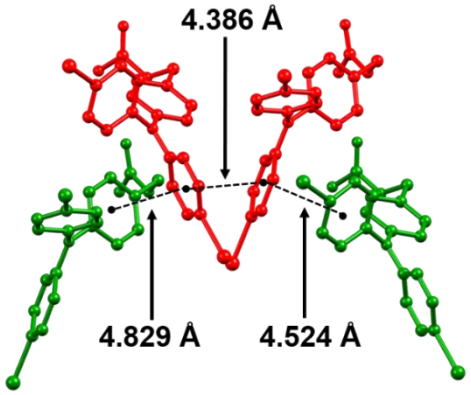

Figure 3.20. Views of the packing of **3** showing face-to-face π-stacking metrics between different TPA units. Distances were measured between phenyl ring centroids. Symmetry equivalent TPA units are colored either red or green. Guest molecules, hydrogen atoms, and non-relevant parts of the structure were removed for

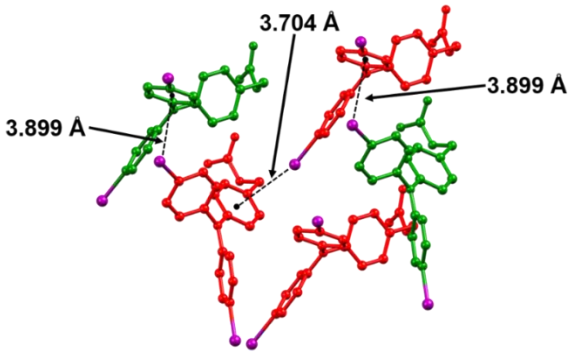

Figure 3.21. Views of the packing **3** showing halogen C-I···π interactions between different TPA units. Distances were measured from the phenyl ring centroids to the covalently bonded iodine. Symmetry equivalent TPA units either colored red or green. Guest molecules, hydrogen atoms, and non-relevant parts of the structure were removed for clarity.

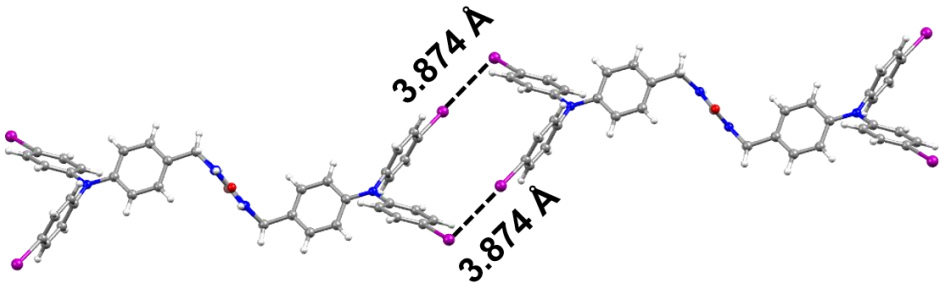

Figure 3.22. Views of packed **3** showing an I···I interaction (halogen bond) with neighbouring TPA. The I···I distance of 3.874 Å less than sum of iodine van der Waals radii (3.96 Å). This halogen bond assists in holding the column together.

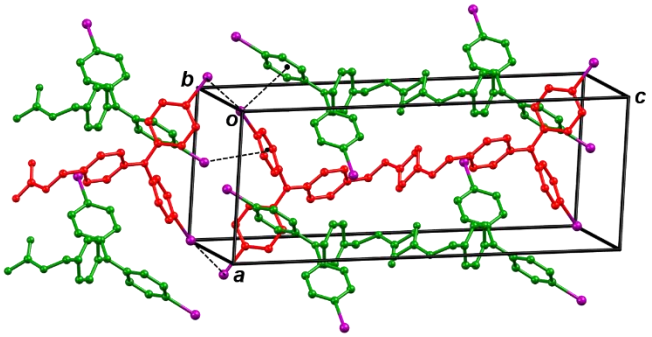

Figure 3.23. Unit cell of 2. Symmetry equivalent TPA units either colored red or green.

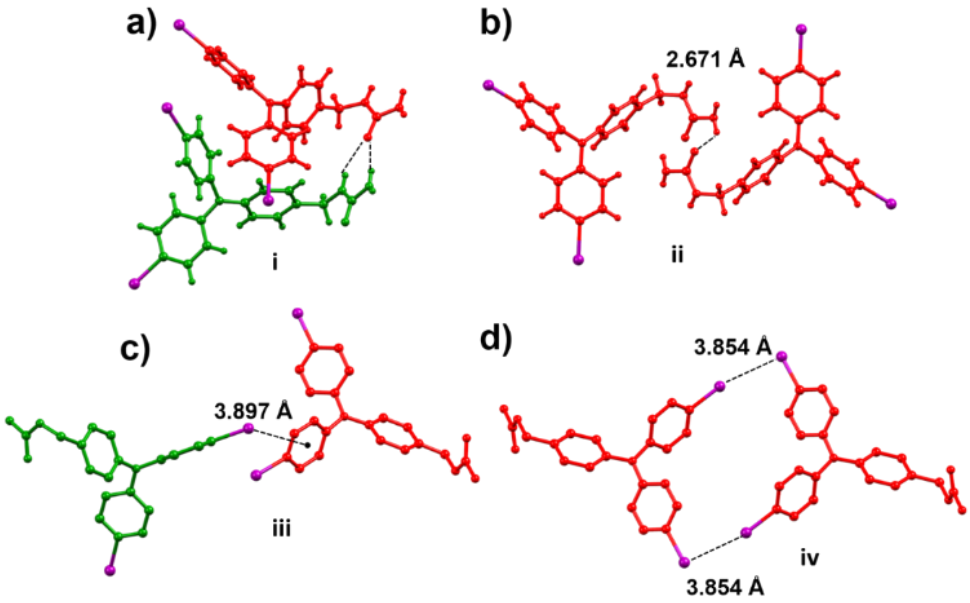

Figure 3.24. Dimer model of 2. Symmetry equivalent TPA units either colored red or green.

3.12 PHOTOPHYSICAL MEASUREMENT

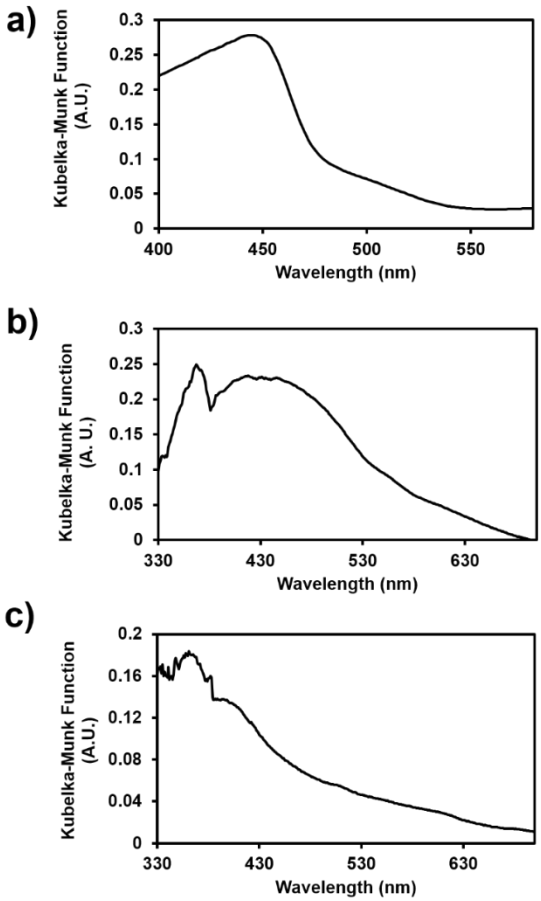

Figure 3.25. Diffuse reflectance experiments performed in bulk crystals. a) Diffuse reflectance spectra of **1**. b) Diffuse reflectance spectra of **2**. c) Diffuse reflectance spectra of **3**.

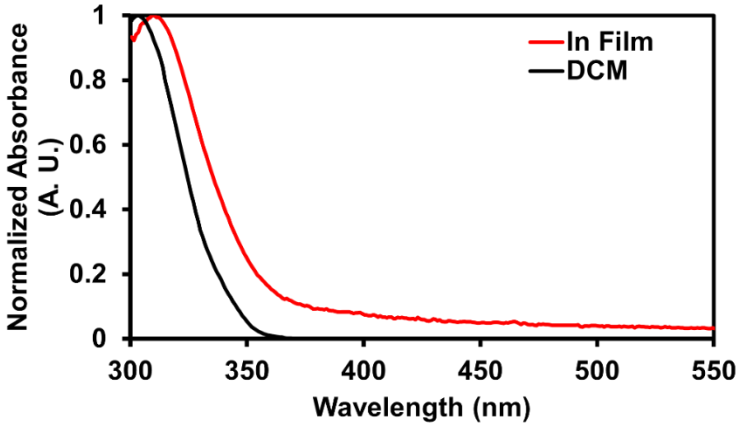

Figure 3.26. UV-vis absorption spectrum of **3** in dry methylene chloride (10 μm) (inset black) and in thin film (inset red).

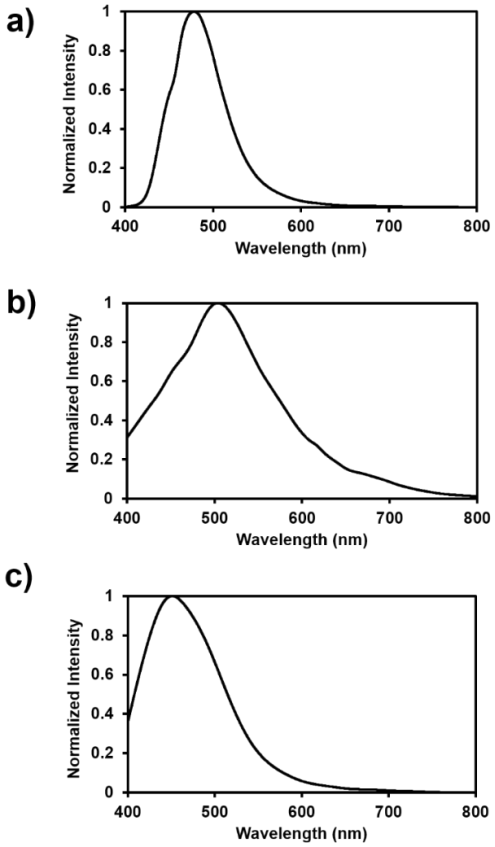

Figure 3.27. Normalized emission spectra of single crystal for compound (a) **1**, (b) **2**, (c) **3**. A 375 nm laser source was used for excitation.

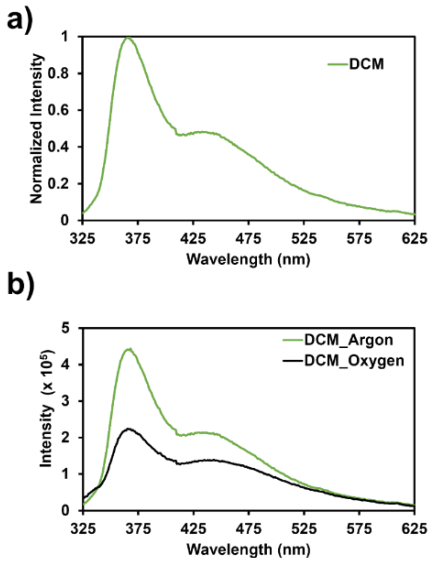

Figure 3.28. UV-vis emission spectrum of **3** in methylene chloride using 300 nm excitation source. a) UV-vis emission spectrum of **3** in dry methylene chloride (10 µM). b) comparison of UV-vis emission spectrum of **3** in dry CH_2Cl_2 (10 µM). (argon purged, inset green) and in CH_2Cl_2 (10 µM) (oxygen purged, inset black).

3.13 CONDUCTIVITY EXPERIMENTS IN SINGLE CRYSTAL

Single crystal was placed on a PMMA coated SiO_2/Si substrate. A gold wire was carefully aligned perpendicular on top of crystal that acted as shadow mask while depositing gold contacts through ebeam evaporation technique. A 100 nm thick gold top contact was deposited at a rate of 2 Å/s. Finally, gold wire and shadow mask were removed, and the device was measured for electrical conductance. There was negligible current while parking the probes on gold pads this mean crystal was not making good electrical contact with them. However, a significant current was observed when measured on top of crystal. Experiment was performed under dark at room temperature.

As an example of conductivity measure in a single crystal of 3

Sample height (thickness) estimated through focusing stage 0.001" = 25.4 μm

Length estimated at 100x resolution = 25 μm

width estimated at 100x resolution = 77 μm

Current 1.1×10^{-10} Amps at 10 V bias

$$\rho = R.\frac{A}{L} = \frac{V}{I}.\frac{A}{L} \qquad (3.1)$$

$\rho=(10/1.1\times10^{-10}) \text{ x } (77 \times 10^{-6} \text{x } 25.4\times10^{-6} / 25\times10^{-6})$

ρ =7112000 Ωm=711200000 Ω.cm

Conductivity = 1.41 x 10^{-9} S/cm

Table 3.3. Conductivity measurement of the single crystal **2**.

Trials #	σ (S/cm)	Length (μm)	Width (μm)	Thickness (μm)
1	6.44E-07	94	239.361	50.8
2	5.4E-07	25	186.16	76
3	2.93E-10	25	405.92	10

Table 3.4. Conductivity measurement of the single crystal **3**.

Trials #	σ (S/cm)	Length (μm)	Width (μm)	Thickness (μm)
1	1.41E-09	25	77	25.4
2	1.77E-08	25	72.48	5
3	1.65E-08	25	75.92	5

Table 3.5. Conductivity measurement of the single crystal **3** at time interval upon UV irradiation using 365 nm light source.

Time (hr)	σ (S/cm)
0	1.65E-08
0.25	1.36E-08
1	9.29E-09
1.5	8.65E-09
2	7.73E-09
3	6.95E-09
4	5.81E-09
5	5.12E-09

Table 3.6. Conductivity measurement of the single crystal of **2** at time interval upon UV irradiation using 365 nm light source

Time (hr)	σ (S/cm)
0	5.39703E-07
0.25	4.00614E-07
0.5	3.86511E-07
0.75	3.85421E-07
1	3.80966E-07
2	3.7467E-07
3	3.62037E-07
4	3.58721E-07
5	3.60915E-07

Table 3.7. Conductivity measurement of the single crystal of **3** in dark after 5 hours of UV irradiation

Time (hr)	σ (S/cm)
0	5.12E-09
0.25	5.99992E-09
0.5	6.1609E-09
0.75	6.16943E-09
1	6.16341E-09
2	5.92247E-09

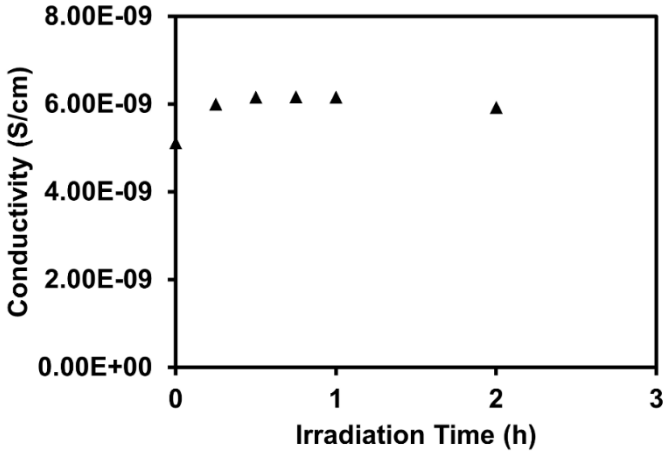

Figure 3.29. Electrical conductivity measurement at time interval in dark at room temperature of single crystals of **3** after 5 hours of UV irradiation

3.14 EPR STUDIES

Table 3.8. Measured Current of LED photoreactor for photon flux calculations.

Sample	Measured Current (amps)
Background	4.1×10^{-11}
LED 1	2.13×10^{-6}
LED 2	2.29×10^{-6}
LED 3	2.25×10^{-6}
LED 4	2.04×10^{-6}
LED 5	2.40×10^{-6}
Average	2.22×10^{-6}
Background subtracted average	2.22×10^{-6}
Multiplied by number of LEDs in photoreactor (120)	2.67×10^{-4}

The current for single LEDs from the LED strip were measured at the same distance from the photodiode as the sample distance in the photoreactor (3.5 cm). The average current measured for 5 LEDs was background subtracted from ambient light and multiplied by the number of LEDs in the photoreactor (120). Division of this current value by the responsivity of the photodiode used (0.05 amps/watt at 365 nm) gives the power of the LED strip in watts at the sample distance in the photoreactor (5.33×10^{-3}).

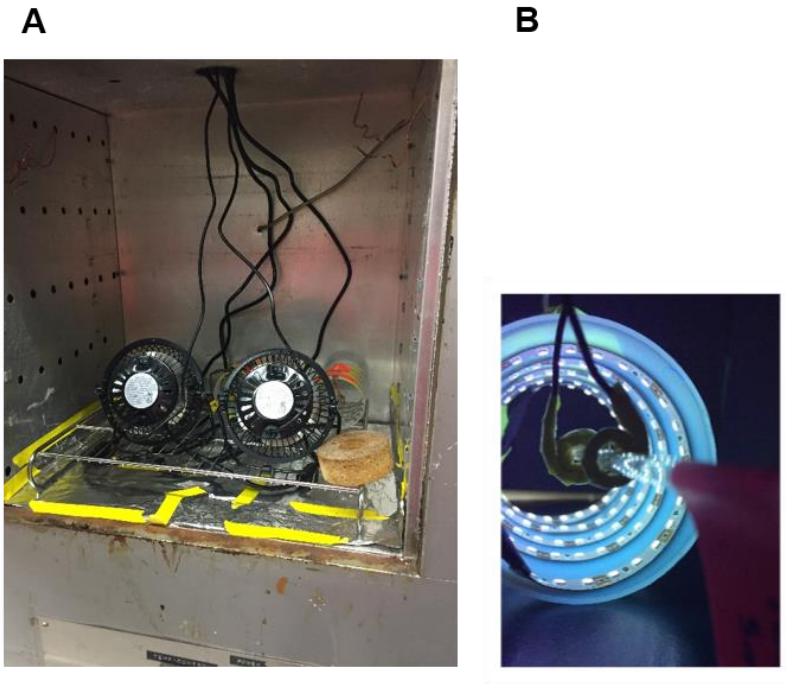

Figure 3.30. Photoreactor used in maximum radical concentration studies. A) View of set-up showing two fans facing the three cylindrical photoreactors. B) View of one cylindrical photoreactor comprised of a wash bottle that was cut open at both ends with a Waveform Lighting real UV LED strip wrapped along the interior of the cylinder.

Solving for E in the equation for photon energy ($E = \frac{hc}{\lambda}$) with λ = 365 nm, gives a photon energy value of 5.45×10^{-19} J. Division of the measured wattage by the photon energy gives a photon flux value of 9.78×10^{15} photons/second delivered to the sample for all persistent radical studies.

Details of EPR experiment

For the measurement dried triply recrystallized samples were loaded in the quartz EPR tubes under argon (g) at room temperature and irradiated using 365 nm UV LEDs (9.78 X 10^{15} photons/s). Then the pre and post-UV irradiated EPR spectra at room temperature were compared. The EPR spectra were continuously monitored upon periodic 2 hours of UV irradiation while we observe no changes in the line shape or the width of

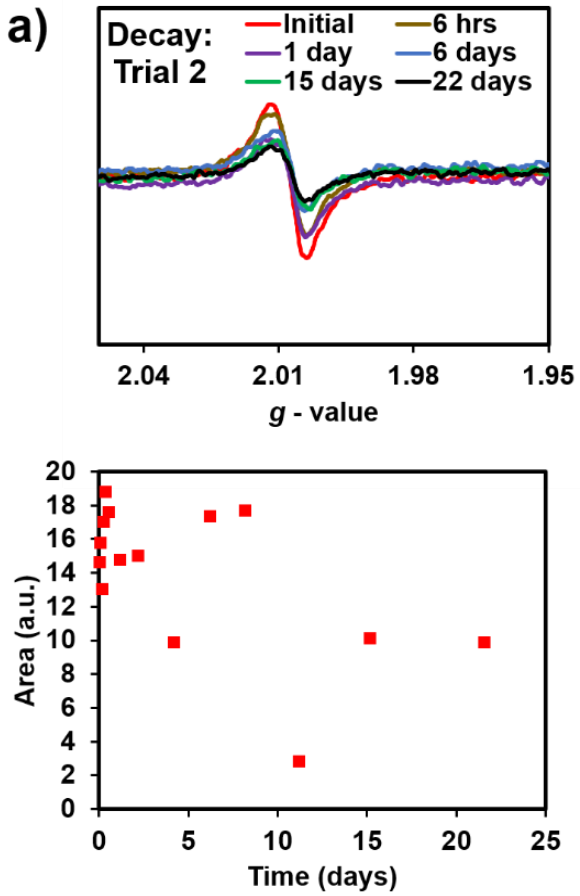

Figure 3.31. EPR data for **3**. EPR spectra over time (top) by keeping the UV irradiated sample under dark under the protection of argon. EPR spectra were doubly integrated to obtain the area plotted vs the time under dark (bottom)

the spectra further suggest the stability of the crystals. Then the radical concentration was approximated by comparing the area of the EPR spectra with a calibration curve of standard

concentration of magic blue in dry methylene chloride (Figure SX). We continuously monitored the EPR spectra until observe a plateau in the radical concentration. From this comparison, the estimated radical concentration was 0.11% and 0.12% for two different trials of 3 using 8.1 mg and 7.7 mg of crystals. Next, the stability of the radical was estimated by dark decay study while keeping the sample in dark under argon (g) and monitored by EPR spectra over time.

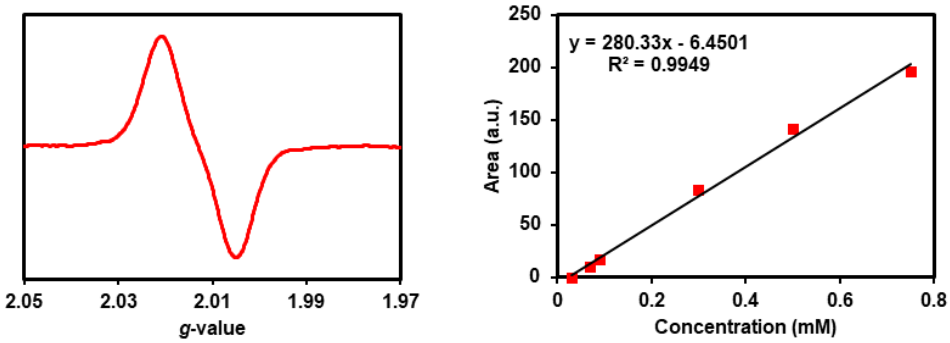

Figure 3.32. EPR data to determine the radical concentration using the calibration curve of magic blue. EPR spectra for 1 mM solution of magic blue in degassed dry dichloromethane (left) and calibration curve (right).

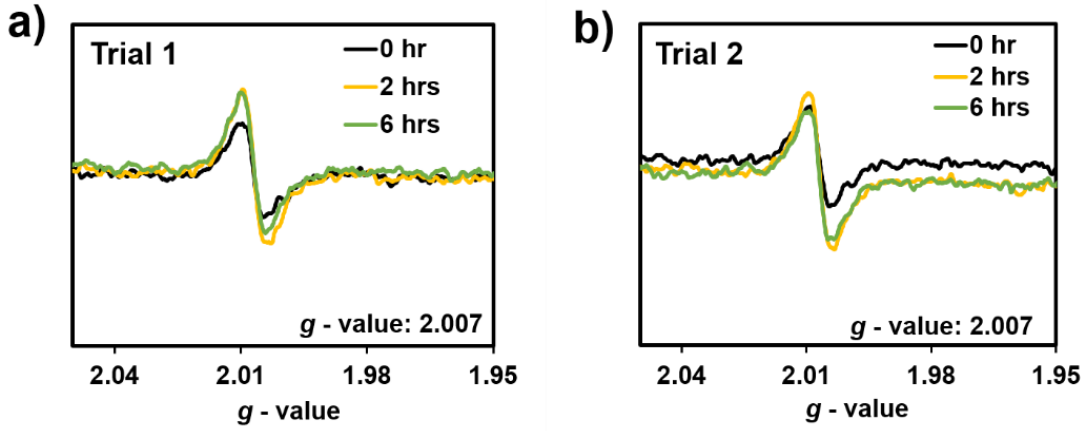

Figure 3.33. EPR data for the urea tethered **2**. EPR spectra over time of UV irradiation.) Trial 1: EPR spectra for triply recrystallized 6.4 mg of **2**. b) Trial 2: EPR spectra for triply recrystallized 6.1 mg of **2**. UV irradiation was performed using 365 nm UV LED source.

3

3.15 COMPUTATIONAL DETAILS

For the Simulation of Absorption Spectra in Solution

Polarizable Continuum Model (PCM): The implicit solvation model PCM were used to

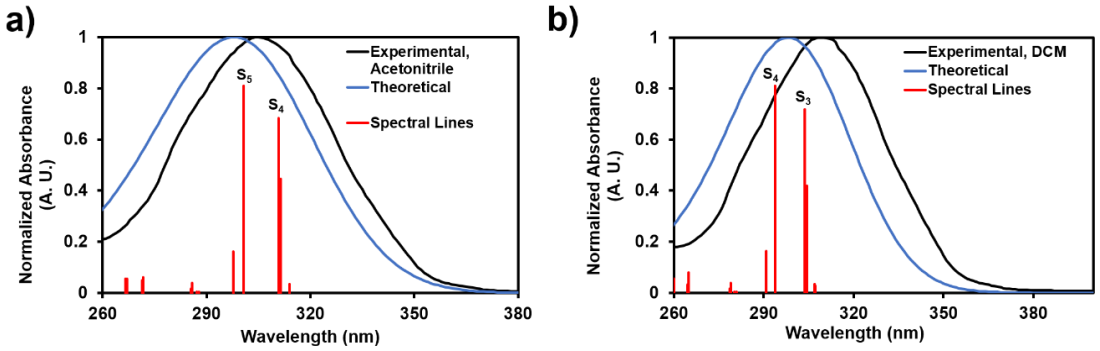

Figure 3.34. PCM solvation model to simulate the experimental absorption spectra of **3** in solution. a) Experimental absorption spectrum in acetonitrile. (inset black), theoretical absorption spectrum in acetonitrile (inset blue) and corresponding spectral lines (inset red). b) Experimental absorption spectrum in methylene chloride. (inset black), theoretical absorption spectrum in methylene chloride (inset blue) and corresponding spectral lines (inset red).

describe the effects of solvent dichloromethane (DCM), and acetonitrile on the absorption and structural properties of compound **3**. For this purpose, the ground-state geometry of **3** were optimized by using wB97X-D[39]/LANL2DZdp methods in gas phase to avoid convergence error due to the presence of diffuse functions. The obtained geometry considered as energy minimum as corresponding frequency analysis did not provide any negative values. TD-DFT were applied to simulate the absorption spectra of methylene chloride and acetonitrile (using the ground state geometry) utilizing CAM-B3LYP/LANL2DZddp methods. 25 excited states were sufficient to reproduce the absorption spectra similar to the experimental absorption spectra. Only a shift of 7 nm and 11 nm was observed for acetonitrile and methylene chloride simulated absorption spectrum compared with experimental absorption spectrum. These reproducible results suggest the

utilization of CAM-B3LYP/LANL2DZdp methods should be suitable to describe the electronic structure of these urea tethered iodinated derivatives.

Table 3.9. Optimized geometry of **3** using ωB97X-D /LANL2DZdp Methods in the gas phase

Atom	X (Å)	Y (Å)	Z (Å)
I	1.9251733	7.3622759	2.2067721
I	-5.3216789	-0.6963784	1.7364714
O	0.9032877	3.717482	11.940059
N	-1.145643	4.1173248	12.878764
H	-1.9558781	3.6279478	13.236487
N	-0.7987445	2.2104713	11.596228
H	-1.8072995	2.1900304	11.499612
N	-1.2583447	2.7525937	5.1243779
C	-0.2565949	3.3702223	12.123491
C	-0.0557742	1.4479379	10.603125
H	-0.2291883	0.3788578	10.778129
H	1.0046491	1.6490869	10.793307
C	-0.4026736	1.7926899	9.1679823
C	-0.4265451	3.1259484	8.7320857
H	-0.2032677	3.9265326	9.435932
C	-0.7274862	3.44214	7.4114194
H	-0.7502624	4.4824038	7.0936256
C	-0.9823849	2.4260069	6.4760138
C	-0.9525542	1.0920432	6.9015791
H	-1.1479044	0.293174	6.1896684
C	-0.6810914	0.7882948	8.2365624
H	-0.6684067	-0.2560285	8.5495061
C	-0.5365483	3.7882603	4.4831256
C	0.8343043	3.9657816	4.7177846
H	1.3566207	3.3024222	5.4034048
C	1.5357398	4.9891799	4.0805843
H	2.598827	5.1135395	4.2748337
C	0.8734134	5.8338862	3.185016
C	-0.4921948	5.6621613	2.9373464
H	-1.0178507	6.3184869	2.2475919
C	-1.1920022	4.651672	3.593303
H	-2.2566364	4.5250758	3.4090477
C	-2.1704983	1.9762218	4.3713557
C	-1.8663403	1.6074379	3.0530138
H	-0.9202113	1.9145028	2.6131848
C	-2.766007	0.856629	2.2990603

H	-2.5114333	0.581653	1.2785231
C	-3.9767043	0.4482806	2.8655167
C	-4.2883088	0.8002641	4.1832598
H	-5.2309437	0.4900246	4.6296084
C	-3.3920875	1.5673306	4.9265891
H	-3.6392725	1.8490784	5.9478171
I	-0.3396464	0.9476589	23.210891
I	8.8507848	3.6247678	18.0051
N	2.5406457	3.5924696	18.252403
C	-0.6226625	5.1915072	13.708555
H	-0.0172896	5.8449882	13.071999
H	-1.4831339	5.7784036	14.054943
C	0.2128945	4.7450382	14.896557
C	-0.1126511	3.6052152	15.638936
H	-0.9608742	2.9847942	15.350148
C	0.6535378	3.2150658	16.73545
H	0.3951387	2.3137574	17.28696
C	1.7576384	3.9806432	17.133713
C	2.0833415	5.1321355	16.404394
H	2.942597	5.7308129	16.699452
C	1.3257729	5.4944836	15.292435
H	1.6104738	6.3774116	14.720916
C	1.9112408	3.0118469	19.37854
C	0.7349267	3.571433	19.898753
H	0.3171149	4.4651945	19.440562
C	0.0931708	2.9881069	20.990008
H	-0.8208248	3.4333085	21.376584
C	0.6347316	1.8444808	21.585834
C	1.8162139	1.2877395	21.087689
H	2.243155	0.3955571	21.539732
C	2.4433969	1.8644935	19.9845
H	3.3531242	1.4183647	19.589136
C	3.9527843	3.6130208	18.174242
C	4.7089057	3.9598004	19.304094
H	4.2017726	4.2259475	20.228897
C	6.1005795	3.9583789	19.255224
H	6.6695327	4.2252637	20.142957
C	6.7542196	3.6296632	18.06283
C	6.0127714	3.3017823	16.924097
H	6.5110929	3.0408667	15.992755
C	4.6187815	3.2864735	16.984138
H	4.0453741	3.0168606	16.100057

Simulation of diffuse reflectance and details of electronic structure calculation

TD-DFT were used to analyze the electronic excitations. All calculations were performed using Q-Chem 5.3[40] and Spartan18[41]. Basis set exchange were used for the selected bases.[42] SC-XRD data (positions of heavy atoms) were used to perform the calculations in gas phase. B3LYP-D3[43]/6-31G*[44] level theory was used to optimize the positions of all hydrogen atoms. The TD-DFT calculations are based on CAM-B3LYP functional paired with the effective core potential basis LANL2DZdp. CAM-B3LYP is a hybrid exchange-correlation functional that combines the long-range correction (Coulomb Attenuation Method) with the popular hybrid functional B3LYP for better description of the charge-transfer excited states. The results obtained with CAM-B3LYP functional are reported in Tables 3.10-12. The theoretical UV-vis spectra were generated as sums of Gaussian functions broadening of the spectral lines as given by equation 3.2.

$$g(x) = \sqrt{\frac{1}{\pi\sigma^2}} \sum_{\mathrm{n}} f_n \, \mathrm{e}^{-\frac{(x-x_n)^2}{\sigma^2}} \qquad (3.2)$$

In eqn (1), f_n and x_n stands for the oscillator strength and the position of the nth line (in nm) respectively; x represents the energy variable in nm. The broad feature of the experimental spectra was matched by standard deviation parameter σ set to 25. The frontier molecular orbitals (HOMO, LUMO) and the natural transition orbitals (HONTO, LUNTO) were visualized using IQmol v2.14.0 with isovalue 0.04.

Table 3.10. Excited state transitions of hydrogen bonded dimer of **3** in the gas phase using CAM-B3LYP/LANL2DZdp methods implemented in TD-DFT. SC-XRD data of **3** were used as coordinates of heavy atoms. The energies were scaled by multiplying with 0.829 which were used to assign the spectral lines shown in Figure 3.7.

State	Energy (nm)	Oscillator Strength (f_{osc})
S_1	484	5.07E-07
S_2	482	1.5E-07
S_3	477	2.27E-06
S_4	476	4.93E-08
S_5	471	1.88E-07
S_6	466	1.16E-06
S_7	462	5.3E-07
S_8	457	5.65E-08
S_9	425	3.96E-08
S_{10}	423	5.28E-07
S_{11}	423	8.29E-07
S_{12}	422	2.37E-06
S_{13}	419	2.82E-07
S_{14}	412	2.24E-08
S_{15}	400	6.62E-08
S_{16}	399	7.89E-07
S_{17}	381	1.02E-07
S_{18}	377	9.14E-07
S_{19}	375	1.17E-07
S_{20}	374	8.38E-07
S_{21}	374	5.2E-06
S_{22}	373	4.02E-06
S_{23}	373	2.19E-06
S_{24}	372	0.088529
S_{25}	367	1.7E-06
S_{26}	365	8.01E-07
S_{27}	364	6.48E-05
S_{28}	363	5.03E-05
S_{29}	363	0.055991
S_{30}	361	0.203067

Table 3.11. Excited state transitions of hydrogen bonded dimer of **2** in the gas phase using CAM-B3LYP/LANL2DZdp methods implemented in TD-DFT. SC-XRD data of **2** were used as coordinates of heavy atoms. The energies were scaled by multiplying with 0.763 which were used to assign the spectral lines shown in Figure 3.7.

State	Energy (nm)	Oscillator Strength (f_{osc})
S_1	532	9.42E-08
S_2	520	4.91E-07
S_3	516	1.04E-07
S_4	507	5.86E-08
S_5	464	2.98E-07
S_6	462	5.54E-07
S_7	449	3.4E-09
S_8	432	6.78E-08
S_9	414	4.3E-09
S_{10}	413	2.24E-08
S_{11}	406	1.49E-07
S_{12}	405	2.28E-07
S_{13}	404	2.63E-07
S_{14}	403	0.10691
S_{15}	398	1.74E-08
S_{16}	396	2.45E-08
S_{17}	394	0.166528
S_{18}	387	0.061611
S_{19}	383	4.64E-07
S_{20}	380	3.84E-08
S_{21}	372	0.000143
S_{22}	371	8.25E-07
S_{23}	371	0.241359
S_{24}	370	0.000555
S_{25}	369	0.126994
S_{26}	368	0.105731
S_{27}	367	0.390429
S_{28}	366	1.01E-06
S_{29}	364	9.73E-06
S_{30}	363	0.127813

Table 3.12. Excited state transitions of dimer of **1** in the gas phase using CAM-B3LYP/LANL2DZdp methods implemented in TD-DFT. SC-XRD data of **1** were used as coordinates of heavy atoms. The energies were scaled by multiplying with 0.730 which were used to assign the spectral lines shown in Figure 3.7.

State	Energy (nm)	Oscillator Strength (f_{osc})
S_1	633	2.5E-07
S_2	625	3.32E-07
S_3	567	9.31E-07
S_4	565	3.3E-07
S_5	551	5.4E-09
S_6	551	2.82E-08
S_7	501	1.27E-06
S_8	499	7.2E-07
S_9	463	9.45E-08
S_{10}	462	0.001847
S_{11}	462	0.001399
S_{12}	459	1.86E-07
S_{13}	455	0.213675
S_{14}	445	0.690742
S_{15}	423	1.16E-07
S_{16}	423	6.8E-08
S_{17}	417	1.19E-07
S_{18}	415	2.79E-07
S_{19}	415	0.024467
S_{20}	413	9.72E-08

3.16 NMR SPECTRA PRE AND POST UV

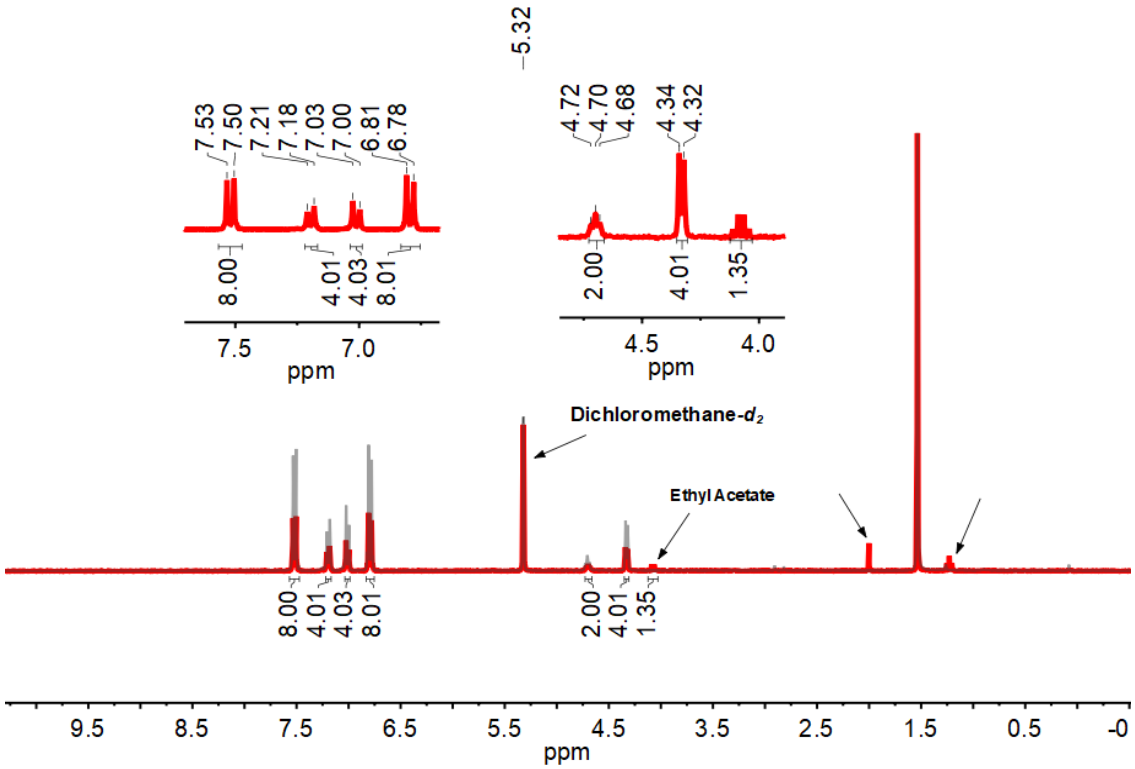

Figure 3.35. ^{1}H NMR spectra of compound **3** after EPR studies (CD_2Cl_2-d_2, 300 MHz) (red). ^{1}H NMR spectra of freshly synthesized compound **3** (black). EPR sample were dissolved in NMR solvent prior measurement. Integrals and peaks are the for the **3** after EPR experiments. No changes were observed after EPR experiments. We observe the presence of encapsulate ethyl acetate with a host-guest ratio 3: ethyl acetate = 1 : 0.68 compared to the ratio of SC-XRD 1 : 0.72.

3.17 XPS STUDY PRE AND POST UV

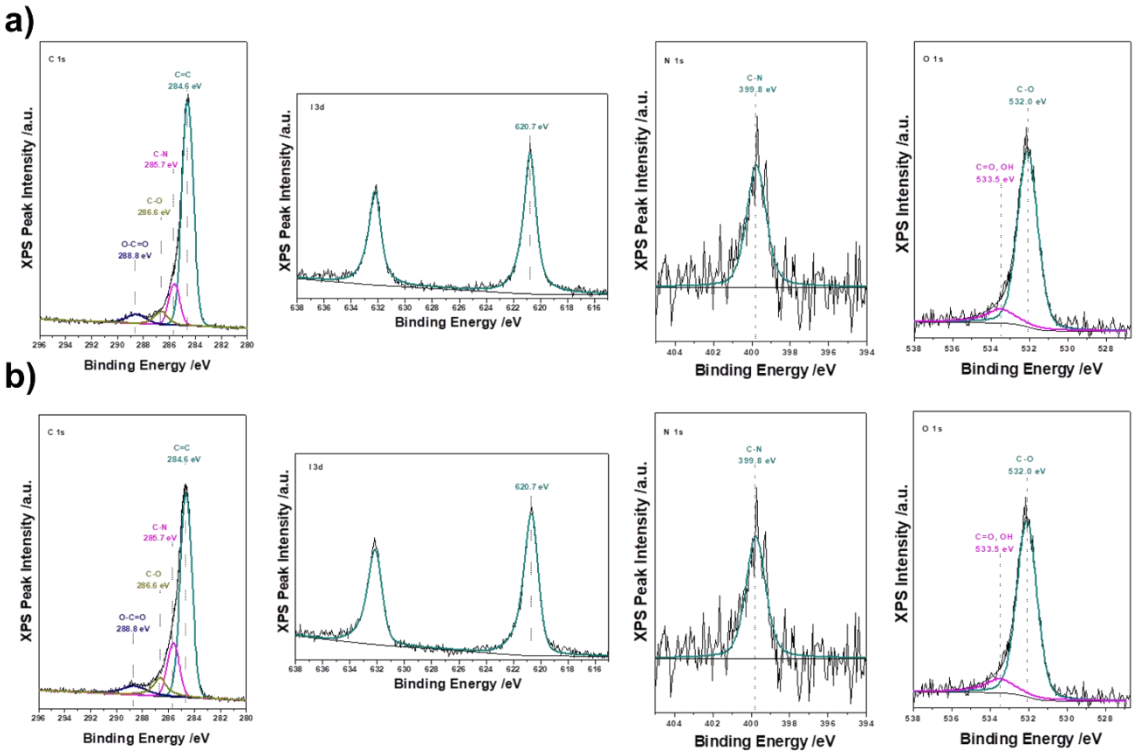

Figure 3.36. XPS analysis on pre and post-UV irradiated crystalline sample of **3**. UV irradiation was performed in situ (24 hours) a) Binding energy of XPS core level peaks (from left) C 1s, I 3d, N 1s, O 1s pre-UV irradiation. b) Binding energy of XPS core level peaks (from left) C 1s, I 3d, N 1s, O 1s post UV irradiation. No changes or shift were observed in the binding energy of the core level peaks compared with the post-UV irradiated sample. These XPS results can be attributed to the stability of the crystalline **3** during UV irradiation.

3.18 REFERENCES

(1) Mills, M. B.; Wohlhauser, T.; Stein, B.; Verduyn, W. R.; Song, E.; Dechambenoit, P.; Rouzières, M.; Clérac, R.; Preuss, K. E. Magnetic Bistability in Crystalline Organic Radicals: The Interplay of H-Bonding, Pancake Bonding, and Electrostatics in 4-(2′-Benzimidazolyl)-1,2,3,5-Dithiadiazolyl. *J. Am. Chem. Soc.* **2018**, *140* (49), 16904–16908.

(2) Liu, M.; Zhang, L.; Wang, T. Supramolecular Chirality in Self-Assembled

Systems. *Chem. Rev.* **2015**, *115* (15), 7304–7397.

(3) Würthner, F.; Saha-Möller, C. R.; Fimmel, B.; Ogi, S.; Leowanawat, P.; Schmidt, D. Perylene Bisimide Dye Assemblies as Archetype Functional Supramolecular Materials. *Chem. Rev.* **2016**, *116* (3), 962–1052.

(4) Agarwala, P.; Kabra, D. A Review on Triphenylamine (TPA) Based Organic Hole Transport Materials (HTMs) for Dye Sensitized Solar Cells (DSSCs) and Perovskite Solar Cells (PSCs): Evolution and Molecular Engineering. *J. Mater. Chem. A.* **2017**, 1348–1373.

(5) Petrus, M. L.; Schutt, K.; Sirtl, M. T.; Hutter, E. M.; Closs, A. C.; Ball, J. M.; Bijleveld, J. C.; Petrozza, A.; Bein, T.; Dingemans, T. J.; et al. New Generation Hole Transporting Materials for Perovskite Solar Cells: Amide-Based Small-Molecules with Nonconjugated Backbones. *Adv. Energy Mater.* **2018**, *8* (32), 1801605.

(6) Zhao, J.; Yang, Z.; Chen, X.; Xie, Z.; Liu, T.; Chi, Z.; Yang, Z.; Zhang, Y.; Aldred, M. P.; Chi, Z. Efficient Triplet Harvesting in Fluorescence-TADF Hybrid Warm-White Organic Light-Emitting Diodes with a Fully Non-Doped Device Configuration. *J. Mater. Chem. C* **2018**, *6* (15), 4257–4264.

(7) Hai, X.; Guo, Z.; Lin, X.; Chen, X.; Wang, J. Fluorescent TPA@GQDs Probe for Sensitive Assay and Quantitative Imaging of Hydroxyl Radicals in Living Cells. *ACS Appl. Mater. Interfaces* **2018,** *10*, 5853-5861.

(8) Roquet, S.; Cravino, A.; Leriche, P.; Alévêque, O.; Frère, P.; Roncali, J. Triphenylamine-Thienylenevinylene Hybrid Systems with Internal Charge Transfer as Donor Materials for Heterojunction Solar Cells. *J. Am. Chem. Soc.*

2006, *128* (10), 3459–3466.

(9) Flood, A. H.; Stoddart, J. F.; Steuerman, D. W.; Heath, J. R. Whence Molecular Electronics? *Science (80-.).* **2004**, *306* (5704), 2055–2056.

(10) Chen, H.; Fraser Stoddart, J. From Molecular to Supramolecular Electronics. *Nat. Rev. Mater. 2021 69* **2021**, *6* (9), 804–828.

(11) Blanchard, P.; Malacrida, C.; Cabanetos, C.; Roncali, J.; Ludwigs, S. Triphenylamine and Some of Its Derivatives as Versatile Building Blocks for Organic Electronic Applications. *Polym. Int.* **2019**, *68* (4), 589–606.

(12) Fahlman, M.; Fabiano, S.; Gueskine, V.; Simon, D.; Berggren, M.; Crispin, X. Interfaces in Organic Electronics. *Nat. Rev. Mater. 2019 410* **2019**, *4* (10), 627–650.

(13) Nyrkova, I.; Moulin, E.; Armao, J. J.; Maaloum, M.; Heinrich, B.; Rawiso, M.; Niess, F.; Cid, J. J.; Jouault, N.; Buhler, E.; et al. Supramolecular Self-Assembly and Radical Kinetics in Conducting Self-Replicating Nanowires. *ACS Nano* **2014**, *8* (10), 10111–10124.

(14) Busseron, E.; Cid, J. J.; Wolf, A.; Du, G.; Moulin, E.; Fuks, G.; Maaloum, M.; Polavarapu, P.; Ruff, A.; Saur, A. K.; et al. Light-Controlled Morphologies of Self-Assembled Triarylamine-Fullerene Conjugates. *ACS Nano* **2015**, *9* (3), 2760–2772.

(15) Shi, D.; Qin, X.; Li, Y.; He, Y.; Zhong, C.; Pan, J.; Dong, H.; Xu, W.; Li, T.; Hu, W.; et al. Spiro-OMeTAD Single Crystals: Remarkably Enhanced Charge-Carrier Transport via Mesoscale Ordering. *Sci. Adv.* **2016**, *2* (4).

(16) Armao, J. J.; Rabu, P.; Moulin, E.; Giuseppone, N. Long-Range Energy Transport

via Plasmonic Propagation in a Supramolecular Organic Waveguide. *Nano Lett.* **2016**, *16* (4), 2800–2805.

(17) Sindt, A. J.; Smith, M. D.; Berens, S.; Vasenkov, S.; Bowers, C. R.; Shimizu, L. S. Single-Crystal-to-Single-Crystal Guest Exchange in Columnar Assembled Brominated Triphenylamine Bis-Urea Macrocycles. *Chem. Commun.* **2019**, *55* (39), 5619–5622.

(18) Shimizu, L. S.; Salpage, S. R.; Korous, A. A. Functional Materials from Self-Assembled Bis-Urea Macrocycles. *Acc. Chem. Res.* **2014**, *47* (7), 2116–2127.

(19) Hossain, M. S.; Sindt, A. J.; Goodlett, D. W.; Shields, D. J.; O'Connor, C. J.; Antevska, A.; Karakalos, S. G.; Smith, M. D.; Garashchuk, S.; Do, T. D.; et al. Effects of Self-Assembly on the Photogeneration of Radical Cations in Halogenated Triphenylamines. *J. Phys. Chem. C* **2021**, *125*, 19991-20002.

(20) Li, Z.; Dong, Q.; Xu, B.; Li, H.; Wen, S.; Pei, J.; Yao, S.; Lu, H.; Li, P.; Tian, W. New Amorphous Small Molecules - Synthesis, Characterization and Their Application in Bulk Heterojunction Solar Cells. *Sol. Energy Mater. Sol. Cells* **2011**, *95* (8), 2272–2280.

(21) Zhong'an Li; Tenglin Ye; Sun Tang; Can Wang; Dongge Ma; Zhen Li. Triphenylamine-Based π-Conjugated Dendrimers: Convenient Synthesis, Easy Solution Processability, and Good Hole-Transporting Properties. *J. Mater. Chem. C* **2015**, *3* (9), 2016–2023.

(22) Tian, H.; Yang, X.; Chen, R.; Zhang, R.; Hagfeldt, A.; Sun, L. Effect of Different Dye Baths and Dye-Structures on the Performance of Dye-Sensitized Solar Cells Based on Triphenylamine Dyes. *J. Phys. Chem. C* **2008**, *112* (29), 11023–11033.

(23) Dubinina, G. G.; Price, R. S.; Abboud, K. A.; Wicks, G.; Wnuk, P.; Stepanenko, Y.; Drobizhev, M.; Rebane, A.; Schanze, K. S. Phenylene Vinylene Platinum(II) Acetylides with Prodigious Two-Photon Absorption. *J. Am. Chem. Soc.* **2012**, *134* (47), 19346–19349.

(24) Bondi, A. Van Der Waals Volumes and Radii. *J. Phys. Chem.* **1964**, *68* (3), 441–451.

(25) Moulin, E.; Niess, F.; Maaloum, M.; Buhler, E.; Nyrkova, I.; Giuseppone, N. The Hierarchical Self-Assembly of Charge Nanocarriers: A Highly Cooperative Process Promoted by Visible Light. *Angew. Chemie Int. Ed.* **2010**, *49* (39), 6974–6978.

(26) Armao, J. J.; Maaloum, M.; Ellis, T.; Fuks, G.; Rawiso, M.; Moulin, E.; Giuseppone, N. Healable Supramolecular Polymers as Organic Metals. *J. Am. Chem. Soc.* **2014**, *136* (32), 11382–11388.

(27) Spackman, M. A.; Jayatilaka, D. Hirshfeld Surface Analysis. *CrystEngComm* **2009**, *11* (1), 19–32.

(28) Moulder, J. F.; Stickle, W. F.; Sobol, P. E. ’; Bomben, K. D.; Chastain, J. *Handbook of X-Ray Photoelectron Spectroscopy;* Perkin-Elmer: Eden Prairie, MN, 1992.

(29) Du, X.; Liu, B.; Li, L.; Kong, X.; Zheng, C.; Lin, H.; Tong, Q.; Tao, S.; Zhang, X. Excimer Emission Induced Intra-System Self-Absorption Enhancement-a Novel Strategy to Realize High Efficiency and Excellent Stability Ternary Organic Solar Cells Processed in Green Solvents. *J. Mater. Chem. A* **2018**, *6* (46), 23840–23855.

(30) Li, Y.; Li, H.; Zhong, C.; Sini, G.; Brédas, J.-L. Characterization of Intrinsic Hole

Transport in Single-Crystal Spiro-OMeTAD. *npj Flex. Electron. 2017 11* **2017**, *1* (1), 1–8.

(31) Yanai, T.; Tew, D. P.; Handy, N. C. A New Hybrid Exchange-Correlation Functional Using the Coulomb-Attenuating Method (CAM-B3LYP). *Chem. Phys. Lett.* **2004**, *393* (1–3), 51–57.

(32) Hay, P. J.; Wadt, W. R. Ab Initio Effective Core Potentials for Molecular Calculations. Potentials for the Transition Metal Atoms Sc to Hg. *J. Chem. Phys.* **1985**, *82* (1), 270–283.

(33) Wu, X.; Jin, M.; Xie, J.; Malval, J.-P.; Wan, D. Molecular Engineering of UV/Vis Light-Emitting Diode (LED)-Sensitive Donor–π–Acceptor-Type Sulfonium Salt Photoacid Generators: Design, Synthesis, and Study of Photochemical and Photophysical Properties. *Chem. – A Eur. J.* **2017**, *23* (62), 15783–15789.

(34) *APEX III Version 2016.5-0 and SAINT+* Version 8.37A. Bruker AXS, Inc., Madison, WI **2016**.

(35) Krause, L.; Herbst-Irmer, R.; Sheldrick, G. M.; Stalke, D. Comparison of Silver and Molybdenum Microfocus X-Ray Sources for Single-Crystal Structure Determination. *J. Appl. Cryst* **2015**, *48* (1), 3–10.

(36) Sheldrick, G. M. *Acta Crystallogr. Sect. A* **2015**, *A* (71), 3–8.

(37) SHELXL: Sheldrick, G.M. Acta Cryst. 2015, C71, 3-8.

(38) Dolomanov, O. V.; Bourhis, L. J.; Gildea, R. J.; Howard, J. A. K.; Puschmann, H. OLEX2: A Complete Structure Solution, Refinement and Analysis Program. *J. Appl. Crystallogr.* **2009**, *42* (2), 339–341.

(39) Chai, J. Da; Head-Gordon, M. Long-Range Corrected Hybrid Density Functionals

with Damped Atom-Atom Dispersion Corrections. *Phys. Chem. Chem. Phys.* **2008**, *10* (44), 6615–6620. https://doi.org/10.1039/b810189b.

(40) Shao, Y.; Gan, Z.; Epifanovsky, E.; Gilbert, A. T. B.; Wormit, M.; Kussmann, J.; Lange, A. W.; Behn, A.; Deng, J.; Feng, X.; et al. Advances in Molecular Quantum Chemistry Contained in the Q-Chem 4 Program Package. *Mol. Phys.* **2015**, *113* (2), 184–215. https://doi.org/10.1080/00268976.2014.952696.

(41) *Spartan'18*, ver. 1.4.4; Wavefunction, Inc,: Irvine, CA, 2019.

(42) Pritchard, B. P.; Altarawy, D.; Didier, B.; Gibson, T. D.; Windus, T. L. New Basis Set Exchange: An Open, Up-to-Date Resource for the Molecular Sciences Community. *J. Chem. Inf. Model.* **2019**, *59* (11), 4814–4820.

(43) Devlin, F. J.; Finley, J. W.; Stephens, P. J.; Frisch, M. J. Ab Initio Calculation of Vibrational Absorption and Circular Dichroism Spectra Using Density Functional Force Fields: A Comparison of Local, Nonlocal, and Hybrid Density Functionals. *J. Phys. Chem.* **1995**, *99* (46), 16883–16902.

(44) Ditchfield, R.; Hehre, W. J.; Pople, J. A. Self-Consistent Molecular-Orbital Methods. IX. An Extended Gaussian-Type Basis for Molecular-Orbital Studies of Organic Molecules. *J. Chem. Phys.* **1971**, *54* (2), 724–728.

CHAPTER 4

SYNTHESIS AND CRYSTALLIZATION OF FLUORO-SUBSTITUTED TRIPHENYLAMINE BIS UREA MACROCYCLE & A STRUCTURAL INVESTIGATION

4.0 ABSTRACT

Fluoro substituted triphenylamine (TPA) *bis*-urea macrocycles self-assemble into robust 1-dimensional columns organized by urea hydrogen bonds. The columns pack via C-F···H-C_{aryl} halogen bond interactions to afford porous materials, similar to other TPA *bis*-urea macrocycles. Time-dependent density functional theory (TD-DFT) suggests the spin density is localized in the phenyl rings substituted by fluorine; whereas in the unsubstituted TPA macrocycle, the spin density resides near methylene urea. Future studies will be focused on probing the generation and localization of the radical cation/anion pairs by the combination of electron paramagnetic resonance (EPR) and ^{19}F NMR spectroscopy.

4.1 INTRODUCTION

Triphenylamine (TPA) and its derivatives have been employed successfully as electron donor materials in a wide range of applications ranging from dye-sensitized solar cell[1], perovskite solar cell[2], fullerene donor-acceptor conjugates[3], and other optoelectronic applications.[4,5] The donor character of TPA is raised by strong π conjugation which makes it suitable for hole transfer, while its propeller shape supports solution processability and stable radical cations.[6] Once stabilized, the radical cation can be detected by a wide range of spectroscopic techniques including transient absorption spectroscopy, electron paramagnetic resonance (EPR) spectroscopy, and UV-vis spectroscopy.[7,8] After the electron transfer, a radical anion is also formed, which is typically localized on the electron acceptor molecule in conjugation with TPA. The radical anion can be detected by similar spectroscopic techniques. TPA derivatives that lack an electron acceptor moiety have also been found to undergo these processes with both the radical cation and anion then localized within neighboring TPAs. This process was investigated in a series of linear urea tethered

TPA derivatives discussed in Chapter 2.[7] In this case, the TPA radical anion is very short-lived and challenging to detect. To aid in the detection of both the TPA radical cation and

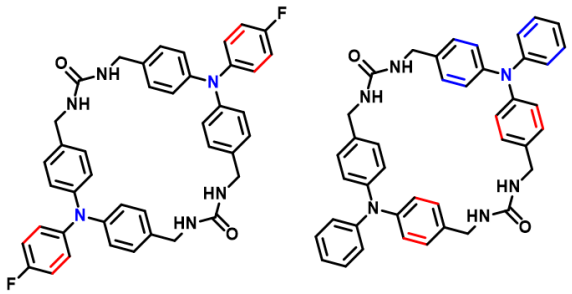

Figure 4.1. Spin density distribution of radical cation/anion pair suggested by TD-DFT. Anion spin density colored in red. Cation spin density colored in blue.

radical anion, a fluorinated TPA bis-urea macrocycle was synthesized and crystallized. The *para* position of the external phenyl ring of the TPA substituted by a fluorine atom and theoretical study was performed to check the viability of using ^{19}F NMR to detect the localization of radical anion within the supramolecular framework.

Fluorine can be used as a valuable probe to investigate interactions in the biological system[9], conformational changes in protein[10], detecting key reaction intermediates[11], and drug discovery[12]. Although not abundant, ^{19}F NMR can be used to characterize transient species. Compared to ^{1}H chemical shift (~15 ppm), ^{19}F nucleus is highly sensitive to the change of local chemical environment with chemical shifts spanning nearly 400 ppm. The strong dipolar couplings of ^{19}F nuclei resulting in ^{19}F-^{19}F and ^{1}H-^{19}F nuclear Overhauser enhancement (NOE) effects can be further tailored as distance constraints to understand structural information.[13] For example, Olah and his group characterized short-lived trifluoromethanide anion by low temperature ^{19}F NMR and ^{13}C NMR spectroscopy.[14] Shiotani and his coworkers investigate the reduction kinetics of poly(tetrafluoroethylene) by radical anion using a high resolution ^{19}F NMR method.[15] Popov and his group were able to show reversible dimerization of $C_{70}(CF_3)_{10}^-$ radical anion by ^{19}F NMR

spectroelectrochemistry.[16] These examples show the potential of using ^{19}F NMR to investigate the transient radical anion species which is otherwise difficult to detect with other spectroscopic techniques.

Previously, we have investigated the generation, stability, and lifetime of TPA radical cation in a series of halogenated TPA dimers tethered through methylene ureas.[7] While the fluoro, chloro, bromo, and iodo derivatives were all prepared, we were unsuccessful in crystallizing the fluoro derivative. These TPA dimers assemble through urea hydrogen bonds forming tape-like structures. Furthermore, the packing of the iodo derivative is controlled by halogen bonding interaction. Once assembled, these derivatives

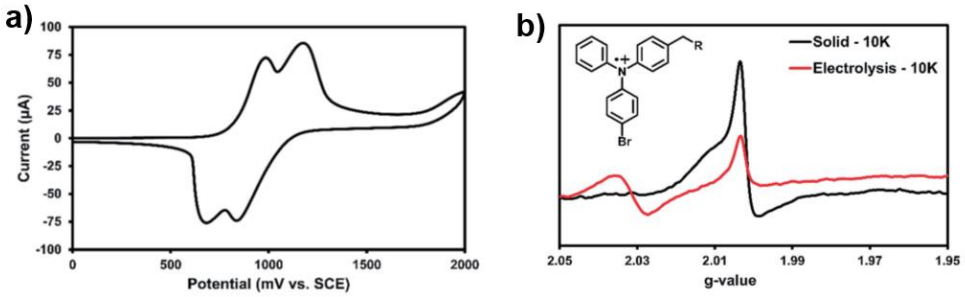

Figure 4.2. a) CV for 1mM bromo derivative in a 0.1M $(n\text{-}Bu)_4N^+PF^-_6$ DCM solution, scan rate 100 mV s^{-1}, SCE = saturated calomel electrode. b) Solution EPR of bromo derivatives at 10k after bulk electrolysis at first oxidation peak (red). Solid state EPR of bromo derivatives at 10k after 3 hours of UV irradiation (black). Inset: proposed structure of radical generation after UV irradiation.

can afford photogenerated radical cation/anion pair which can undergo reverse electron transfer to return to the starting material without degradation. Electrochemical studies on bromo derivative (Figure 4.2a) suggest TPA undergo oxidation at 1.0 V versus a saturated calomel electrode (SCE).[17] Bulk electrolysis at this potential produced EPR spectra that were comparable to the solid-state, indicating a radical cation is generated in both samples (Figure 4.2b). Transient absorption spectroscopy on the nanocrystal suspension of bromo derivative in the water further supports the formation of radical cation, which was

simulated with TD-DFT.[7] The macrocyclic counterparts of the linear structure are expected to have a greater chance of crystallizing as previous evidence suggests employing two urea groups TPA can more efficiently direct organize into columnar nanotubes.[18] We aim to investigate the effect of fluoro substitution on both the packing of TPA and probe if the position of the fluorine is sensitive enough to act as a reporter for transient radical cation and anion species formed during UV irradiation.

To understand the localization of radical anion species, the fluoro-substituted TPA macrocycle host **1F** was synthesized and crystallized. A structural study by SC-XRD and Hirshfeld surface analysis suggest that the assembly is directed by urea hydrogen bonding interactions while the individual columns are held together by C-F⋯H-C_{aryl} halogen bond. Spin density calculation by time-dependent density functional theory (TD-DFT) suggests radical anion localization on the fluoro-substituted phenyl rings for host **1F** compared to host **1H** where radical anion localized on the phenyl ring attached to methylene urea. Future studies will be focused on using ^{19}F NMR, and ^{13}C NMR studies on pre and post-UV irradiated samples of host **1F** and host **1H** to investigate the changes in the local chemical environment in the phenyl rings of the TPA and subsequent localization of radical anion species. The stability of the framework will be tested by thermogravimetric analysis (TGA) to empty the solvent of crystallization from the channel and will be examined via SC-XRD. We are also planning to load electron acceptor molecules into the channels. In this case, the radical anion would reside in the channel while the Fluorine reporter is on the exterior of the macrocycle. The Fluorine chemical shift in a series of host-guest complexes will be compared before and after photoinduced electron transfer. Finally, the assignment of the NMR spectroscopic data will be validated by TD-DFT calculation.

4.2 SYNTHESIS AND CRYSTALLIZATION

Macrocycle **1F** was synthesized by six steps following the previously established

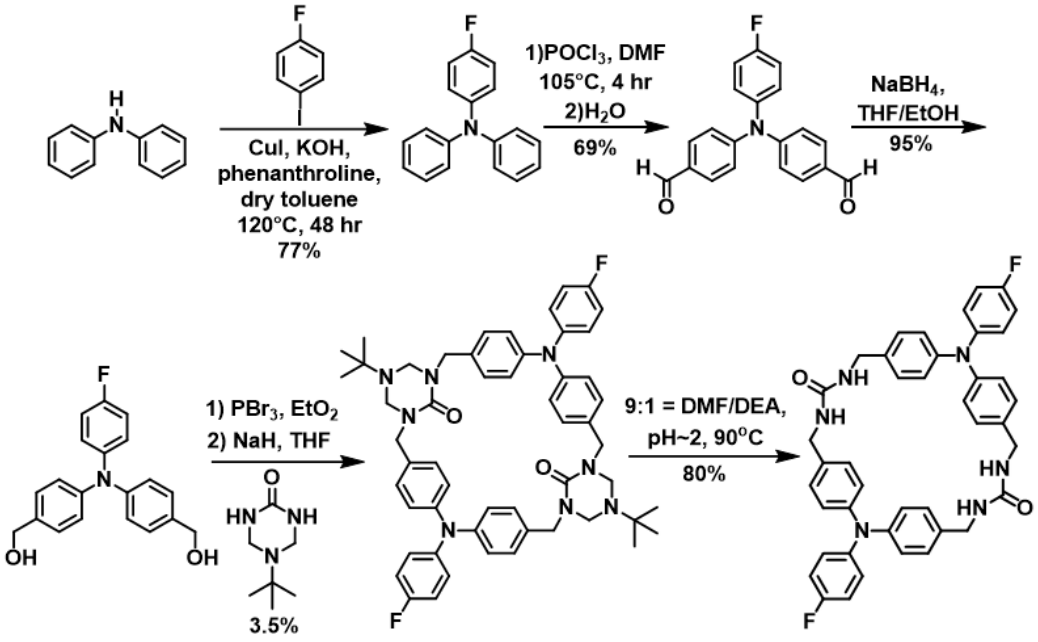

Scheme 4.1. Synthetic scheme of Host **1F**

procedure (Scheme 4.1).[18] In the first step, partially fluoro-substituted parent TPA was synthesized by a modified Ullmann coupling reaction with commercially available diphenylamine and 4-fluoro-1-iodobenzene.[19] Then the two open *para* positions of the phenyl rings were converted to aldehydes by a Vilsmeier-Haack reaction,[20] which was followed by reduction[21] and bromination[22]. Finally, the dibromide was reacted with triazinanone under basic conditions to form protected partially fluoro-substituted TPA macrocycle. Deprotection was carried out under acidic conditions. Solvated crystals of protected **1F** were obtained by cooling chloroform solution. Host-guest crystals of **1F** were obtained by vapor diffusion of 1,2-dimethoxyethane (DME) into DMSO solution (2.5 mg/ML).

4.3 CRYSTAL COMPARISON

Host **1F** crystallized in the triclinic system in space group *P*-1 (No. 2). The urea

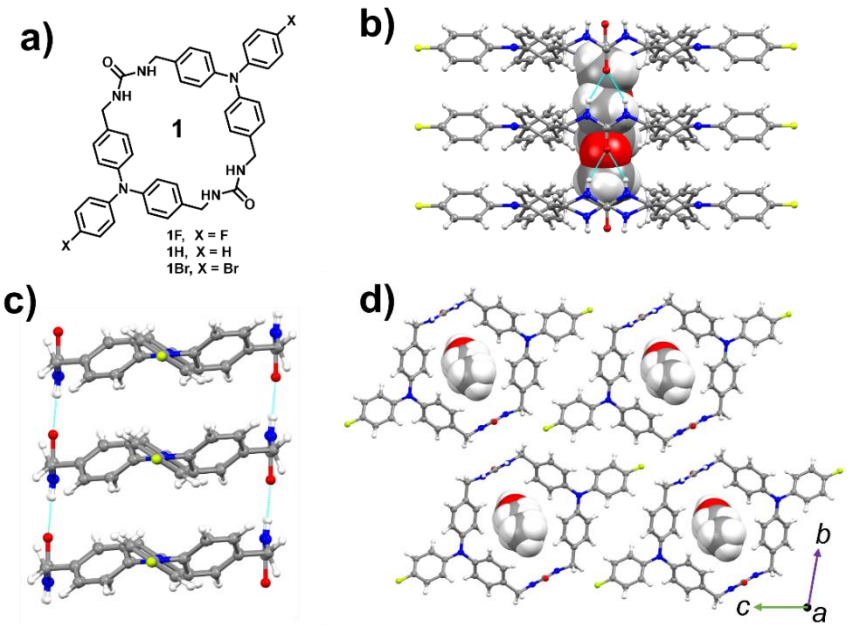

Figure 4.3. a) ChemDraw of synthesized TPA macrocycle **1** (X = H, F or Br). b) View of a single column of **1F** generated by urea tape demonstrate host:guest ratio 2:1. c) Single column of host **1F** showing *anti* conformation of urea. d) Crystal packing of host **1F** with guests. Disorder was omitted for clarity.

groups are aligned in the opposite direction as *anti*-conformation encapsulates DME as guest with a host-guest ratio of 2:1 (Figure 4.3b-c). The individual macrocyclic units stacks via three centered urea hydrogen bonds (d(N···O) = 2.876 (2), 2.882 (2) Å) and offset π stacking interactions. The neighboring tubes are held together by C-F···H-C_{aryl} halogen bond with a distance of 2.513 Å, which is less than the sum of the vdW radii of F···H (2.67 Å).[23] To probe the effect of fluorine substitution on the packing of TPA, the host **1F** structure was further compared with similar host frameworks previously prepared by our group as can be seen in figure 4.4.[18] The *para* position of the external phenyl rings of host **1H** remains unsubstituted, while in the case of host **1Br** this position is substituted by a bromine atom. Both host **1H** and host **1Br** crystallized in the monoclinic system with $P2_1/c$

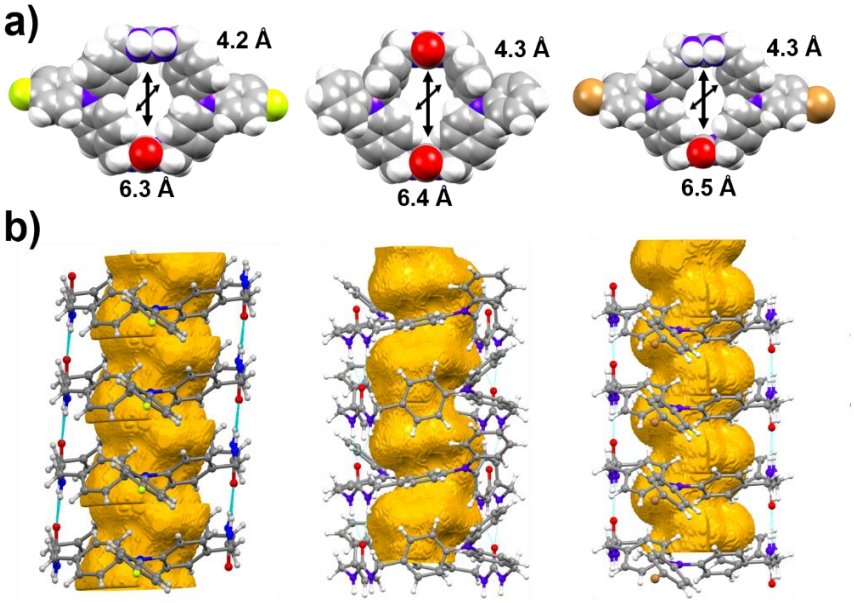

Figure 4.4. Comparison of pore sizes and void space of different *bis* urea macrocycle. a) pore size calculated by subtracting the vdW radii, from left **1F**, **1H**, and **1Br**. b) 1-dimensional column generated by urea hydrogen bonding and their corresponding void space.

and $P2_1/n$ space group respectively. In contrast, host **1F** adopts a triclinic unit cell with approximately half the volume compared to host **1Br** (11.74 $Å^3$ versus 32.73 $Å^3$). Each neighboring column of cycles of host **1F** is related by simple translation of a unit cell which organizing the column in the same orientation. In comparison, host **1Br** contains two differently oriented cycles per unit cell, with columns related by a combination of two-fold rotational and mirror symmetry with respect to their neighbors in the cell. The pore aperture of host **1F** is slightly shorter 6.3 X 4.2 Å compared to host **1H** (6.4 X 4.3 Å) and host **1Br** (6.5 X 4.3 Å). In host **1H**, the edge to face π stacking interactions generates a channel with curves that oscillates back and forth along the column highlighted in yellow in figure 4.4b. Although similar offset π stacking interaction was observed in host **1F** and **1Br**, pronounced oscillation of curvature was observed in host **1Br** in comparison to host **1F**.

To further quantify intermolecular contacts that promoted the packing of TPA and guide the assembly, Hirshfeld surface analysis and subsequent fingerprint plots were

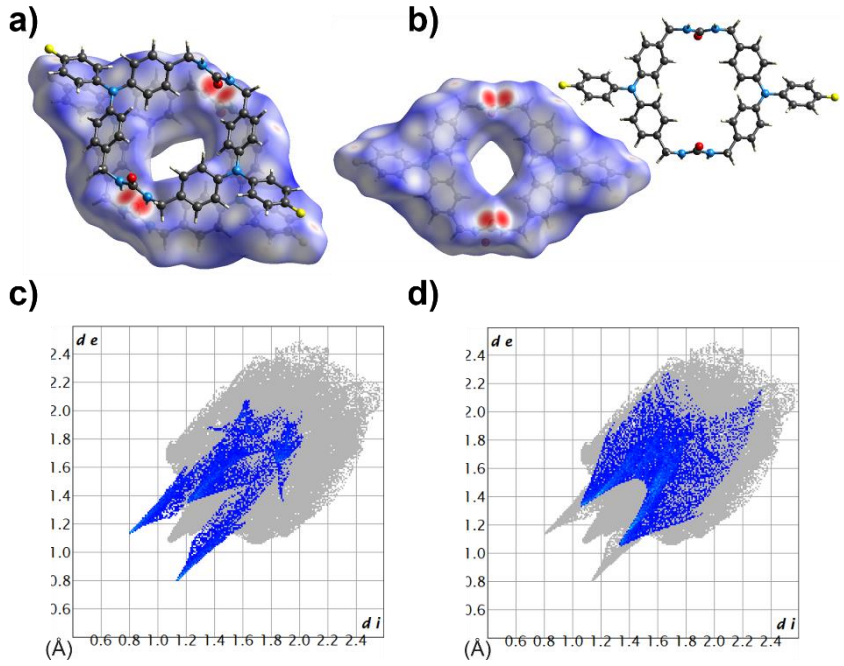

Figure 4.5. Hirshfeld surface analysis of host **1F**. a) Bifurcated hydrogen bonding indicated in red. Red regions corresponding to the distance shorter than the sum of the vdW radii. b) C-F···H-C_{aryl} interactions between neighboring macrocycles. c) O···H/H···O contacts resolved by fingerprint plot. d) F···C/C···F contacts resolved by fingerprint plot.

generated and compared for host **1F** and **1H**. (Figure 4.5, 4.7).[24] Understanding the local chemical environment around each fluorine atom is important as it will have a pronounced effect on solid state ^{19}F NMR. Both host **1F** and host **1H** show key three-centered urea-urea hydrogen bonding interaction indicated in red, which is further resolved by fingerprint plot (Figure 4.5a, 4.7a). As can be seen in figure 4.5c and 4.7c, both the fingerprint plot shows spikes at *de* = *di* ~ 1.2 Å and ended at around 2.2 Å which is in agreement with C-O···H-N hydrogen bond contact distance. In both cases, hydrogen bond contact contributes to a similar surface area of 8.1% for host **1F** and 8.3% for host **1H**. To further resolve the C-F···H-C_{aryl} halogen bond, fingerprint plot shows the major concentration in the vicinity

of *de* = *dj* ~ 2.2 Å with the highest surface area 11.2%. This contact can be ascribed as the formation of the C-F···H-C_{aryl} halogen bond, which is less than the sum of the vdW radii

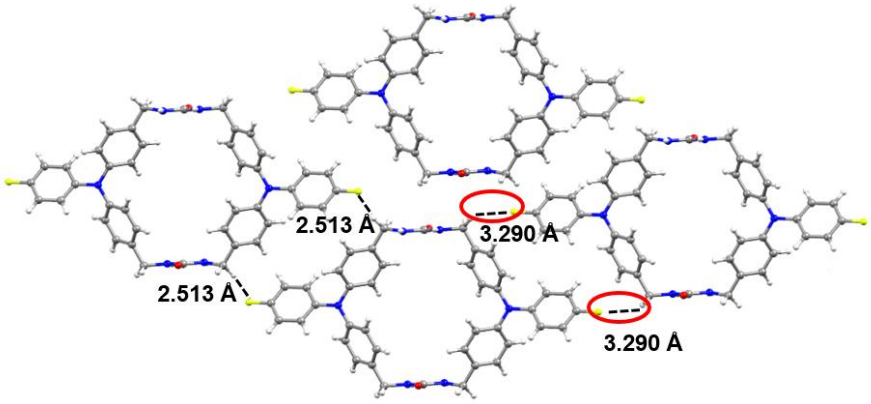

Figure 4.6. Packing structure of host **1F** showing halogen bonding interactions. The contact distance between C-F···H-C_{aryl} longer than 2.67 Å are not considered as halogen bonds.

of F···H (2.67 Å). In each macrocyclic unit, only one fluorine atom making the halogen bond. The contact distance of C-F···H-C_{aryl} for the fluorine in the *para* position of the opposite TPA is 3.290 Å longer than the sum of the vdW radii F···H (2.67 Å) which can be seen in Figure 4.6 (indicated in red). Based on these two different intermolecular contact distances on individual fluorine atoms suggest that ^{19}F NMR resolve for two different fluorine nuclei. This pattern of assembly can be viewed further by the columnar structure of host **1F** in figure 4.4b, which is slightly tilted. For comparison, fingerprint plot also resolved for C_{aryl}···C_{aryl} stacking interaction in host **1H** which can be seen in Figure 4.7d. The fingerprint plot shows a higher concentration (19.1%) at the surface area *de* = *dj* ~ 2.4 Å which is in the agreement of C_{aryl}···C_{aryl} stacking interaction less than the sum of vdW radii (3.4 Å). Overall Hirshfeld surface analysis and comparison with host **1H** suggest that there is asymmetric electron density distribution on individual fluorine atoms for host **1F**.

4.4 VISUALIZATION OF SPIN DENSITY BY TD-DFT

To further investigate the viability of host **1F** to detect the localization of radical anion species by ^{19}F NMR, TD-DFT was employed. We investigate the spin density

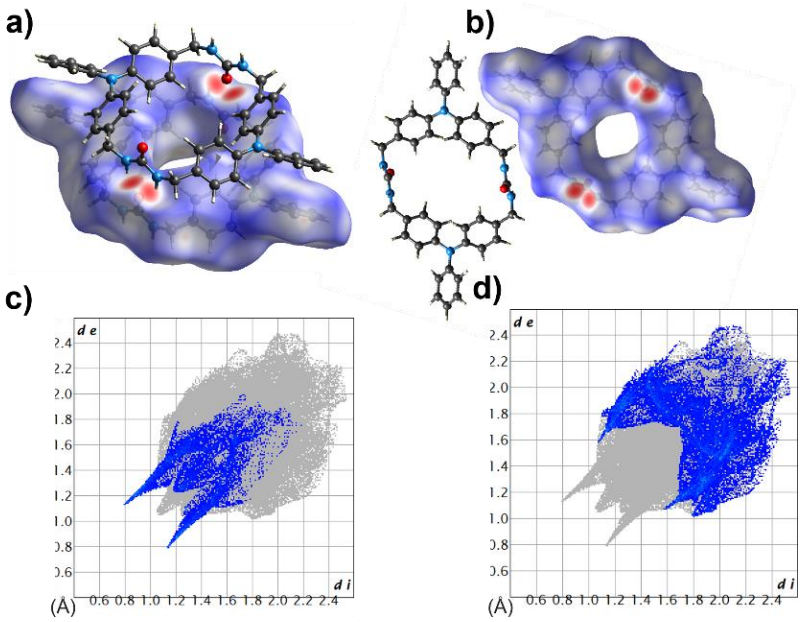

Figure 4.7. Hirshfeld surface analysis of host **1H**. a) bifurcated hydrogen bonding indicated in red. Red regions corresponding to the distance shorter than the sum of the vdW radii. b) $C_{aryl}\cdots C_{aryl}$ interactions between neighboring macrocycle. c) O···H/H···O contacts resolved by fingerprint plot. d) $C_{aryl}\cdots C_{aryl}$ contacts resolved by fingerprint plot.

distribution of host **1F** at its neutral and charged state (radical cation, and radical anion). As a control, the spin density distribution was also computed for host **1H**, which contains no fluorine atom at the exterior phenyl ring. These calculations were performed in Qchem[25] and Spartan program[26]. Heavy atoms coordinate from SC-XRD data were used and disordered guests were removed. Only the hydrogens were optimized using B3LYP-D3[27]/6-31G*[28] methods. A single-point energy calculation was performed for the neutral, radical cation, and radical anion species using CAM-B3LYP[29]/6-31G[28] method. Finally, the spin density was calculated using IQmol and visualized at isovalue 0.04. The generated

spin density distribution in host **1F** and host **1H** for the (from left) neutral, radical cation, and radical anion was depicted in figure 4.8.

As expected, both host **1F** and host **1H** show no spin density distribution at the neutral state. In the radical cation state, both host **1F** and host **1H** show the concentration

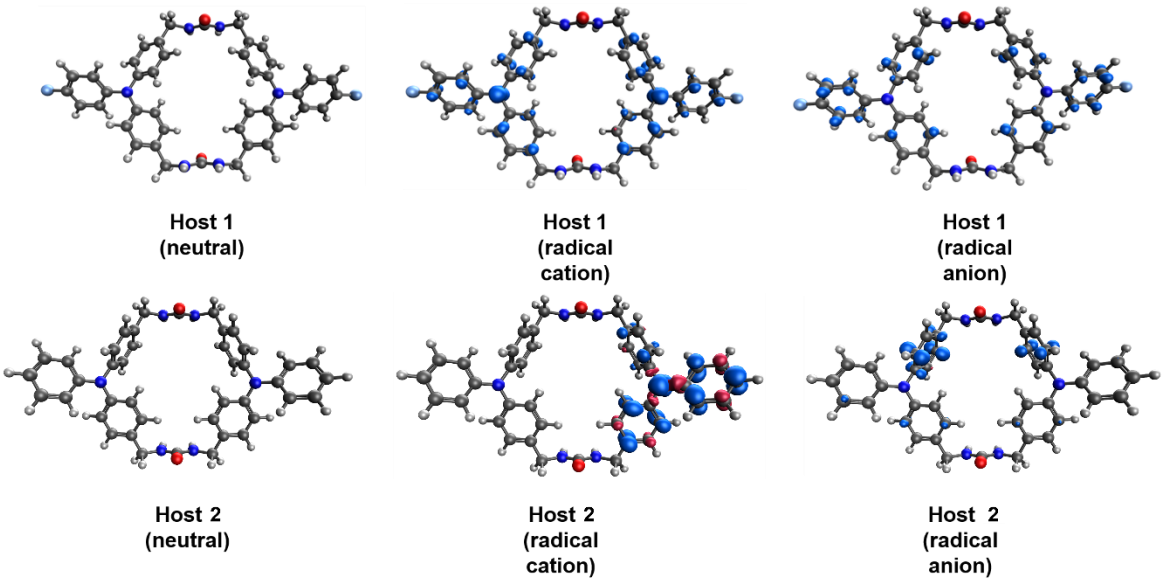

Figure 4.8. Spin density distribution or singly occupied molecular orbital (SOMO), from left hosts **1**F and **1**H neutral, host **1**F and **1**H radical cations, and host **1**F and **1**H radical anions generated using CAM-B3LYP/6-31G methods. Visualized at Isovalue 0.04.

of spin in the N center. It is known TPA generates N-centered radical cation by chemical, electrochemical, or photoinduced processes, which has been extensively characterized by our group.[7,18] While host **1F** shows equal spin density distribution in both TPA units, host **1H** displays spin density distribution on only one of the TPA units concentrated at the exterior phenyl ring. For the radical anion state, host **1H** displays spin density distribution on the phenyl ring attached to urea. In comparison, host **1F** exhibits spin density distribution on the exterior phenyl ring which is *para*-substituted by fluorine. Both the host **1F** and **1H** show no spin density distribution on methylene urea. These results suggest the substitution of hydrogen with fluorine effect the SOMO or spin density distribution. Also,

radical anion distribution on the exterior phenyl ring on host **1F** supports the viability of using ^{19}F NMR to investigate the changes in the local chemical environment.

We have performed solid state ^{19}F NMR experiments on bulk crystals of protected **1F** on pre and post-UV irradiated samples. Analysis of the spectra shows a sharp singlet at 120.10 ppm with spinning side bands. The pre and post-UV irradiated unassembled protected **1F** shows no changes in NMR spectra which is expected as previous evidence suggests radical cation/anion pairs generation facilitates through urea assembly. Note that the solid-state probe is not currently accessible and will be available in January.

4.5 FUTURE WORK

The intrinsic property of the TPA bis urea macrocycles is the generation of radical cation/anion pair upon UV irradiation. The radical cation/anion pair undergo charge recombination and has a pronounced effect on the electron density distribution. Future studies will be focused on performing high field EPR spectroscopy to characterize the radical cation/anion pair upon UV irradiation. We are also planning to perform ^{19}F and ^{13}C solid state NMR experiments on the bulk crystals of **1F** and **1H**. We will perform these experiments at variable temperatures as we are expecting transient radical cation/anion pair would have a longer lifetime at low temperature which will facilitate the characterization. We are expecting to observe two asymmetric ^{19}F NMR signal as the local chemical environment are different for both fluorine atom suggested by SC-XRD analysis. We will also investigate the rigidity of the framework of **1F** upon removing the guest DME by TGA and SC-XRD. Then an electron acceptor molecule will be loaded in the empty channel containing heavy atom to aid the SC-XRD structure refinement. In this case, radical anion will generate in the guest which will be far away from the fluorine reporter group. This

host-guest structure can be used as a control and will help assign the changes of the local chemical environment. Finally, the NMR spectroscopic data will be assigned by TD-DFT calculations.

4.6 SUMMARY AND CONCLUSION

In summary, a fluorinated TPA *bis*-urea macrocycle was synthesized and crystallized in which the *para* position of the external phenyl ring was substituted by fluorine. The individual macrocycle packs into 1-dimensional columns directed by urea hydrogen bonding interactions. Structural comparison with similar TPA *bis*-urea macrocycles suggest that the individual column are held together by halogen bonding interaction. Surprisingly only one fluorine atom contributes to the halogen bond suggesting that the local chemical environment around each fluorine is different. TD-DFT calculations predict that the fluorine reporter group effect the electron density distribution and shows localization of radical anion species on the phenyl rings substituted by fluorine. Future studies will focus on probing the localization of radical cation/anion pairs by EPR, ^{19}F NMR spectroscopy.

4.7 EXPERIMENTAL

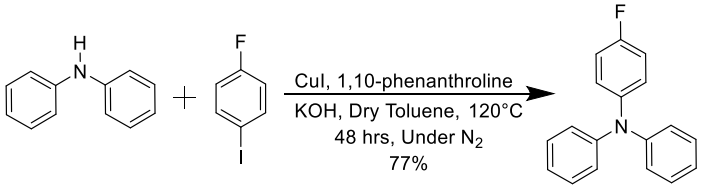

4-fluoro-N,N-diphenylaniline: Compound was synthesized according to the previous literature procedure.[19] In an oven-dried schlenk flask, commercially available diphenylamine (23.64 mmol, 1 equiv.), 1-fluoro-4-iodobenzene (28.36 mmol, 1.2 equiv.), copper (I) iodide (6.15 mmol, 0.26 equiv.), 1,10-phenanthroline (6.62 mmol, 0.28 equiv.),

potassium hydroxide (94.56 mmol, 4 equiv.) were added under the protection of N_2. Next, 20 mL dry toluene was added, and the reaction mixture degassed using freeze pump thaw methods for three times. The mixture was heated at 120°C under N_2 atmosphere for 48 h. Then the reaction mixture was cooled, quenched with H_2O (1 X 30 mL), extracted with methylene chloride (3 X 30 mL), and combined organics dried over anhydrous $MgSO_4$. The solvent was removed by rotary evaporation and the crude material purified by column chromatography using silica and 100% hexane as eluent to afford the product as white solid (4.788 g, 77%). ^{1}H NMR (400 MHz, CDCl3): δ (ppm) 7.26- 7.19 (m, 4H), 7.10−7.01 (m, 6H), 7.10−6.92 (m, 4H), 7.03−6.99 (m, 4H); 13C NMR (101 MHz, CDCl3): δ (ppm) 158.9 (d, *J* = 242.5 Hz), 147.9, 143.8, 129.2, 126.4 (d, *J* = 7.7 Hz), 123.5, 122.5, 116.0 (d, *J* = 22.0 Hz); HRMS-APCI (+) [M+H]+: calculated, 264.1183; found: 264.1176.

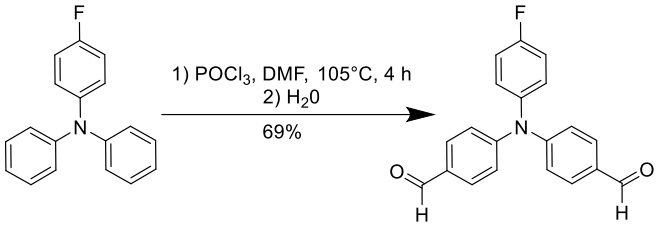

4,4'-((4-fluorophenyl)azanediyl)dibenzaldehyde: The compound was synthesized similar to literature procedures.[20] With proper protection (elevated flow rate in the hood and personal protective equipment), phosphoryl chloride (178.2 mmol, 9.8 equiv.) was added dropwise at 0°C to N, N-dimethylformamide (236.38 mmol, 13 equiv.). The mixture was then stirred at room temperature for 1 h under N_2. Next, 4-fluoro-N,N-diphenylaniline (18.18 mmol, 1 equiv.) was added to the reaction mixture and the solution heated at 105°C for 4 h. Once cooled to room temperature, 100 mL ice-cold water was carefully added, and the solution further diluted with 500 mL water. Then the resulting suspension was filtered and the crude material was purified by column chromatography (Hexanes:Diethyl ether =

3:1). The final product was obtained as yellow solid (4.00 g, 69%). ^{1}H NMR (300 MHz, $CDCl_3$) δ (ppm) 9.90 (s, 2H), 7.82 – 7.75 (m, 4H), 7.20 – 7.07 (m, 8H). HRMS (EI): calculated, 319.1009; found: 319.1011.

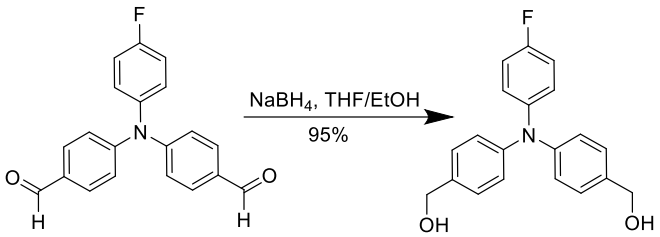

(((4-fluorophenyl)azanediyl)bis(4,1-phenylene))dimethanol: Compound was synthesized according to literature procedure.[21] The aldehyde from the previous step (12.53 mmol, 4.00 g) was dissolved in 320 mL in a 2:1 mixture of dry THF/ethanol mixture and sodium borohydride (27.55 mmol, 1.05 g) was added. Then the resulting mixture was heated at 40°C overnight in the dark. Once cooled to room temperature, 350 mL of water was added and the organics were extracted with $CHCl_3$ (3 X 200 mL) and the combined organics dried over anhydrous $MgSO_4$. Then the solvent was removed by rotary evaporation and the final product was obtained as a white solid (11.90 mmol, 3.8492 g). ^{1}H NMR (300 MHz, DMSO-d_6) δ (ppm) 7.27 – 7.18 (m, 4H), 7.17 – 7.07 (m, 2H), 7.04 – 6.95 (m, 2H), 6.95 – 6.88 (m, 4H), 5.10 (t, J = 5.7 Hz, 2H), 4.43 (d, J = 5.7 Hz, 4H). ^{13}C NMR (75 MHz, DMSO-d_6) δ (ppm) 159.14, 156.76, 146.11, 143.91, 143.89, 136.98, 127.87, 125.64, 125.56, 123.09, 116.30, 116.08, 62.58. HRMS (EI): calculated, 324.1394; found: 324.1386.

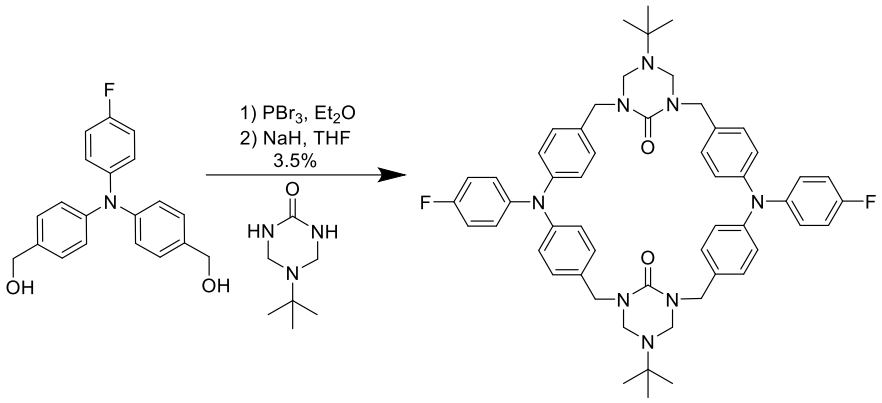

15,75-di-tert-butyl-4,10-bis(4-fluorophenyl)-4,10-diaza-1,7(1,3)-ditriazinana-3,5,9,11(1,4)-tetrabenzenacyclododecaphane-12,72-dione: Compound was synthesized by modifying a reported literature procedure.[22] Product from the previous step (11.90 mmol, 3.8492 g) was dissolved in 130 mL dry diethyl ether and cooled to 0°C. Then phosphorus tribromide (1.36 mL, 14.29 mmol) was added dropwise as a solution in 10 mL dry diethyl ether. Then the reaction mixture was stirred at room temperature overnight at dark. The next morning 140 mL ice-cold water and 70 mL $NaHCO_3$ was added to quench the reaction. The organics were extracted with 140 mL of dichloromethane and further washed with (3 X 70 mL) brine and dried over anhydrous $MgSO_4$. The solvent was removed by rotary evaporation and the crude material was used for the next step without further purification. *Tert*-butyl triazinanone (47.72 mmol, 1.91 g), and sodium hydride (11.81 mmol, 1.86 g) were suspended in 300 mL of dry THF and were heated at reflux for 2 h. Then mixture was cooled to room temperature and the crude material was added. The solution was heated at reflux for 2 days in the dark. Once completed, the reaction was cooled to room temperature and quenched with 1N HCl (24 mL) and of water (88 mL). The solution was reduced in vacuo to ~330 mL and 58 mL of 1N HCl and 200 mL of water were added. The solution was then extracted with dichloromethane (3 X 300 mL). The organics were washed with (1 X 300 mL) brine and dried over anhydrous $MgSO_4$. The

solvent was removed by rotary evaporation and recrystallized from chloroform. The product was obtained as a white powder (0.160 g). ^{1}H NMR (300 MHz, $CDCl_3$) δ (ppm) 7.21 (d, *J* = 8.2 Hz, 8H), 7.07 (dd, *J* = 9.0, 4.8 Hz, 4H), 6.95 (dd, *J* = 15.5, 8.1 Hz, 12H), 4.46 (s, 8H), 4.23 (s, 8H), 0.73 (s, 18H). ^{13}C NMR (75 MHz, $CDCl_3$) δ (ppm) 160.22, 157.80, 155.62, 147.53, 143.64, 132.46, 130.38, 126.33, 126.25, 123.60, 116.33, 116.11, 100.13, 77.48, 77.16, 76.84, 60.39, 54.48, 47.17, 28.31. HRMS (EI): calculated, 889.4724; found: 889.4727.

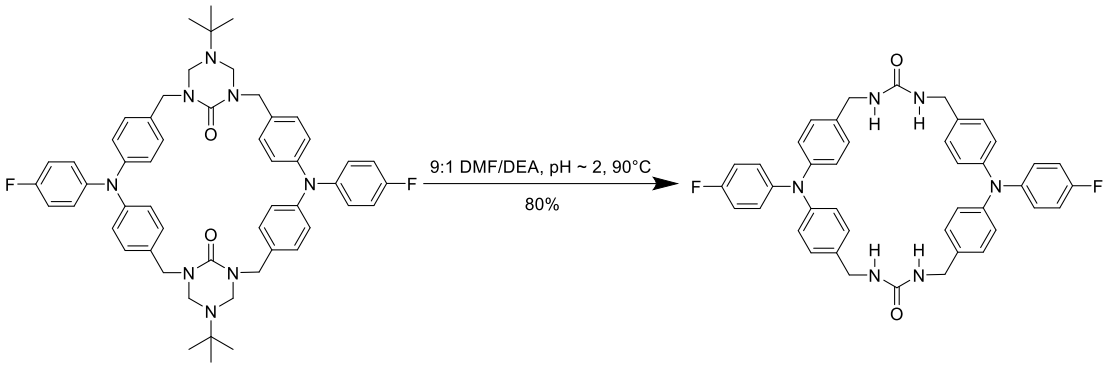

2,10-bis(4-fluorophenyl)-2,5,7,10,13,15-hexaaza-1,3,9,11(1,4)-tetrabenzenacyclohexadecaphane-6,14-dione: Protected macrocycle (0.118 mmol,

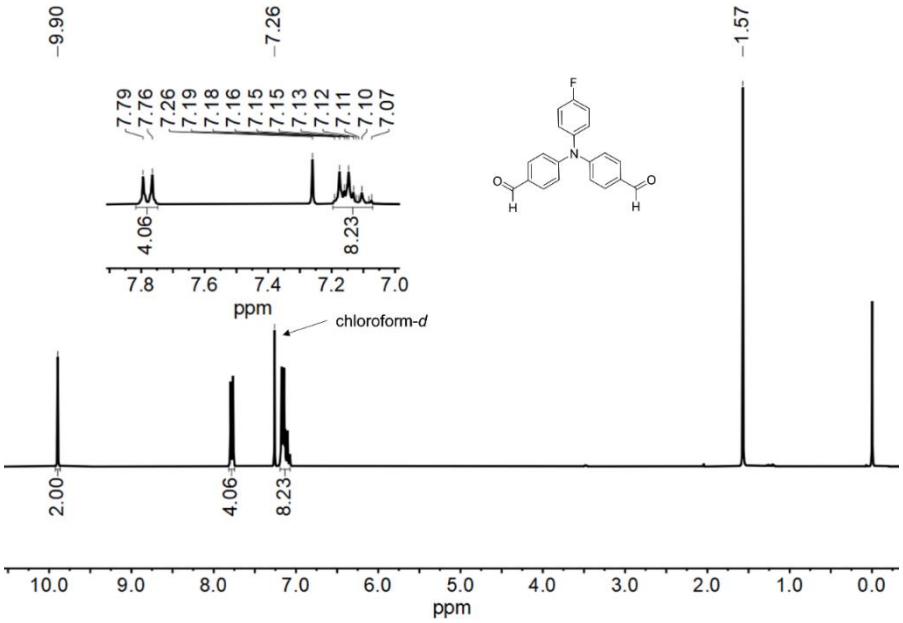

Figure 4.9. ^{1}H NMR ($CDCl_3$, 300 MHz) of the dialdehyde.

0.105 g) was dissolved 105 mL of a 9:1 mixture of DMF and diethanolamine mixture and the pH was adjusted to 2 using 12 M aqueous HCl. Then the resulting mixture was heated at reflux for three days under dark and pH was readjusted to 2 at every 12 hrs interval. Once cooled to room temperature, the reaction mixture was neutralized by adding $NaHCO_3$ and diluted with 500 mL of water. The solution was filtered and further washed with 500

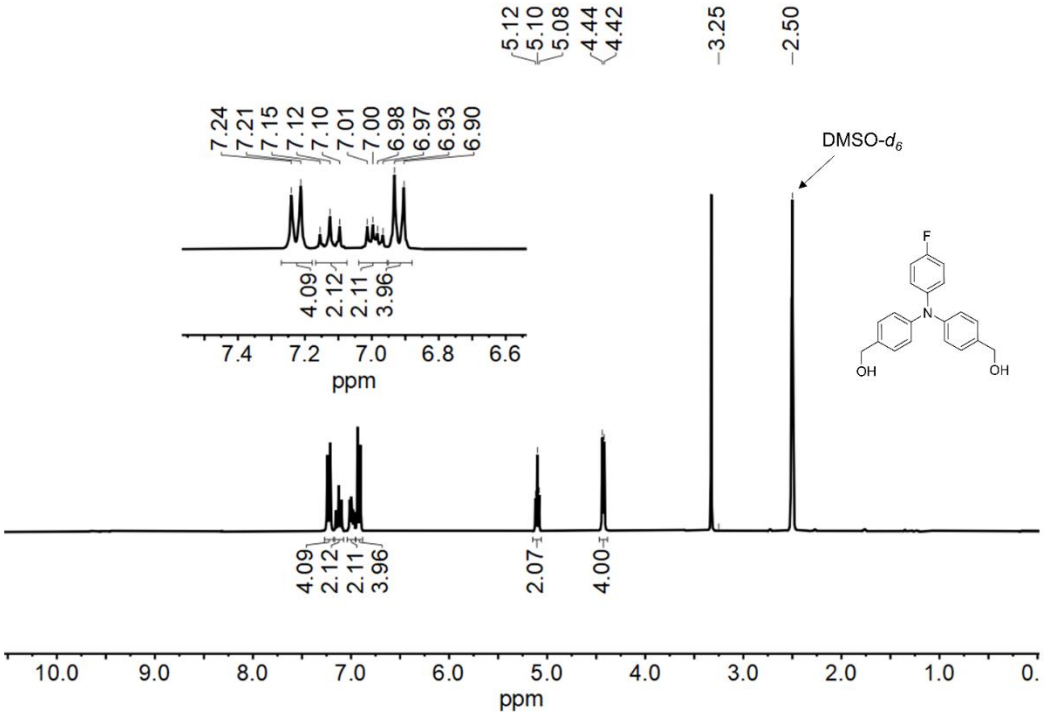

Figure 4.10. ^{1}H NMR ($(CD_3)_2SO$, 300 MHz) of the diol.

mL of water. The final product was obtained as white solid (0.065 g, 80%). ^{1}H NMR (300 MHz, DMSO-d_6) δ (ppm) 7.11 (t, J = 7.9 Hz, 13H), 6.98 (dd, J = 8.9, 4.9 Hz, 4H), 6.88 (d, J = 8.4 Hz, 7H), 6.50 (t, J = 6.2 Hz, 4H), 4.17 (d, J = 6.3 Hz, 8H)

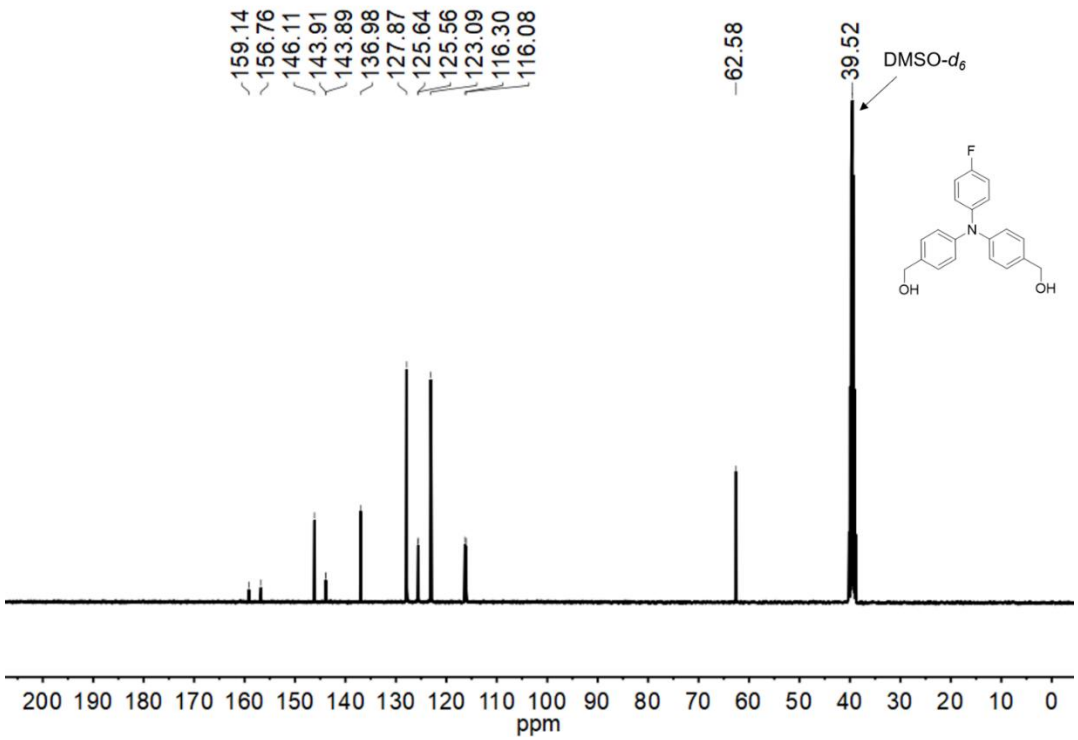

Figure 4.11. ^{13}C NMR ($(CD_3)_2SO$, 75 MHz) of the diol.

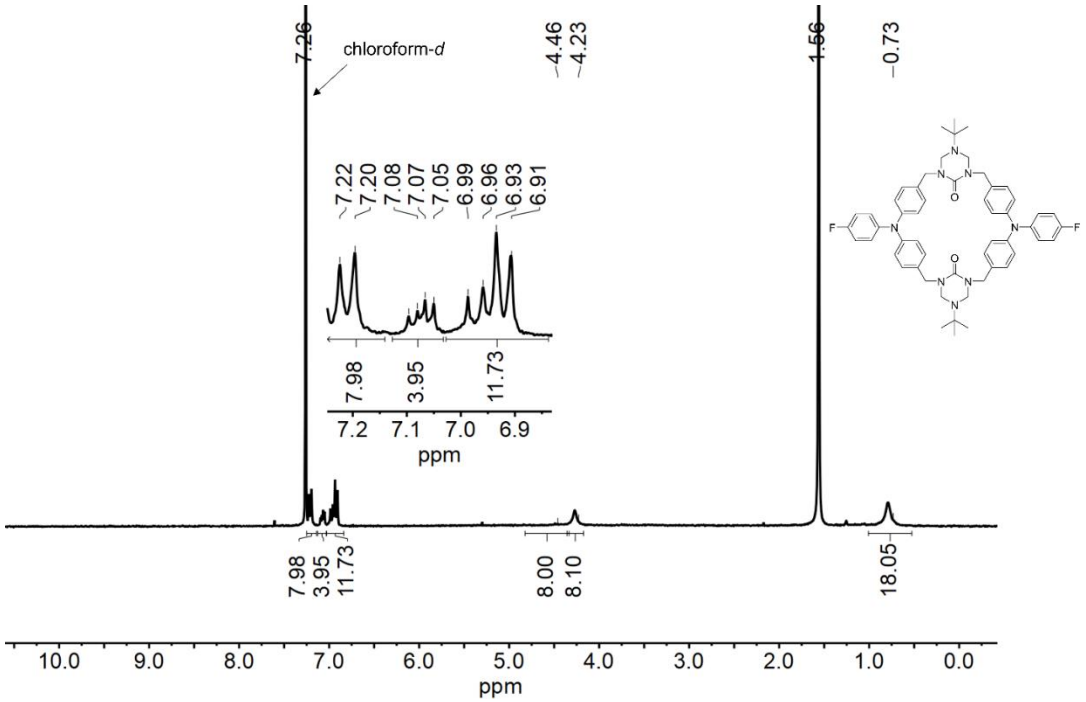

Figure 4.12. ^{1}H NMR ($CDCl_3$, 300 MHz) of the protected macrocycle.

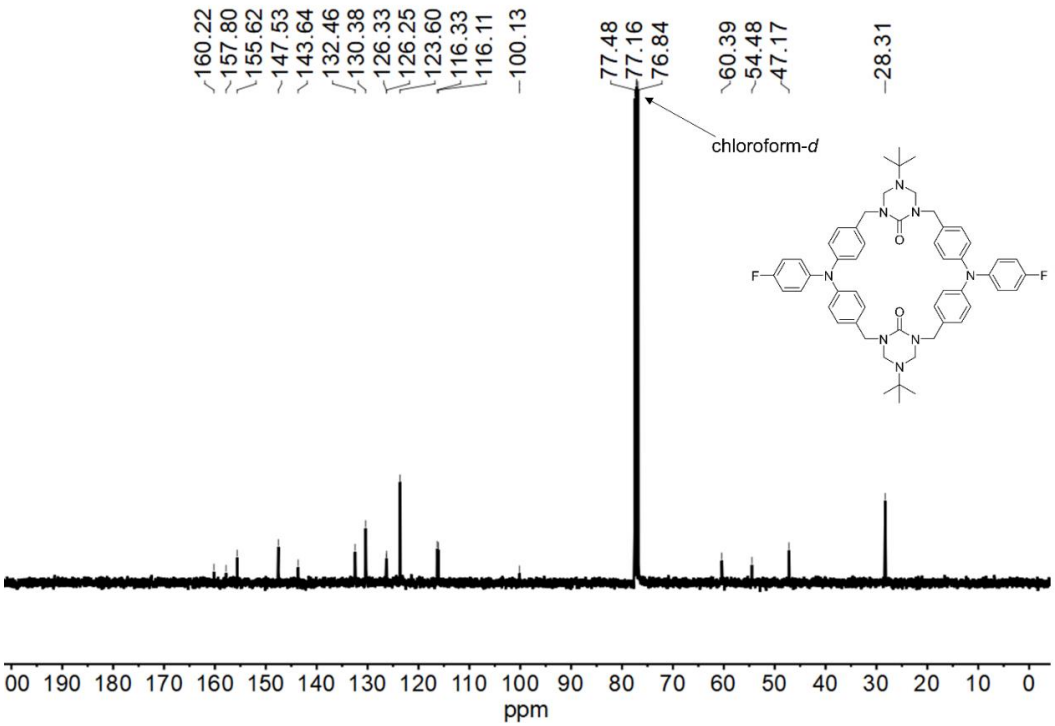

Figure 4.13. ^{13}C NMR ($CDCl_3$, 75 MHz) of the protected macrocycle.

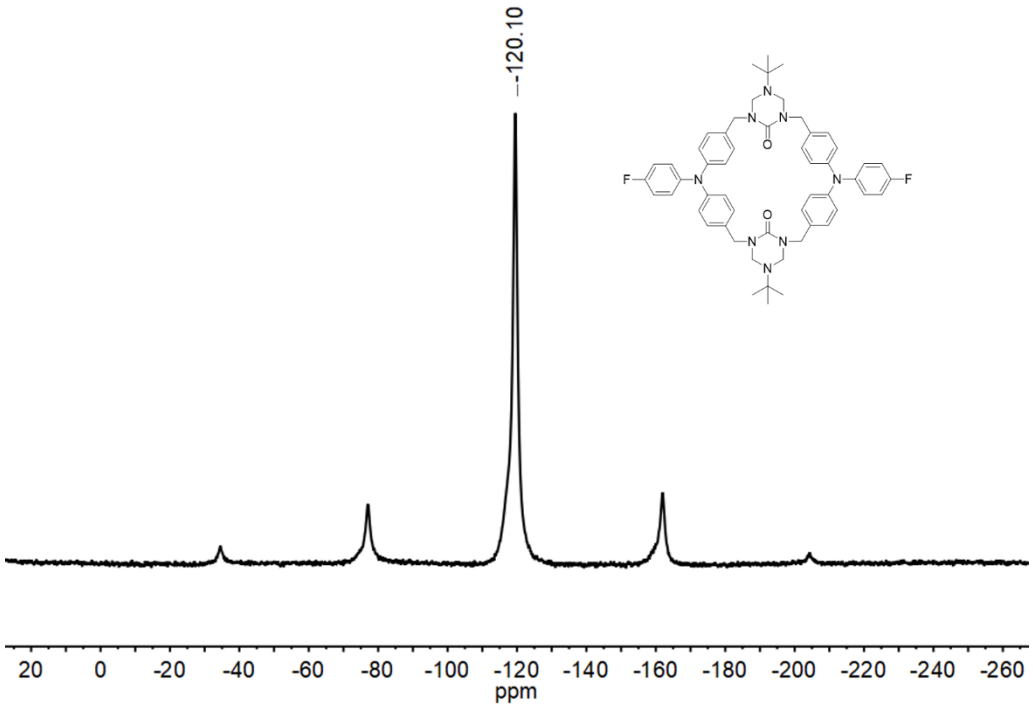

Figure 4.14. ^{19}F solid state NMR

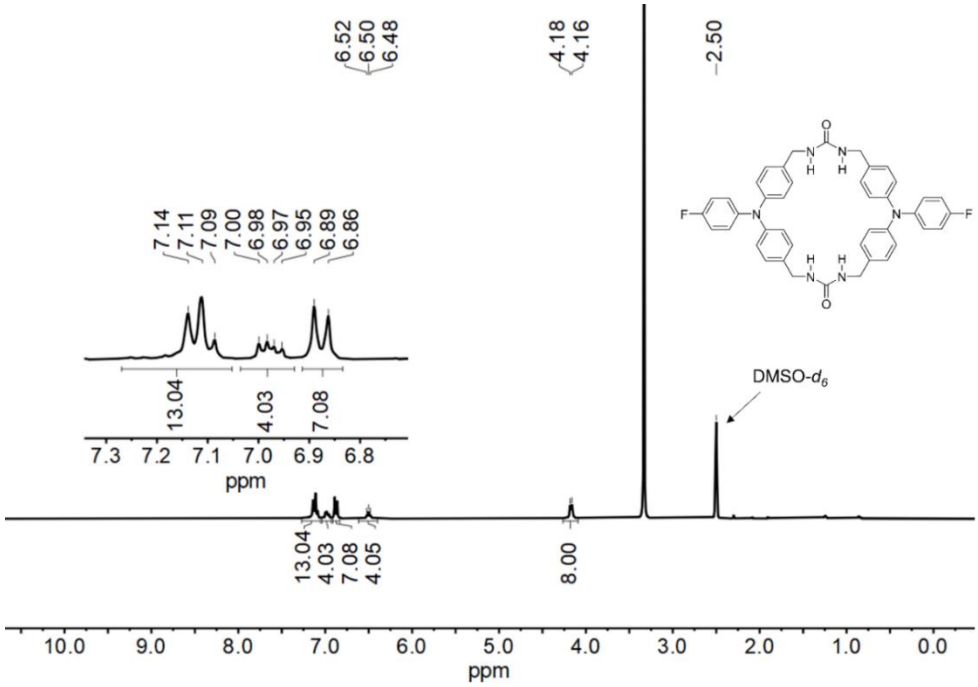

Figure 4.15. ^{1}H NMR ($(CD_3)_2SO$, 300 MHz) of **1F**.

4.8 CRYSTAL DATA AND STRUCTURE REFINEMENT

X-Ray Structure Determination, $C_{54}H_{58}F_2N_8O_2 \cdot 8(CHCl_3)$

X-ray intensity data from a colorless plate were collected at 100(2) K using a Bruker D8 QUEST diffractometer equipped with a PHOTON-II area detector and an Incoatec microfocus source (Mo Kα radiation, λ = 0.71073 Å). The raw area detector data frames were reduced, scaled and corrected for absorption effects using the Bruker APEX3, SAINT+ and SADABS programs.[30,31] The structure was solved with SHELXT.[32] Subsequent difference Fourier calculations and full-matrix least-squares refinement against F^2 were performed with SHELXL-2018[32] using OLEX2.[33]

The compound crystallizes in the triclinic system. The space group *P*-1 (No. 2) was confirmed by structure solution. The asymmetric unit consists of half of one $C_{54}H_{58}F_2N_8O_2$ cycle, which is located on a crystallographic inversion center, and four independent

chloroform molecules. The unique *tert*-butyl group C24-C27 is rotationally disordered over two orientations with occupancies of A/B = 0.85(1)/0.15(1). All four independent $CHCl_3$

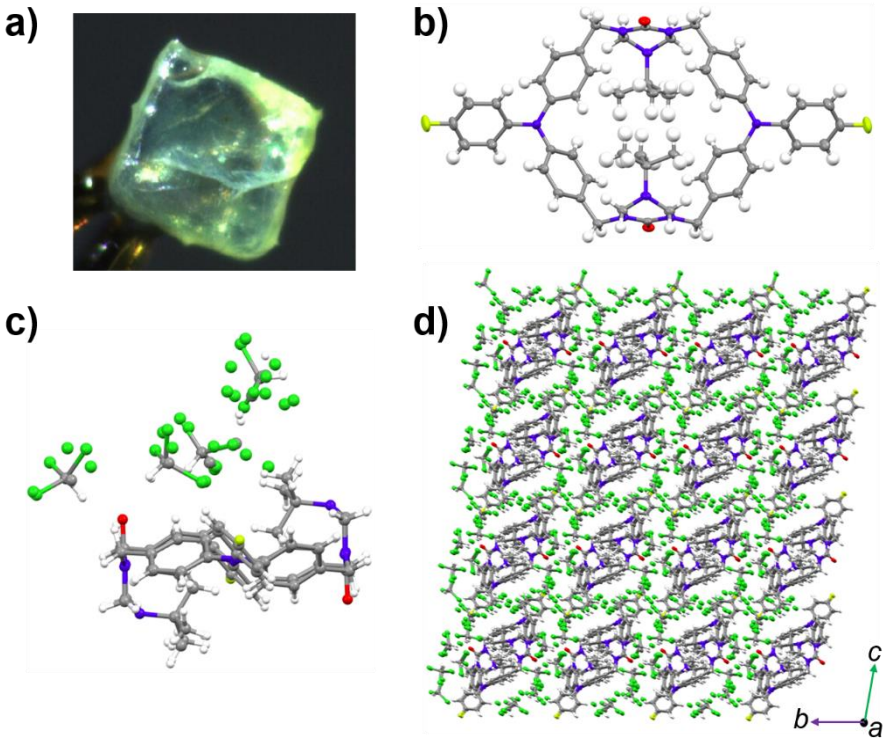

Figure 4.16. Crystals views of protected host **1F**·$(CHCl_3)_8$. a) Data crystal. b) Displacement ellipsoid plot of the cycle. Displacement ellipsoids drawn at the 40% probability level. Superscripts denote symmetry-equivalent atoms. Minor t-butyl disorder omitted. c) One unit cell. d) Crystal packing along *a*-axis.

molecules are disordered. They were modeled with either two (Cl1-Cl3/C31 and Cl4-Cl6/C32), three (Cl7-Cl9/C33), or four (Cl10-Cl21/C34-C37) orientations. Total group occupancies were constrained to sum to one. The minor $CHCl_3$ disorder components were restrained to be geometrically similar to Cl1A-Cl3A/C31A using SHLX SAME instructions. All non-hydrogen atoms were refined with anisotropic displacement parameters except for atoms of minor disorder components (isotropic). Hydrogen atoms were placed in geometrically idealized positions and included as riding atoms with *d*(C-H)

= 1.00 Å and *U*iso(H) = 1.2*U*eq(C) for methine hydrogen atoms, *d*(C-H) = 0.95 Å and *U*iso(H) = 1.2*U*eq(C) for arene hydrogen atoms, *d*(C-H) = 0.99 Å and *U*iso(H) = 1.2*U*eq(C) for methylene hydrogen atoms, and *d*(C-H) = 0.98 Å and *U*iso(H) = 1.5*U*eq(C) for methyl hydrogens. The methyl hydrogens were allowed to rotate as a rigid group to the orientation of maximum observed electron density. The largest residual electron density peak in the final difference map is 0.65 $e^{-}/Å^{3}$, located 0.89 Å from Cl15.

X-Ray Structure Determination, $C_{42}H_{36}F_2N_6O_2 \cdot (C_4H_{10}O_2)_{0.465(2)}$

The compound crystallizes in the triclinic system. The space group *P*-1 (No. 2) was confirmed by structure solution. The ordered part of the asymmetric unit consists of half of one $C_{42}H_{36}F_2N_6O_2$ cycle located on a crystallographic inversion center. Three additional

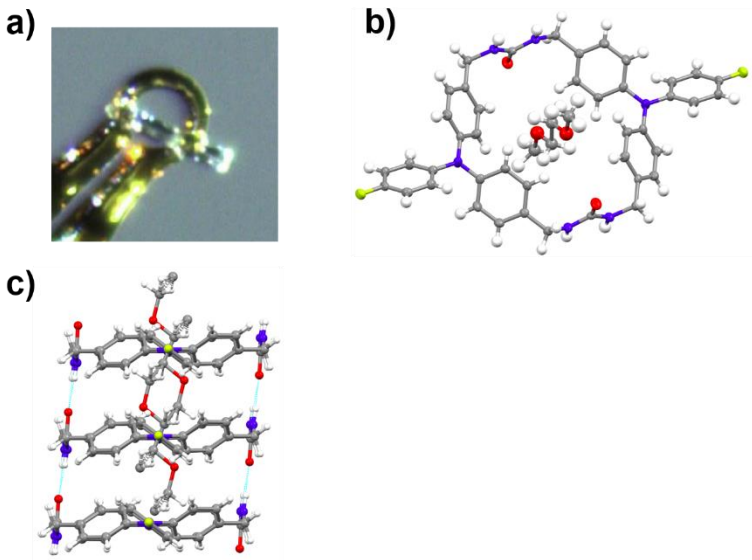

Figure 4.17. Crystal views of host **1F**·$(DME)_{0.465}$. a) Data crystal. b) Components of structure. Displacement ellipsoids drawn at the 50% probability level. Macrocycle and DME located on crystallographic inversion centers. c) DME disordered inside the host.

electron density peaks well above background were observed located inside the tubular channels created by columns of $C_{42}H_{36}F_2N_6O_2$ molecules. The three peaks modeled well

as half (two carbon, one oxygen) of a partially occupied and disordered dimethoxyethane (glyme) molecule, also located on a crystallographic inversion center. The glyme molecule is also located near another symmetry-equivalent, and thus its maximum occupancy is 0.5. Refinement of the glyme group occupancy parameter gave 0.465(4). C-O and C-C distance restraints were applied to maintain a chemically reasonable geometry. All non-hydrogen atoms were refined with anisotropic displacement parameters except for atoms of the disordered glyme guest, which were refined isotropically. Hydrogen atoms bonded to carbon were placed in geometrically idealized positions and included as riding atoms with *d*(C-H) = 0.95 Å and *U*iso(H) = 1.2*U*eq(C) for arene hydrogen atoms, *d*(C-H) = 0.99 Å and *U*iso(H) = 1.2*U*eq(C) for methylene hydrogen atoms and with *d*(C-H) = 0.96 Å and *U*iso(H) = 1.5*U*eq(C) for methyl hydrogen atoms. The two urea hydrogen atoms were located in difference maps and refined freely. The largest residual electron density peak in the final difference map is 0.33 $e^-/Å^3$, located 0.78 Å from H1SC.

Table 4.1. Data Collection and Refinement

Identification code	Host **1F** protected	Host **1F**·$(DME)_{0.465}$
Empirical formula	$C_{62}H_{66}Cl_{24}F_2N_8O_2$	$C_{43.86}H_{40.65}F_2N_6O_{2.93}$
Formula weight	1844.02	736.67
Temperature/K	100(2)	100(2)
Crystal system	triclinic	triclinic
Space group	P-1	P-1
a/Å	12.4509(4)	4.6057(3)
b/Å	12.5093(5)	13.4637(7)
c/Å	13.6812(5)	16.1697(9)
α/°	94.2764(12)	108.437(2)
β/°	104.5147(11)	96.059(2)
γ/°	95.8525(11)	96.921(2)
Volume/$Å^3$	2040.99(13)	933.23(9)
Z	1	1
$\rho_{calc}g/cm^3$	1.500	1.311
μ/mm^{-1}	0.850	0.091
F(000)	936.0	387.0
Crystal size/mm^3	0.4 × 0.36 × 0.18	0.16 × 0.02 × 0.02
Radiation	MoKα (λ = 0.71073)	MoKα (λ = 0.71073)
2Θ range for data collection/°	3.96 to 50.05	4.844 to 50.124
Index ranges	$-14 \le h \le 14$, $-14 \le k \le 14$, $-16 \le l \le 16$	$-5 \le h \le 5$, $-16 \le k \le 16$, $-19 \le l \le 19$
Reflections collected	42997	14094
Independent reflections	7190 [R_{int} = 0.0900, R_{sigma} = 0.0550]	3313 [R_{int} = 0.0492, R_{sigma} = 0.0452]
Data/restraints/parameters	7190/224/551	3313/2/257
Goodness-of-fit on F^2	1.080	1.097
Final R indexes [I>=2σ (I)]	R_1 = 0.0655, wR_2 = 0.1709	R_1 = 0.0532, wR_2 = 0.1098
Final R indexes [all data]	R_1 = 0.0992, wR_2 = 0.1857	R_1 = 0.0765, wR_2 = 0.1185
Largest diff. peak/hole / e $Å^{-3}$	0.65/-0.56	0.33/-0.24

4.9 REFERENCES

(1) Mahmood, A. Triphenylamine Based Dyes for Dye Sensitized Solar Cells: A Review. *Sol. Energy* **2016**, *123*, 127–144.

(2) Petrus, M. L.; Schutt, K.; Sirtl, M. T.; Hutter, E. M.; Closs, A. C.; Ball, J. M.; Bijleveld, J. C.; Petrozza, A.; Bein, T.; Dingemans, T. J.; et al. New Generation Hole Transporting Materials for Perovskite Solar Cells: Amide-Based Small-Molecules with Nonconjugated Backbones. *Adv. Energy Mater.* **2018**, *8*, 1801605.

(3) Pinzón, J. R.; Gasca, D. C.; Sankaranarayanan, S. G.; Bottari, G.; Torres, T.; Guldi, D. M.; Echegoyen, L. Photoinduced Charge Transfer and Electrochemical Properties of Triphenylamine Ih-Sc3N@C80 Donor−Acceptor Conjugates. *J. Am. Chem. Soc.* **2009**, *131*, 7727–7734..

(4) Zhao, J.; Yang, Z.; Chen, X.; Xie, Z.; Liu, T.; Chi, Z.; Yang, Z.; Zhang, Y.; Aldred, M. P.; Chi, Z. Efficient Triplet Harvesting in Fluorescence-TADF Hybrid Warm-White Organic Light-Emitting Diodes with a Fully Non-Doped Device Configuration. *J. Mater. Chem. C* **2018**, *6*, 4257–4264.

(5) Wu, J. H.; Liou, G. S. Substituent and Charge Transfer Effects on Memory Behavior of the Ambipolar Poly(Triphenylamine)S. *ACS Appl. Mater. Interfaces* **2015**, *7*, 15988–15994.

(6) Sophie Roquet; Antonio Cravino; Philippe Leriche; Olivier Alévêque; Pierre Frère, and; Roncali*, J. Triphenylamine−Thienylenevinylene Hybrid Systems with Internal Charge Transfer as Donor Materials for Heterojunction Solar Cells. *J. Am. Chem. Soc.* **2006**, *128*, 3459–3466.

(7) Saddam Hossain, M.; J. Sindt, A.; W. Goodlett, D.; J. Shields, D.; J. O'Connor, C.; Antevska, A.; G. Karakalos, S.; D. Smith, M.; Garashchuk, S.; D. Do, T.; et al. Effects of Self-Assembly on the Photogeneration of Radical Cations in Halogenated Triphenylamines. *J. Phys. Chem. C* **2021**, *125*, 19991-20002.

(8) Moulin, E.; Niess, F.; Maaloum, M.; Buhler, E.; Nyrkova, I.; Giuseppone, N. The Hierarchical Self-Assembly of Charge Nanocarriers: A Highly Cooperative Process Promoted by Visible Light. *Angew. Chemie Int. Ed.* **2010**, *49*, 6974–6978.

(9) Marsh, E. N. G.; Suzuki, Y. Using 19F NMR to Probe Biological Interactions of Proteins and Peptides. *ACS Chem. Biol.* **2014**, *9*, 1242–1250.

(10) Pomerantz, W. C.; Wang, N.; Lipinski, A. K.; Wang, R.; Cierpicki, T.; Mapp, A. K. Profiling the Dynamic Interfaces of Fluorinated Transcription Complexes for Ligand Discovery and Characterization. *ACS Chem. Biol.* **2012**, *7*, 1345–1350.

(11) Rayment, E. J.; Mekareeya, A.; Summerhill, N.; Anderson, E. A. Mechanistic Study of Arylsilane Oxidation through 19F NMR Spectroscopy. *J. Am. Chem. Soc.* **2017**, *139*, 6138–6145.

(12) Dalvit, C.; Vulpetti, A. Ligand-Based Fluorine NMR Screening: Principles and Applications in Drug Discovery Projects. *J. Med. Chem.* **2018**, *62*, 2218–2244.

(13) Krems, B.; Bachert, P.; Zabel, H. J.; Lorenz, W. J. 19F-{1H} Nuclear Overhauser Effect and Proton Decoupling of 5-Fluorouracil and α-Fluoro-β-Alanine. *J. Magn. Reson. Ser. B* **1995**, *108*, 155–164.

(14) Prakash, G. K. S.; Wang, F.; Zhang, Z.; Haiges, R.; Rahm, M.; Christe, K. O.;

Mathew, T.; Olah, G. A. Long-Lived Trifluoromethanide Anion: A Key Intermediate in Nucleophilic Trifluoromethylations. *Angew. Chemie Int. Ed.* **2014**, *53*, 11575–11578.

(15) Sakurai, H.; Kubo, Y.; Shiotani, M.; Yahiro, H.; Okuda, Y. Reduction of poly(tetrafluoroethylene) by aromatic radical anions: An ESR and NMR study. *J. Appl. Polym. Sci.* **1999**, *74*, 286-289.

(16) Zalibera, M.; Machata, P.; Clikeman, T. T.; Rosenkranz, M.; Strauss, S. H.; Boltalina, O. V.; Popov, A. A. 19F NMR-, ESR-, and Vis-NIR-Spectroelectrochemical Study of the Unconventional Reduction Behaviour of a Perfluoroalkylated Fullerene: Dimerization of the C70(CF3)10− Radical Anion. *Analyst* **2015**, *140*, 7209–7216.

(17) Sindt, A. J.; Dehaven, B. A.; McEachern, D. F.; Dissanayake, D. M. M. M.; Smith, M. D.; Vannucci, A. K.; Shimizu, L. S. UV-Irradiation of Self-Assembled Triphenylamines Affords Persistent and Regenerable Radicals. *Chem. Sci.* **2019**, *10*, 2670–2677.

(18) Sindt, A. J.; Dehaven, B. A.; Goodlett, D. W.; Hartel, J. O.; Ayare, P. J.; Du, Y.; Smith, M. D.; Mehta, A. K.; Brugh, A. M.; Forbes, M. D. E.; et al. Guest Inclusion Modulates Concentration and Persistence of Photogenerated Radicals in Assembled Triphenylamine Macrocycles. *J. Am. Chem. Soc.* **2020**, *142*, 502–511.

(19) Wang, L.; Shi, Y.; Zhao, Y.; Liu, H.; Li, X.; Bai, M. Push-Pull 1,8-Naphthalic Anhydride with Multiple Triphenylamine Groups as Electron Donor. *J. Mol. Struct.* **2014**, *1056–1057*, 339–346.

(20) Li, Z.; Dong, Q.; Xu, B.; Li, H.; Wen, S.; Pei, J.; Yao, S.; Lu, H.; Li, P.; Tian, W. New Amorphous Small Molecules - Synthesis, Characterization and Their Application in Bulk Heterojunction Solar Cells. *Sol. Energy Mater. Sol. Cells* **2011**, *95*, 2272–2280.

(21) Tian, H.; Yang, X.; Chen, R.; Zhang, R.; Hagfeldt, A.; Sun, L. Effect of Different Dye Baths and Dye-Structures on the Performance of Dye-Sensitized Solar Cells Based on Triphenylamine Dyes. *J. Phys. Chem. C* **2008**, *112*, 11023–11033.

(22) Dubinina, G. G.; Price, R. S.; Abboud, K. A.; Wicks, G.; Wnuk, P.; Stepanenko, Y.; Drobizhev, M.; Rebane, A.; Schanze, K. S. Phenylene Vinylene Platinum(II) Acetylides with Prodigious Two-Photon Absorption. *J. Am. Chem. Soc.* **2012**, *134* (47), 19346–19349.

(23) Bondi, A. Van Der Waals Volumes and Radii. *J. Phys. Chem.* **1964**, *68*, 441–451.

(24) Spackman, M. A.; Jayatilaka, D. Hirshfeld Surface Analysis. *CrystEngComm* **2009**, *11*, 19–32.

(25) Shao, Y.; Gan, Z.; Epifanovsky, E.; Gilbert, A. T. B.; Wormit, M.; Kussmann, J.; Lange, A. W.; Behn, A.; Deng, J.; Feng, X.; et al. Advances in Molecular Quantum Chemistry Contained in the Q-Chem 4 Program Package. *Mol. Phys.* **2015**, *113* (2), 184–215.

(26) *Spartan'18*, ver. 1.4.4; Wavefunction, Inc.: Irvine, CA, 2019.

(27) Devlin, F. J.; Finley, J. W.; Stephens, P. J.; Frisch, M. J. Ab Initio Calculation of Vibrational Absorption and Circular Dichroism Spectra Using Density Functional Force Fields: A Comparison of Local, Nonlocal, and Hybrid Density

Functionals. *J. Phys. Chem.* **1995**, *99* , 16883–16902.

(28) Ditchfield, R.; Hehre, W. J.; Pople, J. A. Self-Consistent Molecular-Orbital Methods. IX. An Extended Gaussian-Type Basis for Molecular-Orbital Studies of Organic Molecules. *J. Chem. Phys.* **1971**, *54*, 720–723.

(29) Yanai, T.; Tew, D. P.; Handy, N. C. A New Hybrid Exchange-Correlation Functional Using the Coulomb-Attenuating Method (CAM-B3LYP). *Chem. Phys. Lett.* **2004**, *393* (1–3), 51–57.

(30) APEX III, Version 2016.5-0 and SAINT+, Version 8.37A; Bruker AXS, Inc., Madison, Wisconsin, USA, 2016.

(31) Krause, L.; Herbst-Irmer, R.; Sheldrick, G. M.; Stalke, D. Comparison of Silver and Molybdenum Microfocus X-Ray Sources for Single-Crystal Structure Determination. *J. Appl. Crystallogr*, **2015**, *48*, 3–10.

(32) Sheldrick, G. M. SHELXT – Integrated Space-Group and Crystal-Structure Determination. *Acta Crystallogr. A* **2015**, *71*, 3–8.

(33) Dolomanov, O. V.; Bourhis, L. J.; Gildea, R. J.; Howard, J. A. K.; Puschmann, H. OLEX2: A Complete Structure Solution, Refinement and Analysis Program. *J. Appl. Crystallogr*. **2009**, *42*, 339–341.

APPENDIX A:

PERMISSION TO REPRINT CHAPTER 2

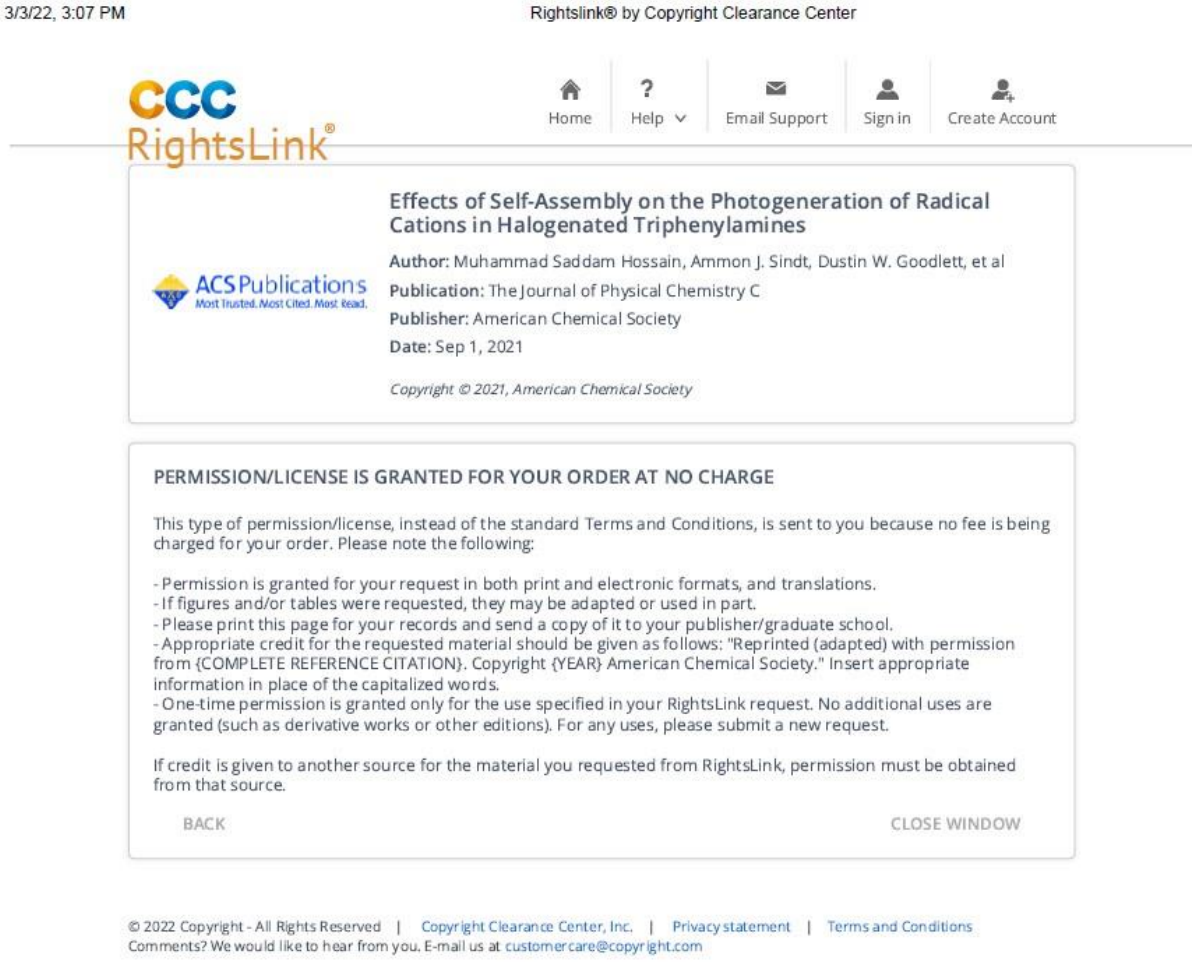

3/3/22, 3:07 PM Rightslink® by Copyright Clearance Center

CCC RightsLink®

Home | Help | Email Support | Sign in | Create Account

ACS Publications
Most Trusted. Most Cited. Most Read.

Effects of Self-Assembly on the Photogeneration of Radical Cations in Halogenated Triphenylamines

Author: Muhammad Saddam Hossain, Ammon J. Sindt, Dustin W. Goodlett, et al
Publication: The Journal of Physical Chemistry C
Publisher: American Chemical Society
Date: Sep 1, 2021

Copyright © 2021, American Chemical Society

PERMISSION/LICENSE IS GRANTED FOR YOUR ORDER AT NO CHARGE

This type of permission/license, instead of the standard Terms and Conditions, is sent to you because no fee is being charged for your order. Please note the following:

- Permission is granted for your request in both print and electronic formats, and translations.
- If figures and/or tables were requested, they may be adapted or used in part.
- Please print this page for your records and send a copy of it to your publisher/graduate school.
- Appropriate credit for the requested material should be given as follows: "Reprinted (adapted) with permission from {COMPLETE REFERENCE CITATION}. Copyright {YEAR} American Chemical Society." Insert appropriate information in place of the capitalized words.
- One-time permission is granted only for the use specified in your RightsLink request. No additional uses are granted (such as derivative works or other editions). For any uses, please submit a new request.

If credit is given to another source for the material you requested from RightsLink, permission must be obtained from that source.

BACK CLOSE WINDOW

© 2022 Copyright - All Rights Reserved | Copyright Clearance Center, Inc. | Privacy statement | Terms and Conditions
Comments? We would like to hear from you. E-mail us at customercare@copyright.com